



Novel Thermoresponsive Hydrogels Based on Poly(2-oxazoline)s and Poly(2-oxazine)s and their Application in Biofabrication

Neuartige Thermoresponsive Hydrogele Basierend auf Poly(2-oxazoline) und Poly(2-oxazine) und die Anwendung in der Biofabrikation

Dissertation zur Erlangung des naturwissenschaftlichen Doktorgrades
der Graduate School of Life Sciences,
Julius-Maximilians-Universität Würzburg

Vorgelegt von

Lukas Hahn

aus

Haßfurt

Würzburg **2021**



Eingereicht am:

Bürostempel

Mitglieder des Promotionskomitees:

Vorsitzende/r: Prof. Dr. Carmen Villmann

1. Betreuer: Prof. Dr. Robert Luxenhofer

2. Betreuer: Prof. Dr. Tessa Lühmann

3. Betreuer: Prof. Dr. Gregor Lang

Tag des Promotionskolloquiums:

Doktorurkunden ausgehändigt am:

Content

Danksagung	III
List of Publications	V
Abbreviations and Symbols	VIII
1 Introduction	1
2 State of Knowledge	3
2.1 Hydrogels as Biomaterials	3
2.1.1 Definitions, Classifications and the 1 st Generation of Hydrogels	3
2.1.2 Thermoresponsive Hydrogels	6
2.1.3 <i>In Situ</i> Covalent Crosslinking	9
2.1.4 Double Network-, Multi-Component- and Composite Hydrogels	11
2.2 Bioprinting: A Technology of Biofabrication for Tissue Engineering and Regenerative Medicine	12
2.2.1 Definitions	12
2.2.2 Bioprinting Technologies	13
2.2.3 Bioink Development	15
2.2.3.1 Rheology of Bioinks	17
2.2.3.2 Printability of Bioinks	21
2.2.3.3 Materials for Bioink Development	22
2.3 Poly(2-oxazoline)s and Poly(2-oxazine)s	25
2.3.1 Synthesis	25
2.3.2 Aqueous Solubility and Self-Assembly	31
2.3.3 Biomaterial Applications	35
2.3.3.1 Nanoformulations	35

	2.3.3.2 Hydrogels	38
3	Summary	41
4	Zusammenfassung	42
5	Main Part	43
	Chapter I	44
	Chapter II	56
	Chapter III	104
	Chapter IV	129
6	Discussion	146
	6.1 Drug Encapsulation	146
	6.2 Self-Assembly and Inverse Thermogelation	148
	6.3 Inverse Thermogelling Hydrogels for Biofabrication	152
	6.4 Thermogelling POx/POzi Hydrogels for Biofabrication	154
7	References	156
8	Material and Methods	170
	Declaration of Authorship	171
	Affidavit	177
	Eidesstattliche Erklärung	177
	Curriculum Vitae	178

Danksagung

Zunächst möchte ich mich bei Allen bedanken, die mit mir den spannenden und formenden Weg dieser wissenschaftlichen Arbeit gegangen sind.

Insbesondere bedanke ich mich bei meinem Doktorvater Prof. Dr. Robert Luxenhofer. Bereits die ersten Treffen waren geprägt von Interesse und Respekt, wissenschaftlichem Enthusiasmus und der uneingeschränkten Bereitschaft mich zu fordern und fördern, wissenschaftlich und persönlich. Das in mich gesetzte Vertrauen ermöglichte mir eine sehr freie Projekt- und Interessensgestaltung, wofür ich sehr dankbar bin. Auch die Integration in verschiedenste Forschungsprojekte ermöglichte es mir meine wissenschaftliche Entwicklung voranzutreiben. Die Teilnahme an wissenschaftlichen Konferenzen, Tagungen, Seminarrunden und Kursen wurde stets unterstützt, was ich sehr wertschätze.

Frau Prof. Dr. Tessa Lühmann und Herrn Prof. Dr. Gregor Lang danke ich für die wissenschaftliche Begleitung meiner Promotion im Rahmen des Promotionsstudiums der *Graduate School of Life Science* der Universität Würzburg. Dem gesamten Team der graduierten Schule der Universität Würzburg danke ich für das strukturierte Promotionsprogramm.

Dem gesamten Lehrstuhl für chemische Technologie der Materialsynthese danke ich für die professionelle Atmosphäre. Ulrike Mitbö und Diana Stürmer danke ich für die Hilfe bei organisatorischen Fragen. Ausdrücklich möchte ich mich bei Sandra Stockmann bedanken, welche ein sicheres Arbeiten in allen Laboren gewährleistete und gerade in der COVID 19-Pandemie mit der Umsetzung eines funktionierenden Hygienekonzeptes den wissenschaftlichen Lehrstuhlbetrieb weiterhin ermöglichte.

Die technische Unterstützung im Laboralltag von Anna Kucharski und Christian May waren das Fundament jeglicher wissenschaftlichen Arbeit. Gerade die Durchführung zweier „Kg-Batches“ wären ohne Christian nicht zu realisieren gewesen.

Auf die Expertise von Dr. Guntram Schwarz war allseits Verlass. Auch die Bewältigung eines „Cyber“-Angriffes blieb dank dir ohne größere Schäden.

Ich möchte allen Doktoranden und Studenten des AK Luxenhofers danken (inklusive Robin, Mira und Markus). Das gemeinsame Mittagessen, die jährlichen Ausflüge (Boseln und Kanufahren), die Weihnachtsfeiern und der Triumph beim „Chem-Cup“ 2019 kann uns keiner mehr nehmen. Vielen Dank Thomas, Niklas, Michael, Haider, Daniel, Jochen, Julian, Christine, Solomiia, Mengshi, Chen und Sebastian. Vielen Dank Stefan für die tolle Zeit im besten Büro des Gebäudes.

Ich möchte mich für die synergistischen Effekte bei allen Kooperationspartnern bedanken; Hatice Genc, Stephan Altmann, Prof. Dr. Regina Ebbert, David Sonnleitner, Prof. Dr. Gregor Lang, Dr. Miroslav Mrlik, Tillmann Esser, Prof. Dr. Felix Engel, Dr. Constantin Berger, Dr. Daniela Zdzieblo, Phillip Stahlhut, Dr. Bernhard Schummer, Dr. Benedikt Sochor, Dr. Sebastian Jacksch, Theresa Zorn, Prof. Dr. Ann-Christin Pöppler, Vanessa Flegler, Prof. Dr. Bettina Böttcher, Emine Karakaya, Dr. Rainer Detsch, Ruben Scheuring, Vanessa Trossmann, Prof. Dr. Thomas Scheibel, Leo Forster, Tobias Kielholz, Prof. Dr. Maike Windbergs, Marius Gensler, Dr. Nikita Durandin, Prof. Dr. Timo Laaksonen, Josef Kehrein, Prof. Dr. Christoph Sotriffer und Dr. Vladimir Aseyev. Der Einblick in verschiedenste Methoden, Arbeitsweisen und Diskussionen haben sowohl die wissenschaftliche Arbeit, als auch meinen persönlichen Horizont erweitert.

Ausdrücklich möchte ich mich bei Matthias Beudert und Prof. Dr. Tessa Lühmann für die gemeinschaftliche Bearbeitung des DFG geförderten SFB TRR225 Teil-Projekt A03 bedanken.

Ich möchte mich nochmals bei Prof. Dr. Robert Luxenhofer bedanken für die Möglichkeit die Lehre und Betreuung von Studenten im Rahmen von Praktika und Abschlussarbeiten aktiv mitzugestalten. In diesem Zusammenhang möchte ich mich bei den Projektstudenten Lando Polzin und Anna-Lena Ziegler, Bacheloranden Simon Hammer, Maxim Melnikov und Max Lindner, und den Masteranden Matthias Maier, Fabian Töppke, Alexander Altmann, Dario Polzin und Larissa Keßler bedanken. Eure wissenschaftlichen Projekte und eure Persönlichkeiten haben mich geprägt und wissenschaftlich und persönlich weiterentwickelt. Vielen Dank für diese Erfahrungen.

Darüber hinaus möchte ich mich bei Sophia Löffelsend, Larissa Keßler und Dario Polzin für euren Einsatz als Hilfwissenschaftler danken.

Ich möchte mich bei der Gesellschaft Deutscher Chemiker, dem Freistaat Bayern und insbesondere der Deutschen Forschungsgemeinschaft für die Finanzierung meiner Forschungsarbeiten und –Reisen bedanken. Insbesondere danke ich dem gesamten Forschungsverbund SFB TRR225.

Als letztes möchte ich mich bei meinen Liebsten bedanken. Großer Dank gebührt meiner Familie, insbesondere meinen Eltern. Ohne euch wäre ich nicht das geworden, was ich heute bin. Auch wenn nicht jede meiner Lebensentscheidungen verstanden wurde, so wurden diese doch immer akzeptiert und unterstützt. Als aller letztes bedanke ich mich bei meiner Partnerin Sarah. Mit dir an meiner Seite kann ich alle „Ups“ and „Downs“ des Lebens meistern.

Für Leonard

List of Publications

All printed manuscripts are highlighted in bold letters.

Drug Encapsulation

[M1]

Drug Specificity, Synergy and Antagonism in Ultrahigh Capacity Poly(2-oxazoline)/Poly(2-oxazine) Based Formulations

Lübtow M.M., Hahn L., Haider M.S., Luxenhofer R., *Journal of the American Chemical Society* **2017**, 139 (32), 10980-10983

[M2]

Investigating the Influence of Aromatic Moieties on the Formulation of Hydrophobic Natural Products and Drugs in Poly(2-oxazoline)-Based Amphiphiles

Hahn L., Lübtow M.M., Lorson T., Schmitt F., Appelt-Menzel A., Schobert R., Luxenhofer R., *Biomacromolecules* **2018**, 19 (7), 3119-3128

[M3]

Low Dose Novel PARP-PI3K Inhibition via Nanoformulation Improves Colorectal Cancer Immunoradiotherapy

Landry M.R., DuRoss A.N., Neufeld M.J., Hahn L., Sahay G., Luxenhofer R., Sun C., *Materials Today Bio* **2020**, 8, 100082

Hydrogels

[M4]

Temperature-Dependent Rheological and Viscoelastic Investigation of a Poly(2-methyl-2-oxazoline)-b-poly(2-iso-butyl-2-oxazoline)-b-poly(2-methyl-2-oxazoline)-Based Thermogelling Hydrogel

Lübtow M.M., Mrlik M., Hahn L., Altmann A., Beudert M., Lühmann T., Luxenhofer R., *Journal of Functional Biomaterials* **2019**, 10(3), 36

[M5]

Inverse Thermogelation of Aqueous Triblock Copolymer Solutions into Macroporous Shear-Thinning 3D Printable Inks

Hahn L., Maier M., Stahlhut P., Beudert M., Flegler V., Forster S., Altmann A., Töppke F., Fischer K., Seiffert S., Böttcher B., Lühmann T., Luxenhofer R., *ACS Applied Materials and Interfaces* **2020**, 12 (11), 12445-12456

[M6]

Improving Printability of a Thermoresponsive Hydrogel Biomaterial Ink by Nanoclay Addition

Hu C., Hahn L., Yang M., Altmann A., Stahlhut P., Groll J., Luxenhofer R., *Journal of Materials Science* **2021**, 56 (1), 691-705

[M7]

From Thermogelling Hydrogels Towards Functional Bioinks: Controlled Modification and Cytocompatible Crosslinking

Hahn L.*, Beudert M.*, Gutmann M., Keßler L., Stahlhut P., Fischer L., Karakaya E., Lorson T., Thievensen I., Detsch R., Lühmann T., Luxenhofer R., *Macromolecular Bioscience* **2021**, DOI: 10.1002/mabi.202100122

*Contributed equally

[M8]

An Inverse Thermogelling Bioink Based on an ABA Type Poly(2-oxazoline) Amphiphile

Hahn L., Karakaya E., Zorn T., Sochor B., Maier M., Stahlhut P., Forster S., Fischer K., Seiffert S., Pöppler A.-C., Detsch R., Luxenhofer R., *Biomacromolecules* **2021**, 22 (7), 3017-3027

[M9]

Development of a 3D Printable and Highly Stretchable Ternary Organic-Inorganic Nanocomposite Hydrogel

Hu C., Haider M.S., Hahn L., Yang M., Luxenhofer R., *Journal of Materials Chemistry B* **2021**, 9, 4535-4545

[M10]

ABA Type Amphiphiles with Poly(2-benzhydryl-2-oxazine) Moieties: Synthesis, Characterization and Inverse Thermogelation

Hahn L., Keßler L., Polzin L., Fritze L., Forster S., Helten H., Luxenhofer R., *Macromolecular Chemistry and Physics* **2021**, 222: 2100114, DOI: 10.1002/macp.202100114

[M11]

Tuning the Thermogelation and Rheology of Poly(2-oxazoline)/Poly(2-oxazine)s Based Thermosensitive Hydrogels for 3D Bioprinting

Haider M.S., Ahmad T., Yang M., Hu C., Hahn L., Stahlhut P., Groll J., Luxenhofer R., *Gels* **2021**, 7 (3), 78, DOI:10.3390/gels7030078

[M12]

Unravelling a Novel Mechanism in Polymer Self-Assemblies: An Order-Order Transition Based on Molecular Interactions Between Hydrophilic and Hydrophobic Polymer Blocks

Hahn L., Zorn T., Kehrein J., Kielholz T., Ziegler A.-L., Forster S., Sochor B., Lisitsyna E.S., Durandin N., Laaksonen T., Aseyev V., Sottriffer C., Windbergs M., Pöppler A.-C., Luxenhofer R., ChemRxiv. Cambridge: Cambridge Open Engage; **2021**; This content is a preprint and has not been peer-reviewed

[M13]

A Thermogelling Organic-Inorganic Hybrid Hydrogel with Excellent Printability, Shape Fidelity and Cytocompatibility for 3D Bioprinting

Hu C., Ahmad T., Haider M.S., Hahn L., Stahlhut P., Groll J., Luxenhofer R., *Biofabrication* **2021**, accepted manuscript

[M14]

Freeform Direct Laser Writing of Versatile Topological 3D Scaffolds Enabled by Intrinsic Support Hydrogel

Hasselmann S., Hahn L., Lorson T., Schätzlein E., Sebastien I., Beudert M., Lühmann T., Neubauer J.C., SEXTL G., Luxenhofer R., Heinrich D., *Materials Horizons* **2021**, 8, 3334-3344

Others

[M15]

Structure and Nucleic Acid Binding Properties of KOW Domains 4 and 6-7 of Human Transcription Elongation Factor DSIF

Zuber P.K., Hahn L., Reinl A., Schweimer K., Knauer S.H., Gottesman M.E., Rösch P., Wöhrl B.M., *Scientific Reports* **2018**, 8 (1), 1-12

[M16]

Matrix Decoded- A Pancreatic Extracellular Matrix with Organ Specific Cues Guiding Human iPSC Differentiation

Berger C., Bjørlykke Y., Hahn L., Mühlemann M., Kress S., Walles H., Luxenhofer R., Ræder H., Metzger M., Zdziebło D., *Biomaterials* **2020**, 244, 119766

Abbreviations and Symbols

Abbreviations and symbols that appear in a reprinted manuscript are not listed here. Such abbreviations and symbols are explained in the respective manuscript.

General Abbreviations

AM	additive manufacturing
CEST	central European summer time
c_{gel}	critical gelation concentration
COVID	Coronavirus disease
CRC	colorectal cancer
CROP	cationic ring opening polymerization
CTLA-4	cytotoxic T-lymphocyte-associated protein 4
CUR	curcumin
DBB	droplet-based bioprinting
DLS	dynamic light scattering
EBB	extrusion-based bioprinting
ECM	extracellular matrix
EIP	ethyl-isonipecotate
e.g.	<i>lat. exempli gratia</i> (engl. “for example”)
hADSC	human adipose derived stem cells
IPN	interpenetrating network
LBB	laser-based bioprinting
LCST	lower critical solution temperature
LVE	linear viscoelastic
MEW	melt electro writing
NMR	nuclear magnetic resonance
PARP	poly-adenosine diphosphate-ribose-polymerase
PISA	polymerization-induced self-assembly
PI3K	phosphoinositide 3-kinase
PTX	paclitaxel
RGD	Arg-Gly-Asp, Arginine-Glycine-Aspartate

RM	regenerative medicine
SAXS	small-angle X-ray scattering
SANS	small-angle neutron scattering
SchA	schizandrin A
SI	supporting information
TE	tissue engineering
TEM	transmission electron microscopy
t_{gel}	critical gelation temperature
UCST	upper critical solution temperature
UV	ultraviolet
WHO	World Health Organization
2D	two-dimensional
2PP	two-photon polymerization
3D	3-dimensional

Monomers and (Bio)Polymers

Alg	alginate
DNA	deoxyribonucleic acid
EGDMA	ethylene glycol dimethacrylate
GelMA	gelatin methacryloyl
HA	hyaluronic acid
L-PEI	linear polyethylenimine
L-PPI	linear polypropylenimine
MC	methylcellulose
MeOx	2-methyl-2-oxazoline
MeOzi	2-methyl-2-oxazine
Ox	2-substituted-2-oxazoline
Ozi	2-substituted-2-oxazine
PB	poly(butadiene)
PBhOx	poly(2-benzhydryl-2-oxazoline)
PBhOzi	poly(2-benzhydryl-2-oxazine)
PButenOx	poly(2-(3-butenyl)-2-oxazoline)
PBzOx	poly(2-benzyl-2-oxazoline)
PBzOzi	poly(2-benzyl-2-oxazine)
PCL	poly(ϵ -caprolactone)
PEG	polyethylene glycol
PEtOx	poly(2-ethyl-2-oxazoline)
PEtOzi	poly(2-ethyl-2-oxazine)
PHEMA	poly(2-hydroxyethyl methacrylate)
PiBuOx	poly(2-iso-butyl-2-oxazoline)
PLGA	poly(lactic-co-glycolic acid)
PNAGA	poly(N-acryloyl glycinamide)
PnBuOx	poly(2-n-butyl-2-oxazoline)
PnBuOzi	poly(2-n-butyl-2-oxazine)
PNIPAAM	poly(N-isopropylacrylamide)
PnPrOx	poly(2-n-propyl-2-oxazoline)
PnPrOzi	poly(2-n-propyl-2-oxazine)

POx	poly(2-oxazoline)
POzi	poly(2-oxazine)
PPhenEtOx	poly(2-phenethyl-2-oxazoline)
PPhenEtOzi	poly(2-phenethyl-2-oxazine)
PPheOx	poly(2-phenyl-2-oxazoline)
PPheOzi	poly(2-phenyl-2-oxazine)
PPO	poly(propylene oxide)
PVA	poly(vinyl alcohol)

Symbols and Units

D	dispersity
G'	storage modulus
G''	loss modulus
T_{CP}	cloud point temperature
$\tan(\delta)$	loss factor
®	registered trademark symbol
η	viscosity
η_0	zero shear viscosity
$\dot{\gamma}$	shear rate
ω	angular frequency
π	mathematical constant (pi)
τ	shear stress
τ_f	flow stress
τ_0	yield stress
°C	degree Celsius
g	gram
h	hours
L	liter
nm	nanometer
kPa	kilopascal
s	second
wt. %	weight percent

1 Introduction

On December 30, 2019, the World Health Organization (WHO) registered the first coronavirus disease 19 (COVID-19) case and the worldwide pandemic started. “Globally, as of 6:02 pm CEST, 22 April 2021, there have been 143,445,675 confirmed cases of COVID-19, including 3,051,736 deaths, reported to WHO.”¹ However, there is also a ray of hope, as years of fundamental research opened the possibility to develop novel vaccines in a very short time. “As of 22 April 2021, a total of 889,990,259 vaccine doses have been administered.”¹

The vaccine from Moderna together with the National Institute of Allergy and Infectious Diseases is among the most important COVID-19 vaccines. This vaccine contains, inter alia, surfactants such as PEGylated lipids to stabilize and solubilize the active pharmaceutical ingredient.² Thus, the vaccine contains the hydrophilic synthetic polymer polyethylene glycol (PEG). This example shows that polymers can be found everywhere in our daily life, including biomaterials. Polymers were first described by Hermann Staudinger 101 years ago. In his paper “*Über Polymerisation*” several reactions (polymerizations) were presented.³ The products were macromolecules with high molecular weight comprising a large number of small molecules (repeating units) linked by covalent bonds. This innovative concept covering natural and synthetic polymers was the basis for a huge set of polymeric materials and related applications.

Especially, PEG-based materials have a long history in the development of novel biomaterials and therefore PEG is referred as the gold standard material. Hence, PEG based materials are processed in cosmetics and various other household products, which is why most people have been exposed to PEG. This can lead to the production of anti-PEG antibodies in the blood.⁴ Consequently, the administration of PEGylated formulations during a clinical therapy can potentially cause the loss of therapeutic efficacy and an increase in adverse effects due to an enhanced immune response. Considering this, there is a tremendous need for the development of novel polymers with tunable physicochemical properties and a biological safe profile.

In the attempt to find alternatives, the polymer classes of poly(2-oxazoline)s (POx) and poly(2-oxazine)s (POzi) repeatedly come to the fore. These polymer classes offer a great chemical versatility in combination with consistently good biological properties. As such, they have already been used in drug delivery, surface coatings and regenerative medicine (RM). One promising POx-drug conjugate system tackling different highly relevant diseases such as Parkinson’s disease, is currently in Phase II clinical trials being developed by Serina Therapeutics®.^{5,6}

Modern cell cultures try to take into account the hierarchical 3-dimensional (3D) structure of the natural microenvironment of cells. In recent years, the idea has evolved to generate functional tissue models and in the end implants consisting of matured autologous tissue with defined form and function using the principles of additive manufacturing (AM). The young research field, which dedicates itself to this challenging task, is called biofabrication. One of the biggest challenges in this research area is to develop materials that allow precise manufacturing in combination with biological functionality in order to obtain a functional tissue model. In this context, hydrogels have proven to be promising materials since they can be optimized with regard to biologically important parameters such as strength and water content and be processed with various fabrication technologies like 3D bioprinting. Hydrogels comprising POx/POzi, however, are rarely discussed in literature, especially when it comes to biofabrication.

In order to address specific applications, first, the underlying molecular mechanism should be understood. Therefore, in this work, structure-property relationships of novel POx/POzi-based hydrogels are studied in detail, thus unravelling unique gelation mechanisms. Furthermore, the hydrogels were discussed in different approaches in the upcoming research area of biofabrication.

2 State of Knowledge

2.1 Hydrogels as Biomaterials

“The term ‘gel’ is used so indiscriminately that it has become ambiguous.” Moreover, the “gel state [...] is easier to recognize than to define.”

With these words, Kramer and co-workers start a very detailed and descriptive discussion on the various definitions of a gel in 1992 (the year I was born).⁷ In the first issue of the journal *Polymer Gels and Networks*, they deal controversially with the different definitions in the literature and at the end try to define the minimum criteria of a gel.

2.1.1 Definitions, Classifications and the 1st Generation of Hydrogels

Hydrogels are challenging to define due to the different characteristics of a gel and their use by scientists from a wide variety of fields, including biology, physical chemistry and material science. The terms **hydrosol** (liquid phase) and **hydrogel** (gelatinous phase) were already introduced in 1864 by Thomas Graham, who studied the properties of silicic acid in water.⁸ By replacing the water with alcohol, he defined alcosols and alcogels, which are nowadays called organogels. At this time, physicochemical methods for studying different states of matter were not yet established, which is why phenomenological characteristics were used for definitions. Thus, a gel must contain at least two components:⁹ a liquid, which is water in the case of a hydrogel, and a gelator. A formed hydrogel can relieve its own weight and reacts under mechanical stress with the phenomenon of strain (**See 2.2.3.1 Rheology of Bioinks**). Later, Flory introduced that all gels have a continuous structure and defined four types of gel systems.¹⁰

(I) Well-ordered lamellar structures, including gel mesophases.

(II) Covalent polymeric networks, completely disordered.

(III) Polymer networks formed through physical aggregation.

(IV) Particulate, disordered structures.

Compounds able to form gels defined by Flory are versatile as inorganic clays, (bio)polymers, proteins, colloids and small organic compounds. In line with Flory, hydrogels are additionally divided into different classes. According to their source, a distinction is made between natural and synthetic hydrogels containing natural and synthetic polymers, respectively. Additionally, the gelling agent can

be crosslinked via covalent bonds or non-covalent interactions, resulting in chemical crosslinked (Flory II) or physical crosslinked (Flory I, III, IV) hydrogels. Other classifications include differences in degradability, the method of preparation and the chemical composition, among others.

In the years 1950-1955, Wichterle stated important requirements for synthetic materials in direct contact to living matrices, like tissue.¹¹ An ideal material should contain no extractable impurities, have a high permeability to nutrition, be resistant to rapid degradation and have mechanical properties that match those of the surrounding tissue.

In the following decades, the 1st generation of hydrogels was prepared, mainly by copolymerization in free radical chain-addition reactions of water-soluble monomers with a multifunctional crosslinker (Figure 1 A) or by crosslinking of hydrophilic polymers (Figure 1 B,C). At that time, most commonly, poly(acrylamide) (PAM), poly(2-hydroxyethyl methacrylate) (HEMA), poly(vinyl alcohol) (PVA) and PEG based hydrogels were prepared. A comprehensive and critical historical overview of the properties and biomaterial applications of the 1st generation hydrogels was given by Hennink and co-workers.¹² As one of the first biomaterials, PAM was used to encapsulate the enzymes glucose oxidase and lactic dehydrogenase¹³, as well as microbial cells¹⁴, strategies still used in ongoing biomedical research. Driven by his own postulated requirements for biomaterials, Wichterle, in collaboration with Lim, synthesized hydrogels by free radical polymerization of HEMA and the crosslinker ethylene glycol dimethacrylate, leading to the first soft contact lenses.¹⁵ Over the years, optimization of oxygen permeability and swelling as well as tunable mechanical and optical properties of PHEMA based contact lenses were achieved by copolymerization of HEMA with N-vinylpyrrolidone, substituted acrylamides, vinyl acetate and substituted methacrylates.¹² Furthermore, the diffusivity was comprehensively studied and correlated with the crosslinking density, swelling and pore sizes of the hydrogels.¹⁶ In consequence, PHEMA was employed as one of the first controlled drug releasing depots of various drugs.¹⁷⁻²¹

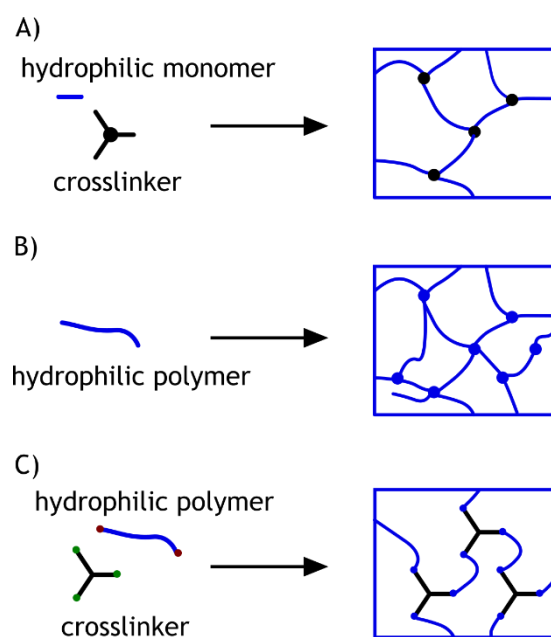


Figure 1. 1st Generation of hydrogels via free radical polymerization (A), crosslinking of a hydrophilic polymer via high-energy radiation (B) and controlled chemical crosslinking using an appropriate crosslinker (C).¹²

PVA hydrogels synthesized by the methods described in Figure 1 B,C were used as swelling controlled-hydrogels in drug delivery. The dry polymer/drug mixture released the drug upon swelling in biological fluids.²² The crosslinking of PEG, at this time reported as a biocompatible and low protein absorbing polymer, was achieved via high-energy radiation (Figure 1 B). Purely hydrophilic chemical crosslinked PEG hydrogels were used early as drug depots and anti-fouling biomaterials.²³ In addition to PEG homopolymers, in particular copolymers of PEG, the so-called poloxamers, which form physical hydrogels, were intensively investigated starting in the 1960s. As early as 1965, hydrogels containing PEG were commercialized, for example as contraceptives²⁴ and wound coverings²⁵, which is why a large market emerged very quickly and PEG became the gold standard in the field of biomaterials.

In addition to the hydrogels already presented, other polymers were of course used to generate hydrogels. For example, hydrogel formation was observed by specific end group reactions of methacrylate- and isocyanate- with alcohol functionalities.²⁶ The semi-synthetic derivative of the natural biopolymer hydroxypropyl methylcellulose was investigated very early as drug depot.²⁷⁻²⁹

The hydrogel properties were all controlled by parameters, such as concentration and molar ratios of the reactants, which influence the polymerization. Therefore, after curing of the hydrogel, the control of swelling or mechanical properties is limited. To overcome this limitations, stimuli responsive hydrogels have been investigated. The control and change of properties through an external stimulus and/or through environmental conditions to manipulate certain actions is continuous in the focus of current state-of-the-art research.

2.1.2 Thermoresponsive Hydrogels

The complexity of nature is only possible because of the principle of stimulus and reaction. Material properties such as morphology, size and appearance can change due to the impingement of energy, for example, by light³⁰, temperature³¹, electric³² and magnetic³³ fields. Furthermore, changes or gradients in salinity or pH-values can cause significant alteration of material properties.³⁴ More specific, the crosslinking state, -density and/or -distribution of hydrogels can be affected and lead to sol/gel transitions, absorption (swelling) or repulsion (shrinkage) of water thereby altering mechanical properties. Among hydrogels, thermoresponsive systems, in which a reaction (sol/gel transition, change in swelling, or turbidity) is triggered by an increase or decrease in temperature, are probably best studied. Thermoresponsive hydrogels are quite interesting systems, as the parameter temperature is easily controlled. Especially, in the research areas of tissue engineering (TE), RM and biofabrication, *in situ* gelling systems are of great interest. On the one hand, all required additives, such as active ingredients or particles, can be homogeneously distributed in the sol state, and on the other hand, the processing as a solution e.g. in injectable formulations, is often easier in comparison to a cured gel structure. However, after gelation the properties of the gel are immediately present.

Thermoresponsive hydrogels are mostly based on biopolymers or synthetic homopolymers and block copolymers. Describing thermoresponsive hydrogels the terms lower critical solution temperature (LCST) and upper critical solution temperature (UCST) behavior are of great importance. In a system with LCST behavior, the polymer and the solvent (water) form a homogeneous miscible one-phase status (a solution) below a critical temperature.³⁵ Above this temperature, phase separation occurs, resulting in turbidity of the system, precipitation of the polymer or macroscopic gelation. In UCST systems the phase separation is observed below a critical temperature.³⁶ In the literature, thermogelling systems (thermogels) are closely associated with the term LCST-type hydrogels and inverse thermogelling systems (inverse thermogels) with the term UCST-type hydrogels. In non-ionic polymers LCST/UCST is often characterized by the ability to form hydrogen bonds between the polymer functionalities such as amides and the water molecules above/below a certain temperature.

In 1968, Heskins and Guillet described the temperature dependent phase transition of poly(N-isopropylacrylamide) (PNIPAAm) in aqueous solutions.³⁷ Surpassing the LCST, inter- and intramolecular hydrogen bonds between PNIPAAm chains were preferred over the entropically unfavorable water-amide hydrogen bonds. Using light scattering and viscosimetry, the reversible phase transition temperature was found to be at around 32 °C, e.g. between room and body temperature, which is beneficial for the use as an injection medium.^{38,39} At high concentration, however, a pronounced syneresis was observed, resulting in a dehydrated collapsed system with a tremendous loss of water (approx. 90%) above the phase transition temperature.

Other thermogels are predominantly formed by amphiphilic block copolymers with varying compositions. Some poloxamer ABA type triblock copolymers of PEG-b-poly(propylene oxide)-b-PEG (PEG-PPO-PEG), also known as Pluronics (tradename BASF), show pronounced thermogelling properties. Exceeding a critical gelation concentration (c_{gel}), these polymers form hydrogels in a certain temperature range creating a densely packed micellar network, while they are liquid at both higher and lower temperatures. Micellization is a self-assembly process observed by amphiphilic molecules in aqueous solutions. In most-described systems spherical micelles are obtained. However, also worm-like micelles and vesicles depending on the volume fraction of the hydrophilic and hydrophobic blocks are known (See 2.3.2 Aqueous Solubility and Self-Assembly). As described for Pluronics, such assemblies can lead to hydrogel formation. For micellar hydrogels different packing mechanisms were described, known as individual micellar packing, inter-micellar bridged packing and micellar corona collapse packing. For a detailed overview the reader is referred to the review article by Loh and co-workers.⁴⁰

As early as the 1990s, it was reported that the above-mentioned poloxamer hydrogels can release ophthalmics⁴¹, cytostatics⁴² and hormones⁴³, demonstrating their potential for biomedical applications. However, poloxamers also show some limitations, such as weak mechanical properties, intrinsic instability and non-biodegradability. To overcome these, variations of the systems were introduced by changing the arrangement of the blocks and replacing PPO with other polyesters. Therefore, predominantly poly(lactide)⁴⁴⁻⁴⁷, poly(lactic-co-glycolic acid) (PLGA)⁴⁸⁻⁵⁶ (Figure 2), poly(ϵ -caprolactone) (PCL)⁵⁷⁻⁵⁹ and poly(ϵ -caprolactone-co-lactide)⁶⁰⁻⁶² were used as hydrophobic B blocks in ABA, AB and BAB block copolymers in combination with the hydrophilic PEG (A blocks).

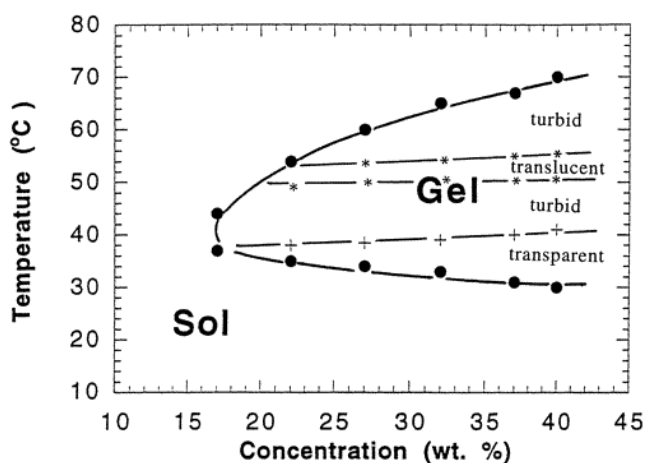


Figure 2. A representative phase diagram of PEG-PLGA-PEG triblock copolymer aqueous solutions. The triblock composition was achieved by coupling two PEG-PLGA diblock copolymers via urethane linkage of the PLGA endgroups (*: sol-gel transition temperature, +: transparent-turbid transition temperature, *: translucent region). Reprinted with permission from reference 48.

In addition to the introduction of biodegradable units and the adaptation of the mechanical properties, the tuning of t_{gel} (critical gelation temperature) and c_{gel} was also described, for example by adjusting the hydrophilic/hydrophobic ratio and variations of the block lengths. Furthermore, alternating multiblock copolymers, star-shaped and branched architectures with adjustable thermogelling properties were reported.⁶³⁻⁶⁹ An example of a biopolymer capable of forming thermoreversible hydrogels is methylcellulose (MC). Below LCST, the MC chains are hydrated with hydrogen bonds between water molecules and hydroxyl groups of the MC. Increased temperature, above the LCST, triggers the loss of

hydration and in consequence hydrophobic intra- and intermolecular hydrophobic associations of the methyl-groups are observed leading to gelation.⁷⁰

One of the most prominent examples for an inverse thermogel is the natural biopolymer gelatin. Gelatin is derived from collagen via hydrolytic degradation. In solution, above 30 °C, gelatin is in the soluble coil conformation. Below 30 °C, a reverse coil to helix transition takes place stabilized by hydrogen bonds. Above a critical concentration, the helix growth induces chain association and thus the creation of a 3D network.⁷¹

Synthetic UCST-type hydrogels are rarely discussed in the literature. This is due to the fact that the phase transition for most polymers would take place under conditions where the solvent is no longer liquid (below 0°C, above 100 °C).⁷²

Nevertheless, in 2016 Fu and Zhao reported an ABA type block copolymer comprising poly(acrylamide-co-acrylonitrile) as A block in combination with a hydrophilic poly(polyethylene glycol methyl ether methacrylate) B block.⁷³ There, reversible inverse gelation in water was observed by adjusting the block lengths, chemical composition and polymer concentration. At low temperatures the outer blocks of the ABA block copolymers collapse and self-assemble into different micellar cores. In consequence, the middle block forms inter micelle bridges, connecting the micelles, which results in the formation of a physically crosslinked hydrogel.

Beyond that, the polymer poly(N-acryloyl glycinamide) (PNAGA), firstly reported in 1964⁷⁴, exhibits dual hydrogen bond acceptors and donors and a pronounced UCST behavior.⁷⁵ Depending on the concentration inverse thermogelling systems are observed resulting from hydrogen bonds (hydrogen bond acceptors and donors) between the polymer chains upon cooling. In 2014, Boustta used the inverse thermogelling properties of PNAGA to establish a temperature responsive injectable drug delivery system. In the sol state different model compounds were dissolved. In the gel state, sustained release of the model compounds was verified and supported by first *in vivo* studies.⁷⁶ Very recently, Majstorovic and Agarwal established an interpenetrating network of PNAGA and poly(glycidyl methacrylate) coupled with a fluorescein isocyanate to introduce UCST-type thermosensitivity to control the volume changes and a temperature-controlled fluorescence signal, which can be used as a thermosensitive control device.⁷⁷

2.1.3 *In Situ* Covalent Crosslinking

In the last subchapter, mainly hydrogels resulting from physical interactions were described. But as already shown in **2.1.1 Definitions, Classifications and the 1st Generation of Hydrogels**, hydrogels can also be built up by a covalently linked 3D network. Here, *in situ* gelling systems are of particular relevance in various applications. Therefore, this section deals with tunable hydrogels from a synthesis perspective formed by covalent crosslinking of polymers using complementary functional groups. With respect to biomedical applications, systems that crosslink under physiological conditions without toxic byproducts are relevant. Furthermore, the reaction should be fast, selective and efficient by controlling the crosslinking kinetics and density. These reactions can additionally be implemented in double network hydrogels combining physical and chemical crosslinking and multi-component hydrogels (**See 2.1.4 Double Network-, Multi-Component- and Composite Hydrogels**). In this part, the focus is on the various crosslinking reactions rather than the crosslinked materials. The list of reactions and examples of *in situ* covalent crosslinked hydrogels is extremely long.⁷⁸

Photo-activated free radical polymerization is widely used to crosslink hydrogels. Highly reactive unsaturated vinyl-groups in (meth)acrylates or acrylamides, which can be easily introduced into synthetic- and natural polymers, undergo a free radical chain-growth polymerization by photo irradiation.⁷⁹ Only the irradiated areas are involved, which offers a great spatial control of the crosslinking reaction. By precise illumination the formation of patterned hydrogels and non-uniform properties can be introduced. With regard to applications in the biomedical field, the respective photoinitiators starting the radical polymerization should be cytocompatible. Therefore, Bryant and co-workers studied the cytocompatibility of various photoinitiators at different concentrations and light intensities in 2000.⁸⁰ To prevent uncontrolled crosslinking via visible light, ultraviolet light (UV)-initiators, such as Irgacure 2959, are typically used.⁸¹ However, there are studies showing deoxyribonucleic acid (DNA) damage by UV radiation.⁸² Furthermore, UV radiation was claimed to induce tissue aging⁸³ and cancer onset.⁸⁴ In addition, the light attenuation of initiator limits the attainable cure depth to few millimeters. Therefore it is challenging to produce large and stable hydrogel constructs.

One powerful chemoselective crosslinking strategy for hydrogel preparation is the use of click reactions. The term was first introduced by Sharpless and co-workers for region specific reactions of nearly perfect “spring-loaded” reactions.⁸⁵ The most investigated reaction is the copper-catalyzed Huisgen 1,3-dipolar cycloaddition of an alkyne and azide (Figure 3 A). However, alkyne-azide cycloadditions generally require the use of toxic catalysts, such as copper, limiting their application in the biomedical field. Recently, copper-free click chemistry by strain promoted precursors has been established, as well as other copper-free examples.⁸⁶

Several other crosslinking reactions are employed over the years to fabricate hydrogels, including Diels-Alder reactions (Figure 3 B), Michael addition (Figure 3 C), imine- (Figure 3 D), oxime- (Figure 3 E) and hydrazone formation (Figure 3 F). The selective [4+2] cycloaddition, also known as Diels-Alder reaction, between an electron-rich diene and an electron-poor dienophile, which is free from side reactions and byproducts, is often used as a one-step crosslinking reaction.⁸⁷ It requires no initiator, catalyst or coupling agent and takes place under physiological conditions. Michael addition occurs between nucleophiles (Michael Donor) such as amines, thiols and phosphines and activated electrophilic olefins and alkynes (Michael acceptors) including acrylate esters, acrylamides and maleimides, among others. The coupling kinetics of Diels-Alder and Michael type additions can be modulated using different combinations of functional groups with respect to their reactivity. Interestingly, the maleimide functionality is suitable for Diels-Alder and Michael type addition.⁸⁸

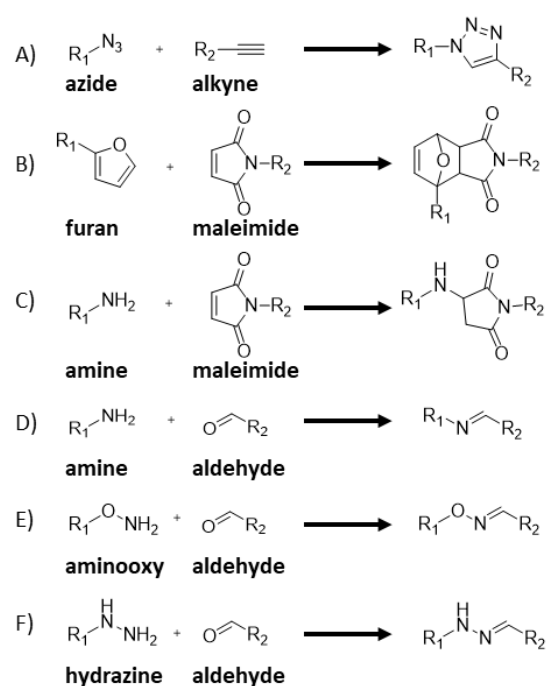


Figure 3. Overview of crosslinking reactions. A) 1,3-Dipolar cycloaddition. B) Diels-Alder reaction. C) Michael addition. Imine- (D), oxime- (E) and hydrazone formation (F). Here, no byproducts, reaction conditions and catalysts are shown. Furthermore, the reaction arrow does not reflect the type of reaction.

Schiff base (imine) formation is observed by reactions between amine and aldehyde functionalities.⁸⁹ Hydrogels formed by these reactions showed self-healing properties due to the dynamic equilibrium of the reaction.⁹⁰ Aldehydes and ketones in combination with aminoxy- or hydrazine derivatives form oximes and hydrazones. This route is quite elegant due to the fact, that biopolymers such as proteins do not contain aldehydes or ketones and so the reaction will not interfere with protein functionalities. Interestingly, oximes are more stable than hydrazones, which can be used for tuning properties such as degradation.⁹¹

This section showed a selection of frequently used *in situ* covalent crosslinking strategies. These reactions can be used in a variety of ways in double network-, multi-component and composite hydrogels to address different applications in drug delivery, TE and biofabrication.

2.1.4 Double Network-, Multi-Component- and Composite Hydrogels

In double network hydrogels at least two individual crosslinking reactions and/or materials are combined. Early examples include pH and temperature sensitive materials. Also, a combination of ionic and covalent stabilization was investigated in interpenetrating networks with synergistic effects of different hydrogel properties. In the design of novel hydrogels, physical (**See 2.1.2 Thermoresponsive Hydrogels**) and *in situ* chemical crosslinking (**See 2.1.3 In situ Covalent Crosslinking**) is combined. More specifically, thermoresponsive hydrogels combined with chemical crosslinking of radicals or complementary groups can be used to establish dual gelling systems. In 2008, Vermonden et al. described a methacrylated thermogelling ABA type triblock copolymer comprising poly(N-(2-hydroxypropyl) methacrylamide lactate) as the A blocks and the hydrophilic PEG as B block.

By subsequent photopolymerization of methacrylates the mechanical properties and stability of the hydrogel were improved. Cytocompatibility was confirmed by seeding mesenchymal stem cells onto the hydrogel surface. In addition, first cytocompatible cell encapsulation experiments were performed. In this study, the researchers outlined potential applications in the field of TE. Three years later the same research group described similar hydrogels for AM, especially for bioprinting of chondrocytes (**See 2.2 Bioprinting: A Technology of Biofabrication for Tissue Engineering and Regenerative Medicine**).⁹² Cell viability was confirmed in the printed constructs after one and three days. However, cell proliferation and the production of extracellular matrix (ECM) by the embedded chondrocytes was limited.

To obtain the best of two worlds - tunable material properties and bioactivity - synthetic and natural polymers are combined. The two polymers in the multi-component system can either be physically mixed with no chemical crosslinking points between the two species^{93,94}, or crosslinked e.g. via complementary functional groups.⁹⁵

If further compounds are added to induce bioactivity or to tailor mechanical properties, composite hydrogels are obtained. The addition of calcium phosphate⁹⁶ and hydroxyapatite⁹⁷ induced mineralization essential for bone tissue formation. To improve mechanical and rheological properties ceramics⁹⁸, fibers e.g. PCL-based⁹⁹, carbon nanotubes¹⁰⁰ and nanoclays¹⁰¹ were investigated. The incorporation of micro-¹⁰² and nanoparticles¹⁰³ can be used for encapsulation of different payloads, such as small drug molecules or growth factors to modify their release behavior.

2.2 Bioprinting: A Technology of Biofabrication for Tissue Engineering and Regenerative Medicine

2.2.1 Definitions

The ECM is an essential part of the microenvironmental niche of every cell. The ECM provides not only structural support to cells but also enables cell-ECM and cell-cell communication, thereby influencing cellular processes, such as proliferation, differentiation, migration and apoptosis.¹⁰⁴ In order to generate tissue analogues in the fields of TE and RM, mimicking structural and functional aspects of the ECM is therefore of great importance. In this context biomaterial-based strategies that implement the 3D structure and the hierarchy of the native ECM have accordingly become established in cell culture experiments. Therefore, with the rise of AM¹⁰⁵, biofabrication has found its way into TE and RM research.

In 2016 leading scientist of the field revised a definition of biofabrication for TE and RM as follows:

“The automated generation of biologically functional products with structural organization from living cells, bioactive molecules, biomaterials, cell aggregates such as micro-tissues, or hybrid cell-material constructs, through bioprinting or bioassembly and subsequent tissue maturation processes.”¹⁰⁶

Thus, in this research field, biofabrication focuses on bioprinting and bioassembly technologies, that contain cells and materials as building blocks, which are in consequence used for TE and RM applications.

According to Guillemot et al., bioprinting uses computer-aided transfer processes by patterning and assembling living and non-living materials in a prescribed two-dimensional or 3D organization to finally produce bio-engineered structures.¹⁰⁷ In contrast, in bioassembly pre-formed cell containing fabricated units are assembled in a 3D organization via cell-driven self-organization or bottom-up approaches.¹⁰⁶ In future research, in order to generate advanced and versatile bioproducts, bioprinting and bioassembly will probably be applied partly in combination.

2.2.2 Bioprinting Technologies

Already in 1907 it was demonstrated that isolated tissue fragments can rearrange into a homogenous new tissue as observed by the coalescence phenomena of dissociated sponges.¹⁰⁸ However, it needed several decades and novel technologies to recognize the potential impact of this fundamental observation for TE.

The first work in which cells were actually part of the manufacturing process, there called “organ printing”, was described by Wilson and Boland in 2003.^{109,110} The work was inspired by the flow and fusion behavior of the viscoelastic embryonic tissues demonstrated by fusing and morphing of isolated myocardial segments consisting of embryonic avian heart cell aggregates into a single and synchronized beating heart tube overnight (Figure 4 A-C).^{111,112} However at this point it was unclear if the fusion process was triggered by the remodeling of the ECM, cell migration or cell-cell communication and how all these events are related to each other. In the first bioprinting experiments an ink jet printer was used for the fabrication process (Figure 4 D,E).

At this time, bovine aortic endothelial cells and smooth muscle cells were printed on a substrate gel (Matrigel™ and collagen, respectively). Cell survival and fusion of cells were successfully demonstrated (Figure 4 F,G), which opened a new avenue for the fabrication of living materials using bioprinting. In the second part of the manuscript, a thermoresponsive hydrogel (PNIPAAm Gel) as a structure supportive material (**See 2.2.3.3 Materials for Bioink Development**) was introduced to establish real 3D printing in a layer-by-layer approach. This work was the kick-off event for bioprinting, and several key technologies were introduced since then.

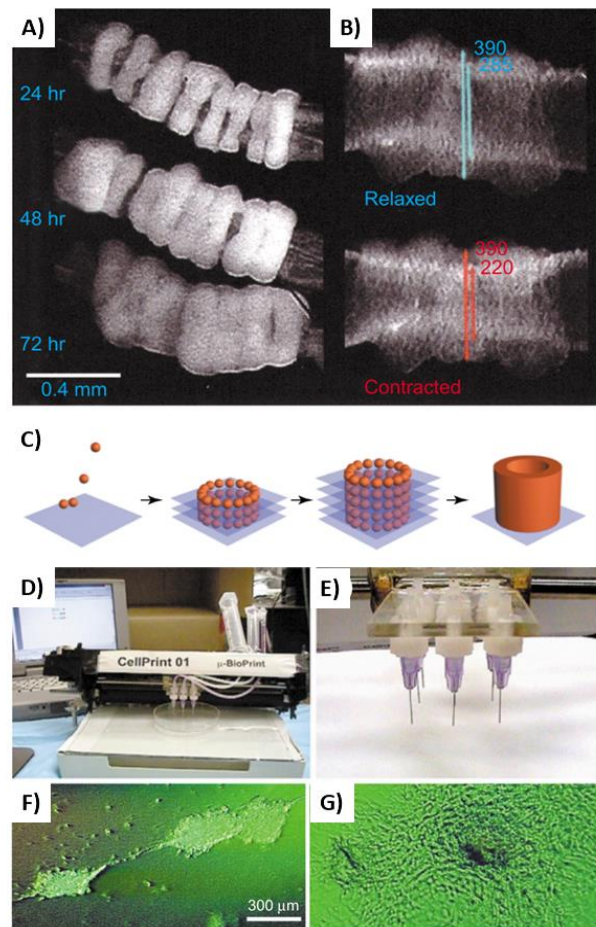


Figure 4. The Idea of Bioprinting. A) Myotube assembly and the synchronized beating after 72h (B). Reprinted with permission from reference 111. C) Schematic representation of the assembly of automated processed tubular constructs as one of the first bioprinting ideas. Reprinted with permission from reference 112. D), E) Pictures of one of the first bioprinters with multiple nozzles. Reprinted with permission from reference 112. Images of fabricated cells before (F) and after cell fusion (G). Reprinted with permission from reference 110.

In general, bioprinting can be classified into three major types, depending on their underlying physical mechanism and deposition method: Extrusion-based bioprinting (EBB), droplet-based bioprinting (DBB) and laser-based bioprinting (LBB) (Figure 5).¹¹³ The choice of method depends on the material to be used and the size, topology, resolution, biofunctionality, etc. of the structure to be produced.

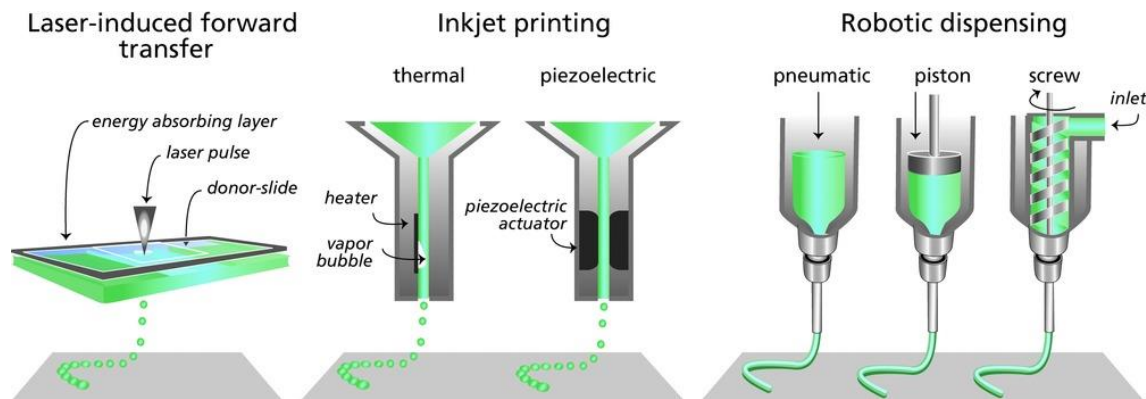


Figure 5. The three main bioprinting techniques. Laser-induced forward transfer as example of LBB. Inkjet printing as example of DBB and EBB (also called robotic dispensing). Reprinted with permission from reference 118.

In EBB an ink is deposited as a continuous filament driven by means of pneumatic or mechanical force during the automated movement of the printhead relative to the printbed (Figure 5 right). In contrast, in DBB an electrical, thermal or acoustic impulse is used to generate single droplets deposited in close proximity to each other in a drop-on-demand fashion (Figure 5 middle). Laser energy is used in LBB either for photopolymerization in stereolithography and two-photon polymerization techniques, or cell transfer mechanisms as used in laser-induced forward transfer bioprinting to process the material and generate the scaffold (Figure 5 left).

The majority of researchers in the bioprinting community use EBB due to its user friendliness. Using this technology, scalable and stable constructs with clinical relevance can be produced in a relatively short time.¹¹⁴ However, the progress of the field is restricted to the development of suitable extrudable materials (**See 2.2.3 Bioink Development**).¹¹³ In high throughput applications for drug screening and disease modelling the tissue equivalents are often generated via DBB techniques with a medium resolution.¹¹⁵ However, only low-viscous or diluted inks are compatible with DBB to prevent clogging in the droplet formation system. In contrast, LBB technologies yield constructs with outstanding resolution and well-defined complex 3D shapes in a nozzle-free approach.¹¹⁶ Challenges are limitations with respect to biocompatibility of the photo-polymerization processes, used chemicals and transfer steps. Furthermore, it is challenging to produce structural integrated and thick constructs in a meaningful time period. For the future, it would be useful to integrate all complementary techniques here described into a single bioprinter in combination with a simultaneous use to overcome the limitations of each modality, including resolution, scalability and the availability of suitable bioinks.¹¹⁷

2.2.3 Bioink Development

Without a doubt, great progress has been made in bioprinting in recent years, using natural and synthetic hydrogels. Nevertheless, many hydrogels developed for use as inks either have problems in ensuring the desired biological function or can only be processed with insufficient resolution and stability. In order to print defined constructs, the hydrogel must meet certain physical properties that are often poorly compatible with the biological requirements for good proliferation, migration and differentiation of the embedded cells. The lack of such versatile hydrogel platforms was postulated in the community as a key issue in the so-called biofabrication window (Figure 6).¹¹⁸

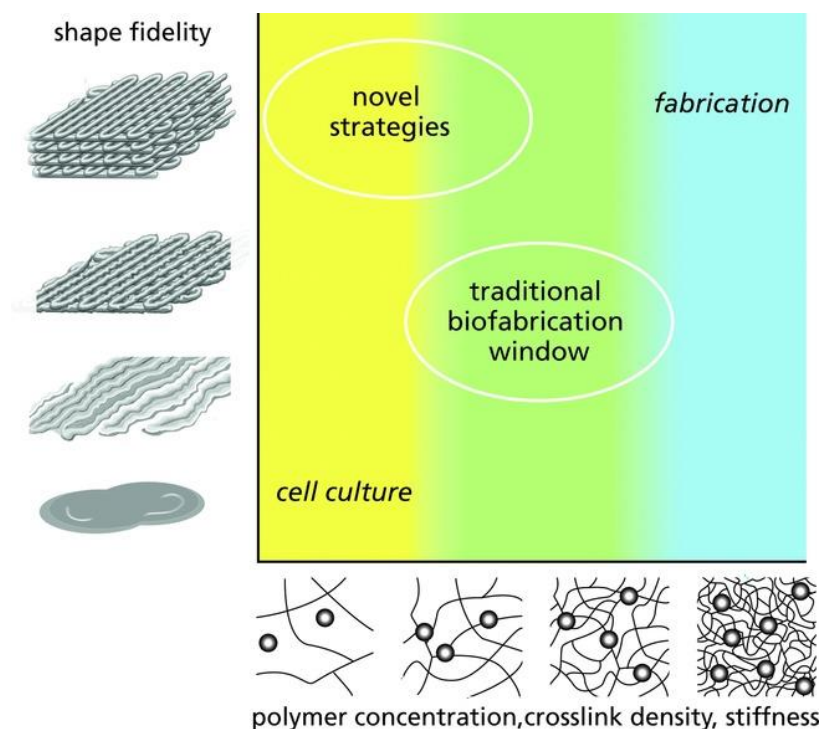


Figure 6. The Biofabrication window. Optimal cell culture conditions are often in conflict with material properties for fabrication with high shape fidelity. Novel strategies have to mature to expand the traditional biofabrication window. Reprinted with permission from 118.

To ensure good printability (See 2.2.3.2 Printability of Bioinks), high solid contents and crosslinking densities are usually required. However, cells mature best in an aqueous environment wherein migration and formation of new ECM is not affected. The goal is to develop novel systems that combine both worlds: high resolution printing in combination with biological functionality.

In general, a distinction is made between bioinks and biomaterial inks.¹¹⁹ A biomaterial ink is a printable material, which has a certain function such as structural support or cell guidance. As the cells are not part of the fabrication process, the physicochemical demands for a biomaterial ink are less stringent and thus allow for a much wider window of processing parameters including high pressures, temperatures and organic solvents. In contrast, a bioink must contain living cells. The cells are usually embedded in

the hydrogel matrix during the complete fabrication process, which makes the design of bioinks more challenging. Therefore, every step in the bioprinting process: pre-printing, during the printing and post-printing, needs to be cytocompatible.

For bioprinting, in principle, liquid-phase and gel-phase bioinks are discussed in the literature (Figure 7).¹²⁰

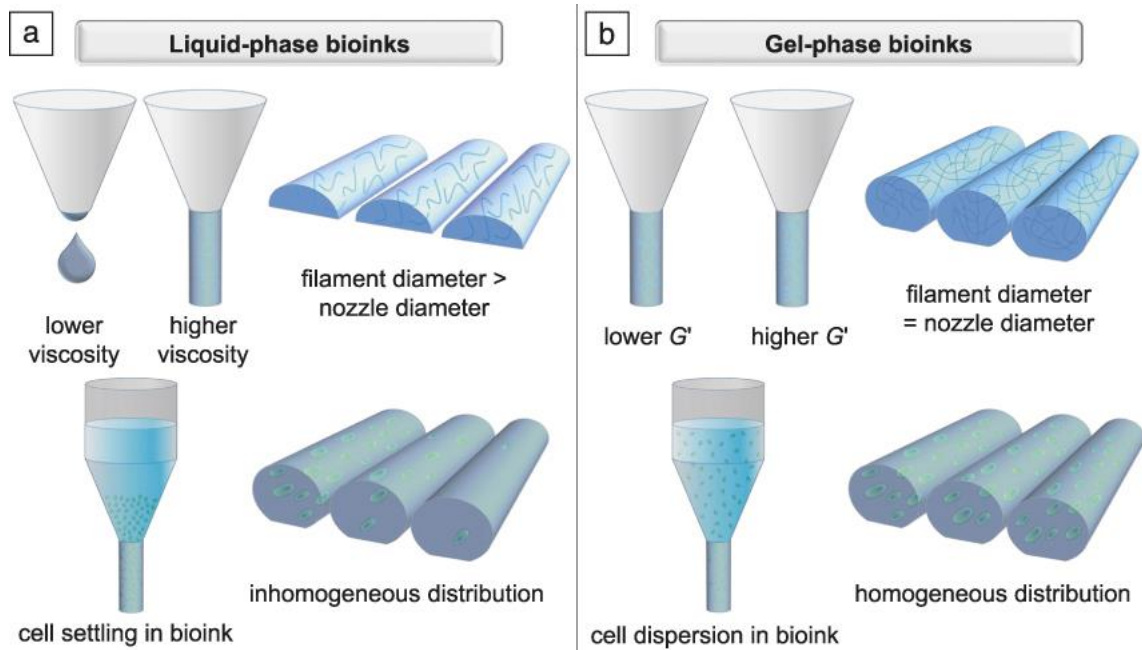


Figure 7. Liquid-phase bioinks (a) and gel-phase bioinks (b). The differences and the impact on filament diameter and cell distribution for liquid- vs gel-phase bioinks are highlighted. Reprinted with permission from 120.

In liquid-phase bioinks the gelation is induced e.g. by UV light, addition of crosslinker or temperature change after the printing process^{121,122} or during the printing process in the nozzle.¹²³ Therefore, the gelation must be very fast. However, the filament diameter is often greater than the nozzle diameter. Furthermore, it is challenging to stack several layers on top of each other without layer fusion and a collapse of the structure. In addition, in the barrel cell sedimentation is possible due to the liquid nature of the ink, which causes inhomogeneous cell distributions alongside the final construct. The cell sedimentation was recently studied as a function of polymer concentration in a sodium alginate (Alg) bioink system.¹²⁴ An increased sedimentation velocity of the cells was observed by decreased polymer concentrations.

In gel-phase bioinks, the precursor solution undergoes a pre-printing rapid sol/gel transition via different mechanisms, such as thermogelation or via dynamic covalent bonds.¹²⁵ The gel properties (**See 2.2.3.1 Rheology of Bioinks**) prevent cell sedimentation in the printing barrel. In an ideal fashion, the filament diameter is equal to the nozzle diameter and several layers can be stacked on top of each other (**See**

2.2.3.2 Printability of Bioinks). In both approaches typically a post-printing stabilization process via additional chemical or physical crosslinking to ensure long-term stability of the construct is necessary.

2.2.3.1 Rheology of Bioinks

For all different bioprinting techniques (See **2.2.2 Bioprinting Technologies**), the materials need to fulfill distinct criteria. In this work, the focus is on EBB. In comparison to injectable hydrogel formulations, which has been intensively studied over the past decades¹²⁶, the properties for cell-containing hydrogels in EBB are even more stringent. Injectable formulations are applied in the sol state. After the injection into a mold or cavity the solution gels and forms for example a drug-loaded depot. In contrast, in bioprinting a defined structure that is based on a biological model, for example a cartilage substitute, is aimed.

The rheological properties, which are described by the deformation and flow behavior of materials under an applied force, are important physicochemical parameters of hydrogels and are used to characterize bioinks and to predict printability. A rheometer working on the principle of rotation and oscillation is therefore used.¹²⁷

The viscosity η of a material, investigated in experiments in rotational mode, is defined as the ratio of the shear stress τ to the shear rate $\dot{\gamma}$, and represents the resistance of a fluid to flow under an applied stress.¹²⁸ In contrast, in oscillation experiments the viscoelasticity of a material is investigated. Viscoelasticity is characterized by an elastic or solid-like component as well as viscous flow or liquid-like behavior. With the two parameters storage (or elastic) modulus G' and loss (or viscous) modulus G'' these properties are quantified.¹²⁸ Viscoelastic materials exhibit both G' and G'' , which is often expressed by the damping factor (loss factor, loss tangent or $\tan(\delta)$), the ratio of G'' and G' . In liquids G'' is superior to G' ($G' < G''$). Upon gelation, G' increases and the gelation point (sol/gel transition) corresponding to the point at which G' crosses G'' is reached.

In the following, experiments are discussed, which are used to characterize gel materials and especially hydrogels for gel-phase EBB.

To investigate viscoelasticity amplitude/oscillatory stress sweeps (Figure 8 A) and frequency sweeps (Figure 8 B) are performed. In amplitude sweep, G' and G'' are recorded as a function of the applied amplitude/ τ . For gel samples in the linear viscoelastic (LVE) range, both G' and G'' are linear and independent of the τ .¹²⁸ In the LVE, hydrogels exhibit almost constant low damping factors and $G' > G''$ (**criterion 1 for a gel material**). With a frequency sweep, in which G' and G'' are recorded as a function of the angular frequency ω , the time dependency of material properties can be characterized. Thus, conclusions can be drawn about the dynamic of the system and a distinction of liquids and viscoelastic solutions from gel materials can be conducted. In principle, a hydrogel should exhibit almost constant

G' and G'' values in a distinct frequency range with $G' > G''$ (**criterion 2 for a gel material**). Gel-like materials are generally less frequency dependent than viscoelastic fluids. In addition, the values should be consistent in both experiments, the amplitude and frequency sweep.

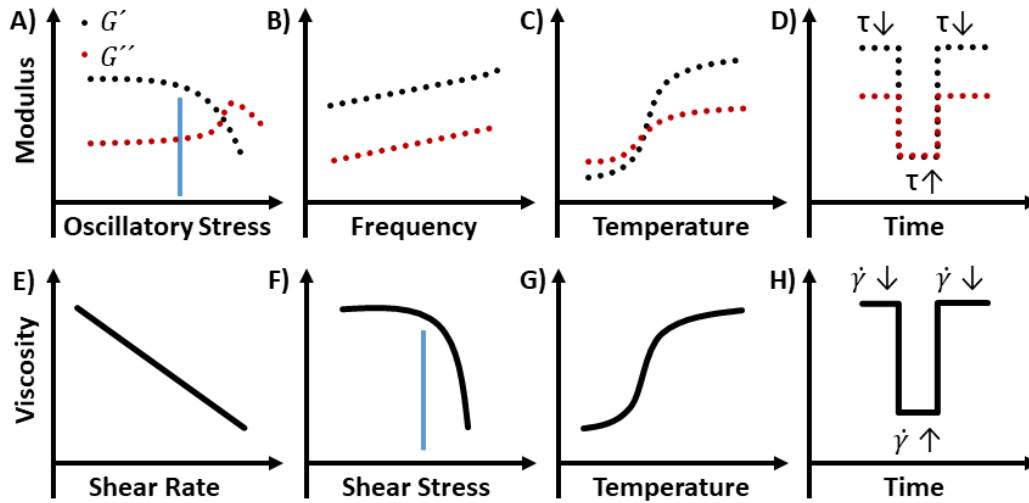


Figure 8. Important rheological experiments to characterize bioinks in oscillation mode (A-D) and rotational mode (E-H). The yield stress is highlighted as vertical blue lines in the amplitude sweep (A) and τ ramp (F). The high and low τ and $\dot{\gamma}$ regimes are highlighted with arrows, respectively (D,H). The figure was designed according to Cooke and Rosenzweig.¹²⁷

Bioinks should have flow and shape retention properties at different stages of the fabrication process. Newtonian fluids exhibit a linear relationship between τ and $\dot{\gamma}$. Materials with decreasing or increasing ratios are defined as non-Newtonian fluids, which can be classified into time independent (shear-thinning and shear-thickening) and time-dependent fluids (thixotropic or rheopectic).¹²⁸ Shear-thinning materials, in which η decreases upon increased shear forces, are used in EBB (Figure 8 E).¹²⁹ However, deformation and flow is only observed above a critical τ , which is called the yield point at a certain yield stress τ_0 (**criterion 3 for a gel material**). In oscillation experiments, the end of LVE region is defined as the yield point.¹³⁰ At higher τ , in the subsequent yield zone, the material is deformed permanently. The end of the yield zone is marked by the intersection of G' and G'' , the so-called flow point, at which the material starts to flow (flow stress τ_f at the flow point).¹²⁸ The yield point can also be characterized in rotational experiments by recording $\dot{\gamma}$ as a function of τ (Figure 8 F).¹³¹ Often, at very low $\dot{\gamma}$, a plateau region with nearly constant η values (= zero shear viscosity η_0) is observed. The onset of η decrease can be defined as the yield point.

The described material properties and rheological parameters are of great importance for the three different steps (pre-printing, printing, post-printing) of the extrusion process (Figure 9).

○ *Pre-printing*

At the beginning the bioink should be ideally in a free flowing liquid state ($G' < G''$, $\tan(\delta) > 1$) to facilitate good mixing of all components (gelator, additives, biomolecules, living cells, among others) with low shear forces. This bioink can be easily and quantitatively transferred into the printing cartridge by casting or pipetting without undesired material gradients or air bubbles occurring. Then, a cytocompatible stimulus should induce a pre-printing stabilization of the bioink. Therefore, stimuli responsive hydrogels are ideal candidates, especially thermoresponsive physical hydrogels due to the easy control of the parameter temperature.¹³² However, several other strategies such as pH sensitive gelation¹³³, dynamic covalent bonds¹³⁴, host-guest interactions¹³⁵ or defined chemical pre-crosslinking¹³⁶ are also employed. A rapid sol/gel transition, e.g. via thermogelation, which can also be characterized via rheology performing a temperature sweep in either oscillation (Figure 8 C) or rotational mode (Figure 8 G), prevents cell sedimentation and nozzle bleeding. At this stage high G' values ($G' > G''$) and τ_0 are favorable. In addition, a pronounced LVE region and frequency independence are beneficial.

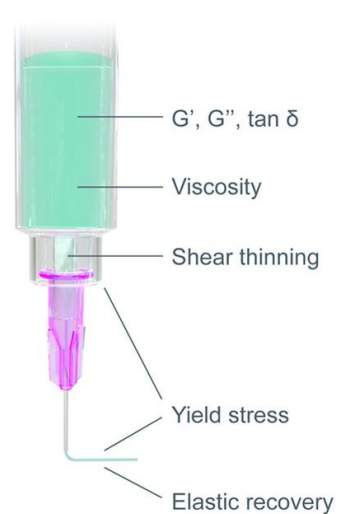


Figure 9. Important rheological parameters and properties for gel-phase bioinks at different fabrication stages. Reprinted with permission from 130.

○ *Printing*

The bioink, which is first in a bulk resting state in the barrel, is exposed to high shear condition while flowing through the nozzle. Hence, physical hydrogels exhibit promising properties for bioink development since they can fulfill the needed characteristics for EBB. During printing the applied τ caused e.g. by pneumatic forces has to exceed the yield point of the system to start the material flow.¹³¹ Pronounced shear-thinning properties are needed for a smooth material flow through the thin nozzle preventing cell damage and guarantying the deposition of a well-defined filament (also termed as strand or strut).

○ *Post-printing*

After the printing, the material reaches a second resting state. To guarantee good printing outcomes with high resolution, a rapid regelation (elastic recovery) of the material after being deposited is necessary. This property is often examined with a three-step experiment (often repeated several times, e.g. 10 times). Here, a low shear/stress regime is followed by a high and then a further low shear/stress regime recording G'/G'' (Figure 8 D) or the η (Figure 8 H), respectively. At the second low shear/stress regime an immediate and full regelation reaching the initial gel values should be observed.¹³¹ Furthermore, in

order to stack several layers on top of each other high yield points, high G' and low $\tan(\delta)$ values are needed to prevent collapse of the printing construct.

To obtain a long-term stable construct, often a post fabrication stabilization step by a second crosslinking mechanism is necessary. In general, the strategies explained in the sections **2.1.2-2.1.4** are used. It should be noted here, however, that so far there is no clear picture in the community as to which rheological parameters are decisive for the printing outcome. Rather, it is important to establish and characterize further new materials and compare as much rheological parameters as possible in a reproducible fashion. Therefore, it is necessary to establish uniform measurement and analysis protocols for rheological characterization of bioinks in combination with the evaluation of printability.¹²⁷

2.2.3.2 Printability of Bioinks

When discussing a bioink, the term printability is often used. However, the printability of a material cannot only be described by its rheological properties. So far, no straight consensus in the biofabrication community exist to call a bioink formulation “printable”. In the last years terms like extrudability, filament characterization and shape fidelity have been discussed (Figure 10).^{130,137}

Extrudability of filaments with respect to filament formation¹³⁸, -planar orientation and stacking can be characterized.¹²¹ Starting the extrusion the formation of a continuous filament or droplet can be investigated.¹³¹ The filament formation is related to the shear-thinning and shear recovery properties of the material.¹³¹ Further, the uniformity of single deposited lines can be examined.¹³⁸

The stackability, which is related to the shape fidelity, represents the integrity of single filaments stacked on top of each other.^{139,140} In an ideal bioink, there is no creeping or collapse of the structures due to merging of filaments and layers. Merging of filaments and layers can occur when the yield point and/or G' of the ink is too low to counteract gravity forces and surface tension. The ability to print structures without filament collapse along the axial direction is beneficial, especially to realize large gaps between structural components or ink overhangs.

The ability to counter gravity forces is evaluated by printing a filament over a pillar array, bridging gaps with increasing distances.¹⁴¹ Furthermore, to test filament fusion parallel filaments with a stepwise narrowing of the filament spacing was reported to evaluate the printing limits of fine details like small pores with sharp angles.¹⁴¹ However, not only the yield stress and or G' as straightforward indicators for stackability and filament fusion are important as also time-dependent effects can cause printing artifacts. In addition, the shape fidelity is evaluated by measuring the filament width (x-y plane) and thickness (z-axis) at different points alongside a single fiber, a planar or multilayered construct and comparing the results to the original dimensions of the computer-aided design file.¹³⁰

By modifying a bioink, e.g., changing composition, concentration or introducing chemical modifications the whole workflow of printability assessment including rheological measurements should be repeated.

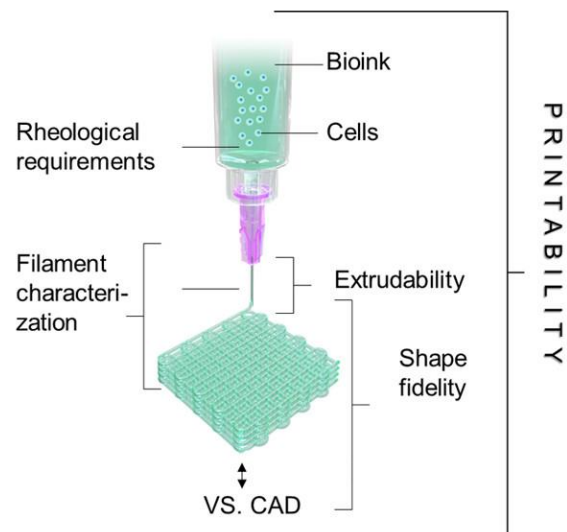


Figure 10. Visualization of all aspects of printability. Reprinted with permission from 130.

In literature, there are different excellent review articles available dealing with printability of bioinks.^{130,137,142}

It should be mentioned that other aspects such as printing parameters (pressure, speed, and nozzle height), the printing equipment (e.g. nozzles), swelling/shrinkage properties of the material, degradation processes, the cell culture conditions (static or dynamic culture), the sterilization method and the cell lines and cell densities, among others, have significant influence on the bioprinting process. In the end, all aspects need to be investigated to generate functional tissue models. However, not all of these aspects can be discussed in detail in this work.

2.2.3.3 Materials for Bioink Development

A well-considered material selection is one of the most important aspects in hydrogel design and influences the final biofunctionality and mechanical properties of the construct, which is crucial for a good bioprinting result. In principle, all cytocompatible materials, which are suitable for hydrogel formation and which have the ability to be extruded can be used as a bioink.

A systematic study published 2020 showed that the most common materials in EBB in declining order are Alg, gelatin, gelatin methacryloyl (GelMA), hyaluronic acid (HA), cellulose, collagen, PEG derivatives, agarose, chitosan and PCL.¹²⁵

In bioprinting, most researches started with established hydrogel systems. Therefore, natural hydrogels created by Alg, agarose, collagen, gelatin, fibrin, decellularized ECM components or mixtures, HA and silk are translated from the classical TE and RM to the field of biofabrication. Natural polymers are known to have structural similarities to the native ECM and exhibit good cytocompatibility.¹²⁵ Furthermore, hydrogels based on collagen, gelatin or fibrin exhibit inherent signaling molecules such as cell adhesion motives. However, natural materials often lack good printability and mechanical stability. In addition, batch-to-batch variations with respect to the rheological properties is discussed as problematic.¹⁴³

In contrast, synthetic hydrogels based on (macro)molecular building blocks as described in the previous chapter (**See 2.1.2 Thermoresponsive Hydrogels**), such as PEG and Pluronic®, are less used in bioprinting. However, these polymers can be designed with tunable mechanical properties and lower batch-to-batch variations. But, synthetic polymers lack bioactive molecules for cell adhesion and migration, as well as enzyme-mediated degradation and remodeling of the matrix.¹⁴³ Furthermore, synthetic hydrogels can be used e.g. to improve the printability of the bioink. In recent years, several approaches were established to improve the outcome in bioprinting. In this context, so-called sacrificial structures or materials were introduced (Figure 11).¹⁴⁴ Often stimuli responsive hydrogels are used as sacrificial ink materials as the material can be easily removed from the construct e.g. in the liquid state of the material. For example, a sacrificial ink can be printed separately to introduce cavities and channels

into a scaffold (Figure 11 top left). Using this approach Lewis and co-workers established a perfusable and thick (> 1 cm) tissue mimicking construct with parenchyma-, stroma- and endothelium- like compartments in 2016.¹⁴⁵ The researchers used Pluronic F-127 as sacrificial biomaterial ink to print defined channels blended with thrombin, which crosslinks the cell (human mesenchymal stem cells and human neonatal dermal fibroblasts) containing gelatin-fibrin bioink. The sacrificial biomaterial ink was removed and subsequently seeded with human umbilical vein endothelial cells. Furthermore, overhangs can be temporary stabilized using a sacrificial support material. General properties of a support material in bioprinting to support overhangs are highlighted by Chua and co-workers.¹⁴⁴ In 2018, a methylcellulose hydrogel was introduced by Gelinsky and co-workers as support material to realize overhangs in calcium phosphate cement ink acting as main structure.¹⁴⁶ Recently, other promising approaches, such as in-gel printing (freeform reversible embedding of suspended hydrogels)¹⁴⁷ (Figure 11 top right) and the use of coaxial nozzles (Figure 11 bottom left) were established.¹⁴⁸⁻¹⁵⁰ However, these two methods are not described in this work.

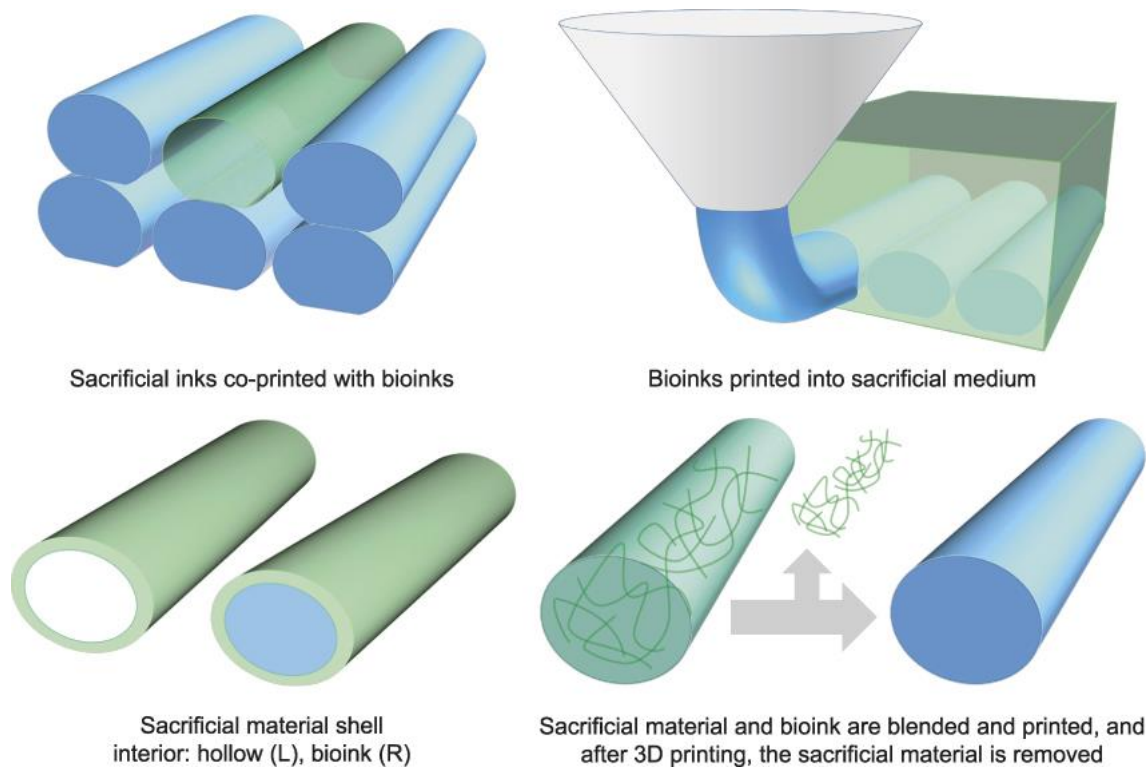


Figure 11. The idea of sacrificial materials in EBB. Reprinted with permission from reference 120.

Last, sacrificial materials can be blended into a bioink formulation to tune rheological properties (Figure 11 bottom right). This means that e.g. biological materials such as Alg, which cannot be printed without the use of a sacrificial material with good printability, can also be printed. By removing the sacrificial material after the printing process and stabilizing step ideally only the main bioink component is present in the stable construct. A positive effect on the porosity of the final product can also be observed as demonstrated in 2016 for Alg/pluronic F127 bioink.¹⁵¹ The removal of the sacrificial material leaves

voids, thus more space for the living cells and an increased diffusivity for the nutrition transport is observed.

Of course, there are now other more advanced developments in the field of bioprinting. For example, fibers and scaffolds (often PCL based) are generated by melt-extrusion¹⁵², electrospinning¹⁵³ and melt electro writing (MEW)¹⁵⁴, which subsequently fulfill a supporting or cell guiding function in the final construct. In addition, bioreactors¹⁵⁵ and organ on a chip¹⁵⁶ approaches are also being pursued. However, like the work on the realization and investigation of bioprinting in space¹¹³, these are not the focus of this work.

Post-printing usually an additional crosslinking step is performed to stabilize the constructs. The most used crosslinking strategies, ionic, temperature induced and UV-mediated, can be correlated to the three most used materials Alg, gelatin and GelMA. Alg is predominantly crosslinked via ionic coordination bonds. This is ensured by the addition of bivalent cations such as Ca^{2+} .¹⁵⁷ In gelatin hydrogels, a temperature triggered formation of a gel network consisting of triple helices is used as stabilizing step.¹⁵⁸ Chemical crosslinking using UV light is usually used for materials modified with methacrylated groups such as GelMa, HAMA, AlgMA or PEGMA.¹²⁵ In principle, all strategies highlighted in the previous chapters (**See 2.1 Hydrogels as Biomaterials, especially 2.1.2-2.1.4**) for hydrogel design can be adapted for bioink development considering the necessary material properties for bioinks, the biofabrication window and especially the needed biological features. Both physical and chemical crosslinked hydrogels are considered as candidates in bioink development. Often, the dynamic nature and reversibility of physical gels is advantageous for the printing process (shear thinning properties), but their mechanical stability after printing is often low. Chemical crosslinked hydrogels, in contrast, are mechanically strong. However, these hydrogels based on covalently linked 3D networks usually lack shear thinning properties, which limits printability. Therefore, often a combination of both types of gelation mechanisms is used. This can be realized either by a one material approach, in which both components, a physical gelation mechanism and moieties for chemical crosslinking are present in the same (bio)polymer, or by a multimaterial blend or hybrid system of different (bio)polymers with specific functions. For a detailed discussion on bioink materials the reader is referred to different several excellent reviews, among others.^{142,159-162}

In the last years tremendous progress in the design of novel bioinks has been made. However, in the literature the lack of a bigger variety of printable hydrogel systems is often discussed as one major drawback that hampers significantly the progress of the complete field. New material combinations have to be increasingly used in the future in conjunction with clever print design. The field is particularly dependent on the expansion of available (bio)polymers such as stimuli-responsive polymers and their use as printable hydrogels.

In the last decades the polymer classes of POx and POzi are discussed frequently as promising biomaterials. Also, first hydrogels either exclusively of POx/POzi or with POx/POzi moieties or

components were described. However, only little reports dealing with these polymer classes in bioprinting are reported so far. Nevertheless, the overall reported good cytocompatibility in combination with the synthetic versatility of the polymer classes, which are known for decades and are further expanded nowadays, makes these polymers ideal candidates to study hydrogel formation and related applications especially in the field of bioprinting.

2.3 Poly(2-oxazoline)s and Poly(2-oxazine)s

2.3.1 Synthesis

As the title of this section suggests, we are now dealing specifically with the polymer classes of poly(2-oxazolines) (POx) and poly(2-oxazines) (POzi). The building blocks, monomers, which are strung together by defined polymerization are cyclic imino ethers (CIEs). Besides being used as monomers, these heterocyclic molecules are also used as protection groups¹⁶³, synthetic intermediates¹⁶⁴, chiral auxiliaries¹⁶⁴ and metal-ligands¹⁶⁵. Ring sizes from five to seven atoms with the imino ether motive – N=C-O- are known (oxazolines, oxazines and oxazepines). In this work, 2-oxazolines and 2-oxazines with the double bond at 2-position and a further 2-substitution are described (2-substituted-2-oxazolines = Ox, 2-substituted-2-oxazines = Ozi). If, for example, the substituent is a methyl group, the molecules 2-methyl-2-oxazoline (MeOx) and 2-methyl-2-oxazine (MeOzi) are obtained. Ox and Ozi monomers can be synthesized by several strategies. In the one-step Witte and Seeliger approach, a substituted nitrile reacts with 2-aminoethanol or 3-aminopropanol, respectively, in the presence of a Lewis acid catalyst.¹⁶⁶ Other commonly applied methods for monomer synthesis include the direct synthesis using non-activated carboxylic acids¹⁶⁷, the α -deprotonation route¹⁶⁸ and the Wenker method¹⁶⁹. Thus, a large number of different monomers with varying alkyl-, aryl-groups and other functionalities has been realized. To get an impression of the feasible monomers, the reader is here referred to excellent review articles already available in the literature.^{170,171} In this work, the focus was on monomers with different alkyl- and aryl-substitutions in 2-position.

Several equimolar ring-opening reactions of Ox and Ozi using alkyl halides, acyl halides, carboxylic acids, amines, thiols, alcohols and acrylic acids were described resulting in an isomerization of the imino ether to an amide functionality.¹⁷² In principle, CIE can be used in three types of polymerization. By using multifunctional CIEs and e.g. dicarboxylic acid compounds a polyaddition reaction leads to poly(ester amide)s. Furthermore, acrylic acids and the CIEs can spontaneously polymerize, known as spontaneous zwitterionic copolymerization, by the formation of N-acetylated poly(aminoester)s. An overview of the synthesis and application of these types of polymers was published by Kempe in 2017.¹⁷²

The well-known POx/POzi polymers are synthesized by cationic ring opening polymerization (CROP) (Figure 12 A). The first reports of POx and POzi polymers were given in 1966 and 1967, respectively.¹⁷³⁻

¹⁷⁷ The polymer classes are known for the versatile synthesis and favorable biological properties, making them great candidates for use as biomaterials.

Without question, it is very difficult to present a holistic overview of all POx and POzi structures to date in a nutshell, even if one only concentrates on the synthetic aspects and derived properties. For this reason, this work focuses on pure POx and POzi systems with n-alkyl and aryl substituents, considering only structures without another substituent on the aryl function. In particular, linear amphiphilic block copolymers (Figure 12 B) and the polymer analog modifications via a hydrolysis step are discussed.

The CROP mechanism is described by an initiation, propagation and termination step and highlighted in detail in several review articles.^{170-172,178,179}

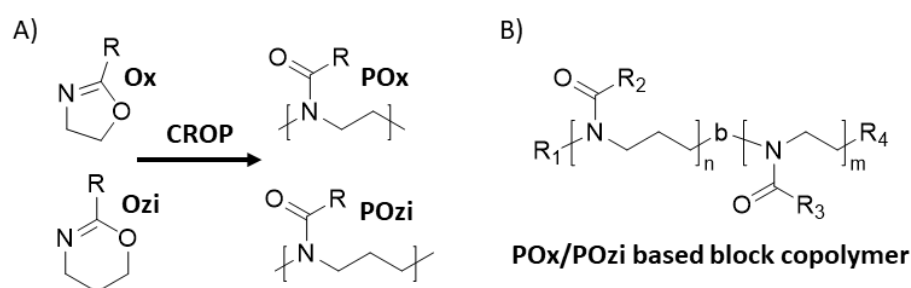


Figure 12. General POx and POzi Structures. A) The polymer classes POx and POzi are synthesized via cationic ring opening polymerization (CROP) of 2-substituted-2-oxazolines (Ox) and 2-substituted-2-oxazines (Ozi) with the substitute R. B) Example of a POx/POzi based block copolymer with the chain length n and m of the POzi and POx block, respectively. Both blocks have different sidechain substitutions (R₂ and R₃). During initiation and termination additional functionalities (R₁, R₄) are introduced.

During initiation, a nucleophilic attack of the nitrogen lone pair of the Ox or Ozi onto an electrophilic initiator creates an oxazolinium cation. Different electrophilic compounds were used as initiators, including sulfonates, nosylates, triflates and halides, oxazolinium salts and Lewis acids, among others.¹⁷⁰ The initiation step can also be used to introduce specific functionalities at the alpha position of the polymer to create semitelechelic and telechelic structures for subsequent coupling reactions, with, for example, drugs, dyes or imaging agents.¹⁸⁰ In order to prevent undesirable side reactions and termination processes during polymerization, however, no unprotected nucleophilic functionality should be present in the initiator structure. An overview of various functional initiators and the related applications of the polymers can be found in a review by Robin and co-workers.¹⁷¹ In this work, all described polymers were initiated with methyl triflate. This ensured a very fast initiation. Furthermore, properties of the various polymers were not affected by using different types of initiators.

In the propagation a series of Ox or Ozi monomers attack the cationic oxazolinium intermediate, forming the POx or POzi polymer backbone by a ring-opening reaction and the formation of an amide by remaining the living oxazolinium chain-end. Ideally, no chain coupling, transfer or termination reactions

during propagation with a first-order kinetics are observed. Fast initiation and the livingness of the polymerization gives control over the molecular weight and a narrow molar mass distribution expressed by the dispersity (D). In addition, different monomers can be used during propagation simultaneous or step by step, resulting in statistical copolymers and defined block copolymers, respectively. In the simultaneous approach, gradient copolymers can be obtained when using monomers with different polymerization kinetics. In general, the kinetics are influenced by the initiation rate and other reaction conditions such as concentration, temperature and solvent. Several studies were conducted comparing reaction kinetics of POx, POzi and combinations. For a detailed overview comparing POx and POzi kinetics in homopolymers and gradient copolymers the reader is referred to comprehensive review articles.^{178,179}

The termination at 5-position is carried out by a nucleophilic attack of an added termination agent (strong nucleophile), such as deprotonated carboxylates and amines, on the living cationic chain-end. Termination on the 2-position has also been reported for weaker nucleophiles, such as water. In addition, functionalities can easily be introduced upon termination with high end-group fidelity yielding semitelechelic and telechelic structures.^{171,180}

In addition to chain end functionalities, tailor made side chains can be used for polymer analogous reactions. Repeat units with specific functionalities, such as a double bond in the case of poly(2-(3-butenyl)-2-oxazoline) (PButenOx), can already be introduced during synthesis.¹⁸¹ Functionalities that affect the polymerization or are expected to undergo a transformation due to the polymerization conditions are accessible through appropriate protection groups. Exemplary, Stamm and collaborators applied monomer protection group chemistry to introduce carboxyl functionalities in a block copolymer for a surface grafting approach.¹⁸² They mistakenly called their polymer carboxyl terminated, although the termination reaction was performed with the secondary amine piperidine and the carboxyl group was introduced in the side chain. Nonetheless, they were able to successfully polymerize the monomer 2-(2-methoxycarbonyl)ethyl-2-oxazoline. The carboxyl functionality was subsequently obtained via controlled ester saponification.

Another straightforward approach is the use of POx/POzi as precursor for the preparation of linear polyethylenimine (L-PEI)/polypropylenimine (L-PPI). L-PEI is obtained via acidic or basic hydrolysis of POx, in which the POx sidechains are removed and the tertiary amide groups are transformed into secondary amines. In a kinetically controlled fashion only a few sidechains are removed yielding POx-PEI copolymers (Figure 13).

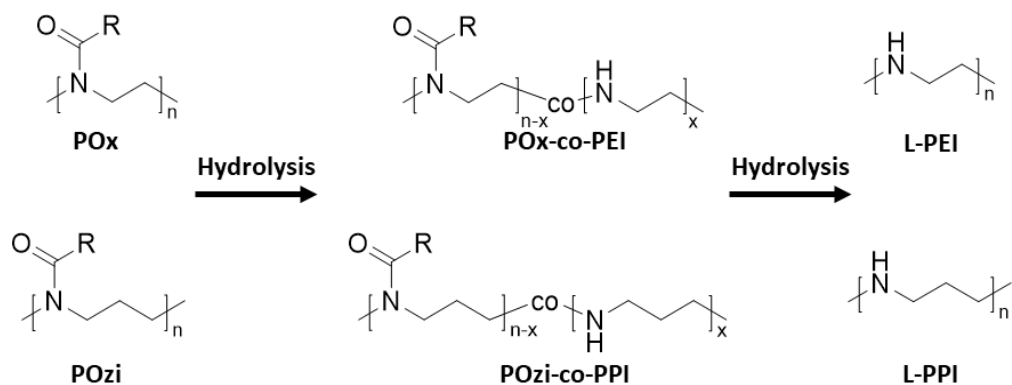


Figure 13. Schematic Overview of the hydrolysis of POx and POzi. Partial hydrolysis yields POx-co-PEI and POzi-co-PPI copolymers. Via full hydrolysis L-PEI and L-PPI are obtained.

For a detailed elucidation of the different mechanism of POx/POzi hydrolysis into PEI/PPI units the reader is referred to excellent review articles.^{179,183}

As the alkaline hydrolysis has been reported to lead to degradation of the polymer backbone, acidic hydrolysis is predominantly used.¹⁸⁴ In addition, the protonated L-PEI is water soluble, while the free base version of L-PEI is not. The water insolubility, however, can cause problems during the reaction in basic conditions.

The first acidic hydrolysis was performed using the polymers PMeOx, poly(2-ethyl-2-oxazoline) (PEtOx) and poly(2-phenyl-2-oxazoline) (PPheOx) and was shown to follow a pseudo-first order kinetics.¹⁸⁵ Due to lowest steric hindrance and best hydration, hydrolysis of PMeOx is faster compared to PEtOx and PPheOx, as discussed by Hoogenboom and co-workers.^{186,187} To control the hydrolysis rate, the temperature and/or the amount of added acid (often aqueous HCl) is altered. In addition, the hydrolysis is accelerated by the formation of seven ring like intermediates between neighboring L-PEI groups.^{183,188,189} This leads to the observation of block like PEI segments alongside the POx-PEI copolymer. Further, it was demonstrated that the degree of polymerization and polymer concentration has no significant impact on the hydrolysis kinetics.¹⁸⁶ In contrast, the polymer sidechain impacts the hydrolysis kinetics. The hydrolysis of POzi polymers is by far less described. It was first described for unsubstituted POzi via alkaline hydrolysis yielding crystalline L-PPI by Saegusa, Nagura and Kobayashi in 1973.¹⁹⁰ The first acidic hydrolysis of a substituted POzi was reported in 1989 by Gunn and collaborators for the homopolymer poly(2-phenyl-2-oxazine) (PPheOzi).¹⁹¹ In 2008, York and Co-workers used L-PPI obtained via acidic hydrolysis of PEtOzi as a polymer electrolyte PPI/lithium triflate system.¹⁹² More recently, Nahm et al. investigated the partially hydrolysis of poly(2-ethyl-2-oxazine) (PEtOzi).¹⁹³ The polymer PMeOzi was also used in acidic hydrolysis to obtain PPI.¹⁹⁴ The benefits of PPI compared to PEI as absorbents for CO₂ capture from ultradilute streams were discussed. To my knowledge, no hydrolysis of a POzi-based block copolymer has been described so far. In contrast, there

are several reports on hydrolysis of POx copolymers by selectively hydrolyzing specific polymer sidechains. Hoogenboom and co-workers achieved a high degree of hydrolysis selectivity in PMeOx₆₀-b-PPheOx₁₅ in ethanol/water (80:20) as solvent.¹⁸⁷ After 240 min, the hydrophilic PMeOx block was 95 % hydrolyzed, whereas the hydrophobic PPheOx block only 10 %. The authors also highlighted the effect of the added ethanol on the hydrolysis kinetics. In 2015, Vlasi and Pispas partially hydrolyzed a gradient copolymer comprising the hydrophilic PMeOx and hydrophobic and aromatic PPheOx.¹⁹⁵ Again, preferentially the PMeOx “block” was hydrolyzed. This partially hydrolyzed copolymer self-assembled in aqueous solution (See 2.3.2 Aqueous Solubility and Self-Assembly). Litt and Lin observed similar selectivities in block copolymers with hydrophilic and hydrophobic moieties. First the hydrophobic units were hydrolyzed.¹⁹⁶ This selectivity’s can be used in the design of novel tailor made biomaterials.

Interestingly, these secondary amine moieties of PEI/PPI can be used for post-polymerization modification by e.g. the coupling of activated carboxylic acids and the nucleophilic PEI/PPI amine units, among other reactions¹⁸³, generating new tertiary amide bonds (Figure 14). This route is quite elegant as novel functional POx/POzi copolymers can be synthesized without the need of synthesizing and purifying new functional Ox/Ozi monomers.

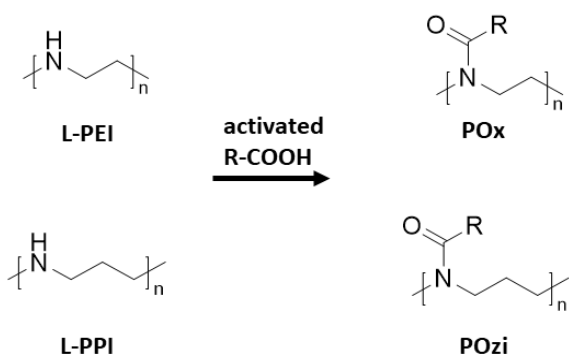


Figure 14. Schematic Overview of the carboxylic acid (R-COOH)/amine coupling. With this route the polymers L-PEI and L-PPI are used as precursor for novel POx/POzi polymers.

This route was already described in great detail in the 1990s for the production of the first POx hydrogels by Chujo and Co-worker. This contributions will be examined in more detail in the section 2.3.3.2 **Hydrogels.**

It should be mentioned here that other polymer architectures, such as polymer stars¹⁹⁷ and brushes¹⁹⁸, besides linear POx/POzi are also feasible. In addition, mixed systems with other polymer classes as described by Yoshinaga and co-workers for poly(tetrahydrofuran)-b-PEtOx block copolymer, can also be synthesized.¹⁹⁹ However, other polymer architectures as well as mixed systems are not in the focus of this work.

In summary, by suitable structure design different polymer compositions with a wide range of functionalities can be introduced in a controlled manner. In addition, the location and number of the functionalities alongside the polymer at defined chain ends and side chains in defined polymer domains and blocks can be controlled.

However, all these modifications and functionalities influence the polymer properties such as the water solubility and self-assembly, which are crucial properties for different biomaterial applications. Both properties in relation to POx/POzi copolymers will be discussed in the following section.

2.3.2 Aqueous Solubility and Self-Assembly

In the design of biomaterials water solubility is one crucial aspect. The water solubility of POx and POzi mainly depends on the side chain. PMeOx and PMeOzi are water soluble due to the hydrophilic polyamide POx and POzi backbone. The higher homologue structures PEtOx, poly(2-n-propyl-2-oxazoline) (PnPrOx), PEtOzi and poly(2-n-propyl-2-oxazine) (PnPrOzi) are characterized by LCST behavior depending on the degree of polymerization, end groups and external influences such as salts (Table 1).^{200,201} Exemplarily, the polymer PEtOzi is water soluble with a chain length of 50 but exhibits a cloud point temperature (T_{CP}) of approximately 56 °C for a polymer with 100 repeating units.²⁰¹

Table 1. Thermoresponsive properties of POx/POzi homopolymers with n-alkyl sidechains. Values were taken from reference [200,201].

Sidechain	T_{CP} [°C] POx/POzi
Methyl	soluble/soluble
Ethyl	94/56
Propyl	25/11
Butyl	insoluble/insoluble

The T_{CP} was determined via turbidity measurements at a degree of polymerization of 100. An overall water solubility and complete insolubility are characterized by the words soluble and insoluble, respectively.

Here it must be noted that in the literature LCST behavior is often performed only at a certain concentration. This, however, determines the T_{CP} . Below the LCST, the polymer is soluble at all concentrations. However, there can be strong deviations between the LCST and the T_{CP} at a certain concentration.

In general, the T_{CP} of POzi are lower compared to the corresponding POx derivative as described by Bloksma et al.²⁰¹ Increasing the sidechain to poly(2-n-butyl-2-oxazoline) (PnBuOx) and poly(2-n-butyl-2-oxazine) (PnBuOzi) leads to water insoluble structures. In addition, homopolymers with aromatic sidechains such as PPheOx and poly(2-benzyl-2-oxazoline) (PBzOx) are water insoluble.¹⁷⁸ The differences in solubility can be used in gradient copolymers and block copolymers combining hydrophilic and thermoresponsive and/or hydrophobic building blocks to tune water solubility, LCST behavior and self-assembly above a critical concentration and/or temperature, which is the basis for many applications (**See 2.3.3 Biomaterial Applications**). In principle above the LCST temperature turbidity and precipitation can be observed. However, the thermoresponsive properties of POx/POzi based copolymers expands the traditional LCST type behavior. Therefore, in recent years temperature-induced self-assembly, crystallization processes and gelation was observed for POx and POzi structures

and very recently reviewed by Zahoranova and Luxenhofer.²⁰² Crystallization processes are not in the scope of the presented thesis. Here, only temperature-driven self-assembly will be discussed. POx/POzi based gelation will be covered in the following section (See 2.3.3 Biomaterial Applications).

Self-assembly of (macro)molecules such as amphiphilic block and gradient copolymers into supramolecular structures with a certain degree of organization is based on non-covalent physical interactions or dynamic covalent bonds.²⁰³⁻²⁰⁵ A certain degree of phase-separation caused by incompatibility of polymer units must be present for self-assembly to arise. In aqueous solution, this is usually ensured by a hydrophilic and a hydrophobic polymer part. Furthermore, thermoresponsive segments can be used to introduce stimuli responsivity.²⁰² In general, ordered structures are controlled by a balance of two types of forces, short-range attractive forces and a long-range repulsive forces as nicely illustrated by Förster and Konrad.²⁰⁵ Different morphologies, such as spherical and worm-like micelles and vesicles, of self-assemblies exist (Figure 15).

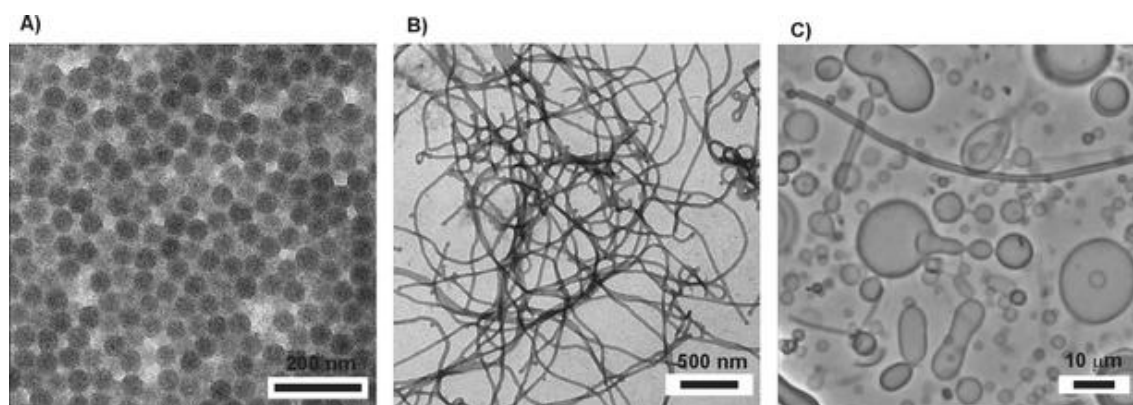


Figure 15. Overview of self-assembled structures of poly(butadiene)-b-poly(ethylene oxide) (PB-b-PEO) block copolymers with different block ratios and block length. The shapes of the aggregates ranged from spherical micelles (PB₂₀₂-b-PEO₃₆₀) via worm-like micelles (PB₁₂₅-b-PEO₁₅₅) to predominantly vesicles (PB₃₇-b-PEO₄₀). Reprinted with permission from reference 208.

But what is the driving force for the generation of different morphologies?

In principle, the balance between attractive and repulsive forces of the hydrophilic and hydrophobic compartments, which are defined by the stretching of the polymer chains, the interfacial energy between the blocks, different interactions among corona-forming chains, the strength of interactions between the blocks and the volume fraction of each block, are decisive for the morphology.^{202,206} These forces cause the arrangement of several macromolecules in such a way that domains and interfaces are formed which reflect the shape of the molecule.²⁰⁵ These interfaces are characterized by a curvature depending on the volume fraction of the microphase-separated polymer blocks.²⁰⁷ A highly curved interface obtained by a small volume fraction of the hydrophobic core-forming block results in spherical micelles (Figure 15 A). A decrease of the hydrophilic/hydrophobic block ratio changes the volume fraction and as a result a shape transition to worm-like micelles (Figure 15 B) and even vesicles (Figure 15 C) with a very less

interfacial curvature is observed as demonstrated by Antonietti and Förster.²⁰⁸ However, also other parameters such as copolymer concentration, added (co-)solvents, ions or homopolymers and the method of self-assembly preparation have a significant impact and leads to a various number of more exotic morphologies such as different rods, large compound assemblies and multilamellar vesicles.²⁰⁹ In addition, the formation and transformation of different morphologies can be recognized by a macroscopic change, such as the occurrence of turbidity, precipitation or gelation, in the sample.

Due to the LCST behavior of certain POx/POzi polymers temperature driven self-assembly of copolymers can be studied. Dworak and co-workers studied the LCST behavior of gradient P(PrOx-co-MeOx)_{grad} copolymers in 2017.²¹⁰ During cooling a hysteresis behavior was observed, which was attributed to the formation of self-assemblies elucidated by dynamic light scattering (DLS) experiments. However, no study was conducted to unravel the morphology of the aggregates. A comprehensive study on the temperature driven self-assembly of a block copolymer comprising a PEtOx block and a block consisting of a statistical copolymer of PEtOx and PnPrOx moieties (PEtOx-b-P(EtOx-co-nPrOx)_{stat}) was performed by Trinh et al. in 2012.²¹¹ Upon heating they observed changes in morphology (unimers+few aggregates→aggregates→smaller micelle-like structures→larger compact aggregates) and transmittance (clear→turbid→clear→turbid) evaluated via DLS, static LS and turbidity measurements. In the study, the concentration was kept at 5 g/L. A variation, especially an increase, of concentration would be interesting to elucidate if a second macromolecular change such as η increase or gelation is observed upon heating. The thermoresponsive behavior of various ABA and BAB triblock copolymers of PMeOx and PnPrOx combinations was investigated by Luxenhofer and co-workers.²¹² Different variations of the η , turbidity and particle radius as a function of temperature were observed. Interestingly, in some cases an increase of the η with temperature (thermothickening) but no thermogelling was observed.

In another approach hydrophobic segments in combination with the hydrophilic PMeOx or the at room temperature soluble PEtOx are used to induce self-assembly in POx/POzi based copolymers. Predominantly PheOx and 2-nonyl-2-oxazoline monomers were used in the past. Other studies used poly(2-(3-ethylheptyl)-2-oxazine) and poly(2-n-nonyl-2-oxazine) and the corresponding POx analogous.²¹³ Interestingly, the POx containing amphiphiles exhibited significant higher micellar diameters compared to POzi. This study, is one of the first describing and comparing the self-assembly of POx and POzi triblock copolymers in aqueous solution. Another very interesting observation was reported by Weberskirch and co-workers in 2015.²¹⁴ The researchers characterized the micellization and mobility of amphiphilic POx based block copolymers comprising hydrophilic PMeOx blocks and different hydrophobic blocks (poly(2-pentyl-, heptyl-, nonyl-2-oxazine)) at different temperature via DLS and nuclear magnetic resonance (NMR) experiments. Temperature-dependent differences with respect to stability and size of the aggregates were confirmed. However, in the polymer structure no thermoresponsive block was used.

The aforementioned hydrophobic and aromatic PPheOx has been very often studied with the hydrophilic units PMeOx and PEtOx especially in gradient copolymers. The synthesis in a statistical copolymerization and the micellization on surfaces via spin-coating of quasi-diblock copolymers comprising PMeOx or PEtOx and PPheOx were described by Schubert, Gohy and co-workers.^{215,216} In 2008, the same research group compared the self-assembly of block and gradient PMeOx₅₀-PPheOx₅₀ copolymers in different ethanol/water ratios.²¹⁷ In both cases, the block and gradient approach, worm-like micelles were shown to be present in water. The addition of ethanol leads to the formation of predominantly spherical micelles. Interestingly, Demetzos and co-workers investigated different ratios of PMeOx and PPheOx units in gradient copolymers and analyzed the self-assembly in water as a function of temperature. Depending on the “block” ratios different sizes of aggregates were obtained. However, the temperature had no significant impact on the self-assembly investigated via DLS.²¹⁸ First triblock copolymers of PMeOx-b-PPheOx-b-PMeOx were studied by Tiller and co-workers. They investigated the self-assembly properties for different block ratios. However, also different degrees of polymerizations were used. Therefore, it is difficult to analyze the observations. In summary, different undefined structures in the range of 15 to 600 nm, very small unimolecular polymer micelles (few nm), polymer micelles (18-44 nm) and polymerosomes (140-460 nm) were discussed.²¹⁹ In the year 2019, Hoogenboom and co-workers presented a strategy to synthesize quasi-diblock and more gradient copolymers using sulfolane and acetonitrile as polymerization solvent, respectively, and compared the self-assembly properties with a control diblock copolymer.²²⁰ Increased blockiness leads to the formation of smaller particles was the overall conclusion. One of the most comprehensive studies on the self-assembly of such gradient copolymers was carried out by Filippov et al. using a set of powerful scattering methods such as small-angle X-ray scattering (SAXS), small-angle neutron scattering (SANS), SLS and DLS in combination with NMR experiments. In the end, the researchers presented a new aggregation mechanism into “bitterball-core” micellar structures.²²¹

Interestingly, already 1967 Levy and Litt synthesized a PPheOzi homopolymer¹⁷⁷, the POzi homologue to the well-studied PheOx. However, no detailed contribution was performed dealing with the self-assembly of a gradient or block copolymer comprising PPheOzi moieties so far. In addition, the higher homologous structures poly(2-benzyl-2-oxazoline) PBzOx in was used in a PBzOx-co-PnBuOx hydrophobic block in ABA type amphiphiles once in 2015 by Kabanov and co-workers²²² for the encapsulation of hydrophobic drugs and the poly(2-benzyl-2-oxazine) PBzOzi is also undescribed so far.

Other very interesting POx/POzi based amphiphilic systems were described in the context of drug encapsulation, which are presented in the following section.

2.3.3 Biomaterial Applications

The polymer classes of POx and POzi exhibit excellent biological properties, which make them serious alternatives to the gold standard PEG in biomaterial development. Thus, for example, it was already demonstrated that different POx structures with different average molar masses showed only low cytotoxicity in different cell lines even at very high polymer concentrations (up to 100 g/L).²²³⁻²²⁷ Further, no strong inflammation triggered response of macrophages was observed *in vitro*.²²⁸ In addition, rapid renal clearance *in vivo* has been demonstrated for POx with sufficiently small molar masses.²²⁹ Based on these properties, POx/POzi based polymers were used in different biomaterial applications including the preparation of polymer-drug²³⁰ and peptide conjugates²³¹, polyplexes²³², drug loaded polymer micelles²³³, hydrogels²³⁴ and anti-fouling and cell adhesion surface coatings²³⁵.

In this subsection, first selected studies dealing with drug encapsulation are presented, which were used as basis for the present thesis (**chapter I-III**). The second part of the subsection is related to POx/POzi based hydrogels introduced with a focus on possible translation towards bioprinting to connect the sections **2.1-2.3** of this state of knowledge part. Further, these fundamental studies were used to design the projects of the **chapters II-IV**.

2.3.3.1 Nanoformulations

As highlighted in the previous subsection, self-assembled core-shell structures, especially polymer micelles, can be used to encapsulate drugs with limited water solubility, predominantly in the core of the formed aggregates. Often it is believed that increasing the hydrophobic/hydrophilic contrast leads to an increase of micellar stability and higher drug loading.²⁰² In 2010, Kabanov and co-workers investigated the solubilization of the water-insoluble drug Paclitaxel (PTX) via the thin-film method (Figure 16 C) using an ABA type triblock copolymer bearing hydrophilic PMeOx A blocks and moderate hydrophobic PnBuOx B block (Figure 16 A).²³³ The researchers achieved extraordinarily high loading capacities of up to 45 wt.% of active drug and a high water solubility of the formulation. In 2012, the same research group used the same polymer to investigate the loading capacities for a huge library of different anti-cancer drugs and observed first structure-property related synergistic effects.²³⁶ Another way to study structure property relationships in drug formulations is to systematically vary the polymer structure, particularly the hydrophobic drug-bearing block.

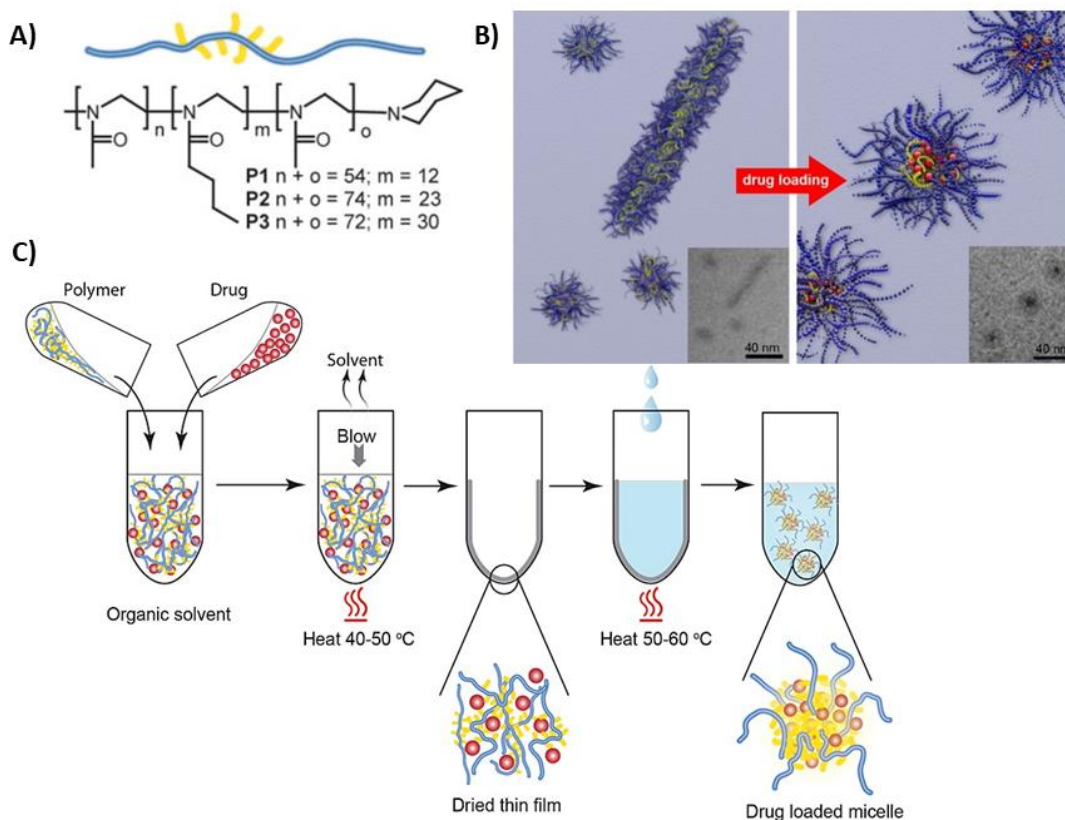


Figure 16. Overview of POx based amphiphiles for drug encapsulation. A) Polymer structure of Me-PMeOx-b-PnBuOx-b-PMeOx-Pip with different block length used for drug encapsulation. Reprinted with permission from reference 233. B) Drug induced morphology switch from short worm-like micelles to spherical micelles. TEM images are shown as inserts. Reprinted with permission from reference 237. Thin-film method for the preparation of drug loaded polymer micelles. Reprinted with permission from reference 222.

Seo and Schulz et al. investigated the influence of the hydrophobic middle block on the encapsulation capacity and efficiency of different taxanes in 2015.²²² Therefore, a series with comparable polymer composition of linear and branched aliphatic POx based hydrophobic blocks of various chain lengths (C4-C9) and one aromatic PBzOx derivative were used. Generally, the polymers with mildly hydrophobic B blocks outperformed the polymers with higher or lower hydrophobicity with regard to drug loading. In contrast, the amphiphiles with strongly hydrophobic B blocks exhibited best colloidal stability. The aforementioned triblock PMeOx-b-PnBuOx-b-PMeOx, however, which showed the highest drug loading, also exhibited very good colloidal stability. Interestingly, upon changing the central block from PnBuOx to the branched PsecBuOx, a significant reduction of loading capacity was observed. In consequence, minor changes of the polymer can lead to significant differences in drug loading.

It is known, that a lot of factors influence the morphology of self-assemblies. Therefore, it was assumed that the interaction of the polymer and the loaded drug can impact the self-assembly process. The unusual high PTX loading of the polymer PMeOx-b-PnBuOx-b-PMeOx was studied in detail by Schulz

et al.²³⁷ A drug-induced morphology switch from short worm-like micelles to small spherical micelles upon drug-encapsulation was investigated with different methods such as DLS, atomic force microscopy, transmission electron microscopy (TEM) and SANS (Figure 16 B).²³⁸

The first study comparing POx and POzi amphiphiles on drug-encapsulation was performed by Luxenhofer and co-workers in 2017. This contribution will be part of the **Chapter I**. In addition, no detailed contribution was performed introducing different aromatic moieties in the polymer structure to study the effects on drug encapsulation of different drugs with a variation of the aromatic character (**Chapter I**).

In particular, the polymer classes of POx and POzi are well suited to study the influence of different factors on self-assembly and, consequently, drug encapsulation. On the one hand, the smallest structural changes can be made relatively easily. On the other hand, POx/POzi have different possibilities to interact with each other and with the loaded drugs. Hydrophobic effects can be studied by introducing hydrophobic blocks. Nevertheless, each repeating unit has a tertiary amide that can act as polar hydrogen bonding acceptors. It is also possible, to synthesize polymers with aromatic units such as PPheOx and PBzOx to study the impact of pi-pi interactions.

2.3.3.2 Hydrogels

In this subsection, the principles of hydrogels as biomaterials and especially for biofabrication are discussed for specific POx/POzi based systems, which were established until August 2018, the beginning of the hydrogel part of this thesis.

In principle, as already demonstrated in the first section (**See 2.1 Hydrogels as Biomaterials**), there are several crosslinking methods such as crosslinking during polymerization^{239,240}, high energy irradiation^{241,242} and crosslinking of polymer precursors²³⁴. The first two methods are hardly suitable for the application of bioprinting (**See 2.2 Bioprinting: A Technology of Biofabrication for Tissue Engineering and Regenerative Medicine**), since harsh conditions (high temperatures, toxic solvents, radiation, etc.) prevail during crosslinking and are therefore not cytocompatible. However, as already shown, the cells should already be distributed in the system during gel formation.

In the late 1980s and early 1990s, Chujo et al. established an inspiring library of POx based hydrogels using several crosslinking reactions. Therefore, predominantly the hydrophilic PMeOx homopolymer was partially hydrolyzed and subsequently modified (**See 2.3.1 Synthesis**) with different moieties to introduce covalent-, dynamic- and supramolecular crosslinking.²⁴³⁻²⁵³ However, at this time, the hydrogels were not discussed with regard to biomedical applications. Furthermore, the predominantly hydrophilic nature of the precursor polymers would probably not allow for precision bioprinting (**See 2.2.3.1 Rheology of Bioinks**).

Since the potential of the POx/POzi polymer classes is only exploited by very few research groups and the research field of biofabrication is a very young discipline, the list of POx/POzi systems dealing with biofabrication is very short. Therefore, selected systems for 3D cell culture, classical TE and hydrogel-based drug delivery are also discussed here in advance.

In 2013, Farrugia and coworkers used a statistical (probably gradient) copolymer comprising the hydrophilic PMeOx and the hydrophobic poly(2-(dec-9-enyl)-2-oxazoline) bearing a terminal alkene functionality.²⁵⁴ The polymer was decorated with RGD (Arg-Gly-Asp, Arginine-Glycine-Aspartate) cell adhesion peptide moieties via thiol-ene reaction and chemically crosslinked using dithiothreitol as crosslinker, Irgacure 2959 as photoinitiator and UV-light. Interestingly, different cell morphologies and orientations of the seeded cells were obtained as a function of RGD decoration. Furthermore, for this POx-based system, cytocompatible cell encapsulation was demonstrated for the first time. Since then, several other studies were described employing similar thiol-ene crosslinking reactions, despite the controversial discussed UV-mediated crosslinking.²⁵⁵ However, no study was conducted to characterize the rheology of the precursor solution before crosslinking. This makes it difficult to assess whether the system described would be useful in bioprinting.

The synthetic POx/POzi based toolbox was also used for the binding and triggered release of DNA alongside a hydrogel matrix. In a copolymer approach, the hydrophilic EtOx was polymerized with a monomer bearing a protected amino functionality.²⁵⁶ After polymerization, deprotection yielded free amine groups suitable for crosslinking with epichlorohydrin and further DNA immobilization. The DNA release from the hydrogel was triggered via polyanionic heparin addition. However, such an approach is not suitable for bioprinting as the very reactive free amine groups can interfere with the embedded cells and medium supplements, thus making the control of the fabrication process challenging. Similar DNA binding studies were conducted using post-polymerization hydrolysis and polymer analogous modification strategies (**See 2.3.1 Synthesis**). In these approaches, the POx polymer was hydrolyzed yielding PEI, which was subsequently modified generating PEI-PButenOx random copolymers with the ability to crosslink the PButenOx double bonds.²⁵⁷

As already mentioned, the polymer classes of POx/POzi are rarely described in the field of biofabrication. However, few reports dealing with solution electrospinning²⁵⁸ and MEW²⁵⁹ exist. In 2016, Sanyal and co-workers reported multireactive POx nanofibers generated via solution electrospinning in dimethylformamide and tetrahydrofuran (1:1).²⁶⁰ Further, the PButenOx containing fibers were stabilized on the fly via thiol-ene reaction. In addition, the fibers were visualized via the attachment of fluorescent dyes using thiol-ene and thiol-maleimide chemistry. Stubbe et al. described the solution electrospinning of the hydrophilic polymer PEtOx in aqueous conditions. They obtained tunable fiber thicknesses depending on the polymer concentration and polymer molar mass.²⁶¹ De Clerck and Hoogenboom combined both approaches by establishing an *in situ* crosslinkable aqueous electrospinning system based on POx. The researchers used partially hydrolyzed PEtOx to introduce selenol moieties. Via electrospinning the formation of diselenide crosslinks was observed.²⁶² However, solution electrospinning is usually a cell-free method of biomaterials. The same is true for MEW. In addition to solution electrospinning, the deposition of a molten fiber in MEW is highly controlled. Therefore, constructs with defined shapes in outstanding resolution are obtained. In 2014, Groll and co-workers processed PEtOx via MEW by varying the crucial instrument parameters such as temperature, pressure, voltage and collector distances and spinnerets sizes.²⁶³

So far, true bioprinting, in which the cells are part of the printing process, was only reported once for the polymer classes of POx/POzi by Lorson et al.²⁶⁴

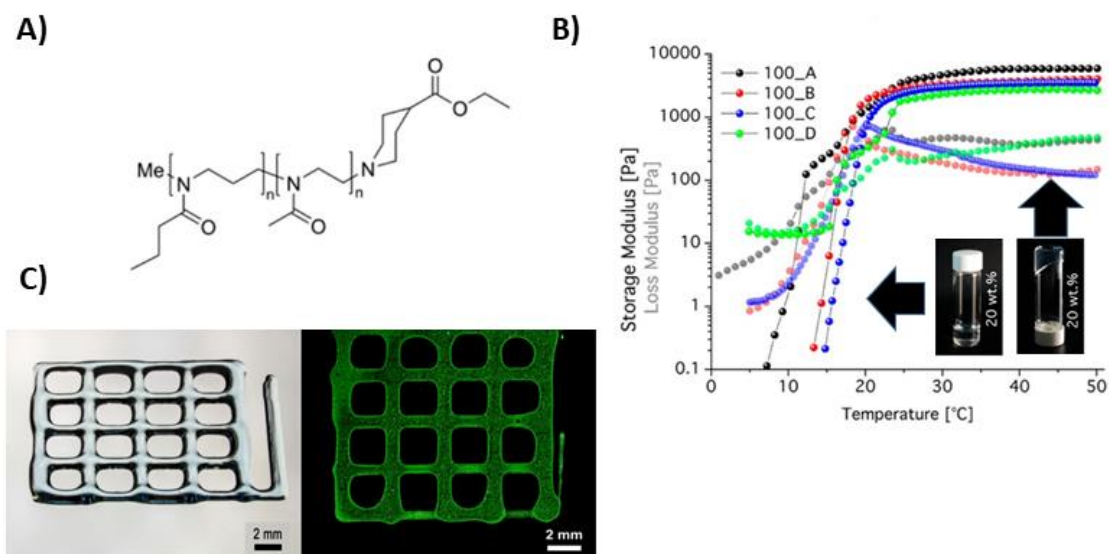


Figure 17. First bioprinting of a POx/POzi based hydrogel. A) Polymer structure of Me-PMeOx-b-PnPrOzi-EIP (EIP: Ethyl isonipecotate). B) Thermogelling properties of different polymer batches from approximately 5 to 50 °C. Inserted pictures are a low viscous solution at low temperature and a physical hydrogel above t_{gel} . C) 3D printed lattice structure. Pre-stained fibroblasts were homogenously distributed in the lattice scaffold. Reprinted with permission from reference 264.

The researchers established a thermogelling POx/POzi based diblock copolymer comprising a hydrophilic PMeOx block and a thermoresponsive PnPrOzi block (degree of polymerization 100 and 200, PMeOx/PnPrOzi 1:1) (Figure 17 A). Above a critical concentration (20 wt.%) an aqueous solution undergoes a reversible sol/gel transition upon heating. A comprehensive rheological study was performed evaluating t_{gel} and recording G' and G'' as a function of temperature (Figure 17 B). In addition, the rheological properties of the gel were analyzed with a focus on gel-phase EBB. The hydrogel exhibited highly shear-thinning properties and fast structure recovery of G' to 4-5 kPa after deformation was observed. Using SANS, the authors were furthermore able to describe the gelation mechanism: Upon heating, a bicontinuous sponge-like network is formed comprising interconnected and channeling vesicles. In the end, first EBB experiments were described whereby the cytocompatibility of the material and the fabrication process was confirmed after 24 h using fibroblasts (Figure 17 C). At this point, no long-term cell culture was possible due to the physical nature of the crosslinking. Concluding the manuscript, the researchers outlined the versatility of the polymer classes of POx/POzi, which can be applied to the described diblock copolymer to overcome certain limitations and to use the hydrogel for further basic and applied research especially in biofabrication (**Chapter IV**). This work also showed that unusual polymer properties can be observed by synthesizing novel polymers. It shows very nicely how these can then subsequently be used for novel applications. This approach is the basis for the **Chapters II and III**.

3 Summary

In this work, the influence of aromatic structures on drug encapsulation, self-assembly and hydrogel formation was investigated. The physically crosslinked gelling systems were characterized and optimized for the use in biofabrication and applied in initial (bio)printing experiments.

Chapter I: The cytocompatible (first *in vitro* and *in vivo* studies) amphiphile PMeOx-b-PBzOx-b-PMeOx (A-PBzOx-A) was used for the solubilization of PTX, schizandrin A (SchA), curcumin (CUR), niraparib and HS-173.

Chapter II: Compared to the polymers A-PPheOx-A, A-PBzOx-A and A-PBzOzi-A, only the polymer A-PPheOzi-A showed a reversible temperature- and concentration-dependent inverse thermogelation, which is accompanied by a morphology change from long wormlike micelles in the gel to small spherical micelles in solution. The worm formation results from novel interactions between the hydrophilic and hydrophobic aromatic polymer blocks. Changes in the hydrophilic block significantly alter the gel system. Rheological properties can be optimized by concentration and temperature, which is why the hydrogel was used to significantly improve the printability and stability of Alg in a blend system.

Chapter III: By extending the side chain of the aromatic hydrophobic block, the inverse thermogelling polymer A-poly(2-phenethyl-2-oxazoline)-A (A-PPhenEtOx-A) is obtained. Rapid gelation upon cooling is achieved by inter-correlating spherical micelles. Based on ideal rheological properties, first cytocompatible bioprinting experiments were performed in combination with Alg. The polymers A-poly(2-benzhydryl-2-oxazoline)-A (A-PBhOx-A) and A-poly(2-benzhydryl-2-oxazine) (A-PBhOzi-A) are characterized by two aromatic benzyl units per hydrophobic repeating unit. Only the polymer A-PBhOzi-A exhibited inverse thermogelling behavior. Merging micelles could be observed by electron microscopy. The system was rheologically characterized and discussed with respect to an application in 3D printing.

Chapter IV: The thermogelling POx/POzi system, in particular the block copolymer PMeOx-b-PnPrOzi, was used in different applications in the field of biofabrication. The introduction of maleimide and furan units along the hydrophilic polymer part ensured additional stabilization by Diels-Alder crosslinking after the printing process.

4 Zusammenfassung

In dieser Arbeit wurde der Einfluss von aromatischen Strukturen auf die Wirkstoffeinkapselung, der Selbstassemblierung und die Hydrogelbildung untersucht. Die physikalisch vernetzten Gele wurden für den Einsatz in der Biofabrikation charakterisiert und optimiert und fanden ersten (Bio)druckversuchen Anwendung.

Kapitel I: Das zytokompatible (erste *in vitro* und *in vivo* Studien) Amphiphil PMeOx-b-PBzOx-b-PMeOx (A-PBzOx-A) eignet sich hervorragend für die Solubilisierung von PTX, Schizandrin A (SchA), Curcumin (CUR), Niraparib und HS-173.

Kapitel II: Ausschließlich das Polymer A-PPheOzi-A zeigt im Vergleich zu den Polymeren A-PPheOx-A, A-PBzOx-A und A-PBzOzi-A eine reversible temperatur- und konzentrationsabhängige inverse Thermogelierung, welche durch eine Morphologie-Änderung von langen wurmartigen Mizellen im Gel zu kleinen sphärischen Mizellen in Lösung begleitet wird. Die Wurmbildung entsteht durch neuartige Wechselwirkungen zwischen den hydrophilen Polymerblöcken und den hydrophoben aromatischen Polymerblöcken. Veränderungen der hydrophilen Blöcke verändert signifikant das Gelsystem. Die rheologischen Eigenschaften können durch Konzentration und Temperatur optimiert werden, weshalb in einem Blendsystem die Druckbarkeit und Stabilität von Alginat signifikant verbessert wurde.

Kapitel III: Durch Verlängerung der Seitenkette des aromatischen hydrophoben Blocks erhält man das inverse thermogelierende Polymer A-Poly(2-phenethyl-2-oxazolin)-A (A-PPhenEtOx-A). Die schnelle Gelierung bei Abkühlung wird durch miteinander korrelierende sphärische Mizellen erzielt. Auf Grundlage idealer rheologischer Eigenschaften, konnten erste zytokompatible Biodruckversuche in Kombination mit Alginat durchgeführt werden. Die Polymere A-Poly(2-benzhydryl-2-oxazolin)-A (A-PBhOx-A) und A-Poly(2-benzhydryl-2-oxazine) (A-PBhOzi-A) sind durch zwei aromatische Benzyl-Einheiten pro hydrophober Wiederholungseinheit charakterisiert. Nur das Polymer A-PBhOzi-A zeigt inverses thermogelierendes Verhalten. Durch Elektronenmikroskopie konnten verschmelzende Mizellen beobachtet werden. Das System wurde hinsichtlich einer Anwendung im Bereich des 3D-Drucks rheologisch charakterisiert und diskutiert.

Kapitel IV: Das thermogelierende POx/POzi System, insbesondere das Blockcopolymer PMeOx-b-PnPrOzi, wurde in weiterführenden Studien im Bereich der Biofabrikation genutzt. Durch die Einführung von Maleimide- und Furan-Einheiten entlang des hydrophilen Polymerteil konnte eine zusätzliche Stabilisierung durch Diels-Alder-Vernetzung nach dem Druckprozess realisiert werden.

5 Main Part

In general, the main manuscripts are included in full length. The supporting information files are not included. They are available on the respective journal homepages (**See 8 Material and Methods**). For all included full manuscripts the permission for reprinting were obtained.

For publications not presented in full length, a representative figure or the graphical abstract was included along with the abstract, new concepts, and highlights, if any. The beginning and the end of the copied part are marked with ***. Permission for reprinting was obtained from the respective journal.

Chapter I

POx based ABA type amphiphiles with varying alkyl sidechains in the hydrophobic B block were used to solubilize different taxanes. In 2017, Lübtow et al. reported the first study comparing POx and POzi alkyl derivatives for the drug encapsulation of PTX and CUR.

*** The following abstract and graphic was reprinted with permission from *Journal of the American Chemical Society* **2017**, 139 (32), 10980-10983

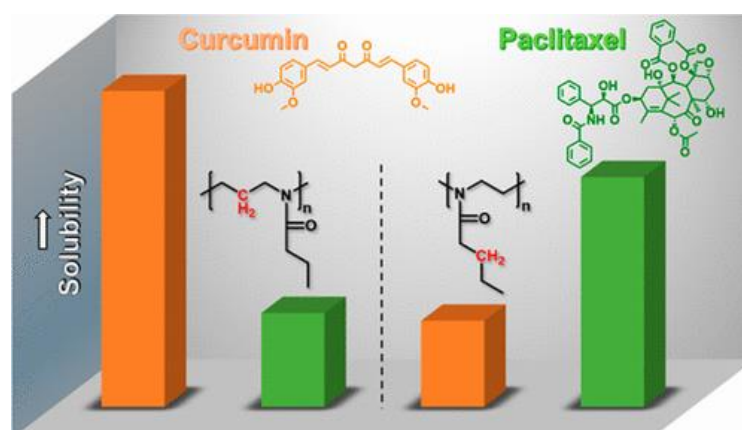
<https://doi.org/10.1021/jacs.7b05376>; © 2017 American Chemical Society

Drug Specificity, Synergy and Antagonism in Ultrahigh Capacity Poly(2-oxazoline)/Poly(2-oxazine) based Formulations

Lübtow M.M., Hahn L., Haider M.S. and Luxenhofer R.

Abstract

Polymer micelles offer the possibility to create a nanoscopic environment that is distinct from the bulk phase. They find applications in catalysis, drug delivery, cleaning, etc. Often, one simply distinguishes between hydrophilic and hydrophobic, but fine-tuning of the microenvironment is possible by adjusting the structure



of the polymer amphiphile. Here, we investigated a small library of structurally similar amphiphiles based on POx and POzi with respect to their solubilization capacity for two extremely water insoluble drugs, CUR and PTX. We found very significant and orthogonal specificities even if only one methylene group is exchanged between the polymer backbone and side chain. More strikingly, we observed profound synergistic and antagonistic solubilization patterns for the coformulation of the two drugs. Our findings shed new light on host–guest interaction in polymer micelles and such pronounced host–guest specificities in polymer micelles may not only be interesting in drug delivery but also for applications such as micellar catalysis. ***

In 2018 we reported the influence of aromatic moieties in the hydrophobic B block on the drug encapsulation. Four different amphiphiles with varying aromatic content for the solubilization of the model compounds PTX, SchA and CUR with rising aromaticity were tested.

The following publication was reprinted with permission from *Biomacromolecules* **2018**, 19 (7), 3119-3128. <https://doi.org/10.1021/acs.biomac.8b00708>; © 2018 American Chemical Society

Investigating the Influence of Aromatic Moieties on the Formulation of Hydrophobic Natural Products and Drugs in Poly(2-oxazoline)-Based Amphiphiles

Lukas Hahn,[†] Michael M. Lübtow,[†] Thomas Lorson,[†] Frederik Schmitt,^{†,‡} Antje Appelt-Menzel,[‡] Rainer Schobert,[§] and Robert Luxenhofer^{*,†}

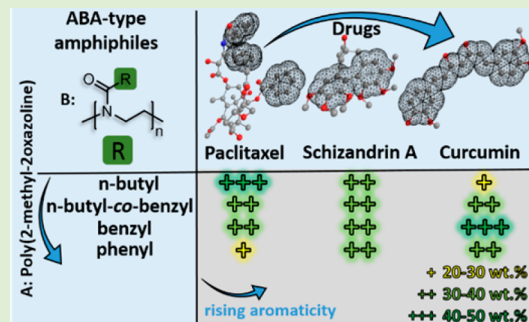
[†]Functional Polymer Materials, Chair for Advanced Materials Synthesis, Department of Chemistry and Pharmacy, Julius-Maximilians-Universität Würzburg, Röntgenring 11, 97070 Würzburg, Germany

[‡]Lehrstuhl Tissue Engineering und Regenerative Medizin and Fraunhofer-Institut für Silicatforschung ISC, Universitätsklinikum Würzburg, Röntgenring 11, 97070 Würzburg, Germany

[§]Organic Chemistry Laboratory, Universität Bayreuth, Universitätsstrasse 30, 95447 Bayreuth, Germany

Supporting Information

ABSTRACT: Many natural compounds with interesting biomedical properties share one physicochemical property, namely, low water solubility. Polymer micelles are, among others, a popular means to solubilize hydrophobic compounds. The specific molecular interactions between the polymers and the hydrophobic drugs are diverse, and recently it has been discussed that macromolecular engineering can be used to optimize drug-loaded micelles. Specifically, π - π stacking between small molecules and polymers has been discussed as an important interaction that can be employed to increase drug loading and formulation stability. Here, we test this hypothesis using four different polymer amphiphiles with varying aromatic content and various natural products that also contain different relative amounts of aromatic moieties. In the case of paclitaxel, having the lowest relative content of aromatic moieties, the drug loading decreases with increasing relative aromatic amount in the polymer, whereas the drug loading of curcumin, having a much higher relative aromatic content, is increased. Interestingly, the loading using schizandrin A, a dibenzo[*a,c*]cyclooctadiene lignan with intermediate relative aromatic content is not influenced significantly by the aromatic content of the polymers employed. The very high drug loading, long-term stability, ability to form stable highly loaded binary coformulations in different drug combinations, small-sized formulations, and amorphous structures in all cases corroborate earlier reports that poly(2-oxazoline)-based micelles exhibit an extraordinarily high drug loading and are promising candidates for further biomedical applications. The presented results underline that the interaction between the polymers and the incorporated small molecules may be more complex and are significantly influenced by both sides, the used carrier and drug, and must be investigated in each specific case.



INTRODUCTION

For many years, natural products have played an important part in drug discovery. In the late 20th century, a majority of drugs were either natural compounds or their derivatives.¹ At the end of their review concerning the importance of natural products for drug discovery, Newman et al. argued that well-defined drug delivery systems could overcome unfavorable physicochemical properties, like aqueous solubility, in the future.² Likewise, via high-throughput screening, new chemical entities or lead structures are being identified and evaluated every day,³ but only a minute fraction ever ripen into an approved drug. Obviously, a large proportion of drug candidates are poorly water-soluble,^{4,5} which calls for effective formulation strategies. Traditionally used surfactants like Cremophor EL and Tween 80 have drawbacks as they can elicit potentially life-threatening side effects and are limited with respect to their solubilizing ability.^{6,7} Polymeric micelles have been discussed and evaluated

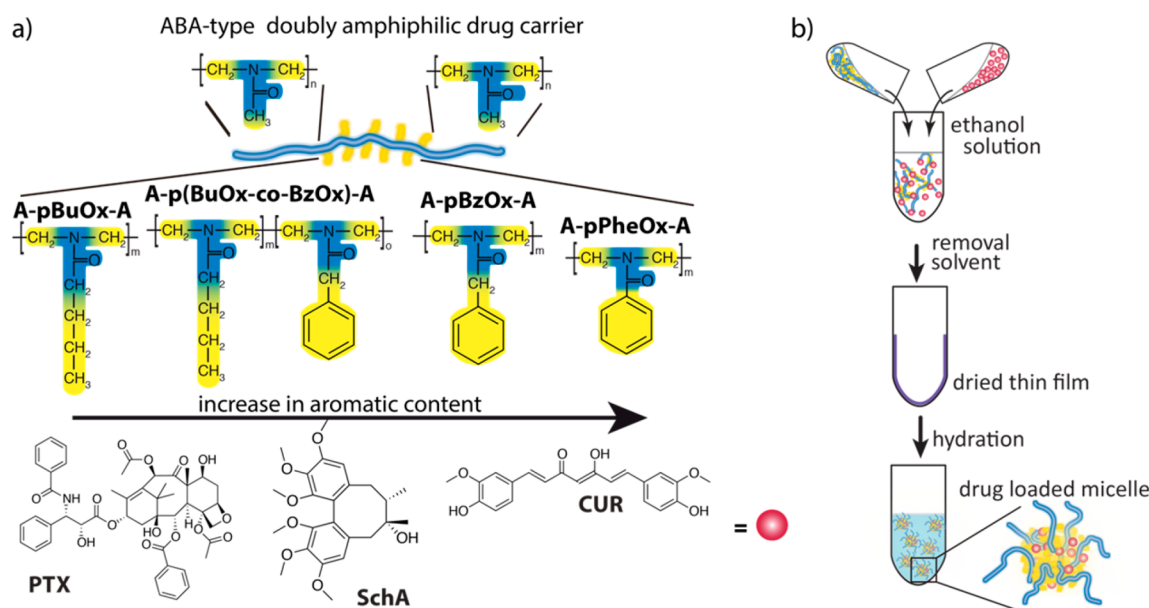
as carriers for hydrophobic molecules for many years, and thousands of papers praising the potential of polymer-based drug delivery systems are published every year.⁸ However, until now, only one micelle-based formulation (Genexol-PM, South Korea) has been used in the clinic with several others being under clinical development.⁹ Zhang et al. argued that the low drug loading capacity and poor in vivo stability typically displayed by polymeric micelles are responsible for this major discrepancy.¹⁰ These major problems concerning nanoformulations, drug delivery, and the advancement of polymeric micelles for clinical cancer therapy were also critically reviewed by other researchers.^{11–13}

Polymer micelles comprising a poly(2-oxazoline) (POx)-based amphiphilic triblock copolymer (poly(2-methyl-2-oxazoline)-

Received: May 2, 2018

Published: May 10, 2018

Scheme 1. Schematic Representation of (a) the Polymers and Insoluble Small Molecules Employed in the Present Study as Well as (b) the Formulation Procedure via the Thin Film Method



line)-*block*-poly(2-butyl-2-oxazoline)-*block*-poly(2-methyl-2-oxazoline) (PMeOx-*b*-PBuOx-*b*-PMeOx = A-**pBuOx-A**)) constitute an unusual exception. Loading capacities (LC) of almost 50 wt % for one of the most commonly used chemotherapeutic agents, paclitaxel (PTX),¹⁴ were reported by Kabanov, Jordan, Luxenhofer, and co-workers.^{15–19} The drug-loaded polymer micelles formed stable and injectable formulations and showed significantly increased therapeutic efficacy in vivo.^{20,21} The combination of high drug loading and stability was specific to block copolymers with poly(2-*n*-butyl-2-oxazoline) as hydrophobic core when a variety of formulations based on amphiphilic ABA POx with structurally different B blocks were investigated.¹⁹ Testing a variety of structurally different taxanes led to similar high drug loadings and stability of the formulations.²² Lübtow et al. investigated a small library of structurally similar ABA-triblock copolymers based on poly(2-oxazoline)s and poly(2-oxazine)s and explored their solubilization capacity for PTX and curcumin (CUR²³), another well-known natural compound featuring extremely low aqueous solubility, bioavailability, and stability.²⁴ The authors observed significant and orthogonal specificities dependent on the positioning of one methylene group in the more hydrophobic repeat unit. This outlines the complexity of drug/carrier interactions.²⁵ More recently, this CUR nanoformulation was characterized in more detail.²⁶

Schisandra chinensis is widely used in traditional Chinese and Japanese herbal medicines for a variety of pharmacological properties.^{27,28} Dibenzo[*a,c*]cyclooctadiene lignan metabolites are thought to be responsible for the majority of these effects.²⁸ Many such lignans have been extracted^{29,30} and chromatographically isolated.^{31–37} Schobert and co-workers established a simplified extraction method followed by one saponification step to obtain the pure dibenzo[*a,c*]cyclooctadiene lignan schisandrol A by column chromatography.³⁸ This was converted to a cinnamate and a titanocene derivative, which both showed promising P-gp inhibition and increased activity against cervix and breast cancer cells.^{38,39} The formation of nanoparticles and nanocrystals to formulate schisantherin A, a related dibenzo[*a,c*]cyclooctadiene lignan, was described by

Cheng et al. The drug/carrier aggregates could pass the hematoencephalic barrier and showed effects potentially useful for the treatment of Parkinson's disease.^{40,41} A recent review on the neuroprotective and cognitive enhancement properties of dibenzo[*a,c*]cyclooctadiene lignans from *Schisandra chinensis* concludes that, before such lignans can enter clinical settings to treat diseases, more studies are needed to improve their bioavailability.⁴²

Several strategies for the development of drug-specific drug delivery platforms have been followed recently. In particular, Luo, Nangia, and co-workers backed the synthetic work with extensive modeling and achieved very high drug loadings paired with excellent therapeutic efficacy.^{43–45} The driving forces considered relevant for drug incorporation are hydrophobic and electrostatic interactions, hydrogen bonding, π - π stacking, and van der Waals forces. The relevance of these interactions for drug formulations is widely discussed.⁴⁶ To stabilize polymeric micelles and thus increase their loading capacity for PTX (28 wt %) and docetaxel (34 wt %), Shi et al. synthesized amphiphilic block copolymers comprising the aromatic monomer *N*-2-benzoyloxypropyl methacrylamide (HPMAm-Bz) as a hydrophobic building block. The π - π interaction significantly increased the stability, loading capacity, and therapeutic index of drug-loaded polymeric micelles.^{47,48} Previously, amphiphilic diblock copolymers containing poly(2-phenyl-2-oxazolin) (PPheOx) and PMeOx were tested on their self-assembly in aqueous milieu, and the hydrophobic indomethacin could be successfully formulated, but potential effects of aromatic moieties on drug loading in POx based micelles have not been investigated in any considerable detail.⁴⁹

Here, we present a small library of POx-based amphiphiles in which the aromatic character was increased systematically and the solubilization capacity for drugs with different aromatic content was investigated (Scheme 1).

■ MATERIALS AND METHODS

All substances and reagents for the polymerizations were obtained from Sigma-Aldrich (Steinheim, Germany) or Acros (Geel, Belgium) and were used as received unless otherwise stated. Curcumin powder

from *Curcuma longa* (Turmeric) was obtained from Sigma-Aldrich (curcumin = 79%; demethoxycurcumin = 17%, bisdemethoxycurcumin = 4%; determined by HPLC analysis). Paclitaxel was purchased from LC Laboratories (Woburn, MA, USA). Deuterated solvents for NMR analysis were obtained from Deutero GmbH (Kastellaun, Germany). All substances used for polymerization, specifically methyl trifluoromethylsulfonate (MeOTf), MeOx, BuOx, PheOx, and BzOx, were refluxed over CaH₂ and distilled and stored under argon. Benzonitrile (PhCN) was dried over phosphorus pentoxide. The monomers 2-*n*-butyl-2-oxazoline (BuOx) and 2-benzyl-2-oxazoline (BzOx) were synthesized following the procedure by Seeliger et al.⁵⁰ The Pt-NHC-complex (Pt-NHC)⁵¹ and the fluorinated curcuminoid derivative (CUR-F₆)⁵² were synthesized according to the literature (Figure S7). Fruits of *Schisandra chinensis* were obtained from Naturwaren-Blum (Revensdorf, Germany) and were dried and powdered prior to the extraction procedure. Schizandrin (SchA) was obtained from powdered *Schisandra chinensis* using the simplified extraction procedure reported by Schobert et al.³⁸ Thin layer chromatography (TLC), NMR-, IR-, UV-vis spectroscopy and electrospray ionization mass spectrometry (ESI-MS) were used for analytical issues. TLC was performed on Sigma-Aldrich TLC Plates containing silica gel matrix (stationary phase) using *n*-hexane/ethylacetate (1:1) as mobile phase. For NMR measurements, a small fraction of the purified compound SchA was dissolved in deuterated dichloromethane and ¹H, ¹³C, correlation spectroscopy (COSY), heteronuclear single quantum coherence (HSQC), and heteronuclear multiple bond correlation (HMBC) experiments were performed. ATR-IR spectroscopic analysis was performed on an FT-IR spectrometer 4100 from 500 to 4000 cm⁻¹ from Jasco (Gross-Umstadt, Germany). For the UV-vis measurement, a 1 g/L ethanolic solution of SchA was filtered through 0.2 μm PTFE filters (Rotilabo, Karlsruhe) and recorded at 25 °C from 700 to 180 nm.

The purity of SchA was determined to be 97.9% by analytical high-pressure liquid chromatography (HPLC). The polymers A-pBuOx-A, A-p(BuOx-co-BzOx)-A, A-pBzOx-A and A-pPheOx-A were synthesized by living cationic ring opening polymerization (LCROP) as described previously.¹⁵ The reactions were controlled by ¹H NMR spectroscopy. The lyophilized polymers were characterized by ¹H NMR and gel permeation chromatography (GPC). The critical micellar concentrations (CMC) of the ABA-triblock copolymers were determined by pyrene fluorescence measurements.^{53,54} The I₁/I₃ ratio in dependence of varying polymer concentrations and the total redshift of I₁ in dependence of varying polymer concentrations were detected and used for the determination of the CMC values. Drug-loaded polymeric micelles were prepared by thin film method (Scheme 1). The loading capacities (LC) and efficiencies (LE) were determined by HPLC measurements according to eqs 1 and 2.

$$LC = \frac{m_{\text{drug}}}{m_{\text{drug}} + m_{\text{excipient}}} \times 100\% \quad (1)$$

$$LE = \frac{m_{\text{drug}}}{m_{\text{drug, added}}} \times 100\% \quad (2)$$

where m_{drug} and $m_{\text{excipient}}$ are the weight amounts of the solubilized drug and polymer excipient in solution and $m_{\text{drug, added}}$ is the weight amount of the drug initially added. It was assumed that no loss of polymer occurred during micelle preparation. The aggregation behavior of the polymers (10 g/L in PBS) and polymer/drug solutions (1:0.5 g/L in PBS) were investigated by dynamic light scattering (DLS) measurements at 27 different angles (temperature was fixed at 25 °C) as outlined in the supporting information in more detail. The glass transition temperatures (T_g) and melting points (mp) were determined by differential scanning calorimetry (DSC) measurements (see Supporting Information).

Primary human dermal fibroblasts (HDF) were cultured in DMEM, GlutaMAX (Gibco, Darmstadt, Germany) culture medium supplemented with 10% fetal calf serum (FCS), and 1% sodium pyruvate. For cell cytotoxicity studies, cells were seeded in a white 96-well plate with a transparent bottom in triplicate per condition (3×10^5 cells/

cm²) and cultured for 24 h at 37 °C and 5% CO₂. Subsequently, medium was removed, and polymer stock solutions in cell specific culture medium ($\rho = 100$ g/L) were diluted with cell-specific culture medium to desired concentrations and applied for 24 h. After the treatment, CellTiter-Glo Luminescent Cell Viability Assay (Promega, Mannheim, Germany) was performed according to the manufacturer's instructions. Briefly, medium was removed, and cells were washed 3× with PBS(+). Equal amounts of cell culture medium and CellTiter-Glo reagent were added to the wells. After shaking for 2 min and resting for 10 min to achieve cell lysis, luminescence was measured with an Infinite 200 (Tecan, Männedorf, Switzerland) at $\lambda_{\text{em}} = 590$ nm ($\lambda_{\text{ex}} = 560$ nm).

Cell viability was determined by eq 3

$$\text{cell viability} = \frac{F_{\text{treated}} - F_{\text{medium}}}{F_{\text{untreated}} - F_{\text{medium}}} \times 100\% \quad (3)$$

where F_{treated} and $F_{\text{untreated}}$ are the luminescence of treated and untreated cells, respectively, and F_{medium} is the luminescence of the culture medium. As negative control, cells were lysed with 10% sodium dodecyl sulfate (SDS). Cell viability experiments were performed with three individual 96-well plates containing each sample concentration in triplicate (considered as one experiment), and results are presented as means \pm SD. Cells were obtained by three individual isolations. All methods are described in more detail in the Supporting Information.

RESULTS AND DISCUSSION

Inspired by reports on benefits for drug delivery via π - π stacking between drug carrier and loaded API,⁵⁵ we wanted to investigate this issue in poly(2-oxazoline)-based polymer amphiphiles to gain more insights into the structure-property relationship. In particular, the Hansen solubility parameters calculated by Dargaville and co-workers suggested a benefit regarding drug loading using polymer amphiphiles comprising a hydrophobic poly(2-phenyl-2-oxazoline) block.⁵⁶ In the case of paclitaxel and docetaxel, Hennink and co-workers reported that incorporation of aromatic side chains into thermosensitive block copolymers of modified hydroxypropyl methacrylamides improves drug loading.⁴⁷ However, it is important to note that, in this study, PTX precipitation rather than release was quantified.^{47,48} The authors argue that this was done as it is difficult to upload proper sink conditions for the extremely poorly soluble PTX. In contrast, in a preliminary study, we did not observe any benefit with respect to PTX formulation when we included aromatic moieties into the hydrophobic block.¹⁹ The inclusion of an aromatic moiety (A-p(BuOx-co-BzOx)-A; LC_{PTX}: 36 wt %) led to significant loss of loading capacity in comparison to A-pBuOx-A (LC_{PTX}: 49 wt %). Therefore, the present study investigates the influence of different proportions of aromatic moieties within poly(2-oxazoline)-based ABA triblock copolymers on the formulation of different hydrophobic drugs with varying aromatic content in more detail. To this end, we used a small library of four different polymers. As in previous work, the hydrophilic block A was poly(2-methyl-2-oxazoline) (pMeOx).²⁵ The hydrophobic blocks were in order of increasing aromatic content poly(2-butyl-2-oxazoline) (A-pBuOx-A), poly(2-butyl-2-oxazoline-co-2-benzyl-2-oxazoline) (A-p(BuOx-co-BzOx)-A), poly(2-benzyl-2-oxazoline) (A-pBzOx-A), and poly(2-phenyl-2-oxazoline) A-pPheOx-A, respectively. The polymers were prepared by living cationic ring opening polymerization (LCROP) and characterized by ¹H NMR and GPC (Table 1 and Supporting Information).

All polymers exhibited CMC values in the low μM range (determined by pyrene fluorescence, Figure S4) often deemed favorable for intravenous administration (Figure S4, Table S1). Interestingly, in the present library, it appears that the

Table 1. Number Average Molar Mass, Dispersity \mathcal{D} , and Yield of the Synthesized Triblock Copolymers

polymer	M_n^a [kg/mol]	M_n^b [kg/mol]	M_n^c [kg/mol]	\mathcal{D}^d	yield [%]
A-pBuOx-A	8.6	8.7	5.6	1.10	88
A-p(BuOx-co-BzOx)-A	9.0	7.8	5.9	1.12	91
A-pBzOx-A	8.7	10.3	5.2	1.25	77
A-pPheOx-A	8.5	8.5	5.3	1.10	92

^aTheoretical value obtained by $[M]_0/[I]_0$. ^bCalculated from ^1H NMR end-group and side chain analysis. ^cObtained from GPC ($T = 40^\circ\text{C}$, flow rate was set to 0.7 mL/min (HFIP) and calibrated using poly(ethylene glycol) standards). ^dObtained from GPC (M_w/M_n).

introduction of aromatic side chains has no marked influence on the CMC values. For polymeric micelles to be used as drug delivery vehicles, the synthesized carriers should exhibit no significant cytotoxicity against human cells. Luxenhofer et al. studied the cytotoxicity of different POx-based homo and block copolymers including A-pBuOx-A in different cell lines.⁵⁷ In this study, even at relatively high carrier concentrations (20 g/L), no significant cytotoxicity could be observed. However, to the best of our knowledge, amphiphilic POx-bearing aromatic moieties have not been investigated regarding their cytotoxicity. Therefore, we evaluated these polymers using primary human dermal fibroblasts (Figure 1).

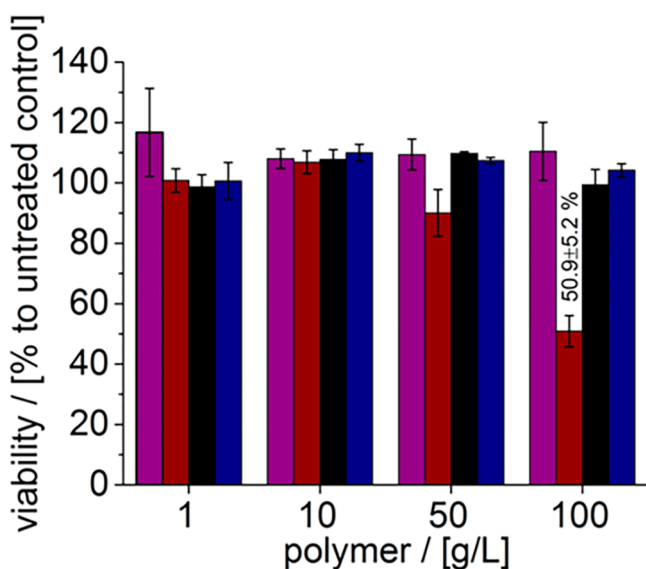


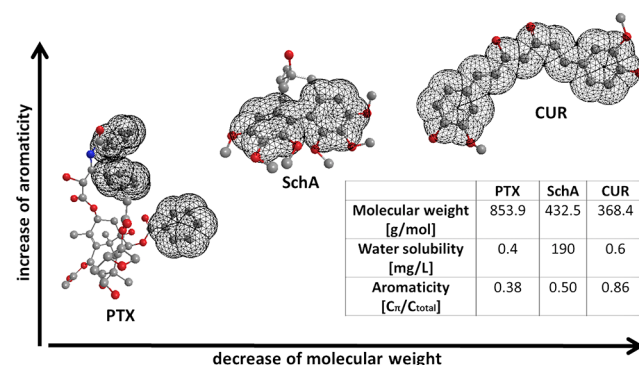
Figure 1. Cell viability of primary human dermal fibroblasts treated with increasing polymer concentrations (1–100 g/L). A-pBuOx-A (purple), A-p(BuOx-co-BzOx)-A (dark red), A-pBzOx-A (black), and A-pPheOx-A (dark blue). Cell viability was assessed using CellTiter-Glo after a 24 h incubation. Data are given as means \pm SD ($n = 3$).

The polymers A-pBzOx-A and A-pPheOx-A, which are comprised solely of aromatic moieties as the building blocks for the hydrophobic core, exhibited no cytotoxicity even at very high polymer concentration of 100 g/L. Interestingly, during the treatment of fibroblasts using the polymer A-p(BuOx-co-BzOx)-A, the viability decreased to $50.9 \pm 5.2\%$ at a polymer concentration of 100 g/L. Only a minor but noticeable reduction of the cell viability was observed at 50 g/L. This is interesting, as neither A-pBuOx-A nor A-pBzOx-A exhibit any cytotoxicity against human fibroblasts. The polymers used in

this study exhibit low dispersities and CMC values in μM range and show a favorable cytotoxicity profile; therefore, they are promising candidates for the solubilization of hydrophobic drugs.

For formulation, we focused on three natural compounds. On one hand, we employed the well-known and extremely water-insoluble compounds paclitaxel (PTX, 0.4 mg/L)⁵⁸ and turmeric curcumin (CUR, 0.6 mg/L).²⁴ On the other hand, we tested the poorly soluble dibenzo[*a,c*]cyclooctadiene lignan schizandrin (SchA, solubility: 0.19 g/L determined via HPLC). These three natural compounds differ in their relative aromatic contents. Whereas PTX contains three phenyl rings at a molar mass of 854 g/mol, SchA contains two rings at 432 g/mol, and CUR also contains two phenyl rings, however, connected with a bridging π -system at a molar mass of 368 g/mol. The ratio of C_{arom} , the carbon atoms, which are included in the conjugated/aromatic system, and C_{total} , the total number of carbon atoms in the hydrophobic compound, represents the aromaticity of the three different cargos (Scheme 2).

Scheme 2. Comparison of the Hydrophobic Drugs PTX, SchA, and CUR with Regard to Aromaticity, Solubility, and Molecular Weight



Additionally, the insoluble compounds Pt-NHC and CUR-F₆ (for structures, please see Figure S7) were investigated, the latter of which can be viewed as derivative of natural compound CUR.

All four polymers were tested for the solubilization of PTX, CUR, and SchA. As previously reported, A-pBuOx-A is an excellent solubilizer for PTX but much less so for CUR²⁵ (Figure 2). Interestingly, SchA, having an intermediate relative aromatic content, was solubilized very well but less than PTX. As previously reported¹⁹ and independently reproduced here using a newly synthesized polymer, the introduction of benzylic moieties (A-p(BuOx-co-BzOx)-A) does not help in the formulation of PTX but rather reduces the maximum drug loading. Interestingly, whereas in the case of SchA the maximum drug loading increased slightly, the LC_{CUR} that could be achieved increased significantly (Figure 2). In the case of A-pBzOx-A, the LC_{PTX} decreased further (35.6 ± 2.1 wt %), whereas LC_{SchA} (44.0 ± 0.3 wt %) and in particular LC_{CUR} (41.0 ± 2.1 wt %) increased further compared to A-pBuOx-A-based formulations. Interestingly, within this small library, A-pBzOx-A is the least selective of the tested polymers. Previously, comparable but somewhat higher loading capacities for PTX and CUR could be achieved (LC_{PTX} : 40.1 ± 1.5 wt %, LC_{CUR} : 48.5 ± 1.7 wt %) using A-p(2-*n*-butyl-2-oxazine)-A.²⁵ Thus, with increasing aromatic character of the polymeric solubilizer, more CUR ($LC_{\text{A-pBuOx-A}}$: 24.4 ± 1.1 wt %, 25

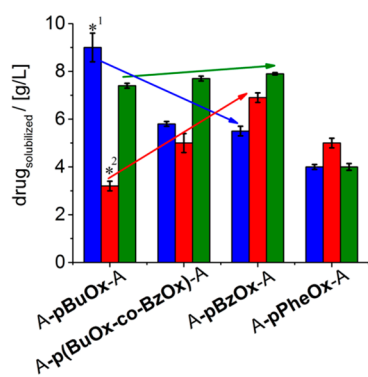


Figure 2. Maximum solubilized aqueous drug concentrations in formulation with the drug carriers (A-pBuOx-A, A-p(BuOx-co-BzOx)-A, A-pBzOx-A, A-pPheOx-A). Maximum solubilization (LE_{minimum} 79%) of the drugs PTX (blue), CUR (red), and SchA (green) using the four polymers. ^{*1} were taken from ref 18; ^{*2} were taken from ref 25. In all cases, the polymer concentration was fixed at 10 g/L. Data are given as means \pm SD ($n = 3$).

$LC_{A-p(\text{BuOx-co-BzOx})-A}$: 33.2 ± 3.7 wt %, $LC_{A-p\text{BzOx}-A}$: 41.0 ± 2.1 wt %) and less PTX ($LC_{A-p\text{BuOx}-A}$: 47.5 ± 0.1 wt %, ²⁵ $LC_{A-p(\text{BuOx-co-BzOx})-A}$: 36.8 ± 1.0 wt %, $LC_{A-p\text{BzOx}-A}$: 35.6 ± 2.1 wt %) could be solubilized, whereas little if any influence was found for SchA. Interestingly, A-pPheOx-A did show a markedly different performance as solubilizer. Although the LC_{PTX} did decrease further (28.6 ± 0.6 wt %), the solubilizations of CUR (LC_{CUR} : 33.4 ± 2.3 wt %) and SchA (LC_{SchA} : 28.6 ± 1.4 wt %) were also less efficient compared to A-pBzOx-A. We hypothesize that the reduced molecular flexibility of pPheOx and the close proximity of the phenyl ring to the polymer backbone may be one contributing factor (as shown, e.g., by a higher T_g , vide infra). It may be noted that this comparably low loading of PTX using A-pPheOx-A was still higher, albeit only slightly, than the highest PTX loading reported by Hennink et al.⁴⁷ In this report, the authors found an increased PTX loading with increasing content of aromatic comonomer, which was attributed to π - π stacking between polymer and drug molecules. Although apparently valid in some cases, it appears that this rationale is not generally helpful to increase drug loading in polymer micelles.

It should be noted that we also attempted formulation of CUR- F_6 , but no stable formulation could be obtained by film hydration method with either polymer. The NHC-Pt complex was solubilized with A-pPheOx-A by film hydration method using dichloromethane. However, it appears the complex does not exhibit sufficient stability as HPLC analysis revealed multiple signals after formulation, whereas the compound was pure initially. Therefore, quantification was not possible.

The drug content was quantified immediately after preparation. To gain a basic understanding of the stability of the drug formulations, we stored the formulation under ambient conditions containing the initial precipitate and took samples after 10 and 30 days. The formulations were centrifuged prior to each measurement. By using this method, it is possible that first precipitated drug could be dissolved over time.⁵⁹ For A-pBuOx-A, we have previously observed excellent stability of the PTX formulation without any precipitation after several months.^{15,17,18} In general, all presently tested formulations of PTX, CUR, and SchA showed very good stability over 30 days (Figure 3). No significant loss of SchA and very little variability of the drug concentration was

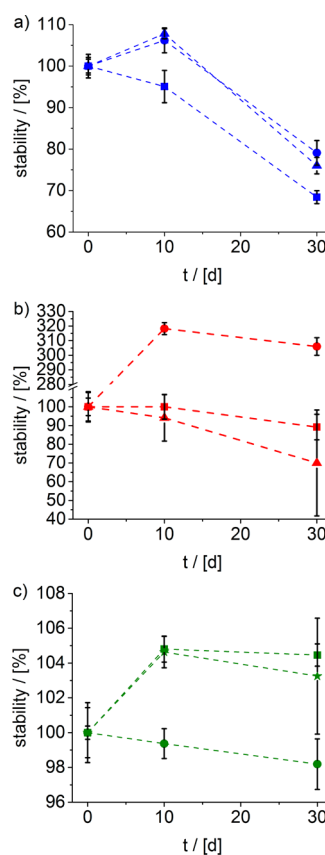


Figure 3. Long-term stability of drug/polymer formulations of PTX (a), CUR (b), and SchA (c). For this study, the maximum loaded formulations were used. The d0 values were set to 100%. In all cases, the polymer concentration was fixed at 10 g/L (squares: A-p(BuOx-co-BzOx)-A, circles: A-pBzOx-A, triangles: A-pPheOx-A, and stars: A-pBuOx-A). Data are given as means \pm SD ($n = 3$).

observed. In the case of PTX, the variability was somewhat higher; nevertheless, overall formulation stability was excellent. The stability compares favorably with π - π interaction stabilized PTX formulations reported by Hennink et al. In that report, 50–100% of the solubilized PTX precipitated within 10 days depending on the aromatic content of the micelles.⁴⁷ In the case of CUR, we made unexpected observations. First of all, the stability of CUR formulated in the POx-based micelles was remarkably high, especially considering the well-established low chemical stability of CUR in aqueous media.²⁴ In the case of A-p(BuOx-co-BzOx)-A and A-pPheOx-A, we did observe some loss of CUR concentration and increased variability after 30 days, but the average drug loading remained high. Notably, according to HPLC analysis, CUR did not show any signs of degradation even though it is often reported that CUR is not stable in an aqueous environment. Interestingly, in the case of A-pBzOx-A, the CUR concentration in solution (after centrifugation and filtration) was much higher on day 10 (LC_{CUR} : 45.6 ± 3.3 wt %) and day 30 (LC_{CUR} : 44.6 ± 4.6 wt %) than on day 0 (LC_{CUR} : 20.8 ± 2.1 wt %). It should be noted, for our stability studies, that the drug formulations were stored under ambient conditions over the pellet of unformulated drug (if any). Thus, it appears that CUR that initially precipitated/coacervated during thin film hydration became incorporated over time into the micelles. We observed a similar phenomenon with POx-based amphiphiles with long aliphatic side chains. Analysis of the precipitate/coacervate revealed that

both drug and polymer are present.⁵⁹ We cannot explain this observation at this point, but more detailed studies are certainly warranted.

In addition to the described single-drug formulations, we also investigated binary coformulations. Previously, several POx-based binary and ternary drug formulations with very high loading of ≥ 58 wt % were reported.^{17,25} Here, we investigated A-pBzOx-A for coformulation of PTX with SchA and CUR, respectively. Both combinations could show interesting pharmaceutical synergies.^{60,61} For these preliminary studies, we fixed the relative drug weight ratio at 1/1 for both combinations (10 g/L A-pBzOx-A and 6 g/L in the case of PTX/SchA and 8 g/L in the case of PTX/CUR). In both combinations, the loading efficiency was excellent, and total LC exceeded 50 wt %. The individual LC for PTX (40.8 wt %) and CUR (40.1 wt %) yielded an overall LC of 58.8 wt %, whereas with the combination of PTX (35.6 wt %) and SchA (36.9 wt %), an overall LC of 53.2 wt % was obtained (Figure 4).

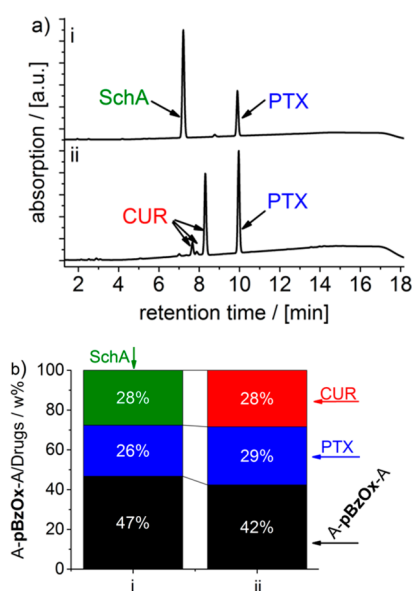


Figure 4. (a) HPLC elugrams ($\lambda = 220$ nm) of coformulations ((i) A-pBzOx-A/PTX/SchA = 10:6:6 w/w/w, (ii) A-pBzOx-A/PTX/CUR = 10:8:8 w/w/w). (b) Overall LCs of coformulations (i) and (ii).

Previously, we have investigated the PTX formulation with A-pBuOx-A in great detail using electron microscopy, dynamic light scattering (DLS), and small-angle neutron scattering.^{16,18} For preliminary elucidation of the aggregation behavior, we investigated aqueous polymer solutions and formulations by DLS (Figure 5). All polymers form aggregates in the size range expected for polymer micelles. The polymers containing aromatic moieties form very small and rather defined polymer micelles. At 10 g/L in PBS, hydrodynamic radii between 10 and 20 nm were found (Figure 5a, Figure S6c). In the case of A-pBuOx-A, we found a rather broad distribution centered around a hydrodynamic radius of $R_h = 25$ nm. Previously, using a different batch of the same polymer, we observed a bimodal size distribution originating from spherical and wormlike micelles.¹⁸ The broad distribution observed in the present case could likely be caused by an unresolved bimodal distribution.

Moreover, we investigated drug formulations of A-pBzOx-A by DLS at a polymer/drug-ratio of 10:5 in PBS. The

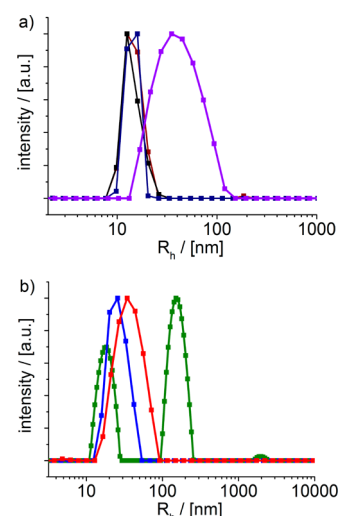


Figure 5. (a) Relative intensity dependent on the unweighted hydrodynamic radius R_h [nm] of the polymers (A-pPheOx-A = dark blue bars, A-p(BuOx-co-BzOx)-A = dark red bars, A-pBzOx-A = black bars, A-pBuOx-A = purple bars) of 10 g/L in PBS solution (scattering angle = 90° , $T = 25^\circ\text{C}$). (b) Relative intensity dependent on the unweighted hydrodynamic radius R_h [nm] of the formulation of the drugs PTX (blue), CUR (red), and SchA (green) with the drug carrier A-pBzOx-A with a polymer/drug-ratio of 10:5 (w/w) in 1 g/L of PBS solution (scattering angle = 90° , $T = 25^\circ\text{C}$).

formulation with SchA exhibited three species with weighted average mean of 23 nm (Figure 5b, Figure S6d). A large species at 2000 nm had a very low intensity and may be attributed to an artifact. In addition, two major distributions at approximately 20 and 150 nm were observed. In contrast, for PTX and CUR nanoformulations, only single and rather narrow distributions were observed with hydrodynamic radii of 21 nm (PTX) and 27 nm (CUR) (Figure 5b, Figure S6e). Obviously, such small sizes are typically considered favorable for parental administration, in particular for cancer chemotherapy.⁶²

The drug formulations studied here are not only potentially interesting as drug-loaded micelles but also in the form of solid dispersions. In this context, it is particularly interesting whether the drug is present in amorphous or crystalline form. Neither polymer exhibited a melting point, therefore being fully amorphous structures with glass transitions temperatures predictable by the Fox equation⁶³ using the T_g values of the homopolymers^{64–66} (Figure 6a, Table S9, eq 6, Table S10). SchA did not undergo thermal degradation at temperatures up to 200°C but exhibited a melting point of 129°C (Figure 6b), which corroborates values found in the literature.⁶⁷ Upon cooling, we did not observe recrystallization at the chosen experimental parameters, but a T_g value was detectable. The second heating cycle revealed a T_g of 30.7°C for SchA. For comparison, we also analyzed a simple physical mixture of SchA and A-pBzOx-A with the nanoformulation (both 1:2, w/w) obtained via thin film hydration and subsequent lyophilization. For the nanoformulation of A-pBzOx-A and SchA, no melting point could be detected in the first heating cycle (Figure 6c). Only a T_g of 67.5°C could be discerned, showing that the nanoformulation with an LC of $\sim 30\%$ was fully amorphous. The fact that only one T_g is observed demonstrates that no independent domains of amorphous drug and amorphous polymer are present but rather that the two entities are

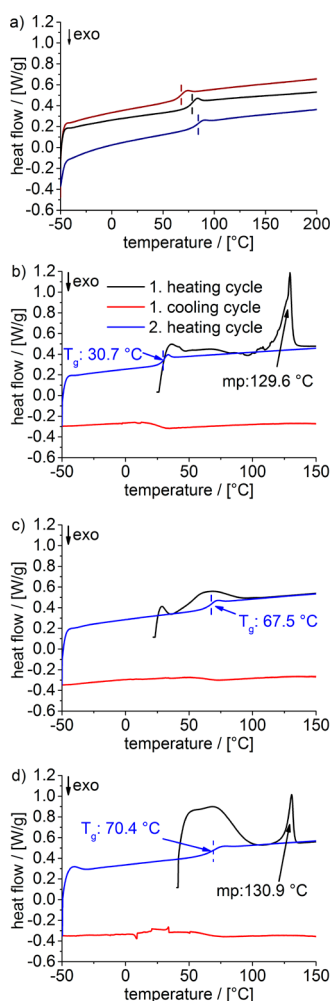


Figure 6. (a) DSC analysis of the triblock copolymers (A-pPheOx-A = dark blue line, $T_g = 81.3$ °C; A-p(BuOx-co-BzOx)-A = dark red line, $T_g = 67.5$ °C; A-pBzOx-A = black line, $T_g = 76.7$ °C). The heat flow [W/g] dependence on the temperature [°C] is shown with the particular glass transition T_g of each polymer marked with vertical lines. DSC analysis of SchA (b), nanoformulation with the polymer A-p(BuOx-co-BzOx)-A (c), and physical mixture of SchA/A-p(BuOx-co-BzOx)-A (d). The heat flow [W/g] dependence on the temperature [°C] is shown for the first heating cycle (black), first cooling cycle (red), and second heating cycle (blue). Melting points (endothermal maximum) were determined in the first heating cycle. The particular T_g values were determined in the second heating cycle. The scans were performed under a N_2 atmosphere using constant cooling and a heating rate of 10 K/min.

intimately and molecularly intertwined.⁶⁸ In the case of the physical mixture, we could clearly observe the melting point of SchA in the first heating cycle (Figure 6d). Also in this case, no recrystallization of SchA was observed upon cooling. The second heating cycle only revealed a T_g at 70.4 °C. Interestingly, the Fox equation predicts a much lower T_g for a mixture of 33 wt % SchA and 66 wt % A-pBzOx-A. Using the experimentally determined T_g values of both components, the Fox equation yields an expected T_g of only 52 °C. The origin of this discrepancy is unclear at this point.

CONCLUSIONS

We investigated the influence of incorporation of aromatic moieties into poly(2-oxazoline)-based ABA triblock copoly-

mers. In addition to the varying degree of aromaticity within the polymers, three cargo compounds with different relative aromatic contents were tested. In contrast to previous reports on a different polymeric system, incorporation of 2-benzyl-2-oxazoline or 2-phenyl-2-oxazoline did not increase drug loading or formulation stability in the case of paclitaxel. The first high capacity and stable formulations of the dibenzo[*a,c*]-cyclooctadiene lignan schizandrin A were realized. Interestingly, the formulation of the natural compound schizandrin A was barely affected by the different polymer structures, whereas the loading with curcumin benefitted significantly from incorporation of 2-benzyl-2-oxazoline but less so for 2-phenyl-2-oxazoline. Therefore, it appears that π - π interactions may be beneficial for drug loading and formulation stability in some cases, but it may not be considered a general phenomenon and must be assessed on a case-by-case basis. Not only are the nature of the drug and the amount of the aromatic moieties in the polymer important, but the nature of the aromatic moieties is also relevant as shown by the different behaviors of benzyl- and phenyl-containing triblock copolymers. Cell viability studies revealed that all studied polymers were highly cytocompatible with negligible effect on the cell viability at 50 g/L or less. Moreover, the first combination formulation could be realized, and the amorphous character of solid dispersions was confirmed by DSC.

ASSOCIATED CONTENT

Supporting Information

The Supporting Information is available free of charge on the ACS Publications website at DOI: 10.1021/acs.biomac.8b00708.

Detailed experimental procedures, monomer and polymer characterization data, extraction procedure, detailed methods description, results of the pyrene fluorescence assay (CMC values), formulation data, dynamic light scattering data, differential scanning calorimetry data, and chemical structures of Pt-NHC and CUR-F₆ (PDF)

AUTHOR INFORMATION

Corresponding Author

*E-mail: robert.luxenhofer@uni-wuerzburg.de.

ORCID

Rainer Schobert: 0000-0002-8413-4342

Robert Luxenhofer: 0000-0001-5567-7404

Notes

The authors declare the following competing financial interest(s): RL is listed as inventor on patents pertinent to the subject matter of the present contribution and co-founder of DelAqua Pharmaceuticals Inc. intent on commercial development of POx-based drug formulations.

ACKNOWLEDGMENTS

We thank Christian May for technical support. We are very grateful for the HDRC-Software version 6.3.1 provided by O. Nirschl and K. Fischer, Physical Chemistry of Polymers at the Johannes Gutenberg University Mainz led by Prof. Dr. Sebastian Seiffert (formerly Prof. Dr. Manfred Schmidt). This work was supported by the Free State of Bavaria and the Deutsche Forschungsgemeinschaft (project #398461692). Start-up funding for R.L. by the University Würzburg and SKZ Das Kunststoff-Zentrum is gratefully acknowledged.

M.M.L. thanks the Evonik Foundation for providing a doctoral fellowship. Light scattering experiments were possible through support of the Deutsche Forschungsgemeinschaft (INST 93/774-1 FUGG).

■ ABBREVIATIONS

API, active pharmaceutical ingredient; DMEM, Dulbecco's modified Eagle medium; Exo, exothermal; FT-IR, Fourier-transform infrared spectroscopy; HFIP, hexafluoroisopropanol; HPLC, high-pressure liquid chromatography; NMR, nuclear magnetic resonance; PBS, phosphate-buffered saline; P-gp, permeability glycoprotein; PTFE, polytetrafluoroethylene; SD, standard deviation; UV–vis, ultraviolet–visible

■ REFERENCES

- (1) Li, J. W.; Vederas, J. C. Drug discovery and natural products: end of an era or an endless frontier? *Science* **2009**, *325* (5937), 161–165.
- (2) Newman, D. J.; Cragg, G. M.; Snader, K. M. The influence of natural products upon drug discovery. *Nat. Prod. Rep.* **2000**, *17* (3), 215–234.
- (3) Lombardino, J. G.; Lowe, J. A. The role of the medicinal chemist in drug discovery—then and now. *Nat. Rev. Drug Discovery* **2004**, *3* (10), 853–862.
- (4) Yang, M.; Gong, W.; Wang, Y.; Shan, L.; Li, Y.; Gao, C. Bioavailability improvement strategies for poorly water-soluble drugs based on the supersaturation mechanism: an update. *J. Pharm. Pharm. Sci.* **2016**, *19* (2), 208–225.
- (5) Lipinski, C. A. Drug-like properties and the causes of poor solubility and poor permeability. *J. Pharmacol. Toxicol. Methods* **2000**, *44* (1), 235–249.
- (6) Gelderblom, H.; Verweij, J.; Nooter, K.; Sparreboom, A. Cremophor EL: the drawbacks and advantages of vehicle selection for drug formulation. *Eur. J. Cancer* **2001**, *37* (13), 1590–1598.
- (7) Bromberg, L. Polymeric micelles in oral chemotherapy. *J. Controlled Release* **2008**, *128* (2), 99–112.
- (8) Duncan, R.; Vicent, M. J. Polymer therapeutics—prospects for 21st century: the end of the beginning. *Adv. Drug Delivery Rev.* **2013**, *65* (1), 60–70.
- (9) Werner, M. E.; Cummings, N. D.; Sethi, M.; Wang, E. C.; Sukumar, R.; Moore, D. T.; Wang, A. Z. Preclinical evaluation of Genexol-PM, a nanoparticle formulation of paclitaxel, as a novel radiosensitizer for the treatment of non-small cell lung cancer. *Int. J. Radiat. Oncol., Biol., Phys.* **2013**, *86* (3), 463–468.
- (10) Zhang, Y.; Ren, T.; Gou, J.; Zhang, L.; Tao, X.; Tian, B.; Tian, P.; Yu, D.; Song, J.; Liu, X.; Chao, Y.; Xiao, W.; Tang, X. Strategies for improving the payload of small molecular drugs in polymeric micelles. *J. Controlled Release* **2017**, *261*, 352–366.
- (11) Houdaihed, L.; Evans, J. C.; Allen, C. Overcoming the road blocks: Advancement of block copolymer micelles for cancer therapy in the clinic. *Mol. Pharmaceutics* **2017**, *14* (8), 2503–2517.
- (12) Sofias, A. M.; Dunne, M.; Storm, G.; Allen, C. The battle of “nano” paclitaxel. *Adv. Drug Delivery Rev.* **2017**, *122*, 20–30.
- (13) Leroux, J. C. Drug delivery: Too much complexity, not enough reproducibility? *Angew. Chem., Int. Ed.* **2017**, *56* (48), 15170–15171.
- (14) Johnson, D. H.; Fehrenbacher, L.; Novotny, W. F.; Herbst, R. S.; Nemunaitis, J. J.; Jablons, D. M.; Langer, C. J.; DeVore, R. F., 3rd; Gaudreault, J.; Damico, L. A.; Holmgren, E.; Kabbinnavar, F. Randomized phase II trial comparing bevacizumab plus carboplatin and paclitaxel with carboplatin and paclitaxel alone in previously untreated locally advanced or metastatic non-small-cell lung cancer. *J. Clin. Oncol.* **2004**, *22* (11), 2184–2191.
- (15) Luxenhofer, R.; Schulz, A.; Roques, C.; Li, S.; Bronich, T. K.; Batrakova, E. V.; Jordan, R.; Kabanov, A. V. Doubly amphiphilic poly(2-oxazoline)s as high-capacity delivery systems for hydrophobic drugs. *Biomaterials* **2010**, *31* (18), 4972–4979.
- (16) Luxenhofer, R.; Han, Y.; Schulz, A.; Tong, J.; He, Z.; Kabanov, A. V.; Jordan, R. Poly(2-oxazoline)s as polymer therapeutics. *Macromol. Rapid Commun.* **2012**, *33* (19), 1613–1631.
- (17) Han, Y.; He, Z.; Schulz, A.; Bronich, T. K.; Jordan, R.; Luxenhofer, R.; Kabanov, A. V. Synergistic combinations of multiple chemotherapeutic agents in high capacity poly(2-oxazoline) micelles. *Mol. Pharmaceutics* **2012**, *9* (8), 2302–2313.
- (18) Schulz, A.; Jaksch, S.; Schubel, R.; Wegener, E.; Di, Z.; Han, Y.; Meister, A.; Kressler, J.; Kabanov, A. V.; Luxenhofer, R.; Papadakis, C. M.; Jordan, R. Drug-induced morphology switch in drug delivery systems based on poly(2-oxazoline)s. *ACS Nano* **2014**, *8* (3), 2686–2696.
- (19) Seo, Y.; Schulz, A.; Han, Y.; He, Z.; Bludau, H.; Wan, X.; Tong, J.; Bronich, T. K.; Sokolsky, M.; Luxenhofer, R.; Jordan, R.; Kabanov, A. V. Poly(2-oxazoline) block copolymer based formulations of taxanes: effect of copolymer and drug structure, concentration, and environmental factors. *Polym. Adv. Technol.* **2015**, *26* (7), 837–850.
- (20) He, Z.; Wan, X.; Schulz, A.; Bludau, H.; Dobrovolskaia, M. A.; Stern, S. T.; Montgomery, S. A.; Yuan, H.; Li, Z.; Alakhova, D.; Sokolsky, M.; Darr, D. B.; Perou, C. M.; Jordan, R.; Luxenhofer, R.; Kabanov, A. V. A high capacity polymeric micelle of paclitaxel: Implication of high dose drug therapy to safety and in vivo anti-cancer activity. *Biomaterials* **2016**, *101*, 296–309.
- (21) Wan, X.; Min, Y.; Bludau, H.; Keith, A.; Sheiko, S. S.; Jordan, R.; Wang, A. Z.; Sokolsky-Papkov, M.; Kabanov, A. V. Drug combination synergy in worm-like polymeric micelles improves treatment outcome for small cell and non-small cell lung cancer. *ACS Nano* **2018**, *12* (3), 2426–2439.
- (22) He, Z.; Schulz, A.; Wan, X.; Seitz, J.; Bludau, H.; Alakhova, D. Y.; Darr, D. B.; Perou, C. M.; Jordan, R.; Ojima, I.; Kabanov, A. V.; Luxenhofer, R. Poly(2-oxazoline) based micelles with high capacity for 3rd generation taxoids: preparation, in vitro and in vivo evaluation. *J. Controlled Release* **2015**, *208*, 67–75.
- (23) Perrone, D.; Ardito, F.; Giannatempo, G.; Dioguardi, M.; Troiano, G.; Lo Russo, L.; De Lillo, A.; Laino, L.; Lo Muzio, L. Biological and therapeutic activities, and anticancer properties of curcumin. *Exp. Ther. Med.* **2015**, *10* (5), 1615–1623.
- (24) Anand, P.; Kunnumakkara, A. B.; Newman, R. A.; Aggarwal, B. B. Bioavailability of curcumin: problems and promises. *Mol. Pharmaceutics* **2007**, *4* (6), 807–818.
- (25) Lübtow, M. M.; Hahn, L.; Haider, M. S.; Luxenhofer, R. Drug specificity, synergy and antagonism in ultrahigh capacity poly(2-oxazoline)/poly(2-oxazine) based formulations. *J. Am. Chem. Soc.* **2017**, *139* (32), 10980–10983.
- (26) Lübtow, M. M.; Nelke, L. C.; Brown, A.; Sahay, G.; Dandekar, G.; Luxenhofer, R. Drug induced micellization into ultra-high capacity and stable curcumin nanoformulations. *Comparing in vitro 2D and 3D-tumor model of triple-negative breast cancer* **2017**, DOI: [10.26434/chemrxiv.5661736.v1](https://doi.org/10.26434/chemrxiv.5661736.v1).
- (27) Hancke, J. L.; Burgos, R. A.; Ahumada, F. Schisandra chinensis (Turcz.) Baill. *Fitoterapia* **1999**, *70* (5), 451–471.
- (28) Lu, Y.; Chen, D. F. Analysis of Schisandra chinensis and Schisandra sphenanthera. *J. Chromatogr. A* **2009**, *1216* (11), 1980–1990.
- (29) Ikeya, Y.; Taguchi, H.; Yosioka, I.; Kobayashi, H. The constituents of schizandra chinensis BAILL. I. isolation and structure determination of five new lignans, Gomisin A, B, C, F and G, and the absolute structure of Schizandrin. *Chem. Pharm. Bull.* **1979**, *27* (6), 1383–1394.
- (30) Dean, J. R.; Liu, B. Supercritical fluid extraction of chinese herbal medicines: investigation of extraction kinetics. *Phytochem. Anal.* **2000**, *11* (1), 1–6.
- (31) He, X. G.; Lian, L. Z.; Lin, L. Z. Analysis of lignan constituents from Schisandra chinensis by liquid chromatography-electrospray mass spectrometry. *J. Chromatogr. A* **1997**, *757* (1), 81–87.
- (32) Zhu, L.; Li, B.; Liu, X.; Huang, G.; Meng, X. Isolation and purification of schisandrol A from the stems of Schisandra chinensis and cytotoxicity against human hepatocarcinoma cell lines. *Pharmacogn. Mag.* **2015**, *11* (41), 131–135.

- (33) Štěrbová, H.; Sevcikova, P.; Kvasnickova, L.; Glatz, Z.; Slanina, J. Determination of lignans in *Schisandra chinensis* using micellar electrokinetic capillary chromatography. *Electrophoresis* **2002**, *23* (2), 253–258.
- (34) Wang, L.; Chen, Y.; Song, Y.; Chen, Y.; Liu, X. GC-MS of volatile components of *Schisandra chinensis* obtained by supercritical fluid and conventional extraction. *J. Sep. Sci.* **2008**, *31* (18), 3238–3245.
- (35) Li, X. Y.; Yang, M.; Huang, J. Y.; Yu, X. X.; Zhao, M. Q.; Liang, Z. K.; Xie, Z. S.; Xu, X. J. Preparative separation and purification of deoxyschizandrin from *Schisandrae Sphenantherae Fructus* by high-speed counter-current chromatography. *J. Pharm. Anal.* **2013**, *3* (6), 429–433.
- (36) Xia, Y. G.; Yang, B. Y.; Liang, J.; Wang, J. S.; Kuang, H. X. Simultaneous quantification of five dibenzocyclooctadiene lignans in *Schisandra chinensis* by HPLC separation and fluorescence detection. *Anal. Methods* **2014**, *6* (15), 5981–5985.
- (37) Hu, B.; Xin, G. Z.; So, P. K.; Yao, Z. P. Thin layer chromatography coupled with electrospray ionization mass spectrometry for direct analysis of raw samples. *J. Chromatogr. A* **2015**, *1415*, 155–160.
- (38) Schobert, R.; Kern, W.; Milius, W.; Ackermann, T.; Zoldakova, M. Synthesis of the first unnatural schisantherins and their effects in multidrug-resistant cancer cells. *Tetrahedron Lett.* **2008**, *49* (21), 3359–3362.
- (39) Gmeiner, A.; Effenberger-Neidnicht, K.; Zoldakova, M.; Schobert, R. A methyltitanocene complex of schisandrol A with high efficacy against multi-drug resistant cervix and breast carcinoma cells. *Appl. Organomet. Chem.* **2011**, *25* (2), 117–120.
- (40) Chen, T.; Li, C.; Li, Y.; Yi, X.; Lee, S. M. Y.; Zheng, Y. Oral delivery of a nanocrystal formulation of schisantherin A with improved bioavailability and brain delivery for the treatment of parkinson's disease. *Mol. Pharmaceutics* **2016**, *13* (11), 3864–3875.
- (41) Chen, T.; Li, C.; Li, Y.; Yi, X.; Wang, R.; Lee, S. M. Y.; Zheng, Y. Small-sized mPEG–PLGA nanoparticles of Schisantherin A with sustained release for enhanced brain uptake and anti-parkinsonian activity. *ACS Appl. Mater. Interfaces* **2017**, *9* (11), 9516–9527.
- (42) Sowndhararajan, K.; Deepa, P.; Kim, M.; Park, S. J.; Kim, S. An overview of neuroprotective and cognitive enhancement properties of lignans from *Schisandra chinensis*. *Biomed. Pharmacother.* **2018**, *97*, 958–968.
- (43) Shi, C.; Guo, D.; Xiao, K.; Wang, X.; Wang, L.; Luo, J. A drug-specific nanocarrier design for efficient anticancer therapy. *Nat. Commun.* **2015**, *6*, 7449.
- (44) Jiang, W.; Wang, X.; Guo, D.; Luo, J.; Nangia, S. Drug-specific design of telodendrimer architecture for effective doxorubicin encapsulation. *J. Phys. Chem. B* **2016**, *120* (36), 9766–9777.
- (45) Jiang, W.; Luo, J.; Nangia, S. Multiscale approach to investigate self-assembly of telodendrimer based nanocarriers for anticancer drug delivery. *Langmuir* **2015**, *31* (14), 4270–4280.
- (46) Li, Y.; Yang, L. Driving forces for drug loading in drug carriers. *J. Microencapsulation* **2015**, *32* (3), 255–272.
- (47) Shi, Y.; Van Steenbergen, M. J.; Teunissen, E. A.; Novo, L.; Gradmann, S.; Baldus, M.; Van Nostrum, C. F.; Hennink, W. E. II–II stacking increases the stability and loading capacity of thermosensitive polymeric micelles for chemotherapeutic drugs. *Biomacromolecules* **2013**, *14* (6), 1826–1837.
- (48) Shi, Y.; Van der Meel, R.; Theek, B.; Blenke, E. O.; Pieters, E. H. E.; Fens, M. H. A. M.; Ehling, J.; Schiffelers, R. M.; Storm, G.; Van Nostrum, C. F.; Lammers, T.; Hennink, W. E. Complete regression of xenograft tumors upon targeted delivery of paclitaxel via II–II stacking stabilized polymeric micelles. *ACS Nano* **2015**, *9* (4), 3740–3752.
- (49) Milonaki, Y.; Kaditi, E.; Pispas, S.; Demetzos, C. Amphiphilic gradient copolymers of 2-methyl- and 2-phenyl-2-oxazoline: self-organization in aqueous media and drug encapsulation. *J. Polym. Sci., Part A: Polym. Chem.* **2012**, *50* (6), 1226–1237.
- (50) Feinauer, R.; Seeliger, W. Über die Anlagerung von Epoxiden an cyclische Iminoester. *Justus Liebigs Ann. Chem.* **1966**, *698* (1), 174–179.
- (51) Muenzner, J. K.; Rehm, T.; Biersack, B.; Casini, A.; De Graaf, I. A. M.; Worawutputtpong, P.; Noor, A.; Kempe, R.; Brabec, V.; Kasparkova, J.; Schobert, R. Adjusting the DNA interaction and anticancer activity of Pt(II) N-heterocyclic carbene complexes by steric shielding of the trans leaving Group. *J. Med. Chem.* **2015**, *58* (15), 6283–6292.
- (52) Schmitt, F.; Gold, M.; Begemann, G.; Andronache, I.; Biersack, B.; Schobert, R. Fluoro and pentafluorothio analogs of the antitumoral curcuminoid EF24 with superior antiangiogenic and vascular-disruptive effects. *Bioorg. Med. Chem.* **2017**, *25* (17), 4894–4903.
- (53) Nakajima, A. Solvent effect on the vibrational structures of the fluorescence and absorption spectra of pyrene. *Bull. Chem. Soc. Jpn.* **1971**, *44* (12), 3272–3277.
- (54) Kalyanasundaram, K.; Thomas, J. K. Environmental effects on vibronic band intensities in pyrene monomer fluorescence and their application in studies of micellar systems. *J. Am. Chem. Soc.* **1977**, *99* (7), 2039–2044.
- (55) Ding, J.; Chen, L.; Xiao, C.; Chen, L.; Zhuang, X.; Chen, X. Noncovalent interaction-assisted polymeric micelles for controlled drug delivery. *Chem. Commun.* **2014**, *50* (77), 11274–11290.
- (56) Raveendran, R.; Mullen, K. M.; Wellard, R. M.; Sharma, C. P.; Hoogenboom, R.; Dargaville, T. R. Poly(2-oxazoline) block copolymer nanoparticles for curcumin loading and delivery to cancer cells. *Eur. Polym. J.* **2017**, *93*, 682–694.
- (57) Luxenhofer, R.; Sahay, G.; Schulz, A.; Alakhova, D.; Bronich, T. K.; Jordan, R.; Kabanov, A. V. Structure-property relationship in cytotoxicity and cell uptake of poly(2-oxazoline) amphiphiles. *J. Controlled Release* **2011**, *153* (1), 73–82.
- (58) Hamada, H.; Ishihara, K.; Masuoka, N.; Mikuni, K.; Nakajima, N. Enhancement of water-solubility and bioactivity of paclitaxel using modified cyclodextrins. *J. Biosci. Bioeng.* **2006**, *102* (4), 369–371.
- (59) Lübtow, M. M.; Keßler, L.; Lorson, T.; Gangloff, N.; Kirsch, M.; Dahms, S.; Luxenhofer, R. More Is less: Curcumin and paclitaxel formulations using poly(2-oxazoline) and poly(2-oxazine) based amphiphiles bearing linear and branched C9 side chains. *ChemRxiv* **2018**, DOI: [10.26434/chemrxiv.5883109.v1](https://doi.org/10.26434/chemrxiv.5883109.v1).
- (60) Sreekanth, C. N.; Bava, S. V.; Sreekumar, E.; Anto, R. J. Molecular evidences for the chemosensitizing efficacy of liposomal curcumin in paclitaxel chemotherapy in mouse models of cervical cancer. *Oncogene* **2011**, *30* (28), 3139–3152.
- (61) Huang, M.; Jin, J.; Sun, H.; Liu, G. T. Reversal of P-glycoprotein-mediated multidrug resistance of cancer cells by five schizandrins isolated from the chinese herb fructus schizandrae. *Cancer Chemother. Pharmacol.* **2008**, *62* (6), 1015–1026.
- (62) Cabral, H.; Matsumoto, Y.; Mizuno, K.; Chen, Q.; Murakami, M.; Kimura, M.; Terada, Y.; Kano, M. R.; Miyazono, K.; Uesaka, M.; Nishiyama, N.; Kataoka, K. Accumulation of sub-100 nm polymeric micelles in poorly permeable tumours depends on size. *Nat. Nanotechnol.* **2011**, *6*, 815–823.
- (63) Fox, T. Static analysis of dilute materials to study surrounding temperature for the polymer. *Bull. Am. Phys. Soc.* **1956**, *1*, 23–135.
- (64) Rettler, E. F. J.; Kranenburg, J. M.; Lambermont-Thijs, H. M. L.; Hoogenboom, R.; Schubert, U. S. Thermal, mechanical, and surface properties of poly(2-N-alkyl-2-oxazoline)s. *Macromol. Chem. Phys.* **2010**, *211* (22), 2443–2448.
- (65) Culbertson, B. M.; Xue, Y. A novel simultaneous semi-interpenetrating polymer network of crosslinked poly(methyl methacrylate) and poly(2-benzyl-2-oxazoline). *J. Macromol. Sci., Part A: Pure Appl. Chem.* **1996**, *33* (11), 1601–1608.
- (66) Beck, M.; Birnbrich, P.; Eicken, U.; Fischer, H.; Fristad, W. E.; Hase, B.; Krause, H. J. Polyoxazoline auf fettchemischer Basis. *Angew. Makromol. Chem.* **1994**, *223* (1), 217–233.
- (67) Kochetkov, N. K.; Khorlin, A. Y.; Chizhov, O. S. Chemical study of *Schizandra chinensis*. I. Schizandrin and related compounds. *Zh. Obshch. Khim.* **1961**, *31*, 3454–3460.

(68) Rausch, K.; Reuter, A.; Fischer, K.; Schmidt, M. Evaluation of nanoparticle aggregation in human blood serum. *Biomacromolecules* **2010**, *11* (11), 2836–2839.

Due to the fact that the cyto-compatible amphiphile A-PBzOx-A showed promising results in the (co)-encapsulation of different hydrophobic drugs, it was further used in an *in vivo* study.

*** The following open access highlights, abstract and graphic was reprinted from *Materials Today Bio*, 2020, 8, 100082, <https://doi.org/10.1016/j.mtbio.2020.100082>

Low Dose Novel PARP-PI3K Inhibition via Nanoformulation Improves Colorectal Cancer Immunoradiotherapy

Landry M.R., DuRoss A.N., Neufeld M.J., Hahn L., Sahay G., Luxenhofer R. and Sun C.

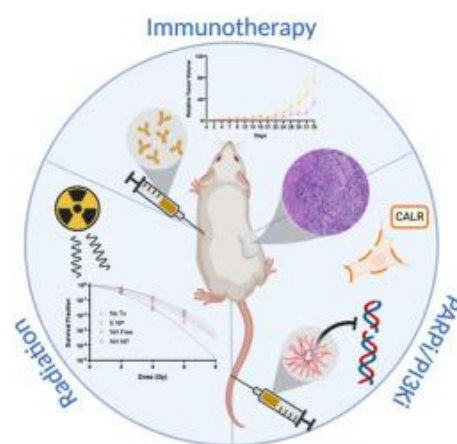
Highlights

- A novel combination of PARP (poly-adenosine diphosphate-ribose-polymerase) and PI3K (phosphoinositide 3-kinase) inhibitors induce radiosensitization *in vitro* and immunogenic cell death *in vitro* and *in vivo*.
- Encapsulation of both niraparib and HS-173 in POx micelles allows for co-delivery to colorectal cancer tumors
- This nanoformulation combined with radiation improve CTLA-4 (cytotoxic T-lymphocyte-associated protein 4) therapy by tumor growth delay and potentially increase the responding population.

Abstract

Multimodal therapy is often used in oncology to overcome dosing limitations and chemoresistance. Recently, combination immunoradiotherapy has shown great promise in a select subset of patients with colorectal cancer (CRC). Furthermore, molecularly targeted agents delivered in tandem with immunotherapy regimens have been suggested to improve treatment outcomes and expand the population of responding patients. In this study, radiation-sensitizing small molecules niraparib (PARP inhibitor) and HS-173 (PI3K inhibitor) are

identified as a novel combination that synergistically enhance toxicity and induce immunogenic cell death both *in vitro* and *in vivo* in a CRC model. These inhibitors were co-encapsulated in a polymer micelle to overcome solubility limitations while minimizing off-target toxicity. Mice bearing syngeneic colorectal tumors (CT26) were administered these therapeutic micelles in combination with X-ray irradiation and anti-CTLA-4 immunotherapy. This combination led to enhanced efficacy demonstrated by improved tumor control and increased tumor infiltrating lymphocytes. This report represents the first investigation of DNA damage repair inhibition combined with radiation to potentiate anti-CTLA-4 immunotherapy in a CRC model. ***



Chapter II

In this chapter, the influence of slightly different aromatic repeating units (PPheOx, PPheOzi, PBzOx and PBzOzi) in ABA type POx/POzi based amphiphiles was described. Only the polymer A-PPheOzi-A showed unusual inverse thermogelation. The hydrogel properties were investigated in the context of biofabrication. Further, the unique gelation mechanism with the influence of the hydrophilic polymer block was investigated.

The following publication was reprinted with permission from *ACS Applied Materials and Interfaces* **2020**, 12 (11), 12445-12456. <https://doi.org/10.1021/acsami.9b21282>; © 2020 American Chemical Society

Inverse Thermogelation of Aqueous Triblock Copolymer Solutions into Macroporous Shear-Thinning 3D Printable Inks

Lukas Hahn, Matthias Maier, Philipp Stahlhut, Matthias Beudert, Vanessa Flegler, Stefan Forster, Alexander Altmann, Fabian Töppke, Karl Fischer, Sebastian Seiffert, Bettina Böttcher, Tessa Lühmann, and Robert Luxenhofer*



Cite This: *ACS Appl. Mater. Interfaces* 2020, 12, 12445–12456



Read Online

ACCESS |



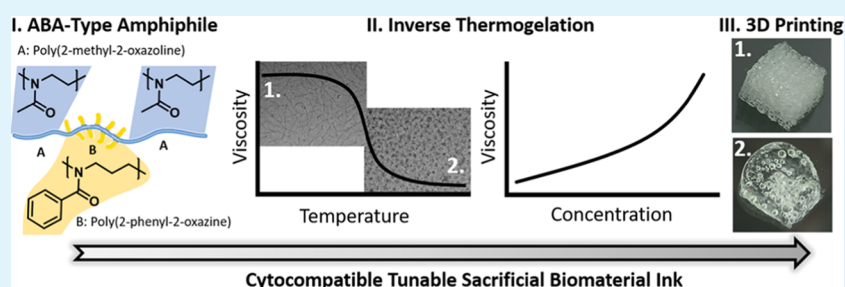
Metrics & More



Article Recommendations



Supporting Information



ABSTRACT: Amphiphilic block copolymers that undergo (reversible) physical gelation in aqueous media are of great interest in different areas including drug delivery, tissue engineering, regenerative medicine, and biofabrication. We investigated a small library of ABA-type triblock copolymers comprising poly(2-methyl-2-oxazoline) as the hydrophilic shell A and different aromatic poly(2-oxazoline)s and poly(2-oxazine)s cores B in an aqueous solution at different concentrations and temperatures. Interestingly, aqueous solutions of poly(2-methyl-2-oxazoline)-*block*-poly(2-phenyl-2-oxazine)-*block*-poly(2-methyl-2-oxazoline) (PMeOx-*b*-PPheOzi-*b*-PMeOx) undergo inverse thermogelation below a critical temperature by forming a reversible nanoscale wormlike network. The viscoelastic properties of the resulting gel can be conveniently tailored by the concentration and the polymer composition. Storage moduli of up to 110 kPa could be obtained while the material retains shear-thinning and rapid self-healing properties. We demonstrate three-dimensional (3D) printing of excellently defined and shape-persistent 24-layered scaffolds at different aqueous concentrations to highlight its application potential, e.g., in the research area of biofabrication. A macroporous microstructure, which is stable throughout the printing process, could be confirmed via cryo-scanning electron microscopy (SEM) analysis. The absence of cytotoxicity even at very high concentrations opens a wide range of different applications for this first-in-class material in the field of biomaterials.

KEYWORDS: poly(2-oxazoline), dispense plotting, biomaterial ink, smart hydrogel, wormlike micelles

INTRODUCTION

Stimuli-responsive polymers, also referred to as smart polymers, undergo changes with respect to their physicochemical properties or morphology when they are exposed to external stimuli such as temperature, pH, and/or light.^{1,2} Thermoresponsive polymers can be primarily categorized into those that exhibit a lower critical solution temperature (LCST), upper critical solution temperature (UCST), or physical gelation.³ Polymers that undergo physical gelation have gained great interest because of their potential applications in drug delivery and release, tissue engineering and regenerative medicine, biofabrication, cosmetics, and smart coatings.⁴ The gelation process is mainly defined by the (reversible) formation and growth of supramolecular structures yielding three-dimensionally (3D), physically cross-linked networks. The molecular interactions defining the network formation may be coulomb interactions, hydrogen

bonding, or hydrophobic/aromatic interactions. Polymers with UCST behavior reversibly phase separate upon cooling, typically leading to precipitation. In some cases, precipitation does not occur; instead, a gel is formed. UCST-type behavior can be observed in solvent mixtures and, though much more rarely, in water.^{5–8} Already in 1979, Wellinghoff et al. described a poly(styrene) and poly(dimethylphenylene oxide) system, which forms gels in organic solvents upon rapid cooling.⁹ In 2015, a thixotropic poly(glycerol sebacate)-

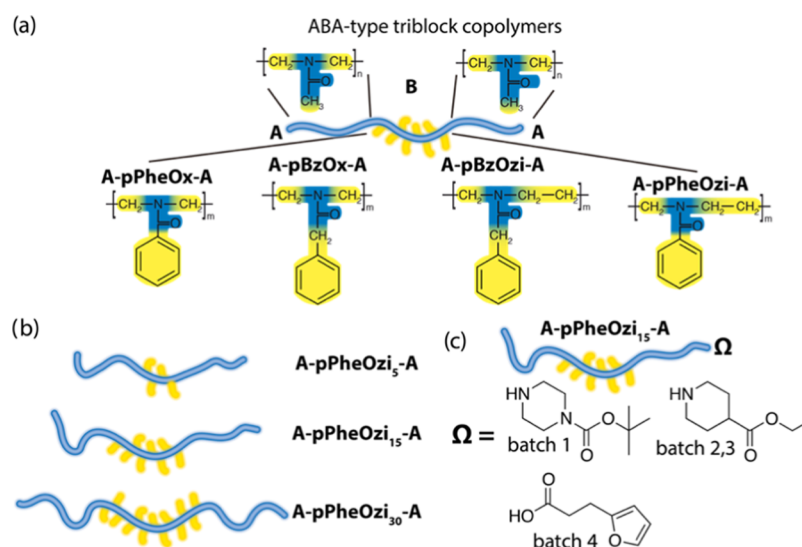
Received: November 22, 2019

Accepted: February 12, 2020

Published: March 6, 2020



Scheme 1. (a) Schematic Illustration of Investigated ABA-Triblock Copolymers Comprising the Hydrophilic Shell Poly(2-methyl-2-oxazoline) and Different Aromatic Hydrophobic Cores Based on Poly(2-oxazoline)s or Poly(2-oxazine)s^a



^aIn the case of A-pPheOzi-A, also (b) different chain lengths of the hydrophobic blocks were synthesized, and for A-pPheOzi₁₅-A, also various batches with varying terminating agents Ω (c) were prepared.

based supramolecular structure with UCST behavior was reported to form a hydrogel at rather low concentrations (5.2%) with self-healing ability with a storage modulus of 100 kPa. The clear liquid turned into a turbid gel upon cooling.¹⁰ Theato and co-workers described polymers based on vinyl-cyclopropane and investigated their UCST and physical gelation behavior in ethanol and ethanol–water mixtures at different concentrations.¹¹ The transition-temperature hysteresis between the heating and the cooling phase was very large (about 45 K). Another class of thermoreversible physically cross-linked hydrogels formed from ABA linear triblock copolymers was reported recently.¹² The polymers feature a hydrophilic poly(poly(ethylene glycol) methyl ether methacrylate) (PPEGMMA) middle block B and flanking UCST-type thermosensitive poly(acrylamide-*co*-acrylonitrile) (P(AAm-*co*-AN)) A blocks. At distinct block lengths, chemical compositions, and polymer concentrations, aqueous solutions of these polymers showed cooling-induced, reversible sol–gel transitions in water.

Polymers of cyclic imino ethers, in particular poly(2-substituted-2-oxazoline)s (POx) and poly(2-substituted-5,6-dihydro-4*H*-1,3-oxazine)s (poly(2-oxazine)s; POzi), are important classes of thermoresponsive polymers^{13,14} and can be synthesized via living cationic ring-opening polymerization to yield different polymeric architectures^{15,16} and compositions.^{17,18} Over the last few decades, POx have been intensively studied as thermoresponsive materials,¹⁹ surface coatings,^{20–22} and in biomedical applications^{23–25} and drug delivery.^{26–29} More recently, Bloksma et al. investigated the thermoresponsive behavior of some POzi homopolymers.³⁰ Interestingly though, only a few reports can be found that show thermogelation in water for pure POx/POzi-based systems. In fact, Zahoranová et al. investigated different triblock copolymers mimicking Pluronic-type polymers based on the hydrophilic poly(2-methyl-2-oxazoline) (PMeOx) and the thermoresponsive poly(2-*n*-propyl-2-oxazoline) (PnPrOx), but no thermogelling could be observed.³¹ In contrast, Lorson et al. established a thermogelling ($G' \sim 4$ kPa), cytocompat-

ible, and printable poly(2-oxazoline)/poly(2-oxazine) (POx/POzi) supramolecular hydrogel.³² These diblock copolymers, comprising a hydrophilic PMeOx block and a thermoresponsive PnPrOzi block of equal or similar block length, undergo thermogelation above a defined sol–gel temperature. Very recently, Hoogenboom and Monnery reported thermogelling ABA-triblock copolymers bearing thermoresponsive PnPrOx and hydrophilic PMeOx block blocks, but block lengths necessary for thermogelation were extremely high.³³ More recently, Lübtow et al. reported on a different ABA-triblock copolymer, again with hydrophilic poly(2-methyl-2-oxazoline) A blocks and a hydrophobic poly(2-*iso*-butyl-2-oxazoline) B block, which forms thermogels, albeit rather weak ones that are barely printable.³⁴ Hoogenboom and co-workers described a UCST-based thermoresponsive micellization of random copolymers comprising poly(2-nonyl-2-oxazoline) and poly(2-phenyl-2-oxazoline) blocks.³⁵ Upon cooling, these structures form micelles in different water–ethanol mixtures. However, to the best of our knowledge, there has been no reported case of UCST-type Pox/POzi in water, nor inverse gelation of POx/POzi-based polymers.

In our ongoing endeavor for an enhanced understanding of the interaction between drugs and polymeric drug delivery systems,^{28,36–40} we recently studied ABA triblocks featuring aromatic hydrophobic B blocks.²⁷ For the B blocks, we used the well-known aromatic polymers poly(2-phenyl-2-oxazoline) (PPheOx) and poly(2-benzyl-2-oxazoline) (PBzOx). Here, we report on first-of-their-kind ABA-triblock copolymers featuring the aromatic poly(2-oxazine)s, specifically poly(2-phenyl-2-oxazine) (PPheOzi) and poly(2-benzyl-2-oxazine) (PBzOzi) (Scheme 1). Together with their POx-based homologues (PPheOx/PBzOx), the rheological properties of aqueous solutions were investigated depending on concentration and temperature. Interestingly, only one polymer, poly(2-methyl-2-oxazoline)-*block*-poly(2-phenyl-2-oxazine)-*block*-poly(2-methyl-2-oxazoline) (PMeOx-*b*-PPheOzi-*b*-PMeOx = A-PPheOzi-A), undergoes inverse thermogelation at around room

temperature at a concentration of 5 wt % and above. The unusual gelation behavior was examined in detail.

EXPERIMENTAL SECTION

Materials and Methods. All substances and reagents for the monomer synthesis and polymerization were purchased from Sigma-Aldrich (Steinheim, Germany) or TCI-chemicals (Eschborn, Germany) and were used as received unless otherwise stated. Deuterated solvents for NMR analysis were obtained from Deutero GmbH (Kastellaun, Germany). All substances used for polymerization, specifically methyl trifluoromethylsulfonate (MeOTf), MeOx, PheOzi, and BuOzi, were refluxed over CaH₂ for several hours and distilled prior to usage. The solvent benzonitrile (PhCN) was dried over phosphorus pentoxide. All dried reagents were stored under dry and inert conditions.

Refractive Index. The refractive index of synthesized monomers was determined on an RFM 870 refractometer from Bellingham + Stanley at 20 °C (Farnborough, England).

Gas Chromatography. The monomers were analyzed via mass spectrometry using an Agilent 5977B MDS system coupled with a gas chromatography (GC) system Agilent 7820A. The GC system was equipped with an Agilent 19091S-433UI HP-5ms ultra-inert column (30 m × 250 μm × 0.25 μm). The temperature gradient was set from 40 to 300 °C with a constant heat rate of 15 °C/min and a constant flow of 1 mL/min.

NMR. NMR was performed on a Bruker Fourier 300 (¹H: 300.12 MHz) spectrometer at 298 K from Bruker BioSpin (Rheinstetten, Germany) and calibrated using the solvent signals.

Gel Permeation Chromatography (GPC). Gel permeation chromatography (GPC) was performed on a Polymer Standard Service PSS (Mainz, Germany) system with the following specifications: pump mod. 1260 infinity, MDS RI-detector mod. 1260 infinity (Agilent Technologies, Santa Clara, California), precolumn: 50 × 8 mm PSS PFG linear M; 2 columns: 300 × 8 mm PSS PFG linear M (particle size 7 μm; pore size 0.1–1.000 kg/mol) with hexafluoroisopropanol (HFIP, containing 3 g/L potassium trifluoroacetate (KTFA)) as the eluent calibrated against PEG standards with molar masses from 0.1 kg/mol to 1000 kg/mol. The columns were held at 40 °C, and the flow rate was set to 0.7 mL/min. Prior to each measurement, samples were dissolved in the eluent and filtered through 0.2 μm polytetrafluoroethylene (PTFE) filters (Rotilabo, Karlsruhe, Germany) to remove particles, if any.

Dynamic Light Scattering (DLS). Dynamic light scattering (DLS) experiments were performed on an ALV SP125 (Langen, Germany) equipped with a He–Ne laser (22 mW, λ = 632.8 nm) and a single photodiode detector. Scattering angles from 30 → 150° were measured at 2.5° angle intervals (T = 293.15 K, correlation time 60 s, average of 3–5 runs). Prior to each measurement, samples were dissolved in methanol (10 g/L) and filtered through 0.02 μm Anotop membrane filters from Whatman GE Healthcare followed by IC Millex-LG 0.2 μm. After evaporation of methanol, the samples were dissolved in prefiltered (Millex-LG 0.2 μm) Millipore water containing 2 mM NaNO₃. Next, 1 g/L samples were filtered (Millex-LG 0.2 μm) into dust-free cuvettes under laminar flow. The decay of the electric field-time autocorrelation function (ACF) was fitted using biexponential fit functions (eq 1) with respect to polydispersities, like used previously²⁷

$$g_1(t) = a_1 \cdot e^{-(t/\tau_1)} + a_2 \cdot e^{-(t/\tau_2)} \quad (1)$$

with the amplitudes a_i and the decay times $\tau_i = \frac{1}{q^2 \cdot D_i}$, with q being the absolute value of the scattering vector and D being the Brownian diffusion coefficient, which is indirectly proportional to the hydrodynamic radius R_h (Stokes–Einstein eq 2)

$$R_h = \frac{k_B \cdot T}{6 \cdot \pi \cdot \eta \cdot D} \quad (2)$$

Here, k_B is the Boltzmann constant and η is the viscosity of the solvent.

In the case of polydispersity, the hydrodynamic radius is obtained by extrapolation to zero angle and in the limit of high dilution given by

$$\langle 1/R_h \rangle_z^{-1} = \frac{\sum_i a_i}{\sum_i a_i \cdot R_i^{-1}}$$

Transmission Electron Microscopy (TEM). For transmission electron microscopy (TEM) investigations, the polymer was dissolved in ultrapure water to a final concentration of 20 g/L. For the negative stain method, 400-mesh copper-rhodium grids (maxtaform) with a homemade carbon layer were glow-discharged in air for 1.5 min at medium power in a Harrick PDC-002 plasma cleaner. The 20 g/L sample was diluted (1/625), and 8 μL was incubated on the grids for 1 min before blotting (Whatman filter paper No 50). Then, the grids were washed with water (3×) and with 2% (w/v) uranyl acetate (3×). For cryo sample preparation, Quantifoil copper grids (400 mesh, R1/2) were used. The undiluted sample (3.5 μL) was applied on the grids and plunge-frozen in liquid ethane with a Vitrobot IV (FEI). The humidity was set to 100%, and the temperature was set to 5, 25, or 40 °C. For imaging, either a single-tilt room-temperature holder (negatively stained samples) or a Gatan 626 cryo-transfer holder (vitrified samples) in an FEI Tecnai T12 Spirit transmission electron microscope equipped with a LaB₆ emitter at 120 kV was used. Images were recorded with an Eagle CCD camera under low-dose conditions. The micrographs were binned two times, resulting in a pixel size of 4.4 Å/pix or 2.2 Å/pix at the specimen level.

Rheology Experiments. Rheology experiments were performed using an Anton Paar (Ostfildern, Germany) Physica MCR 301 system utilizing a plate–plate geometry (25 mm diameter) equipped with a solvent trap and a Peltier element for temperature adjustment. All aqueous samples were stored after dissolution at 5 °C for 48 h. The temperature-sweep measurement was performed in the oscillation mode from 5 to 40 °C (heating rate: 0.05 °C/s), holding the temperature for 60 s, followed by a cooling phase from 40 to 5 °C (cooling rate: 0.05 °C/s) using a fixed amplitude of 0.1% and angular frequency of 10 rad/s. The long-time gelation experiment was performed at an amplitude of 0.1% and an angular frequency of 1 rad/s for several hours. To investigate the viscoelastic properties, the linear viscoelastic region (LVR) was determined by performing amplitude sweeps at different concentrations (5–40 wt %) from 0.01 to 500% strain deformation and a fixed angular frequency of 10 rad/s at 5 °C. Subsequently, frequency sweeps from 0.1 to 100 and 500 rad/s, respectively, were conducted at 0.1% strain deformation and 5 °C. To investigate structure recovery properties, the deformations were alternated from 0.1 to 150% in seven consecutive cycles at a fixed angular frequency of 10 rad/s and 5 °C, and the percentage of structure integrity after deformation was determined after the first and last recovery sequence. For steady shear experiments, the control shear rate mode was used from 0.001 to 100 1/s at 5 °C. The obtained viscosity η decrease was fitted using the power-law expression established by Ostwald–de Waele (eq 3).

$$\eta = K \cdot (\dot{\gamma})^{n-1} \quad (3)$$

where K is the consistency index, n is the flow index, and $\dot{\gamma}$ is the applied shear rate.

To evaluate the yield stress/yield point τ_0 of a hydrogel system, steady stress sweep and dynamic oscillatory stress sweep (amplitude sweep) were performed. Using the steady stress sweep from 5 to 1000 Pa shear stress, the viscosity starts decreasing by several orders of magnitude at a certain shear stress. The onset value of this decrease is referred to as yield point τ_0 . Also, the data of the dynamic oscillatory stress sweep were evaluated using onset determination. The flow point τ_{flow} is determined as the crossing of storage and loss modulus ($G' = G''$) by definition. These values were taken and compared with the steady stress sweep data.

Mechanical Compression. Mechanical compression was tested using an electro force 5500 system (BOSE electro force systems group, Friedrichsdorf, Germany). The experiments were performed in the static mode using a 250 g load cell. Cylindrical samples (4

diameter \times 4 mm height) were prepared and analyzed. The cross-linking of alginate samples was performed using a 40 mM aqueous CaCl_2 solution. For the hybrid system, the 17 wt % samples (2 wt % alginate, 15 wt % A-PPheOzi₁₅-A) were stored for 24 h at 5 °C prior to the cross-linking step. All samples were incubated in 4 mL of deionized water after cross-linking for 24 h at 37 °C. Six individual samples of the hybrid system and pure alginate hydrogels were analyzed and compared. Young's modulus was determined using a linear fit function in the linear material response region, typically in the range of 0.1 \rightarrow 0.2 strain deformation.

Dispense Plotting (3D Printing). Dispense plotting (3D printing) of hydrogel scaffolds was conducted at room temperature using a compact benchtop 3D bioprinter (Inkredible, Cellink, Sweden) working on the principle of an extrusion-based printer following the preparation described in Scheme S2. The printing speed was set to 600 mm/min, and different pressures were applied for different concentrations of the hydrogel using a conical nozzle with 0.25 mm inner diameter. In general, 24 orthogonal stacks (10 \times 10 mm, 0.25 mm layer height and 1 mm strand-center-to-strand-center distance) were printed and analyzed with a stereomicroscope SteREO Discovery.V20 (Carl Zeiss Microscopy, Jena, Germany) equipped with a Zeiss icc 5 color camera (5 MP, 12 bit), two lenses (0.63 \times and 1.5 \times Plan Apo), and a zoom range up to 20:1. For the alginate-A-PPheOzi₁₅-A hybrid ink system, 30 wt % of A-PPheOzi₁₅-A solution was mixed at 37 °C with a 4 wt % alginate solution in the ratio 1/1 (v/v) and stored for several hours at 5 °C. The cross-linking of the 24-layered construct was conducted using 10 mM CaCl_2 solution. The cross-linked hybrid scaffold was then incubated in water (Scheme S3) and analyzed via a stereomicroscope and rheology.

Cell Culture. Cell culture experiments of human embryonic kidney HEK293 cells (HEK-Blue IFN- α/β , Invivogen) were cultured in a growth medium (Dulbecco's modified Eagle's medium (DMEM), 10% fetal calf serum (FCS), 100 U/mL penicillin G, and 100 $\mu\text{g}/\text{mL}$ streptomycin) on 25 cm² culture flasks at 37 °C and 5% CO_2 . Calu-3 cells (human lung adenocarcinoma, ATCC HTB-55) were maintained in a growth medium (minimum essential medium (MEM), 10% FCS, 100 U/mL penicillin G, and 100 $\mu\text{g}/\text{mL}$ streptomycin, 1% nonessential amino acids (NEAs), 1 mM pyruvate, 2 mM glutamine, and 2.88 g/L glucose) at 37 °C and 5% CO_2 . The experiments were performed as described previously.³⁴ For the measurement of cytotoxicity of the polymer, 5000 cells/well of both Calu-3 and HEK cells were seeded in 96-well plates in the growth medium and incubated at 37 °C and 5% CO_2 for 24 h and 48 h, respectively. Final polymer concentrations of 10, 5, 1, and 0.1 wt % were prepared from a stock solution (20 wt %) in a growth medium on ice and added to the cells. After 24 h of cell growth, the medium was removed and replaced by a fresh cell culture medium. Cells were incubated with the WST-1 reagent for 1–4 h at 37 °C according to the manufacturer's manual. The formation of formazan was monitored at 450 and 630 nm using a Spectramax 250 microplate reader from Molecular Devices (Sunnyvale, CA).

Scanning Electron Microscopy (SEM). The polymer solutions were frozen with liquid nitrogen (LN) in the gel state and lyophilized afterwards. The dried powder was mounted on aluminum sample holders with conductive carbon tape and sputtered with a 4 nm layer of platinum in a sputter coater (Leica Microsystems ACE 400, Wetzlar, Germany). The morphology of the samples was subsequently analyzed using a Crossbeam 340 field emission scanning electron microscope (Carl Zeiss Microscopy, Oberkochen, Germany) by setting the acceleration voltage E_{TH} to 2 kV, and detection of a secondary electron (SE) was performed with an Everhart-Thornley detector. To visualize the native hydrogel structure, we also investigated a cryogenic sample preparation procedure. For this, samples were placed between two aluminum holders ($d = 3\text{ mm}$), both containing a notch with a diameter of 2 mm, inclosing the sample and rapidly frozen in slush nitrogen (SN) at -210 °C. The samples were then transferred into the sputter coater with a Leica EM VCT100 cryo-shuttle at -140 °C (Leica Microsystems ACE 400, Wetzlar, Germany). Here, the upper half of the sample was knocked off to create a freshly fractured surface and freeze-etched at -85 °C for 15

min under vacuum ($<1 \times 10^{-3}$ mbar). The samples were finally sputtered with 3 nm platinum and transferred with the cryo-shuttle into the scanning electron microscopy (SEM) chamber. The morphology of the fractured surfaces was imaged at -140 °C, by detecting SE using an acceleration voltage of 2 or 8 kV.

Synthetic Procedures: Monomer Synthesis. The monomers 2-phenyl-2-oxazine (PheOzi) and 2-benzyl-2-oxazine (BzOzi) were synthesized following the procedure by Wittig and Seeliger (Schemes S1–S3).⁴¹ For the reaction, 1 equiv of respective nitrile, 1.2 equiv of 3-amino-propanol, and catalytic amounts of zinc acetate dihydrate were added to an argon-flushed flask and heated to 130 °C under reflux for several days until the reaction mixture turned brown. Reaction progress was controlled by ¹H NMR spectroscopy. After completion, the mixture was dissolved in dichloromethane and washed with H₂O (three times). The organic phase was dried with MgSO_4 and concentrated. The raw product was refluxed with CaH_2 and purified via vacuum distillation under an argon atmosphere to yield the product as a colorless liquid. The resulting compounds PheOzi and BzOzi were characterized via the refractive index, GC-electrospray ionization mass spectrometry (ESI-MS) analysis, and ¹H and ¹³C NMR spectroscopies (see the Supporting Information).

Polymer Synthesis. The polymers were synthesized following a general procedure based on previous reports.^{27,28} Exemplarily, the preparation of methyl-PMeOx₃₅-b-PPheOzi₁₅-b-PMeOx₃₅-N-Boc-piperazine (A-PPheOzi-A, B1) was performed as follows. Under dry and inert conditions, 131 mg (0.80 mmol, 1 equiv) of MeOTf and 2.39 g (28.1 mmol, 35 equiv) of MeOx were added to 23 mL of dry PhCN and stirred for 4 h at 110 °C. Full monomer conversion was verified by ¹H NMR spectroscopy before adding the monomer for the second block. The mixture was cooled to room temperature, and 2.07 g (12.8 mmol, 16 equiv) of PheOzi was added. After stirring overnight at 120 °C, 2.39 g (28.1 mmol, 35 equiv) of MeOx was added. After completion of the third block, termination was carried out using 298 mg (1.6 mmol, 2 equiv) of N-Boc-piperazine and stirring for several hours at 45 °C (termination with 3-(2-furyl)propionic acid was performed with 2.4 equiv of freshly sublimated carboxylic acid and 3 equiv of dried trimethylamine at 60 °C). After cooling to room temperature, 111 mg (0.80 mmol, 1 equiv) of potassium carbonate was added and the mixture was stirred for 5 h. The solvent was removed at reduced pressure, and the flask was placed in a vacuum drying oven at 40 °C and 20 mbar for two days to remove the remaining benzonitrile. The residue was dissolved in deionized water, dialyzed overnight using a membrane with an MWCO of 1 kDa, and freeze-dried (yield: 6.21 g, 88.7%).

RESULTS AND DISCUSSION

We synthesized a small series of ABA-triblock copolymers PMeOx₃₅-b-PPheOzi₁₅-b-PMeOx₃₅, PMeOx₃₅-b-PPheOzi₁₅-b-PMeOx₃₅ (B1, B2, B3, and B4), PMeOx₃₅-b-PPheOzi₃₀-b-PMeOx₃₅, PMeOx₃₅-b-PBzOzi₁₅-b-PMeOx₃₅, PMeOx₃₅-b-PPheOx₁₅-b-PMeOx₃₅,²⁷ and PMeOx₃₅-b-PBzOx₁₅-b-PMeOx₃₅²⁷ by living cationic ring-opening polymerization (LCROP) and characterized the amphiphiles via ¹H NMR spectroscopy and GPC (Table 1 and Figures S1–S14). The successful termination using different terminating agents could be demonstrated via specific signal assignments (see the Supporting Information). Results from ¹H NMR and GPC analyses were also compared with previously reported A-PPheOx-A and A-PBzOx-A.²⁷ The primary structural difference between the novel polymers is one additional methylene group in the backbone and a variation of the degree of polymerization of the hydrophobic block, which leads to different physicochemical properties.

To gain insight into the differences with respect to aggregation, multiangle dynamic light scattering experiments for A-PPheOzi₁₅-A and A-PBzOzi₁₅-A solutions were performed. A-PPheOx₁₅-A and A-PBzOx₁₅-A solutions have been

Table 1. Number Average Molar Mass, Dispersity \mathcal{D} , and Yield of the Synthesized Triblock Copolymers Used in This Study^a

polymer	M_n^b (kg/mol)	M_n^c (kg/mol)	M_n^d (kg/mol)	\mathcal{D}^e	yield (%)
A-PPheOx ₁₅ -A ^a	8.5	8.5	5.3	1.10	88
A-PPheOzi ₁₆ -A (B1)	8.7	8.7	3.7	1.22	89
A-PPheOzi ₁₅ -A (B2)	8.6	8.3	3.8	1.28	83
A-PPheOzi ₁₆ -A (B3)	8.7	9.1	2.8	1.23	81
A-PPheOzi ₁₆ -A (B4)	8.7	8.9	2.3	1.30	89
A-PPheOzi ₅ -A	7.0	6.1	4.0	1.29	70
A-PPheOzi ₃₀ -A	10.9	9.6	4.0	1.26	79
A-PBzOx ₁₅ -A ^a	8.7	10.3	5.2	1.25	77
A-PBzOzi ₁₅ -A	8.8	9.1	4.0	1.18	89

^aThe polymers A-PPheOx-A and A-PBzOx-A were previously described in ref 27 and used herein. ^bTheoretical values obtained from $[M]_0/[I]_0$. ^cValues calculated from ¹H NMR end group analysis. ^dObtained from gel permeation chromatography ($T = 40\text{ }^\circ\text{C}$, 0.7 mL/min (HFIP), poly(ethylene glycol) standards). ^eObtained from GPC by using M_w/M_n .

previously analyzed similarly, and polymer micelles with hydrodynamic radii of 8–10 nm were observed.²⁷ The measured autocorrelation functions were fitted by means of biexponential fit functions, the results of which are shown in Figure 1a for a scattering angle of 90° at $20\text{ }^\circ\text{C}$ and a polymer concentration of 1 g/L. By plotting the inverse hydrodynamic

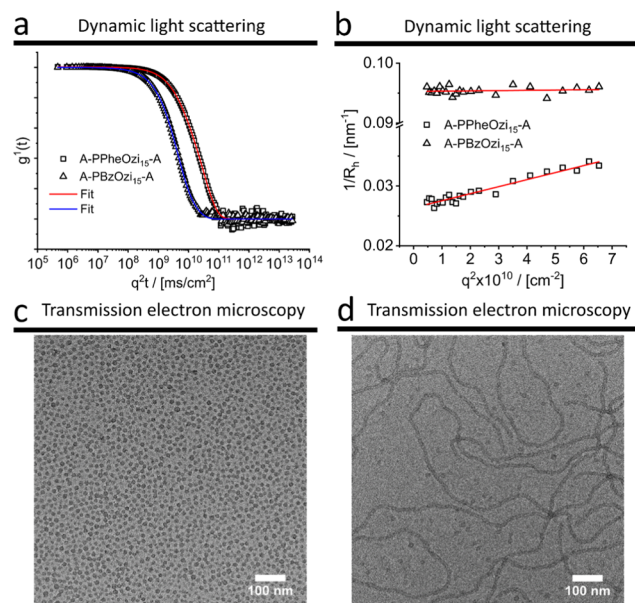


Figure 1. Comparison of A-PPheOzi₁₅-A and A-PBzOzi₁₅-A self-assembly via dynamic light scattering (a, b) and transmission electron microscopy (c, d). (a) Autocorrelation function $g^1(t)$ depending on q^2t at polymer concentration of 1 g/L (2 mM aqueous NaNO₃ solution) fitted by the biexponential fit function. (b) Inverse hydrodynamic radii R_h (nm^{-1}) as a function of the particular scattering vector q^2 . Obtained data were fitted using linear fit functions. (c) TEM image of polymer micelles formed by A-PBzOzi₁₅-A (0.032 g/L). (d) TEM image of polymorph aggregation of A-PPheOzi₁₅-A into wormlike structures and spherical micelles (0.032 g/L).

radius ($1/R_h$) as a function of the scattering vector, A-PPheOzi₁₅-A showed on average three times larger aggregates than A-PBzOzi₁₅-A and the respective poly(2-oxazoline) amphiphiles described previously (Figure 1b). Moreover, whereas the DLS of A-PBzOzi₁₅-A micelles with a hydrodynamic radius of 10 nm shows no angular dependency of $1/R_h$ (nearly monodisperse micelles), the average diffusion coefficient $1/R_h$ of the A-PPheOzi₁₅-A sample exhibits a pronounced angular dependency. This can be attributed to a pronounced polydispersity typical for, e.g., wormlike aggregates (“unlimited” one-dimensional (1D) growth). The aggregation into spherical polymer micelles of the polymer A-PBzOzi₁₅-A could be confirmed by transmission electron microscopy (Figure 1c). Rather homogeneous spherical micelles with hydrodynamic radii of ca. 10 nm were observed, corroborating DLS results. In contrast, for A-PPheOzi₁₅-A, a completely different and polymorph aggregation pattern was observed. This polymer aggregates at room temperature predominantly into wormlike structures with some residual spherical polymer micelles (Figure 1d), again corroborating DLS data. It should be noted that DLS and TEM experiments required different sample preparations. Therefore, different concentrations and sample histories could have affected polymer aggregation.

By dissolving the described amphiphiles in water (20 wt %) and incubating the resulting solutions at 5 and $37\text{ }^\circ\text{C}$, we noticed that the A-PPheOzi-A polymers formed clear hydrogels at different concentrations (Figures 2a,c and S15) in the

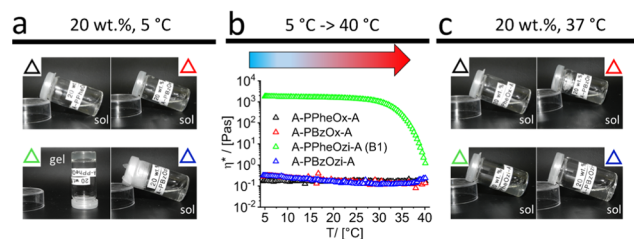


Figure 2. Screening for sol–gel transition of POx/POzi-based ABA-type amphiphiles with varying aromatic cores B. (a) Images of 20 wt % aqueous solutions of A-PPheOx-A (black triangle), A-PBzOx-A (red triangle), A-PPheOzi-A (green triangle), and A-PBzOzi-A (blue triangle) at $5\text{ }^\circ\text{C}$. Obviously, only A-PPheOzi-A forms a hydrogel (gel); all other samples remained liquid (sol). (b) Temperature sweep ($5 \rightarrow 40\text{ }^\circ\text{C}$, heat rate: $0.05\text{ }^\circ\text{C/s}$) of aqueous solutions (20 wt %) of A-PPheOx-A (black), A-PBzOx-A (red), A-PPheOzi-A (green), and A-PBzOzi-A (blue) at a strain of 0.1% and an angular frequency of 10 rad/s. Complex viscosity depending on the applied temperature is shown. (c) Images of 20 wt % aqueous solutions of A-PPheOx-A, A-PBzOx-A, A-PPheOzi-A, and A-PBzOzi-A at $37\text{ }^\circ\text{C}$. All amphiphiles present as low-viscous liquids (sol).

cold. Therefore, we investigated the temperature-dependent rheology properties of all polymer amphiphiles with different hydrophobic B blocks by performing temperature sweeps ($5\text{--}40\text{ }^\circ\text{C}$) after storage for 48 h at $5\text{ }^\circ\text{C}$ (Figure 2b).

Starting as a gel, the aqueous solution of A-PPheOzi-A results in a clear liquid above a critical temperature. Conversely, by cooling the liquid samples, a clear hydrogel is obtained. We also tested the behavior of the polymers A-PBzOx-A, A-PPheOx-A, and the newly synthesized A-PBzOzi-A in aqueous solutions at 20 wt %. Neither solution underwent thermogelation in the temperature range of $5\text{--}40\text{ }^\circ\text{C}$. We noticed that gelation of A-PPheOzi-A does not occur immediately upon cooling. Therefore, the gelation kinetics

were studied in more detail (Figure 3). The storage moduli G' at different concentrations were recorded at 5 and 10 °C for 8

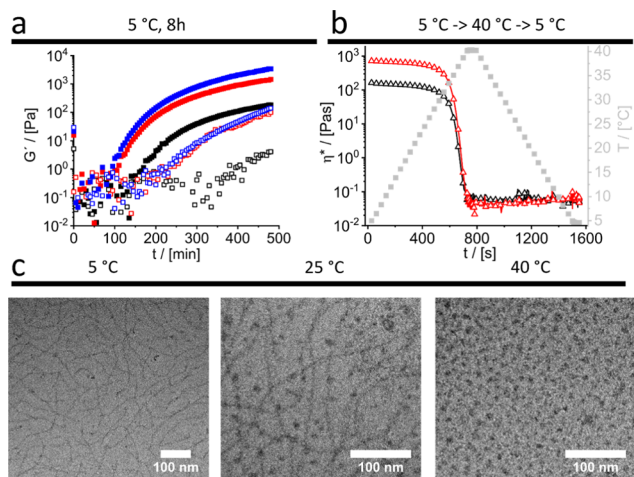


Figure 3. Gelation kinetics depending on concentration and temperature of A-PPheOzi-A hydrogels. (a) Storage moduli of aqueous solutions of A-PPheOzi₁₅-A (B1) (10 wt %, black; 15 wt %, red; 20 wt %, blue) at 5 °C (filled symbols) and 10 °C (open symbols) at constant strain deformation of 0.1% and 1 rad/s angular frequency. The polymer solutions were placed on a precooled rheometer plate and measured subsequently. (b) Temperature sweep of the complex viscosity (5 → 40 → 5 °C, heat/cooling rate: 0.05 °C/s) of the A-PPheOzi₁₅-A hydrogel (red, 15 wt %; black, 10 wt %). The stable precooled hydrogels were mounted on a precooled rheometer plate. (c) cryoTEM analysis of A-PPheOzi₁₅-A temperature-dependent aggregation in aqueous solutions (20 g/L). Samples were stored for 24 h at respective temperatures (5, 25, 40 °C).

h (Figure 3a). At 5 °C, higher concentrations lead to faster gelation. The onset temperature of gelation for a 20 wt % aqueous solution is ~90 min. For a 15 wt % sample, gelation started a few minutes later and ended up with lower G' plateau values compared to the 20 wt % sample. A significant shift toward longer gelation time was observed for 10 wt % samples. By increasing the temperature from 5 to 10 °C, the gelation was also delayed significantly. A temperature sweep revealed that, starting from 5 °C, the complex viscosities of 10 and 15 wt % aqueous solutions remain almost constant until about 30 °C, whereupon they decrease drastically by over 3–4 orders of magnitude and the gel liquefies (Figures 3b and S16). Once the gel is destroyed, no immediate, re-gelation is observed as the system is cooled again.

To further corroborate that hydrogel formation is caused by reversible worm-spherical morphology changes, cryoTEM images were recorded on samples incubated at different temperatures. At 5 °C, the temperature of stable hydrogel formation, a network of interconnected worms could be confirmed (Figure 3c). At intermediate 25 °C, the majority of the polymer is still aggregated as wormlike micelles, but some spherical micelles are apparent. Above the liquefaction temperature of the hydrogel (at 40 °C), only spheres with sizes of ca. 10 nm are visible. After this initial assessment, we investigated the effect of polymer concentration, chain length, and chain termini as well as the reproducibility of the rheological properties between different polymer batches. Amplitude sweeps showed that at 5 wt % and 5 °C, the polymer solutions of A-PPheOzi₁₅-A (B1) represent a weak gel ($G' \sim 135$ Pa). However, both storage and loss modulus could

be greatly modulated by changing the polymer concentration. By increasing the concentration to 40 wt %, the stiffness of the gel increased by 4 orders of magnitude (G' (40 wt %) ~ 110 kPa), whereas the regions of linear viscoelasticity decreased notably (Figure 4a). Frequency sweeps corroborated a strong viscoelastic-solid behavior over a large range of frequencies and concentrations (Figure 4b).

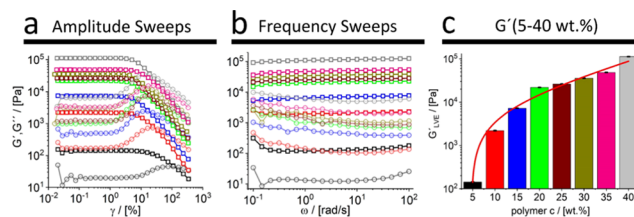


Figure 4. Viscoelasticity of the A-PPheOzi₁₅-A (B1) inverse thermohydrogel at different concentrations. (a) Amplitude sweeps at different concentrations (5 → 40 wt % at 5 wt % steps) at 5 °C and an angular frequency of 10 rad/s with storage moduli ($G' = \blacksquare$) and loss moduli ($G'' = \circ$) shown. (b) Frequency sweeps at 5 °C and an amplitude of 0.1%. Solutions were tempered at 5 °C for 48 h prior to measurements. (c) Exponential increase (red line) of the storage modulus by increasing the polymer concentration (G'_{LVE} : mean value of storage modulus in the plateau region of the respective amplitude sweep).

Apart from changing the hydrophobic core with respect to the chemical structure of the repeat unit, the amphiphilic ratio was adjusted by varying the degree of polymerization within the hydrophobic core, resulting in A-PPheOzi₅-A, A-PPheOzi₁₅-A, and A-PPheOzi₃₀-A. In addition, several batches of A-PPheOzi₁₅-A were synthesized to assess batch-to-batch reproducibility⁴² of the viscoelastic properties of the polymers. The rheological properties of all four batches of A-PPheOzi₁₅-A are quite similar, showing a prominent gel-like character ($G' > G''$) at 15 wt % aqueous solutions at 5 °C with storage moduli around 10 kPa (Figure 5a). Similar properties were also found in the cell culture medium (Figure S17). Unexpectedly, the gel strength decreased significantly when increasing the degree of polymerization of the central hydrophobic block to 30 units with a concomitant increase of the linear viscoelastic region (Figure 5a, black \blacksquare ; see also Figure S18). Decreasing

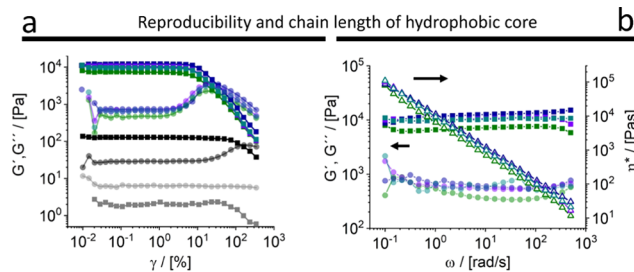


Figure 5. Investigation of reproducibility and influence of the aromatic block chain length of hydrogel formation. (a) Storage ($G' = \blacksquare$) and loss moduli ($G'' = \circ$) in amplitude sweeps of different batches of A-PPheOzi₁₅-A (B1 (green), B2 (blue), B3 (violet), and B4 (cyan)), A-PPheOzi₃₀-A (black), and A-PPheOzi₅-A (gray) at 15 wt % aqueous solutions, 5 °C, and a constant angular frequency of 10 rad/s. (b) Corresponding frequency sweeps of A-PPheOzi₁₅-A (B1, B2, B3, and B4) at 5 °C and an amplitude of 0.1% showing storage modulus ($G' = \blacksquare$) and loss modulus ($G'' = \circ$) as well as complex viscosity η^* (open triangles).

the chain length to 5 units of the PPheOzi-block completely prevented gel formation in the investigated concentration range. At 10 wt %, the gel formed by A-PPheOzi₃₀-A was comparable to a 5 wt % gel of A-PPheOzi₁₅-A.

For solutions of A-PPheOzi₁₅-A at 5 °C and 15 wt %, the frequency had only minor effects on the viscoelastic properties of the gel. The gel character remained unchanged within the investigated frequency range up to 500 rad/s. This corroborates the fact that the physical network is thoroughly developed and surprisingly stable in the entire frequency range investigated. On the other hand, the strongly decreasing complex viscosity values over several orders of magnitude show profound non-Newtonian fluid behavior. Well-defined yield- and flow-points are beneficial properties for hydrogels when used in the field of 3D printing and biofabrication (Figure 6).

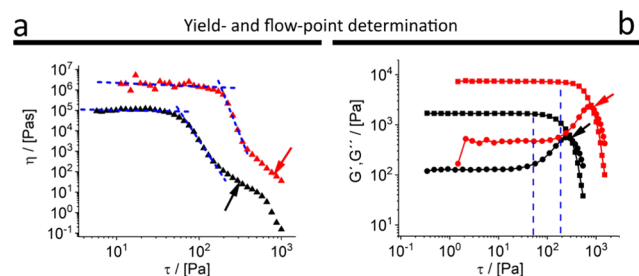


Figure 6. Yield- and flow-point determination using rotational and oscillation rheology approaches. (a) Viscosity depending on the applied shear stresses of 10 wt % (black) and 15 wt % (red) hydrogels at 5 °C. The intersection of dashed lines marks the onset of the viscosity decrease, which is commonly referred to as the yield point τ_0 . (b) Development of storage (G') (squares) and loss (G'') (circles) moduli with increasing shear stresses of 10 wt % (black) and 15 wt % (red) A-PPheOzi₁₅-A hydrogels. The systems' flow point τ_f is defined as the crossover of G' and G'' (arrows).

In the literature, different experiments, namely, steady stress sweep (Figure 6a) and dynamic oscillatory stress sweep (Figure 6b), are discussed to obtain the yield- and flow-points of a system directly from the plotted values. Here, these methods are compared using 10 and 15 wt % A-PPheOzi₁₅-A (B1) hydrogels.

In the steady stress sweep, the shear stress is increased steadily from low (5 Pa) to high (1000 Pa) values. At a certain stress, the viscosity values decrease over several orders of magnitude. The onset, defined by the tangential method, is referred to as the yield point τ_0 of the system (τ_0 (B1 (10 wt %)) = 58 Pa, τ_0 (B1 (15 wt %)) = 180 Pa, Figure 6a). Alternatively, an increase of G'' and decrease of G' during the dynamic oscillatory stress sweep indicate τ_0 (τ_0 (B1 (10 wt %)) = 51 Pa, τ_0 (B1 (15 wt %)) = 190 Pa, Figure 6b). In addition, the crossover of G' and G'' is defined as the flow point τ_f of the system (τ_f (B1 (10 wt %)) = 305 Pa, τ_f (B1 (15 wt %)) = 826 Pa, arrows Figure 6b). The corresponding viscosity values at the flow point can be obtained from the steady stress sweep experiment (η at τ_f (B1 (10 wt %)) = 33 Pa·s, η at τ_f (B1 (15 wt %)) = 74 Pa·s, arrows Figure 6a). Values for the other batches were obtained accordingly (Figures S19–S22) and are summarized in Table 2. The obtained values of the different batches do certainly vary but are all in the same order of magnitude, which indicates a good batch-to-batch reproducibility.

Moreover, pronounced shear thinning (Figure 7a) and rapid structure recovery (Figure 7b) are desired and realized by the

Table 2. Summary of Rheological Data and Parameters of A-PPheOzi₁₅-A Hydrogels (10 and 15 wt %) Obtained from Steady Stress Sweep, Dynamic Oscillatory Stress Sweep, and Steady Rate Sweep Experiments Across Different Batches^a

c (wt %)	batch	τ_0 (osc) (Pa)	τ_0 (rot) (Pa)	τ_f (osc) (Pa)	η at τ_f (Pa·s)	K (Pa·s ⁿ)	n
10	B1	51	58	305	33	180	0.14
	B2	183	148	576	5	333	0.13
	B3	80	134	376	8	237	0.14
	B4	59	137	393	7	230	0.14
15	B1	190	180	826	74	538	0.12
	B2	650	560	1600	nd	856	0.09
	B3	300	410	1100	nd	625	0.10
	B4	350	420	1050	nd	642	0.12

^aThe missing viscosity values could not be obtained, as in rotational steady shear stress experiments, the limit was set to 1 kPa.

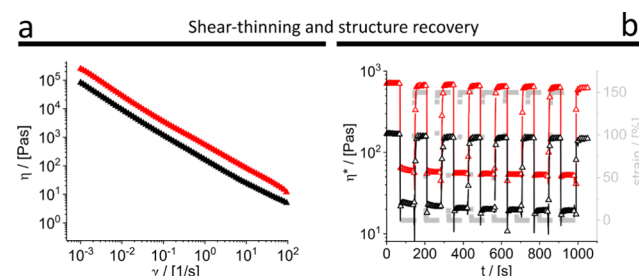


Figure 7. Shear-thinning and structure recovery are crucial requirements for dispense plotting. (a) Viscosity depending on the applied shear rate for 10 wt % (black) and 15 wt % (red) A-PPheOzi₁₅-A hydrogels at 5 °C. (b) Strain-step experiment: complex viscosity depending on the applied strain (0.1 → 150, 7 cycles) at 5 °C and an angular frequency of 10 rad/s.

novel materials.⁴³ Apart from a defined yield point, shear thinning and fast structure recovery are very important for printing purposes. A-PPheOzi₁₅-A exhibited very pronounced shear thinning (Figure 7a) and excellently reproducible structure recovery properties of 93% after the first recovery step and 87% after seven recovery cycles (Figure 7b). The steady rate sweep from 0.001 to 100 1/s was fitted using the power-law expression described by Ostwald–de Waele to obtain the flow index n and the consistency index K to characterize the hydrogel.

Clearly, the novel material is highly shear thinning and follows the power-law expression exhibiting low flow indices n ($n \ll 1$) across all synthesized A-PPheOzi₁₅-A batches ($n < 0.15$) (Table 2). Notably, the gel structure of the system recovers very rapidly (Figure 7b), which is highly favorable for processing, like 3D printing.

To obtain first insights into the morphology and microstructure of the novel hydrogels, we obtained scanning electron microscopy (SEM) images after freeze-drying. At 20 wt %, the hydrogel of A-PPheOzi₁₅-A exhibited a highly porous and rather homogeneously distributed microstructure with pores in the 5–10 μm range (Figure S23). However, as currently strongly discussed in the community, due to slow water evaporation during lyophilization or ice crystal formation during slow freezing, these features could in fact be artifacts of sample preparation. To avoid these, we also conducted cryogenic SEM (cryo-SEM) analysis. It has been shown that for very small hydrogel samples mounted on a TEM grid, liquid nitrogen (LN) as the cooling agent provides sufficient

cooling rates despite the Leidenfrost effect;⁴⁴ for bigger samples however, more efficient cooling agents like slush nitrogen (SN),⁴⁵ liquid ethane,⁴⁶ or high-pressure freezing in LN⁴⁷ are necessary. Here, we used SN to investigate whether the microporous structure observed by SEM was an artifact from freeze-drying or not (Figure 8). The result is rather

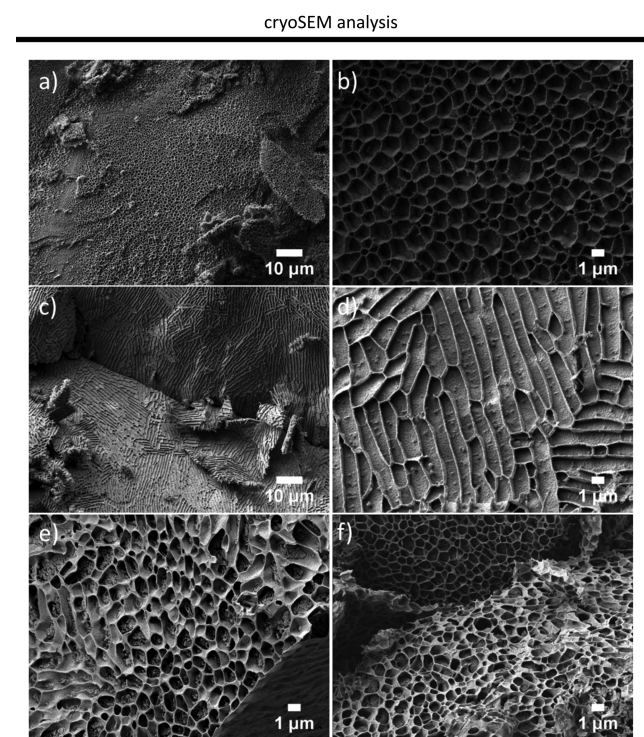


Figure 8. Microstructural analysis of the hydrogel structures. (a, b) Cryo-SEM images of the 5 wt % A-PPheOzi₁₅-A hydrogel at (a) 1k \times magnification and (b) 5k \times magnification. (c, d) Cryo-SEM images of the 5 wt % A-PPheOzi₅-A sol at (c) 1k \times magnification and (d) 5k \times magnification. Cryo-SEM images of the 15 wt % A-PPheOzi₁₅-A hydrogel prior to (e) and after dispense plotting (f) (5k \times magnification).

obvious; clearly, the sample preparation affects the observed morphology. Cryo-SEM images obtained of the gel of A-PPheOzi₁₅-A show a highly ordered porous structure with round pores in the submicrometer to low micrometer range, which is in agreement with the rheological data of a strong physical network (Figure 8a,b). In comparison, for aqueous solutions of A-PPheOzi₅-A, which does not form a hydrogel, rather lamellae-like structures are observed (Figure 8c,d). Therefore, it appears that even though a 3D network is formed, it is too weak to lead to macroscopic gelation, presumably due to a limited correlation length of the underlying physical network. In addition, we investigated the gel morphology of 15 wt % A-PPheOzi₁₅-A before and after dispense plotting (see below) by cryo-SEM (Figure 8e,f). It appears that the microstructural morphology remains unaffected, which also corroborates the rheological data, which show rapid recovery of the gel structure after printing.

From rheological and structural points of view, the hydrogels of A-PPheOzi₁₅-A appear well suited for (bio)printing. Obviously, cytocompatibility represents another critical feature for any hopeful bioink or biomaterial ink. For the present polymers, no dose-dependent cytotoxicity (WST-1 assay) was found for HEK and Calu-3 cell lines at concentrations of up to

10 wt % (Figure 9). In contrast, we found an increased apparent cell viability, which has been found similarly for other POx block copolymers.³²

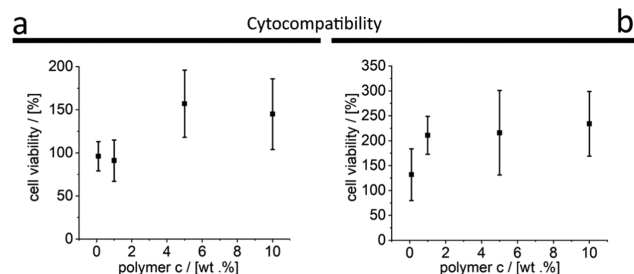


Figure 9. Dose-dependent cell viability of A-PPheOzi₁₅-A (B1) aqueous solutions using the WST-1 assay. Cell viability was assessed for HEK (a) and Calu-3 (b) cell lines ($n = 3$) after 24 h of incubation with polymer solutions.

Finally, the printability of the novel material was assessed (Figure 10). We printed first scaffolds using 10, 15, and 20 wt % of A-PPheOzi₁₅-A and 20 wt % of A-PPheOzi₃₀-A hydrogels using a 3D bioprinter equipped with a conical nozzle with 0.25 mm inner diameter (Figures 10a and S24–S26). To evaluate printing conditions such as speed and pressure, we first printed a four-layer 10 \times 10 line wood-pile structure (Figures S24a–c; S25b, and S26a–c). The strength of a 10 wt % A-PPheOzi₁₅-A hydrogel is insufficient and strand fusion is observed, which is in line with the low yield point of the system. Nevertheless, a 3D cube could be printed (Figure S25c,d). Also, the 20 wt % A-PPheOzi₃₀-A hydrogel could be successfully printed in 24 layers, but again some strand fusion was observed and shape fidelity was not very good (Figure S24d,e). Using the 20 wt % (Figure 10b) and 15 wt % hydrogels of A-PPheOzi₁₅-A and optimized printing parameters, 24-layer constructs of 10 \times 10 lines and 1 mm strand distance could be printed (Figure S26d,e). Excellent shape fidelity and layer integrity were clearly evident (Figure 10c,d, top view; Figure 10e,f, side view).

To highlight the potential of the novel material as, e.g., a sacrificial matrix or component in a hybrid system, we increased the temperature on the previously printed scaffolds, upon which strand fusion and collapse of the hydrogel network (Figure S27) were observed and the gel liquefied rapidly. Accordingly, a mild temperature stimulus compatible with cell culture conditions can be used to remove scaffolds printed with A-PPheOzi₁₅-A. This could be very useful if used as a sacrificial support matrix to assist in printing of materials, which by themselves are not easily 3D printed with good shape fidelity.

Alginate as a biopolymer is an ideal candidate to test this hypothesis, as it can be easily cross-linked by incubation with aqueous CaCl₂ and is often employed in biofabrication but usually suffers from poor printability due to poor rheological properties.^{48,49} To improve the printability of alginate, often pre-cross-linking⁵⁰ or composite systems are used.^{51–54} Here, we present an exceedingly simple alternative. We simply mixed the liquid A-PPheOzi₁₅-A polymer with liquid alginate and cooled the mixture, leading to gelation. We characterized this hybrid system via rheology prior to the printing process (Figure S28). A 17 wt % aqueous hybrid system (A-PPheOzi₁₅-A/alginate 15:2 w/w) exhibited storage moduli of up to 11 kPa (Figure S28a) and a pronounced shear-thinning response favorable for extrusion-based printing (Figure S28b).

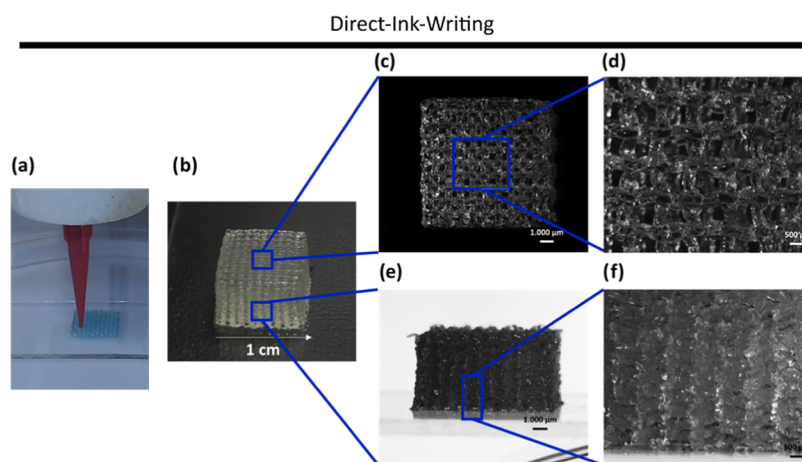


Figure 10. Dispense plotting using A-PPheOzi₁₅-A hydrogels. (a) Extrusion-based printing setup (nozzle: conical; 0.25 mm inner diameter; speed: 600 mm/min; dimensions: 10 × 10 mm; 1 mm strand distance; 0.25 mm layer height). (b) Printed 24-layer scaffold of B1 (20 wt % aqueous solution); (b) photographic image; (c, d) top view; (e, f) side view.

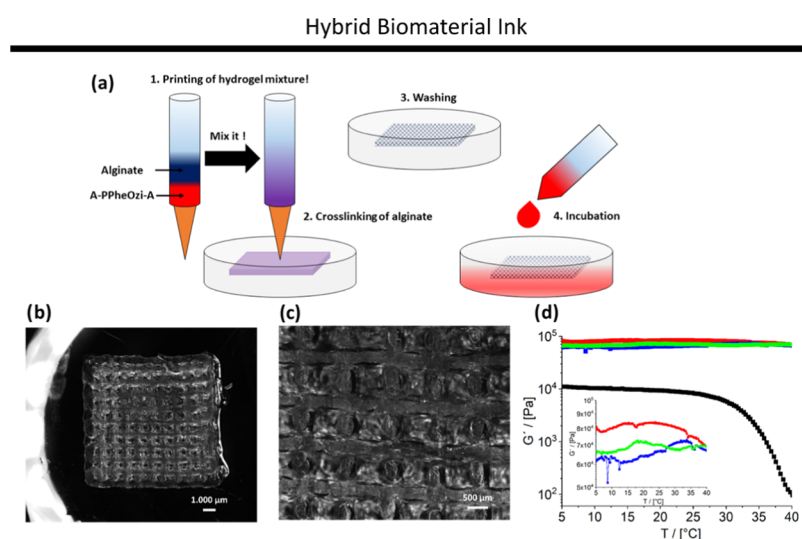


Figure 11. A-PPheOzi-A hydrogels as support materials in dispense plotting of biomaterial inks. (a) Workflow for the preparation of the hybrid material, its printing, and development. (b) Top and (c) side views of printed 24-layer scaffolds of B1/alginate hybrid 17 wt % aqueous solution (B1/alginate 15:2) (extrusion-based bioprinter; nozzle: conical; 0.25 mm inner diameter; speed: 600 mm/min; dimensions: 10 × 10 mm; 1 mm strand distance; 0.25 mm layer height). (d) Storage moduli as a function of temperature (T : 5–40 °C; heat rate: 0.05 °C/s; strain: 0.1%; angular frequency: 1 rad/s) of the B1/alginate hybrid prior to cross-linking (black) and after cross-linking (red) and incubation in aqueous solutions for 48 h (blue) and 72 h (green).

Accordingly, these hybrid systems could also be successfully printed into 3D scaffolds with excellent shape fidelity (Figure 11a,b). Simple addition of $\text{CaCl}_2(\text{aq})$ leads to alginate cross-linking, and subsequent incubation at 37 °C results in the dissolution of the sacrificial component A-PPheOzi₁₅-A. The residual alginate scaffolds stay structurally intact thereafter for at least 4 days being incubated in a water bath without significant shrinkage or loss of shape or stiffness in the temperature range of 5–40 °C (Figure 11b–d). After cross-linking, the storage modulus increases from 11 to 80 kPa, which remained at similar levels (60–70 kPa) for several days during incubation in the aqueous solution (Figure 11d). Important to note, due to the removal of the A-PPheOzi₁₅-A during the curing and developing step, no thermoresponsive behavior was observed for the chemical cross-linked structure. However, the mechanical stability increased significantly. For the hybrid system, a more than 10-fold increase of Young's

modulus (130 ± 12 kPa) compared to native alginate (8 ± 3 kPa) was obtained (Figure S29). We hypothesize that the alginate network could be more regular due to macromolecular crowding and microphase separation during casting and cross-linking. However, a detailed characterization of this observation is outside the scope of the current contribution.

The described hydrogel platform offers highly beneficial properties for a variety of applications such as a sacrificial biomaterial, a component in hybrid systems, as well as a support material in biofabrication, namely, temperature-responsive physical gelation and liquefaction, tunability of the storage modulus over several orders of magnitude, printability, and cytocompatibility. In addition, the polymer platform of POx/POzi offers different modification strategies during synthesis and additional postpolymerization modifications to further utilize and modify the unique aqueous solution properties of A-PPheOzi-A amphiphiles in different applica-

tions in the field of biofabrication, regenerative medicine, and tissue engineering.

CONCLUSIONS

In this study, we investigated the influence of different aromatic moieties on the viscoelastic properties and thermogelation of aqueous solutions of poly(2-oxazoline)/poly(2-oxazine)-based ABA-triblock copolymers. We introduced and characterized ABA-triblock copolymers comprising poly(2-phenyl-2-oxazine) and poly(2-benzyl-2-oxazine) as the hydrophobic core B. Most notably, the polymers bearing PPheOzi moieties undergo inverse and reversible thermogelation at a defined temperature and rather low concentrations of 5 wt %. Presumably, the polymer A-PPheOzi₁₅-A exhibited the right balance of flexibility caused by the poly(2-oxazine)-based backbone and rigidity of the phenyl side chain, as well as amphiphilicity, to form a reversible wormlike network at lower temperatures and a thermoresponsive transition into spherical polymer micelles upon heating. We established important properties for the hydrogels in the context of biofabrication, namely, the printability, as defined by distinct yield- and flow-points and favorable shear-thinning and structure recovery properties, as well as cytocompatibility. By means of cryo-SEM analysis, we obtained first insights into the structure of the hydrogels, which exhibit macroporous features. Also, we highlight the application as a sacrificial support material by 3D printing of excellently resolved and shape-persistent scaffolds of alginate, which is otherwise not printable in 3D due to its poor rheological properties.

ASSOCIATED CONTENT

Supporting Information

The Supporting Information is available free of charge at <https://pubs.acs.org/doi/10.1021/acsami.9b21282>.

Detailed description of monomer and polymer syntheses and characterization; tube inverting test of hydrogels as a function of concentration; detailed rheological characterization of all synthesized polymer batches and the hybrid system; schemes to visualize hydrogel and hybrid system preparation for dispense plotting; microscopy investigations of different printed scaffolds using different batch concentrations and printing architectures; SEM analysis of the lyophilized sample; compression test of alginate hydrogels (PDF)

AUTHOR INFORMATION

Corresponding Author

Robert Luxenhofer – *Functional Polymer Materials, Chair for Advanced Materials Synthesis, Department of Chemistry and Pharmacy and Bavarian Polymer Institute, Julius-Maximilians-University Würzburg, 97070 Würzburg, Germany; Soft Matter Chemistry, Department of Chemistry, Helsinki University, 00014 Helsinki, Finland; orcid.org/0000-0001-5567-7404; Email: robert.luxenhofer@uni-wuerzburg.de, robert.luxenhofer@helsinki.fi*

Authors

Lukas Hahn – *Functional Polymer Materials, Chair for Advanced Materials Synthesis, Department of Chemistry and Pharmacy and Bavarian Polymer Institute, Julius-Maximilians-University Würzburg, 97070 Würzburg, Germany*

Matthias Maier – *Functional Polymer Materials, Chair for Advanced Materials Synthesis, Department of Chemistry and Pharmacy and Bavarian Polymer Institute, Julius-Maximilians-University Würzburg, 97070 Würzburg, Germany*

Philipp Stahlhut – *Department for Functional Materials in Medicine and Dentistry, University of Würzburg, 97070 Würzburg, Germany*

Matthias Beudert – *Institute of Pharmacy and Food Chemistry, Julius-Maximilians-University Würzburg, 97074 Würzburg, Germany*

Vanessa Flegler – *Cryo-Electron Microscopy, Biocenter and Rudolf Virchow Center, Julius-Maximilians-University Würzburg, 97080 Würzburg, Germany*

Stefan Forster – *Functional Polymer Materials, Chair for Advanced Materials Synthesis, Department of Chemistry and Pharmacy and Bavarian Polymer Institute, Julius-Maximilians-University Würzburg, 97070 Würzburg, Germany*

Alexander Altmann – *Functional Polymer Materials, Chair for Advanced Materials Synthesis, Department of Chemistry and Pharmacy and Bavarian Polymer Institute, Julius-Maximilians-University Würzburg, 97070 Würzburg, Germany*

Fabian Töppke – *Functional Polymer Materials, Chair for Advanced Materials Synthesis, Department of Chemistry and Pharmacy and Bavarian Polymer Institute, Julius-Maximilians-University Würzburg, 97070 Würzburg, Germany*

Karl Fischer – *Physical Chemistry of Polymers, Department of Chemistry, Johannes Gutenberg University Mainz, 55128 Mainz, Germany*

Sebastian Seiffert – *Physical Chemistry of Polymers, Department of Chemistry, Johannes Gutenberg University Mainz, 55128 Mainz, Germany; orcid.org/0000-0002-5152-1207*

Bettina Böttcher – *Cryo-Electron Microscopy, Biocenter and Rudolf Virchow Center, Julius-Maximilians-University Würzburg, 97080 Würzburg, Germany; orcid.org/0000-0002-7962-4849*

Tessa Lühmann – *Institute of Pharmacy and Food Chemistry, Julius-Maximilians-University Würzburg, 97074 Würzburg, Germany; orcid.org/0000-0001-7552-6435*

Complete contact information is available at: <https://pubs.acs.org/doi/10.1021/acsami.9b21282>

Notes

The authors declare the following competing financial interest(s): L.H. and R.L. are listed as inventors on patent applications pertinent to materials described in this contribution.

ACKNOWLEDGMENTS

The authors would like to gratefully acknowledge support by the Deutsche Forschungsgemeinschaft (DFG, German Research Foundation)—project number 326998133—TRR 225 (subproject A03) and project number 398461692, awarded to R.L. Furthermore, we thank the Deutsche Forschungsgemeinschaft for funding the crossbeam scanning electron microscope Zeiss CB 340 (INST 105022/58-1 FUGG) within the DFG State Major Instrumentation Programme. In addition, the authors would like to thank Sami Hietala and Tomasz Jüngst for helpful discussions.

REFERENCES

- (1) Theato, P.; Sumerlin, B. S.; O'Reilly, R. K.; Epps, T. H., III. Stimuli Responsive Materials. *Chem. Soc. Rev.* **2013**, *42*, 7055–7056.
- (2) Wei, M.; Gao, Y.; Li, X.; Serpe, M. J. Stimuli-Responsive Polymers and Their Applications. *Polym. Chem.* **2017**, *8*, 127–143.
- (3) Ahn, S.; Kasi, R. M.; Kim, S.; Sharma, N.; Zhou, Y. Stimuli-Responsive Polymer Gels. *Soft Matter* **2008**, *4*, 1151–1157.
- (4) Echeverria, C.; Fernandes, S. N.; Godinho, M. H.; Borges, J. P.; Soares, P. I. P. Functional Stimuli-Responsive Gels: Hydrogels and Microgels. *Gels* **2018**, *4*, No. 54.
- (5) Seuring, J.; Agarwal, S. Non-Ionic Homo- and Copolymers with H-Donor and H-Acceptor Units with an UCST in Water. *Macromol. Chem. Phys.* **2010**, *211*, 2109–2117.
- (6) Niskanen, J.; Tenhu, H. How to Manipulate the Upper Critical Solution Temperature (UCST)? *Polym. Chem.* **2017**, *8*, 220–232.
- (7) Roth, P. J.; Jochum, F. D.; Theato, P. UCST-Type Behavior of Poly[Oligo(Ethylene Glycol) Methyl Ether Methacrylate] (POEG-MA) in Aliphatic Alcohols: Solvent, Co-Solvent, Molecular Weight, and End Group Dependences. *Soft Matter* **2011**, *7*, 2484–2492.
- (8) Koyama, M.; Hirano, T.; Ohno, K.; Katsumoto, Y. Molecular Understanding of the UCST-Type Phase Separation Behavior of a Stereocontrolled Poly(N-Isopropylacrylamide) in Bis(2-Methoxyethyl) Ether. *J. Phys. Chem. B* **2008**, *112*, 10854–10860.
- (9) Wellingshoff, S.; Shaw, J.; Baer, E. Polymeric Materials from the Gel State. The development of fringed micelle structure in a glass. *Macromolecules* **1979**, *12*, 932–939.
- (10) Ye, H.; Ow, C.; Loh, X. J. A Thixotropic Polyglycerol Sebacate-Based Supramolecular Hydrogel Showing UCST Behavior. *RSC Adv.* **2015**, *5*, 48720–48728.
- (11) Seuyep, N.; Szopinski, D.; Luinstra, G. A.; Theato, P. Post-Polymerization Modification of Reactive Polymers Derived from Vinylcyclopropane: A Poly(Vinylcyclopropane) Derivative with Physical Gelation and UCST Behaviour in Ethanol–Water Mixtures. *Polym. Chem.* **2014**, *5*, 5823–5828.
- (12) Fu, W.; Zhao, B. Thermoreversible Physically Crosslinked Hydrogels from UCST-Type Thermosensitive ABA Linear Triblock Copolymers. *Polym. Chem.* **2016**, *7*, 6980–6991.
- (13) Weber, C.; Hoogenboom, R.; Schubert, U. S. Temperature Responsive Bio-Compatible Polymers Based on Poly(Ethylene Oxide) and Poly(2-Oxazoline)s. *Prog. Polym. Sci.* **2012**, *37*, 686–714.
- (14) Lorson, T.; Lübtow, M. M.; Wegener, E.; Haider, M. S.; Borova, S.; Nahm, D.; Jordan, R.; Sokolski-Papkov, M.; Kabanov, A. V.; Luxenhofer, R. Poly(2-Oxazoline)s Based Biomaterials: A Comprehensive and Critical Update. *Biomaterials* **2018**, *178*, 204–280.
- (15) Luxenhofer, R.; Bezen, M.; Jordan, R. Kinetic Investigations on the Polymerization of 2-Oxazolines Using Pluritriflate Initiators. *Macromol. Rapid Commun.* **2008**, *29*, 1509–1513.
- (16) Zhang, N.; Luxenhofer, R.; Jordan, R. Thermoresponsive Poly(2-Oxazoline) Molecular Brushes by Living Ionic Polymerization: Modulation of the Cloud Point by Random and Block Copolymer Pendant Chains. *Macromol. Chem. Phys.* **2012**, *213*, 1963–1969.
- (17) Guillermin, B.; Monge, S.; Lapinte, V.; Robin, J. How to Modulate the Chemical Structure of Polyoxazolines by Appropriate Functionalization. *Macromol. Chem. Phys.* **2012**, *33*, 1600–1612.
- (18) Verbraeken, B.; Monnery, B. D.; Lava, K.; Hoogenboom, R. The Chemistry of Poly(2-Oxazoline)s. *Eur. Polym. J.* **2017**, *88*, 451–469.
- (19) Hoogenboom, R.; Schlaad, H. Thermoresponsive Poly(2-Oxazoline)s, Polypeptoids, and Polypeptides. *Polym. Chem.* **2017**, *8*, 24–40.
- (20) Konradi, R.; Acikgoz, C.; Textor, M. Polyoxazolines for Nonfouling Surface Coatings — a Direct Comparison to the Gold Standard PEG. *Macromol. Rapid Commun.* **2012**, *33*, 1663–1676.
- (21) Zhang, N.; Pompe, T.; Amin, I.; Luxenhofer, R.; Werner, C.; Jordan, R. Tailored Poly(2-Oxazoline) Polymer Brushes to Control Protein Adsorption and Cell Adhesion. *Macro Biosci.* **2012**, *12*, 926–936.
- (22) Morgese, G.; Trachsel, L.; Romio, M.; Divandari, M.; Ramakrishna, S. N.; Benetti, E. M. Topological Polymer Chemistry Enters Surface Science: Linear Versus Cyclic Polymer Brushes. *Angew. Chem., Int. Ed.* **2016**, *55*, 15583–15588.
- (23) Ryma, M.; Blöbbaum, J.; Singh, R.; Sancho, A.; Matuszak, J.; Cicha, I.; Groll, J. Easy-to-Prepare Coating of Standard Cell Culture Dishes for Cell-Sheet Engineering Using Aqueous Solutions of Poly(2-*n*-Propyl-Oxazoline). *ACS Biomater. Sci. Eng.* **2019**, *5*, 1509–1517.
- (24) Alvaradejo, G. G.; Nguyen, H. V. T.; Harvey, P.; Gallagher, N. M.; Le, D.; Ottaviani, M. F.; Jasanoff, A.; Delaittre, G.; Johnson, J. A. Polyoxazoline-Based Bottlebrush and Brush-Arm Star Polymers Via Romp: Syntheses and Applications as Organic Radical Contrast Agents. *ACS Macro Lett.* **2019**, *8*, 473–478.
- (25) Moreadith, R. W.; Viegas, T. X.; Bentley, M. D.; Harris, J. M.; Fang, Z.; Yoon, K.; Dizman, B.; Weimer, R.; Rae, B. P.; Li, X.; Rader, C.; Standaert, D.; Olanow, W. Clinical Development of a Poly(2-Oxazoline) (Poz) Polymer Therapeutic for the Treatment of Parkinson's Disease—Proof of Concept of Poz as a Versatile Polymer Platform for Drug Development in Multiple Therapeutic Indications. *Eur. Polym. J.* **2017**, *88*, 524–552.
- (26) Simon, L.; Vincent, M.; Le Saux, S.; Lapinte, V.; Marcotte, N.; Morille, M.; Dorandeu, C.; Devoisselle, J. M.; Bégu, S. Polyoxazolines Based Mixed Micelles as PEG Free Formulations for an Effective Quercetin Antioxidant Topical Delivery. *Int. J. Pharm.* **2019**, *570*, No. 118516.
- (27) Hahn, L.; Lübtow, M. M.; Lorson, T.; Schmitt, F.; Appelt-Menzel, A.; Schobert, R.; Luxenhofer, R. Investigating the Influence of Aromatic Moieties on the Formulation of Hydrophobic Natural Products and Drugs in Poly(2-Oxazoline)-Based Amphiphiles. *Biomacromolecules* **2018**, *19*, 3119–3128.
- (28) Lübtow, M. M.; Hahn, L.; Haider, M. S.; Luxenhofer, R. Drug Specificity, Synergy and Antagonism in Ultrahigh Capacity Poly(2-Oxazoline)/Poly(2-Oxazine) Based Formulations. *J. Am. Chem. Soc.* **2017**, *139*, 10980–10983.
- (29) Harris, J. M.; Bentley, M. D.; Moreadith, R. W.; Viegas, T. X.; Fang, Z.; Yoon, K.; Weimer, R.; Dizman, B.; Nordstierna, L. Tuning Drug Release from Polyoxazoline-Drug Conjugates. *Eur. Polym. J.* **2019**, *120*, No. 109241.
- (30) Bloksma, M. M.; Paulus, R. M.; van Kuringen, H. P.; van der Woerd, F.; Lambermont-Thijs, H. M.; Schubert, U. S.; Hoogenboom, R. Thermoresponsive Poly(2-Oxazine)s. *Macromol. Rapid Commun.* **2012**, *33*, 92–96.
- (31) Zahoranová, A.; Mrlik, M.; Tomanová, K.; Kronek, J.; Luxenhofer, R. ABA and BAB Triblock Copolymers Based on 2-Methyl-2-Oxazoline and 2-*n*-Propyl-2-Oxazoline: Synthesis and Thermoresponsive Behavior in Water. *Macromol. Chem. Phys.* **2017**, *218*, No. 1700031.
- (32) Lorson, T.; Jaksch, S.; Lübtow, M. M.; Jungst, T.; Groll, J.; Luhmann, T.; Luxenhofer, R. A Thermogelling Supramolecular Hydrogel with Sponge-Like Morphology as a Cytocompatible Bioink. *Biomacromolecules* **2017**, *18*, 2161–2171.
- (33) Monnery, B. D.; Hoogenboom, R. Thermoresponsive Hydrogels Formed by Poly(2-Oxazoline) Triblock Copolymers. *Polym. Chem.* **2019**, *10*, 3480–3487.
- (34) Lübtow, M. M.; Mrlik, M.; Hahn, L.; Altmann, A.; Beudert, M.; Lühmann, T.; Luxenhofer, R. Temperature-Dependent Rheological and Viscoelastic Investigation of a Poly(2-Methyl-2-Oxazoline)-*b*-Poly(2-Iso-Butyl-2-Oxazoline)-*b*-Poly(2-Methyl-2-Oxazoline)-Based Thermogelling Hydrogel. *J. Funct. Biomater.* **2019**, *10*, No. 36.
- (35) Hoogenboom, R.; Lambermont-Thijs, H. M. L.; Jochems, M. J. H. C.; Hoepfener, S.; Guerlain, C.; Fustin, C.-A.; Gohy, J.-F.; Schubert, U. S. A Schizophrenic Gradient Copolymer: Switching and Reversing Poly(2-Oxazoline) Micelles Based on UCST and Subtle Solvent Changes. *Soft Matter* **2009**, *5*, 3590–3592.
- (36) He, Z.; Wan, X.; Schulz, A.; Bludau, H.; Dobrovolskaia, M. A.; Stern, S. T.; Montgomery, S. A.; Yuan, H.; Li, Z.; Alakhova, D.; Sokolsky, M.; Darr, D. B.; Perou, C. M.; Jordan, R.; Luxenhofer, R.; Kabanov, A. V. A High Capacity Polymeric Micelle of Paclitaxel:

Implication of High Dose Drug Therapy to Safety and In vivo Anti-Cancer Activity. *Biomaterials* **2016**, *101*, 296–309.

(37) Luxenhofer, R.; Schulz, A.; Roques, C.; Li, S.; Bronich, T. K.; Batrakova, E. V.; Jordan, R.; Kabanov, A. V. Doubly Amphiphilic Poly(2-Oxazoline)s as High-Capacity Delivery Systems for Hydrophobic Drugs. *Biomaterials* **2010**, *31*, 4972–4979.

(38) Seo, Y.; Schulz, A.; Han, Y.; He, Z.; Bludau, H.; Wan, X.; Tong, J.; Bronich, T. K.; Sokolsky, M.; Luxenhofer, R.; Jordan, R.; Kabanov, A. V. Poly(2-Oxazoline) Block Copolymer Based Formulations of Taxanes: Effect of Copolymer and Drug Structure, Concentration, and Environmental Factors. *Polym. Adv. Technol.* **2015**, *26*, 837–850.

(39) Pöppler, A. C.; Lübtow, M. M.; Schlauersbach, J.; Wiest, J.; Meinel, L.; Luxenhofer, R. Loading-Dependent Structural Model of Polymeric Micelles Encapsulating Curcumin by Solid-State NMR Spectroscopy. *Angew. Chem., Int. Ed.* **2019**, *58*, 18540–18546.

(40) Lübtow, M. M.; Marciniak, H.; Schmiedel, A.; Roos, M.; Lambert, C.; Luxenhofer, R. Ultra-High to Ultra-Low Drug-Loaded Micelles: Probing Host–Guest Interactions by Fluorescence Spectroscopy. *Chem. - Eur. J.* **2019**, *25*, 12601–12610.

(41) Witte, H.; Seeliger, W. Simple Synthesis of 2-Substituted 2-Oxazolines and 5,6-Dihydro-4h-1,3-Oxazines. *Angew. Chem., Int. Ed.* **1972**, *11*, 287–288.

(42) Luxenhofer, R. Polymers and Nanomedicine: Considerations on Variability and Reproducibility When Combining Complex Systems. *Nanomedicine* **2015**, *10*, 3109–3119.

(43) Paxton, N.; Smolan, W.; Böck, T.; Melchels, F.; Groll, J.; Jungst, T. Proposal to Assess Printability of Bioinks for Extrusion-Based Bioprinting and Evaluation of Rheological Properties Governing Bioprintability. *Biofabrication* **2017**, *9*, No. 044107.

(44) Harrass, K.; Krüger, R.; Möller, M.; Albrecht, K.; Groll, J. Mechanically Strong Hydrogels with Reversible Behaviour under Cyclic Compression with MPA Loading. *Soft Matter* **2013**, *9*, 2869–2877.

(45) Craig, S.; Beaton, C. D. A Simple Cryo-Sem Method for Delicate Plant Tissues. *J. Microsc.* **1996**, *182*, 102–105.

(46) Issman, L.; Talmon, Y. Cryo-Sem Specimen Preparation under Controlled Temperature and Concentration Conditions. *J. Microsc.* **2012**, *246*, 60–69.

(47) Walther, P. Recent Progress in Freeze-Fracturing of High-Pressure Frozen Samples. *J. Microsc.* **2003**, *212*, 34–43.

(48) Axpe, E.; Oyen, M. L. Applications of Alginate-Based Bioinks in 3D Bioprinting. *Int. J. Mol. Sci.* **2016**, *17*, No. 1976.

(49) He, Y.; Yang, F.; Zhao, H.; Gao, Q.; Xia, B.; Fu, J. Research on the Printability of Hydrogels in 3D Bioprinting. *Sci. Rep.* **2016**, *6*, No. 29977.

(50) Freeman, F. E.; Kelly, D. J. Tuning Alginate Bioink Stiffness and Composition for Controlled Growth Factor Delivery and to Spatially Direct Msc Fate within Bioprinted Tissues. *Sci. Rep.* **2017**, *7*, No. 17042.

(51) Li, Z.; Huang, S.; Liu, Y.; Yao, B.; Hu, T.; Shi, H.; Xie, J.; Fu, X. Tuning Alginate-Gelatin Bioink Properties by Varying Solvent and Their Impact on Stem Cell Behavior. *Sci. Rep.* **2018**, *8*, No. 8020.

(52) Habib, A.; Sathish, V.; Mallik, S.; Khoda, B. 3D Printability of Alginate-Carboxymethyl Cellulose Hydrogel. *Materials* **2018**, *11*, No. 454.

(53) Ahlfeld, T.; Cidonio, G.; Kilian, D.; Duin, S.; Akkineni, A. R.; Dawson, J. I.; Yang, S.; Lode, A.; Oreffo, R. O. C.; Gelinsky, M. Development of a Clay Based Bioink for 3D Cell Printing for Skeletal Application. *Biofabrication* **2017**, *9*, No. 034103.

(54) Narayanan, L. K.; Huebner, P.; Fisher, M. B.; Spang, J. T.; Starly, B.; Shirwaiker, R. A. 3D-Bioprinting of Poly(lactic Acid) (PLA) Nanofiber–Alginate Hydrogel Bioink Containing Human Adipose-Derived Stem Cells. *ACS Biomater. Sci. Eng.* **2016**, *2*, 1732–1742.

Unravelling a novel mechanism in polymer self-assemblies: An order-order transition based on molecular interactions between hydrophilic and hydrophobic polymer blocks

* This contribution is dedicated to the late Françoise Winnik

Lukas Hahn¹, Theresa Zorn², Josef Kehrein³, Tobias Kielholz⁴, Anna-Lena Ziegler¹, Stefan Forster¹, Benedikt Sochor⁵, Ekaterina S. Lisitsyna⁶, Nikita A. Durandin⁶, Timo Laaksonen,^{6,7} Vladimir Aseyev⁸, Christoph Sotriffer³, Maike Windbergs⁴, Ann-Christin Pöppler,^{2,} and Robert Luxenhofer^{1, 8,*}*

¹Functional Polymer Materials, Chair for Advanced Materials Synthesis, Institute for Functional Materials and Biofabrication, Department of Chemistry and Pharmacy, Julius-Maximilians-University Würzburg, Röntgenring 11, 97070 Würzburg, Germany

²Institute of Organic Chemistry, Department of Chemistry and Pharmacy, Julius-Maximilians-University Würzburg, Am Hubland, 97074 Würzburg, Germany

³Institute of Pharmacy and Food Chemistry, Department of Chemistry and Pharmacy, Julius-Maximilians-University Würzburg, Am Hubland, 97074 Würzburg, Germany

⁴Institute of Pharmaceutical Technology and Buchmann Institute for Molecular Life Sciences, Goethe University Frankfurt, Max-von-Laue-Str. 15, 60438 Frankfurt am Main, Germany

⁵Chair for X-Ray Microscopy, Julius-Maximilians-University Würzburg, Josef-Martin-Weg 63, 97074 Würzburg, Germany

⁶Faculty of Engineering and Natural Science, Tampere University, Korkeakoulunkatu 8, 33720 Tampere, Finland

⁷Division of Pharmaceutical Biosciences, Faculty of Pharmacy, University of Helsinki, Viikinkaari 5 E, 00014 Helsinki, Finland

⁸Soft Matter Chemistry, Department of Chemistry, and Helsinki Institute of Sustainability Science, Faculty of Science, Helsinki University, 00014 Helsinki, Finland

*correspondence to: robert.luxenhofer@helsinki.fi, ann-christin.poeppler@uni-wuerzburg.de

Keywords: Inverse gelation, poly(2-oxazoline), poly(2-oxazine), aromatic moieties, worm-to-sphere transition

Abstract

Thermoresponsive hydrogel formation upon cooling in aqueous media is rarely described for synthetic polymers in the literature. However, if the sol-gel transition occurs in the physiologically relevant range (0-40 °C), there are many possible applications in areas such as drug delivery and biofabrication. Here, we describe a new mechanism of a thermally induced order-order transition in polymer self-assembly of an ABA triblock consisting of hydrophilic A blocks and a hydrophobic aromatic B block. Small-angle X-ray scattering confirmed worm-to-sphere transition upon heating on the nanoscale level while wide-angle X-ray scattering indicated a more uniform ordering of the macromolecular chains on the scale of 4-7 Å. NMR spectroscopy showed reduced mobility of various polymer segments in the hydrogel state, especially in the hydrophobic aromatic region. More importantly however, solution and solid-state NMR investigations also revealed close proximity of hydrophobic and hydrophilic repeat units in the gel state, which is less pronounced in the sol state. This interaction between the hydrophilic and hydrophobic block is responsible for the order-order transition and *–ipso facto–* inverse thermogelation. This unusual interaction is supported *in silico* by molecular dynamics modeling. Changes in the structure of the hydrophilic A blocks can be used to tune the gel strength, persistence, and gelation kinetics. This order-order transition based on unexpected and previously not described interactions between the hydrophilic and the hydrophobic repeat units opens new avenues to control and design macromolecular self-assembly.

Introduction

Thermoresponsive phase separation of polymer solutions upon heating is an entropic effect and widely discussed in literature.¹ Polymers displaying a lower critical solution temperature (LCST) are structurally diverse and can be found in the families of poly(ether)s, poly(acrylamide)s, poly(2-oxazoline)s and many others. In contrast, examples of UCST (upper critical solution temperature) type phase separation are more rarely found, especially for UCST in purely aqueous media.^{2,3} Such systems are discussed for different applications as smart biomaterials if the transition takes place at or around physiological temperatures and in physiological media. In some cases, physical hydrogel formation (sol-gel transition) can be observed instead of precipitation (coil-globule transition) due to changing aggregation patterns. Block copolymers with thermogelling properties are well-known in literature,^{4,5} with Pluronic® F127 being arguably the most prominent example.⁶ Mostly, thermogelation relies on a thermally triggered disorder-order transition from random coils to polymer micelles forming dense colloidal packings.⁷ In contrast, Armes and co-workers described a thermogelling system based on an interesting and unusual heating induced worm-to-sphere order-order transition,⁸ which could be tuned with respect to the critical gelation temperature.⁹ Later, Penfold et al. described a pH- and thermosensitive system that combined pH-responsive vesicle-to-worm transition and thermosensitive worm-to-sphere transition.¹⁰ More recently, a thermoresponsive poly(*N*-(2-hydroxypropyl)methacrylamide)-poly(2-hydroxypropyl)methacrylate diblock copolymer was described, which formed spheres (4 °C, weakly turbid free flowing fluid), worms (22 °C, turbid free standing gel) or vesicles (50 °C, milky-white free flowing dispersion) in aqueous solution.¹¹

Very recently, we described a cooling induced and reversible sphere-to-worm and concurrent sol-gel transition in aqueous solution (Figure 1).¹² A ABA-type block copolymer amphiphile poly(2-methyl-2-oxazoline)-*b*-poly(2-phenyl-2-oxazine)-*b*-poly(2-methyl-2-oxazoline) (pMeOx-*b*-pPheOzi-*b*-pMeOx=A-pPheOzi-A) featuring the novel aromatic PheOzi repeat unit. At 5 °C, the polymer exhibited long interconnected worm-like aggregates, which transformed into small, uniform and spherical polymer micelles upon heating. The temperature, at which the system liquified and its viscosity decreased

several orders of magnitude was 32 °C. While inverse thermoreversible gelation is well known for bio- or bioderived polymers such as agarose or gelatin, there are only few synthetic systems described in the literature.² Arguably best known is poly(N-acryloyl glycinamide) (PNAGA), already described by Haas et al. in 1967.¹³ Fu and Zhao reported gels that form upon cooling of aqueous solutions of various poly(acrylamide-co-acrylonitrile)-b-poly(poly(ethylene glycol) methyl ether methacrylate)-b-poly(acrylamide-co-acrylonitrile) (P(AAm-co-AN)-b-PPEGMMA-b-P(AAm-co-AN))¹⁴ as well as UCST-type nanogels.¹⁵ In addition, Lele and co-workers described hydrophobically modified copolymers that undergo inverse thermogelation.¹⁶ All these known systems have in common that intermolecular and intramolecular hydrogen bonding between polymer repeat units can occur, which is indeed the main driving force for the UCST phenomenon in general. In stark contrast, A-pPheOzi-A cannot undergo such hydrogen bonding between repeat units and neither pMeOx nor pPheOzi are thermoresponsive *per se*. In addition, we believe A-pPheOzi-A is the first example of a cooling induced sphere-to-worm transition. Therefore, the question is: what is the mechanism of this order-order and concomitant inverse thermogelation? Using a variety of state-of-the-art analytic tools complemented by molecular modeling, we aimed to elucidate the molecular origins of this novel gelation mechanism in detail. We found that the order-order transition in self-assembly is based on a previously undescribed interaction between the hydrophilic MeOx repeat units and the hydrophobic, aromatic PheOzi repeat units, leading to a compaction of the former onto the latter, which in turn leads to the sphere-to-worm morphology transition as the packing parameter increases. Testing this suggested mechanism, variation of the hydrophilic repeat units could be successfully used to tune the gelation behavior.

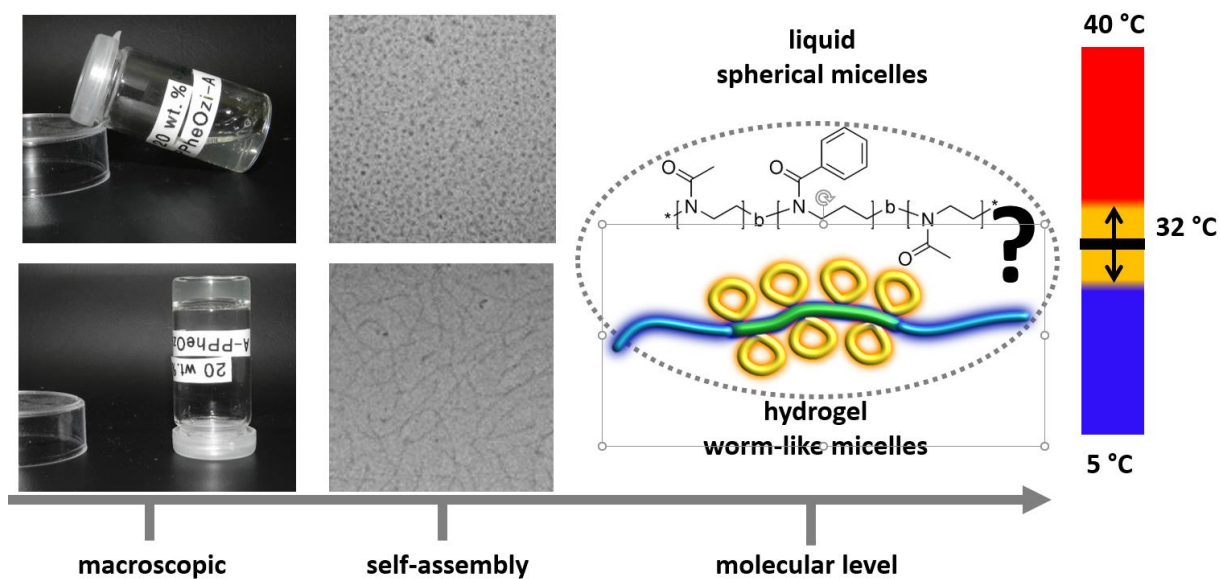


Figure 1| Summary of the study. The polymer amphiphile poly(2-methyl-2-oxazoline)-*b*-poly(2-phenyl-2-oxazine)-*b*-poly(2-methyl-2-oxazoline) (pMeOx-*b*-pPheOzi-*b*-pMeOx = A-PPheOzi-A = A-B-A) showed unique inverse thermogelling properties.¹² In the liquid state, the polymer self-assembled into spherical micelles. Upon cooling an order-order transition into worm-like micelles was observed. (TEM images reprinted with permission from reference [12]). In this study a detailed elucidation of the order-order transition is presented with the focus on polymer interactions on a molecular level. The color code on the right is used throughout this study to highlight the samples macroscopic state.

Materials and Methods

All chemicals and reagents were used from Sigma-Aldrich (Steinheim, Germany) or TCI-chemicals (Eschborn, Germany) and were used as received unless otherwise mentioned. The polymer pMeOx-*b*-pPheOzi-*b*-pMeOx (= A-pPheOzi-A) was prepared and used as described previously.²² The monomers 2-ethyl-2-oxazoline (EtOx) and 2-methyl-2-oxazine (MeOzi) were synthesized like described by Witte and Seeliger.¹⁷ Deuterated dichloromethane (d₂DCM) and D₂O as NMR solvent were obtained from Deutero GmbH (Kastellaun, Germany). Methyl trifluoromethylsulfonate (MeOTf), EtOx, MeOzi and PheOzi were refluxed over CaH₂ for several hours and distilled under reduced pressure. Benzonitrile (PhCN) was dried over phosphorus pentoxide.

Dynamic light scattering

Dynamic light scattering (DLS) experiments were performed using an ALV CGS-3 multi detection goniometry-system (Langen, Germany) equipped with a He-Ne-laser (632.8 nm) and 8 optical avalanche photodiodes-detector with an angular detector spacing of 16 ° (correlation time 45 s, 3 runs). Scattering angles between 20 ° and 147 ° were measured in 4 angle sets (4x8 detectors) and a 5 ° angle interval for each detector at 15 °C and 40 °C. Prior to each measurement, samples were filtered in dust-free cuvettes using Millex-LG 0.2 µm filters under laminar flow. The polymer concentration was 0.1 g/L (2 mM aqueous NaNO₃). All samples were stored at the measurement temperature for 24 h. The decay of the electric field-time autocorrelation function (ACF) was fitted using triexponential fit functions (equation 1) like described previously:¹⁸

$$g_1(t) = a_1 \cdot e\left(\frac{-t}{\tau_1}\right) + a_2 \cdot e\left(\frac{-t}{\tau_2}\right) + a_3 \cdot e\left(\frac{-t}{\tau_3}\right) \quad (1)$$

with the amplitudes a_i and the decay times $\tau_i = \frac{1}{q^2 \cdot D_i}$, where q is the absolute value of the scattering vector. In the case of polydispersity, the translational diffusion coefficient D was obtained by extrapolation to zero angle and in the limit of high dilution given by

$$\langle D \rangle_z^{-1} = \frac{\sum_i a_i}{\sum_i a_i \cdot D_i^{-1}} \quad (2)$$

Using the Stokes-Einstein equation the (apparent) hydrodynamic radius R_h was obtained by

$$R_h = \frac{k_B \cdot T}{6 \cdot \pi \cdot \eta \cdot D} \quad (3)$$

with k_B being the Boltzmann constant, η is the viscosity of the solvent and T the temperature (15 °C or 40 °C).

Small- and wide-angle X-ray scattering (SAXS, WAXS)

SAXS and WAXS experiments were carried out using an in-house setup, which was built by Fraunhofer EZRT (Fürth, Germany). It consists of a MicroMax-007 HF X-ray source (Rigaku, Japan) and a Eiger R 1M detector unit (Dectris, Switzerland). The sample-detector distance can be varied between 5 cm and 3.5 m, which corresponds to possible Q-values between 0.005 and 5 Å⁻¹. The complete setup is operated in a vacuum below 0.1 mbar to reduce air scattering. The sample solutions were placed in quartz capillaries (inner diameter: 1 mm, wall thickness: 10 µm) (Hampton Research, Aliso Viejo, California), which were positioned perpendicularly to the X-ray beam. The presented experiments were done at sample-detector distances of 57 mm, 565 mm and 1560 mm with an integration time of 15 min for the shortest distance and 240 min for the two longer configurations. All distances were calibrated using a silver behenate standard sample. For each sample, data was acquired for different temperatures between 5 °C – 50 °C. To achieve thermal equilibrium, the sample (10 wt.% aqueous solution) was kept at the desired temperature for 15 min prior to each measurement. The SAXS data, which was obtained at the two largest distances, was calibrated in terms of absolute intensities using glassy carbon as a secondary calibration standard.^{19, 20} The scattering curves of the hydrogels were obtained by azimuthal integration taking the samples thickness, X-ray transmission, detector accuracy, setup geometry and solvent scattering into account following the standard procedures described in literature.²¹

Temperature dependent nuclear magnetic resonance (NMR) experiments in solution

All experiments in solution were performed at a Bruker Avance III HD 600 spectrometer (Karlsruhe, Germany) operating at 600.4 MHz equipped with a BBFO 5 mm probe using a BCU-02 temperature control unit. ¹H NMR experiments of a 20 wt.% A-pPheOzi₁₅-A sample in D₂O were acquired with a 30 ° flip angle and 8 or 16 scans without sample spinning. A series of variable temperature experiments

was performed in the range from 2 °C to 39.15 °C in a step size of 3 to 5 °C. The sample was kept at the desired temperature for 10 minutes prior to each measurement. Temperature calibration was done using 4 % MeOH in MeOD and 80 % ethylene glycol in DMSO-d₆. All recorded spectra were referenced using the temperature dependent HDO signal. For quantitative characterization of the temperature induced phase transition the fraction p was calculated with the integrals $I(T)$ and $I(T_0)$ at the respective temperatures T and T_0 using the following equation:²²

$$p = 1 - \frac{I(T)}{I(T_0) * \frac{T_0}{T}} \quad (3)$$

The highest signal intensity was measured at 39.15 °C (T_0). Reductions of signal intensities are indicated by $p < 0$. 2D ¹H-¹H nuclear Overhauser effect NMR spectroscopy (NOESY) experiments at 5 °C and 40 °C were recorded using the noesygpphpp pulse sequence (scans: 32, t_1 increments: 256, relaxation delay: 2.5 s). To ensure discrimination between cross-relaxation and spin-diffusion different mixing times (40 μs, 60 μs, 80 μs, 150 μs and 250 μs) were used. For better visualization of the aromatic region, phase and baseline correction of 2D data was confined to the range of 6-8 ppm and TDeff was set to 2867 in the f2 dimension. Additionally, 1D slices of relevant aromatic regions were extracted. ¹H spin-lattice relaxation times T1 were measured with the inversion recovery pulse sequence t1ir at 5 °C and 40 °C. For measuring the T1 relaxation times of HDO a variable delay from 1-50 s in 12 steps was used with a relaxation delay of 50.0 s. T1 relaxation times of polymer signals were recorded with a variable delay from 0.001-5.0 s in 16 steps and a relaxation delay of 5.0 s. The normalized decay curves for different polymer segments and the HDO signal were fitted using monoexponential fit functions.

Solid-state nuclear magnetic resonance

Solid-state NMR (ssNMR) measurements were performed using a 4 mm double-channel Bruker probe at 9.4 T using between 3 and 5.3 kHz magic angle spinning (MAS). The hydrogel sample was cooled to 273 K prior to measurement. For the ¹³C CP MAS experiment, a 2 ms ramp (50 to 100 %) on the ¹H channel was used during the cross-polarization (CP) contact time for all samples. ¹³C NMR spectra with direct excitation were recorded with short interscan delays of 1 s to probe mobile components. For

heteronuclear decoupling during acquisition, SPINAL64 was employed with a 100 kHz nutation frequency (^1H). The chemical shifts were referenced using adamantane (left signal at 38.48 ppm) by subsequent adjustment of the magnetic field.

Raman spectroscopy

The Raman spectra were recorded on an alpha 300R⁺ confocal Raman microscope from WITec GmbH (Ulm, Germany) equipped with a 50x objective (NA 0.8, Epiplan Neofluar, Zeiss, Germany) and a 532 nm laser (39.4 mW). A 20 wt.% sample was measured after equilibration at 5 °C and 40 °C using a temperature controllable Peltier stage (LTS 120, Linkam Scientific Instruments Ltd., Tadworth, UK). Spectra are shown as average spectrum of 3 spectra at different locations on the same sample, which were recorded with an integration time of 5 s and 10 accumulations. The resulting data were processed with cosmic ray removal and background subtraction. The bulk water signals at 3100 cm^{-1} - 3700 cm^{-1} were fitted using a Gaussian deconvolution method as described elsewhere.^{23, 24}

Fluorescence spectroscopy

The amphiphilic fluorescence probe 2-(4-(dimethylamino)styryl)-1-methylpyridinium iodide (Daspmi) was purchased from Molecular Probes Inc., Life Technologies. The hydrophobic probe 4,4'-difluoro-4-bora-3a,4a-diaza-s-indacene meso-substituted with para-dodecylphenyl (BPC12) was synthesized like described in previous studies.²⁵ Gibco™ Dulbecco's phosphate-buffered saline (DPBS) pH 7.25 was purchased from Thermo Fisher Scientific (Massachusetts, USA). The steady-state fluorescence spectra of Daspmi (5 μM) and BPC12 (5 μM) in aqueous sol and gel samples at a polymer concentration of 20 wt.% were recorded at different temperatures on a FLS-1000 spectrofluorometer (Edinburgh Instruments, UK) equipped with a thermocontrolled cuvette holder ($\lambda_{\text{exc.}}$ (Daspmi): 460 nm, $\lambda_{\text{exc.}}$ (BPC12): 490 nm) comparing the wavelength shift of emission maximum. Fluorescence intensity decay curves were obtained using a time-correlated single photon counting (TCSPC) system (PicoQuant GmbH) equipped with a temperature controlling cuvette holder using quartz cuvettes as described earlier ($\lambda_{\text{exc.}}$: 483 nm, cutoff filter > 490 nm).²⁶ Monitoring wavelengths were 580 nm for Daspmi and 520 nm for BPC12. The fluorescence decays were deconvoluted with the instrumental response to give

the fluorescence lifetime with a resolution of approximately 100 ps. The obtained lifetimes were used for calculating microviscosity values at different temperatures (5 °C, 12 °C, 22 °C and 37 °C) using following equation:

$$\log \tau_f = \log \frac{z}{k_r} + \alpha \log \eta \quad (4)$$

where τ_f is the fluorescence lifetime of Daspmi or BPC12³² in the solution of a known viscosity η , k_r is the radiative rate constant, and z and α are constants. The linear part of the $\log \tau_f$ as a function of $\log \eta$ plot was taken as a calibration function to calculate microviscosity values (Figure S3). The viscosities of different water/glycerol mixtures (80-100 wt.% of glycerol) at different temperatures were determined using a LOVIS 2000M rolling ball microviscosimeter from Anton Paar (Graz, Austria) with a LOVIS 1.8 capillary and a steel ball of 1.5 mm diameter. Prior to viscosity measurements, the density of the sample at the specific temperature was recorded using a DMA 4100M density meter from Anton Paar (Graz, Austria). For the corresponding lifetime measurements a concentration of 5 μ M of Daspmi and BPC12 were used.

Micro calorimetry (μ CAL)

Micro calorimetry measurements were conducted with a Malvern MicroCal PEAQ-DSC microcalorimeter. The heat of the sample was measured relative to pure water and the enthalpy values were normalized to the molar concentration of the aromatic repeat units. After complete dissolution, the samples were stored in the refrigerator at 4 °C for about 48 h, degassed at 5 °C, transferred to the instrument precooled at 2 °C or 10 °C, and kept at the temperature for different times, as indicated, prior to heating. Each sample was heated with the rate of 1 °C/min to 100 °C, after which they were cooled again to the starting temperature with the same rate.

Molecular modeling

We modeled a system containing eight Me-pMeOx₃₅-b-pPheOzi₁₅-b-pMeOx₃₅-EIP polymers (Me = methyl group, EIP = ethyl isonipecotate), in which the hydrophobic pPheOzi blocks faced each other to

form a single inner strand along the Z axis and the hydrophilic pMeOx blocks were bent outwards. Four individual molecules made up the strand and were subsequently duplicated and moved next to the original polymers along the Z axis, ultimately resulting in two layers of polymers in our simulation box. The stretched out, hydrophilic pMeOx blocks were subjected to an energy minimization and a short, 50 ps long simulation with the Noisé-Poincaré-Andersen method^{27,28} (applying the Amber14:EHT force field^{29,30} with the R-field implicit solvation model³¹) to yield a more compact starting conformation, while keeping the inner strand in a straight orientation. Figure S6A depicts the prepared structure. All modeling was performed with MOE (Molecular Operating Environment 2019.01).³² The setup was inspired by previous modeling studies regarding worm-like micelles of small molecules, in which the generation of a continuous micelle was also achieved via initial placement of hydrophobic parts in the inner and hydrophilic moieties in the outer regions of the threadlike structure, which was aligned along one axis of the simulation box.³³⁻³⁵ RESP partial charges³⁶ of single monomers used as building blocks were derived from calculations with Gaussian 09 Rev. C.01³⁷ (Hartree-Fock level of theory, 6-31G* basis set); parameters based on the Amber14ffSB²⁹ and GAFF2³⁸ force fields were assigned via antechamber and parmchk2 of AmberTools18.³⁹ During charge derivation monomer structures were capped with residues of the same type (except for the terminal groups, Me-MeOx and EIP, which were capped with a MeOx monomer). The calculated parameters were used to generate a polymer with an initial straight conformation using tleap.³⁹

Subsequent solvation of the starting structure with TIP3P water⁴⁰ in a simulation box with a minimum border-to-polymer distance of 20 Å in the X and Y directions resulted in a system size of approximately 16 x 18 x 10 nm³ with 76,730 solvent molecules. Water molecules found inside the inner hydrophobic strand after this initial placement were removed if the distance to the pPheOxi blocks was less than 10 Å. Periodic boundary conditions with minimum image convention were applied during the simulation, which allowed for an infinitely sized worm-like micelle along the Z axis and ensured a sufficient distance between polymers of neighboring boxes along the X and Y dimensions. The simulation was performed using NAMD 2.13⁴¹ with 2 fs time steps. An initial energy minimization of 10,000 steps was conducted before slowly heating the system from 100 K to 278 K over the course of 500 ps. Harmonic constraints

were initially applied on all polymers and gradually reduced over an additional 1.6 ns, allowing a rapid reordering of solvent molecules around the polymers. Langevin dynamics and the Nosé-Hoover Langevin piston method (1 atm) were used for temperature and pressure control in an NPT ensemble. After another 2 ns of equilibration, the production run was performed for 600 ns. Semi-isotropic coupling allowed for fluctuations along the Z axis, independent from the X and Y axes. The particle mesh Ewald method⁴² with a cutoff of 1.2 nm was applied and coordinates were saved every 10 ps. Subsequent analyses were performed using cpptraj⁴³ and images were generated with VMD 1.9.3⁴⁴ and PyMOL 2.4.1.⁴⁵ Average densities for polymer groups around PheOzi monomers were retrieved as follows: All PheOzi residues were iteratively aligned onto the same monomer. Next, binned occupancy histograms of different moieties around the center of the aligned residue were calculated for the last 100 ns using the grid command in cpptraj. This was performed on a 1.6 x 1.6 x 1.6 nm³ grid with a 1 Å resolution. After this procedure, the obtained values around each PheOzi monomer were added up at each grid element and divided by the number of analyzed frames (10,000) and monomers (104). Thus, densities represent the average amount of atoms of interest found at each grid element per frame around a single monomer. The first and last PheOzi monomer of each pPheOzi block (16 out of 120) were excluded from this calculation, as these are always situated near the neighboring MeOx residues. Additionally, we analyzed several distances between these PheOzi monomers and the other polymer residues, as well as the angle ω between the plane of nearby amide (N-(C=O)-C) groups and the phenyl ring plane for every 10 ps of the last 100 ns.

Rheology

All experiments were performed using an Anton Paar (Ostfildern, Germany) Physica MCR 301 system utilizing a plate-plate geometry (25 mm diameter) equipped with a solvent trap and Peltier element for temperature adjustment. All aqueous 15 wt.% samples were dissolved at room temperature stirring constantly and incubated at 5 °C for 48 h. In addition, pictures were taken to visualize the gels. A temperature-sweep was performed in oscillation mode from 5-50 °C (heating rate: 0.05 °C/s) using

a fixed amplitude of 0.1 % and angular frequency of 10 rad/s. The long-time gelation experiment at 5 °C was performed at an amplitude of 0.1 % and an angular frequency of 10 rad/s for several hours.

Polymer synthesis

To investigate the influence of the hydrophilic block on the gelation mechanism the polymers Me-pEtOx₃₅-*b*-pPheOzi₁₅-*b*-pEtOx₃₅-EIP and Me-pMeOzi₃₅-*b*-pPheOzi₁₅-*b*-pMeOzi₃₅-PipBoc were synthesized as described several times using MeOTf as initiator and ethyl isonipecotate (EIP) or 1-Boc-piperazine (PipBoc) as terminating agent, respectively.¹² (Detailed characterization of the novel ABA type amphiphiles in SI).

For standard analytics of the synthesized polymer, NMR spectra were recorded on a Bruker Fourier 300 (¹H: 300.12 MHz) spectrometer at 298 K from Bruker BioSpin (Rheinstetten, Germany) and calibrated using the solvent signal of d₂DCM.

Gel permeation chromatography

Gel permeation chromatography (GPC) was performed on a Polymer Standard Service PSS (Mainz, Germany) system. Specifications: pump mod. 1260 infinity, MDS RI-detector mod. 1260 infinity (Agilent Technologies, Santa Clara, California, USA), precolumn: 50 x 8 mm PSS PFG linear M; 2 columns: 300 x 8 mm PSS PFG linear M (particle size 7 µm; pore size 0.1 – 1.000 kg/mol) with hexafluoroisopropanol (HFIP, containing 3 g/L potassium trifluoroacetate (KTFA)) as eluent calibrated with PEG standards (molar masses from 0.1 kg/mol to 1000 kg/mol). The columns were held at 40 °C and the flow rate was set to 0.7 mL/min. Dried polymer powders were dissolved in eluent and filtered through 0.2 µm PTFE filters (Rotilabo, Karlsruhe, Germany).

Differential Scanning Calorimetry (DSC)

All measurements were performed using aluminum crucibles on a calibrated DS 204 F1 Phoenix system from NETZSCH (Selb, Germany) equipped with a CC200 F1 controller unit from -50 °C to 200 °C with

three heating and two cooling phases and a cooling rate of 10 °C/min. The third heating cycle was used to analyze the glass transition temperature of dried polymer powders.

Transmission electron microscopy

For transmission electron microscopy (TEM) experiments, the polymers were dissolved in DI water to a final concentration of 20 g L⁻¹ and stored at room temperature. 400 mesh copper–rhodium grids (maxtaform) with a homemade carbon layer were glow discharged in air for 1.5 min at medium power in a Harrick PDC-002 plasma cleaner. The 20 g L⁻¹ sample was diluted (1/125 or 1/625) and 8 μL were incubated on the grids for 1 min before blotting (Whatman filter paper No. 50). The grids were washed with water (three times) and 2% w/v uranyl acetate (three times). After the last dose of uranyl acetate was applied, the grid was left to incubate for 5 minutes before blotting. A single-tilt room temperature holder in an FEI Tecnai G2 Spirit TWIN transmission electron microscope equipped with a tungsten emitter at 120 kV was used. Images were recorded with an Eagle CCD camera under low-dose conditions. The micrographs were binned two times resulting in a pixel size of 2.2 Å per pixel at specimen level.

Results and Discussion

As previously evidenced by *cryo*TEM investigations, the amphiphile pMeOx-*b*-pPheOzi-*b*-pMeOx reversibly forms worm-like micelles in aqueous media upon cooling.¹² However, these images were recorded at dilute, non-gelling concentrations ($c_{\text{gel}} \approx 5$ wt.%). To confirm that this order-order transition also occurs at higher concentrations, we conducted temperature dependent small-angle X-ray scattering (SAXS) at above c_{gel} (10 wt.%).

The intensity I as a function of Q from the SAXS measurements was plotted for different temperatures. In the hydrogel state (5 °C), a pronounced structure peak (supporting information, Figure 2A, blue) is followed by two clearly defined regions with different slopes at intermediate and high Q -values, which can be assigned to different self-assembled species. Using a power-law expression⁴⁶, the different

slopes can be determined, indicating the presence of spherical micelles and worm-like micelles in the gel state. Above T_{gel} , the worm-like micelles disappear, confirming that the order-order transition found at low concentration also occurs at higher concentration. In addition, the structure peak is shifted towards higher Q-values indicating a lower particle/particle distance in the sol state due to the formation of small spherical micelles (supporting information, Figure 2A, vertical lines). This is a logical consequence of the disintegration of relatively few worm-micelles into much more numerous spherical micelles. The extrapolation of the absolute intensity I to Q_0 (supporting information, Figure S1, horizontal lines) was used as a measure for relative mean particle size, corroborating once more larger particles in gel state (worm-like micelles) in comparison to the sol state (spherical micelles). The qualitative analysis of the SAXS scattering profiles is summarized in more detail in the supporting information (Table S1).

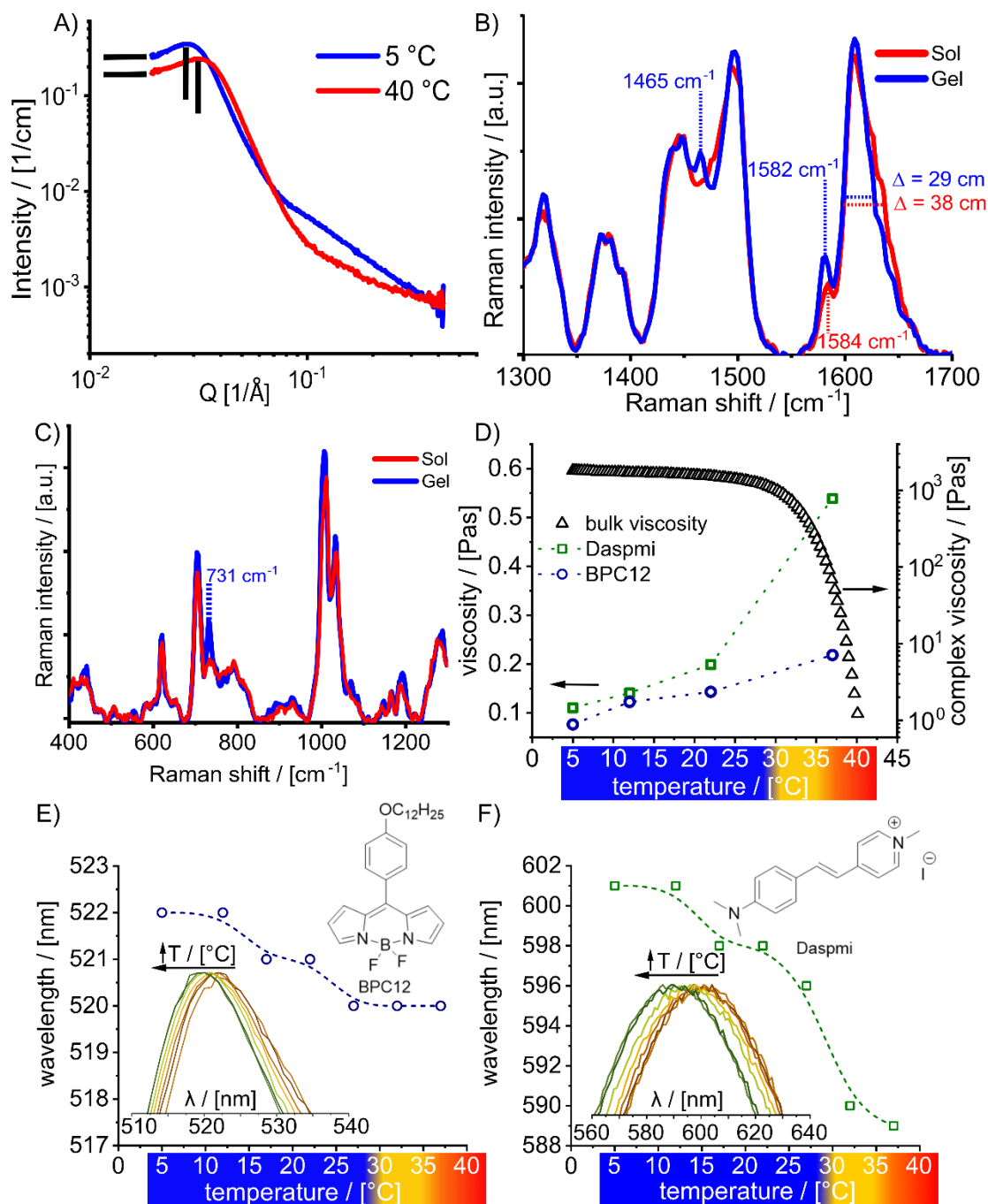


Figure 2] SAXS analysis, microviscosity, and polarity change of aqueous pMeOx-*b*-pPheOzi-*b*-pMeOx solutions.

A) SAXS scattering curves at 5 °C (blue, hydrogel) and 40 °C (red, liquid) at 100 g/L. Two defined slopes regions can be defined (triangles). Further, the position of the structure (vertical lines) and absolute intensity of $Q \rightarrow 0$ (horizontal lines) are different at 5 °C and 40 °C. B) Microviscosity values for Daspmi and BPC12 molecular rotors in a 20 wt.% aqueous polymer sample in fluorescence lifetime experiments as a function of temperature. Bulk viscosity of a 20 wt.% hydrogel was added for comparison using the data obtained in previous studies via oscillatory rheology experiments.¹² Wavelength shift of BPC12 (C) and Daspmi (D) fluorescence emission in steady-state experiments as a function of temperature. In addition, the chemical structure of BPC12 and Daspmi are shown. The color code for the temperature represents the macroscopic state of the sample as described in Figure 1.

Additionally, temperature-dependent wide angle X-ray scattering (WAXS) (Figure S1) provides insights into intra- and interpolymer interactions as previously described for biopolymers⁴⁷ and thermogelling

peptides⁴⁸. In the gel state (5 °C, blue), a rather defined peak centered around 4.2 Å was observed, which could be interpreted to hint towards π - π interactions of the phenyl moieties.⁴⁹ With increasing temperature, the peak position was maintained, but a noticeable broadening between 4.2 Å and 7 Å indicates reduced order and increased degrees of freedom. From a self-assembly point of view, a transition from spherical to worm-like assembly must correlate with a change in the volume fraction of the hydrophilic to the hydrophobic compartment. Specifically, the relative volume of the hydrophilic compartment has to decrease or the volume of the hydrophobic compartment has to increase upon cooling for a sphere-to-worm transition to occur. If the peak in the WAXS scattering curve corresponds to the hydrophobic compartment, it would suggest rather a decrease in volume due to denser packing. This is a first hint that the molecular origins of the order-order transition do not lie in the hydrophobic compartment (alone) and are not connected to π - π stacking as might be assumed.

Infrared and Raman spectroscopy can provide functional group-selective information on non-covalent polymer interactions, conformations and self-assembly. Overall, the Raman spectra for the dried polymer powder, polymer hydrogel (20 wt.%, 5 °C) and polymer sol (20 wt.%, 40 °C) are quite similar (Figure S2A), but some distinct changes hint at differences in the polymer-polymer interactions between sol and gel state. At 1464 cm^{-1} , a small but clearly distinguishable peak is exclusively observed in the gel (Figure 2B). Unfortunately, both aromatic ring vibrations as well as CH_3 and CH_2 deformation vibrations ubiquitous in the polymer backbone and hydrophilic sidechain appear in this region, making an unambiguous assignment challenging.

The maximum amide band at 1608 cm^{-1} does not shift, but the signal has a slightly higher intensity in the gel state. In addition, the full width-half maximum decreases rather significantly by 25 % from 38 cm^{-1} to 29 cm^{-1} . Similarly, a peak at around 1580 cm^{-1} , which is attributed to the phenyl ring of the hydrophobic repeat units shows increased intensity, becomes more defined, and in addition shifts slightly to lower wave numbers from 1584 cm^{-1} (sol) to 1582 cm^{-1} (gel) (Figure 2B). Albeit in a different system (graphene interaction with polystyrene), such a shift has been attributed to electron donation into the aromatic system as observed in π - π stacking.⁵⁰ These observations support the observations

made in WAXS, where a more narrow peak also indicates better defined molecular interactions. In addition, we observed one major differences in the fingerprint region of the Raman spectra. In the gel state, a sharp and moderately intense signal is observed at 731 cm^{-1} , which is much weaker and barely resolved in the sol state. In this spectral region, we expect C-C stretching modes, which are abundant in our polymers. At this point, we cannot hypothesize on the assignment of this signal without further understanding of the system, but will return later to this assignment.

A clear difference between sol and gel state is also observed in the OH region of 3100 cm^{-1} to 3600 cm^{-1} , originating from water molecules. The different types of bonding modes in water molecules can be categorized using Gaussian deconvolution to divide the OH region into areas with different binding strength.^{23, 51, 52} Our data suggest that water is less mobile in the hydrogel compared to the sol (Figure S2B) as indicated by the increased contribution of the peak at 3250 cm^{-1} (Figure S2B, red line, 1).

However, arguably more interesting are the changes in macromolecular mobility with the change in self-assembly. Viscosity sensitive fluorescent probes, namely molecular rotors such as 4,4'-difluoro-4-bora-3a,4a-diaza-s-indacene *meso*-substituted with *para*-dodecylphenyl, BODIPY-C12 (BPC12) and 2-(4-(dimethylamino)styryl)-1-methylpyridinium iodide, Daspmi have been used in this context.²⁶ The fluorescence lifetime of a molecular rotor is affected by the ability to rotate its structural segments with respect to each other, which in turn is strongly dependent on the immediate molecular environment. However, it has to be kept in mind that it is not always clear what this immediate molecular environment is. Here, microviscosities in the sol and gel states were determined by fluorescence lifetime data after appropriate calibration (Figure S3)⁵³ at four temperatures ($5\text{ }^{\circ}\text{C}$, $12\text{ }^{\circ}\text{C}$, $22\text{ }^{\circ}\text{C}$ and $37\text{ }^{\circ}\text{C}$). We intended to probe the temperature-dependent microviscosity of the hydrophobic and the hydrophilic compartment of the self-assemblies by using two different rotors, one being more hydrophobic (BPC12) and the other being more hydrophilic/amphiphilic (Daspmi). Interestingly, in contrast to bulk viscosity (macroviscosity) of the polymer, which is obviously higher in gel state, higher microviscosities were obtained in the sol state and the hydrophilic probe gave almost three times higher values than the hydrophobic one (Figure 2 D). The microviscosities decreased upon gelation and

were similar for both probes below 25 °C. This suggests, albeit indirectly, a more profound change in the hydrophilic compartment upon gelation. Steady-state fluorescence spectroscopy complements the picture. Fluorescence intensity and λ_{max} shift can provide information on polarity changes of the probe's microenvironment.⁵⁴ For both probes, a two-step bathochromic shift was observed at low temperature, indicating an increase in the polarity of the probe microenvironment upon gelation (Figure 2 E,F). This increase supports the suggestion that the probes can be partially expelled from polymeric self-assemblies and become more exposed to polar aqueous solvent. Interestingly, the first polarity change is at a temperature between 12 °C and 17 °C. Again, the change was much more pronounced for Daspmi. Ultimately, the time-resolved and steady-state fluorescence measurements clearly show that the microenvironment of both molecular rotors is more polar and less viscous in the gel state, suggesting that the gelation causes a probe migration out of the condensed polymeric assembly closer to the polymer-water interface. However, this remains indirect evidence.

NMR spectroscopy is a versatile tool to further study the underlying molecular interactions of the order-order transition due to its more straightforward assignability of signals to specific moieties and sensitivity to short-range order phenomena. Therefore, we recorded ¹H NMR spectra of a 20 wt.% polymer sample at different temperatures between 2 °C and 39 °C (40 °C). In a first step, all signals in the ¹H NMR spectra were assigned (Figure 3 A,B). Notably, the aromatic protons in the sidechain of the hydrophobic polymer block show a broad signal at 6.6-7.6 ppm (signal 5), which differs significantly in appearance between sol and gel state (Figure 3B). Four signal areas around 6.9 ppm, 7.2 ppm, 7.4 ppm and 7.5 ppm (signals 5.1-5.4) can be distinguished. In the hydrogel state (2 °C - 31 °C), an overall low signal intensity with a relatively defined peak at 7.5 ppm and a broad shoulder around 7.4 ppm is observed. Increasing the temperature above the sol-gel transition (34 °C - 40 °C) results in significantly increased signal intensities and reduced line widths suggesting a significant mobility increase for the polymer chains, including the aliphatic region (backbone and CH₃ group of MeOx, signals 1-4). The p-ratio (equation (3)) allows a more quantitative assessment of the relative decrease of the respective peak areas, or the mobility of the associated polymer segments (Figure 3C).

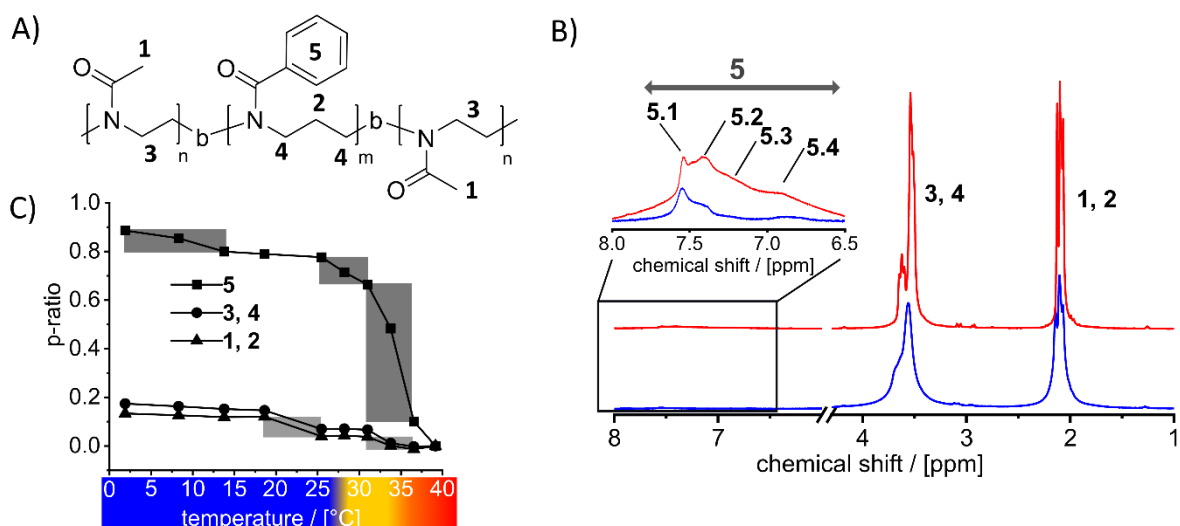


Figure 3 | ¹H NMR experiments of a 20 wt.% sample in D₂O recorded at different temperatures. A) Structure of the amphiphilic ABA type triblock copolymer pMeOx-*b*-pPheOzi-*b*-pMeOx including numbering scheme. B) ¹H NMR spectra at 2 °C (blue) and 39.15 °C (red) of a pMeOx-*b*-pPheOzi-*b*-pMeOx sample alongside signal assignment. C) Calculated *p*-ratio for the intensities of different polymer protons as a function of temperature. The color code for the temperature represents the macroscopic state of the sample as described in Figure 1.

Clearly, the aromatic protons yield the highest *p*-ratio in the gel-state. Upon heating and coinciding with gel liquefaction, the *p*-ratio decreases drastically indicating a much more flexible and mobile hydrophobic compartment for the spherical micelles, which is in line with the WAXS data and in clear contrast to the fluorescence probe microviscosities. This strongly suggests that the molecular interactions in the hydrophobic compartment change significantly at or around T_{gel} . At lower temperature, more pronounced hydrophobic or π - π interactions lead to an improved packing and lower mobility. In addition, two minor steps where the *p*-ratio decreases are observed between 2 °C and 15 °C as well as 25 °C and 30 °C, which will be discussed below. Overall, the hydrophilic block and the backbone appear less affected by the transition corroborating results by Weberskirch et al. and Černoč et al. describing thermoresponsive POx-based homo- and copolymers.^{22, 55} However, also for the MeOx units a change in *p*-ratio is observed at 17-25 °C, followed by a plateau region (20-30 °C), before it drops to zero upon liquefaction. Interestingly, these steps agree with steps observed in steady state fluorescence. Mobility information for the different moieties can also be obtained through the comparison of ¹H longitudinal relaxation times T_1 , which were determined for the sol and gel state, respectively (Figure S4, Table S2). The fact that all polymer segments yield the same trend of decreasing T_1 -values upon increasing temperature supports the assumption that all parts of the

polymer act in concert in the aggregation process. In contrast, higher T1 values for water in the sol state indicates more mobile water molecules compared to the gel state, corroborating Raman spectroscopy and steady state fluorescence results discussed earlier.

To obtain more insights into the spatial proximity between different moieties in the polymer, 2D ^1H - ^1H NOESY NMR experiments were performed in the gel (5 °C) and sol (40 °C) state (Figure 4). 1D horizontal slices are also shown for better visibility. Stronger NOE signals are visible in the hydrogel state (Figure 4, left, blue) compared to the sol (Figure 4, right, red), which agrees with the hypothesized reduced mobility and data from WAXS (Figure 2A).

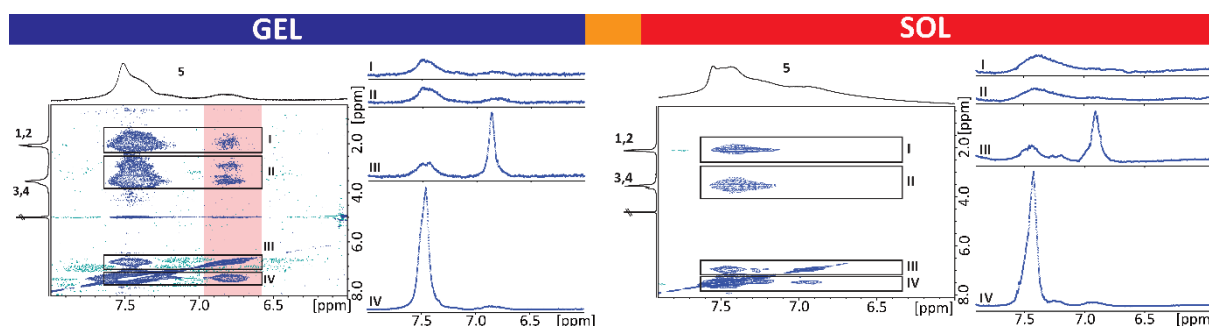


Figure 4 | ^1H - ^1H NOESY NMR experiments of a 20 wt.% sample in D_2O recorded with a mixing time of 40 μs . 5 °C (blue, gel state, worm like micelle). 40 °C (red, sol state, spherical micelle). For signal areas of interest 1D slices were extracted and the assignment in figure 6 for the specific polymer signals was used.

Notably, in the sol and gel state, an intense NOE cross peak originating from the aromatic peak at 7.5 ppm can be correlated to the backbone and MeOx sidechain protons. However, in the gel state an additional second cross peak of the aromatic region at 6.9 ppm with the backbone and MeOx sidechain protons is evident despite the overall lower ^1H signal intensity in this area compared to the sol state (red square, Figure 4). The observation of an additional NOE signal and, therefore, increased spatial proximity of aromatic and hydrophilic units is a first, but crucial hint at a possible molecular mechanism to explain the unique assembly of this amphiphile into worm-like micelles at lower temperature. If the hydrophilic blocks interact with the hydrophobic block in any significant manner upon cooling, this could reduce the hydrophilic/hydrophobic volume ratio and lead to the observed sphere-to-worm transition. Due to its sensitivity to subtle changes in intermolecular interactions and packing on the

molecular level, solid-state NMR is a versatile tool to improve our understanding of the potential contacts identified so far.

Considering their nature as viscoelastic solids, hydrogels can generally be characterized using solid-state NMR experiments.⁵⁶ For shear thinning hydrogels such as the present system, one has to consider the possibility that magic angle spinning (MAS) can exert sufficient force to alter the sample properties, e.g. causing liquefaction. Here, ¹H NMR experiments at different MAS frequencies (3-5.3 kHz) showed no significant differences (Figure S5). Two different ¹³C NMR spectra were recorded either through direct excitation (DE) with short interscan delay (1 s) showing predominantly mobile carbon environments (Figure 5A, grey spectrum), while ¹H-¹³C cross polarization (CP) MAS experiments with a contact time of 2 ms reveal more rigid molecular entities due to their dependence on dipolar interactions (Figure 5A, black spectrum). In the spectrum obtained through DE, only signals that can be attributed to MeOx units were visible. No aromatic signals were observed, corroborating once more the reduced mobility of the latter. In the ¹³C CP MAS NMR spectrum significantly more and broader peaks as well as spinning sidebands (Figure 5A, asterisks in grey spectrum) were observed with phenyl moieties now clearly observable. A MAS rate of 5 kHz or higher is required to avoid substantial overlap between the carbonyl signal of the amide group and the phenyl spinning sidebands. The broader signal (compared to DE spectra) of the amide carbonyl is shifted slightly to smaller ppm values (orange arrow) and additional signals are visible at higher ppm values originating from the phenyl carbonyl groups. Most interesting, however, are two additional signals that are observed in the aliphatic region of the spectrum (red arrows). The signal at 38 ppm is close to the other backbone signals indicating a similar chemical environment, while another new and broad signal appears at 24 ppm adjacent to the signal of the methyl sidechain of the hydrophilic polymer block. In other words, there are two different MeOx populations, one quite mobile and one significantly less mobile.

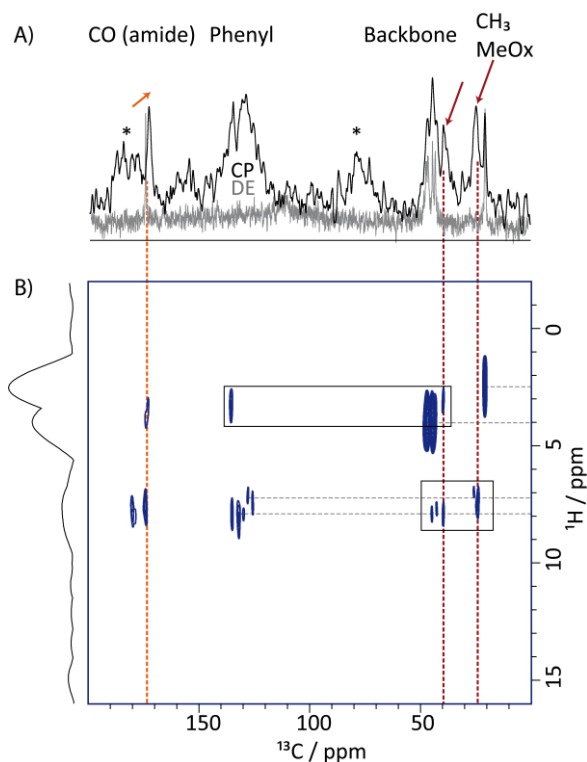


Figure 5] Solid state NMR experiments of a 20 wt.% hydrogel sample. A) Overlay of the ^{13}C NMR spectra recorded at 9.4 T and 5.3 kHz MAS using DE and short interscan delay of 1 s (grey) or CP MAS with 2 ms contact time (black). Spinning sidebands are indicated by asterisks. B) ^1H - ^{13}C HETCOR MAS spectrum recorded at 9.4 T and a MAS rate of 5 kHz using a contact time of 2 ms. 122 t_1 FID increments were acquired using a recycle delay of 2 s, each with 240 co-added transients. The corresponding ^{13}C NMR spectra are shown at the bottom. Direct CH contacts are indicated by dotted grey lines.

To better understand the nature of these new signals and investigate proximities through space in more detail, a 2D ^1H - ^{13}C HETCOR experiment with a contact time of 2 ms was recorded (Figure 5B). Due to the relatively long contact time, intra- and intermolecular proximities can be observed in the 2D spectrum as cross peaks. The ^1H chemical shifts of the CH_3 groups of MeOx, the backbone, and the two major phenyl environments are indicated by grey dotted, horizontal lines. The three signals highlighted in Figure 5A are indicated by dotted, vertical lines. For the carbonyl signal, cross peaks both in the aromatic and aliphatic backbone region are observed, but due to the polymer structure we cannot know whether the proximity is intramolecular or intermolecular. Furthermore, cross peaks between some of the backbone CH_2 signals and the phenyl signal at higher ppm are also visible (black boxes). Considering the larger intramolecular distance between the backbone and the phenyl ring, this interaction is most likely through space. For the remaining carbon signals in the aliphatic region, it is clear that interactions must occur through space. The more rigid CH_3 group of MeOx at 24 ppm only

visible in the CP-MAS experiment is in a different polymer block than the phenyl moiety. Therefore, the cross peak at 24 / 7.2 ppm can only be explained by ^1H - ^{13}C proximity through space ($< 4 \text{ \AA}$) between the hydrophilic and the hydrophobic block. In contrast, the more mobile CH_3 group of MeOx at slightly lower ppm values does not show any cross peaks in the 2D correlation and thus represents the hydrated hydrophilic corona. With this, we can finally formulate a mechanism for the order-order transition and inverse thermogelation in aqueous solutions of pMeOx-*b*-pPheOzi-*b*-pMeOx. Our results show that this thermogelation is due to an unexpected interaction between repeat units in the hydrophilic pMeOx blocks and those in the aromatic hydrophobic pPheOzi block. This reduces the volume of the hydrophilic compartment allowing the order-order sphere-to-worm transition. Polymers that show UCST-type thermotransition typically exhibit H-bonding between polymer repeat units, however, this is not possible in the present case. When starting to investigate this mechanism our first hypothesis was that this transition could be linked to π - π stacking within the hydrophobic compartment, but this hypothesis had to be abandoned quickly. A look into the literature yields two other, we believe more probable candidates, the overlap of the lone electron pairs of the amide carbonyl and the aromatic LUMO: $n_{\text{Am}} \rightarrow \pi^*_{\text{Ar}}$ or interactions of the π -orbitals of the amide and phenyl ring: $\pi_{\text{Am}} \cdots \pi_{\text{Ar}}$. In general, non-covalent $n \rightarrow \pi^*$ interactions have been described to contribute to the thermostability of the proline-rich protein collagen.⁵⁷ Interestingly, proline is the only proteinogenic amino acid that forms tertiary amides akin to the amide groups in POx and POzi. In addition, and even more closely related to the present system, $n \rightarrow \pi^*_{\text{Ar}}$ interactions have been described to contribute to the structure formation in peptoids⁵⁸, which also contain tertiary amides.

The analytically rather elusive $n \rightarrow \pi^*_{\text{Ar}}$ interactions are typically verified by crystallographic data or computational modeling. While the former can be ruled out for our system, we performed an all-atom molecular dynamics (MD) simulation of a single worm-like micelle consisting of full length pMeOx₃₅-*b*-pPheOzi₁₅-*b*-pMeOx₃₅ amphiphiles at 5 °C (Figure S7A). We modeled the pPheOzi blocks as a central inner strand, which is surrounded by the corresponding pMeOx blocks stretching out into the solvent (water). Throughout the 600 ns simulation a single worm-like strand of pPheOzi blocks is preserved.

More interestingly however, the peripheral MeOx repeat units approach the initially solvent-exposed hydrophobic repeat units (Figure 6 A,B), clearly corroborating our model of a hydrophilic shell condensing onto the hydrophobic core.

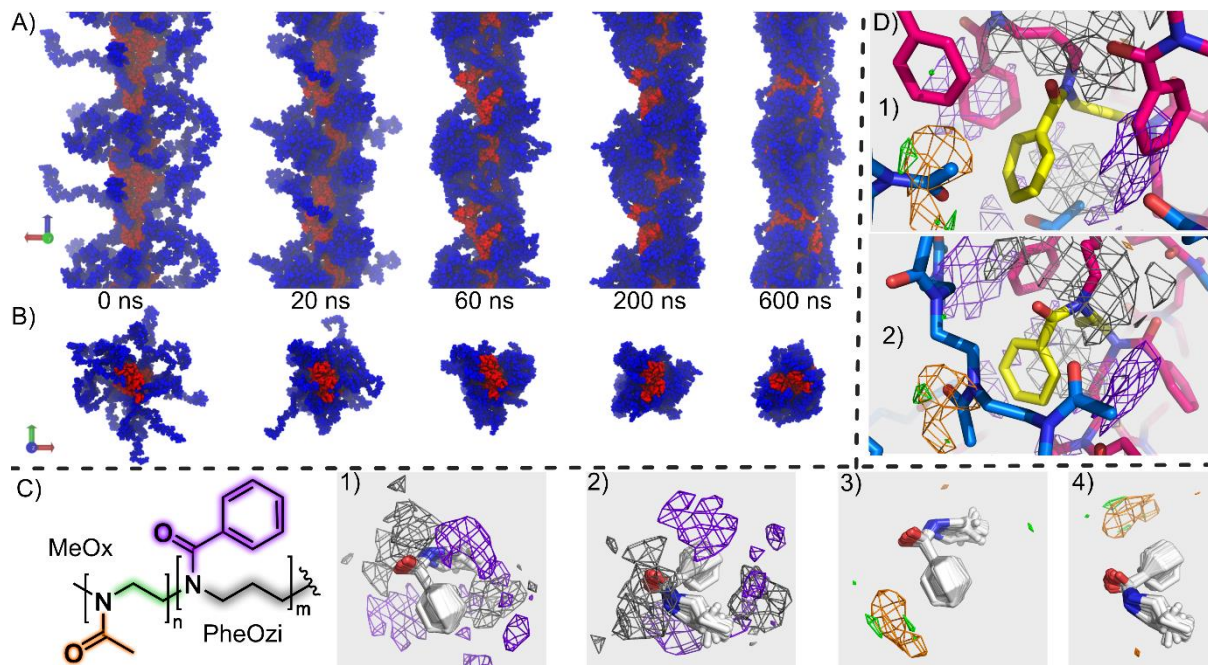


Figure 6| Results of molecular modeling of a worm-like micelle comprising pMeOx-*b*-pPheOzi-*b*-pMeOx amphiphiles. A) Simulation snapshots showing PheOzi monomers as red and MeOx monomers as blue VDW spheres. The simulation box and about half of each neighboring image along the Z axis are illustrated, without solvent molecules depicted. B) Same illustration as seen in A) from an orthogonal perspective (along the Z axis). C) Occupancy density analysis around aligned PheOzi residues (white sticks), showing hotspots for different polymer structures as meshes from two different perspectives. In C-1/2 the violet density represents PheOzi sidechains and the grey density PheOzi backbone atoms (isovalues: 0.08). The two structures on the right in C-3/4 depict densities (isovalues: 0.03) for MeOx backbone atoms (green) and sidechain atoms (orange) from two different perspectives. D) Two example snapshots D-1 and D-2, in which residues at the surface of the micelle overlap with occupancy hot spots depicted in C). pMeOx residues are shown with blue carbon atoms, pPheOzi residues with magenta carbon atoms and the aligned monomer of interest is highlighted in yellow. Densities are shown analogously to C).

Consequently, the radius of gyration of the self-assemblies decreases quickly and reaches a narrow fluctuation range after about 40 ns (Figure S7B, left). While the overall structure becomes clearly more compact, not all pMeOx repeat units come into close contact with pPheOzi residues *in silico*, which in turn are also not completely shielded from the solvent at the end of the simulation, corroborating the observations made in solution NMR spectroscopy. *In silico*, about 53 % of all pMeOx repeat units keep a minimum average distance of more than 5 Å to the pPheOzi blocks over the last 100 ns (including hydrogen atoms for calculation). These would be attributed to the pMeOx repeat units, which were

found more mobile in the ^{13}C DE MAS NMR spectra and which did not show cross peaks with the aromatic rings of pPheOzi in the ^1H - ^{13}C HETCOR spectrum. We analyzed the solvent-accessible surface area of all pPheOzi units and noticed that this value is mostly decreasing early in the simulation for the aromatic sidechains, indicating that pMeOx monomers are preferably shielding these moieties against water molecules (Figure S7B, middle). The amount of water within 5 Å around polymer residues also decreases quickly, especially for the pMeOx monomers (Figure S7B, right).

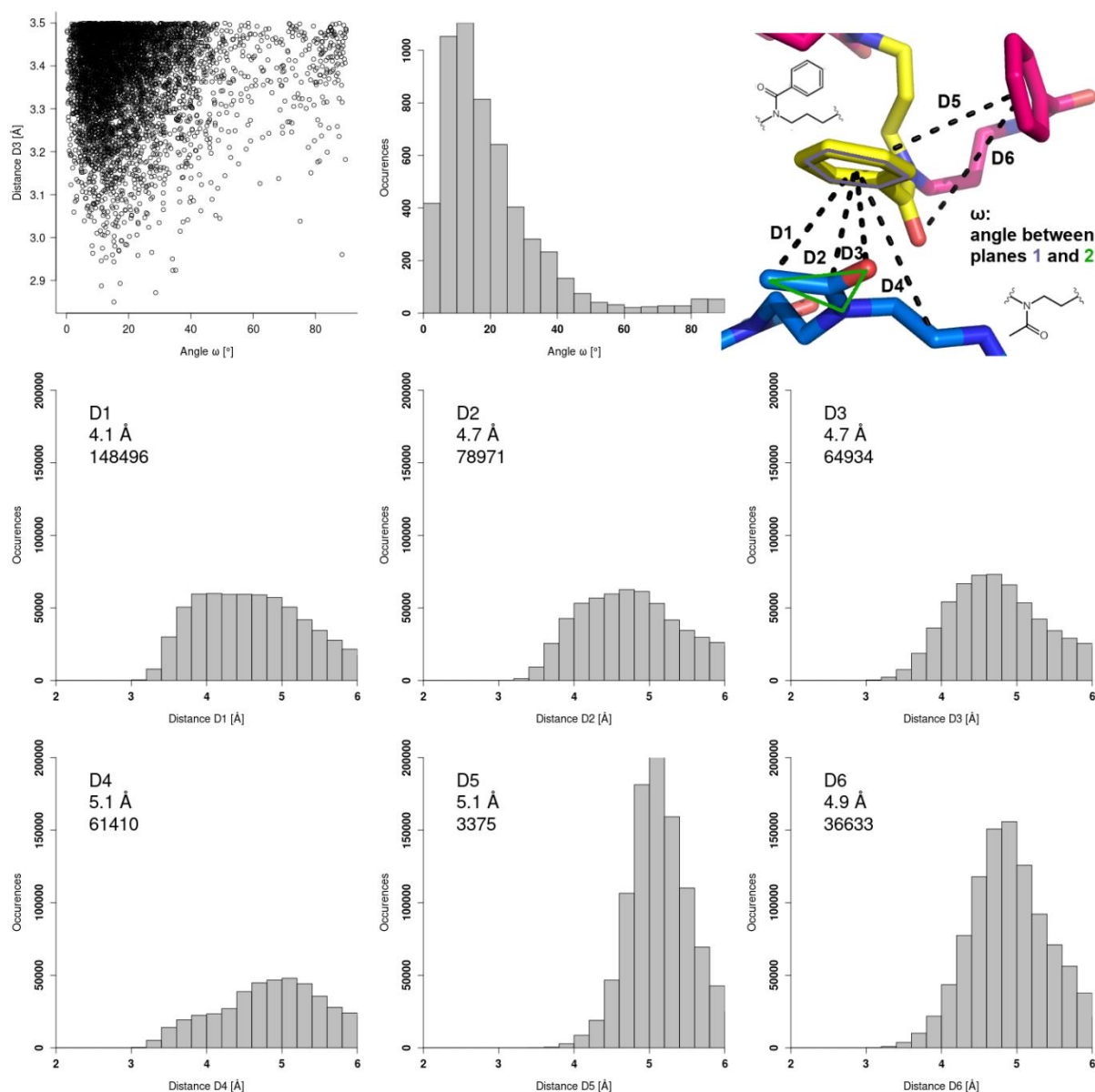


Figure 7] Distribution of computationally derived distances and angles between the amide group and the phenyl ring centroid. Histograms for all distances up to 6 Å between PheOzi moieties and the nearest polymer atoms (excluding hydrogen atoms). An illustration describing the distances and the angle ω is given in the top right. Plots show the total amount of occurrences for all snapshots of all 104 pPheOzi residues which were used for density calculation. Numbers in the top left of each histogram illustrate the maximum bin value below 6 Å (bin size: 0.2 Å), as well as the sum of all occurrences between 0 and 4 Å. Additionally, the plot in the top left

shows measurements of the angle ω for all pMeOx carbonyl oxygen atoms which are located nearer than 3.8 Å to the ring centroid (corresponding to distance D3). A histogram for this angle is depicted in the middle of the top row, with a 5 ° bin size.

An illustration of the average occupancy densities of polymer moieties around pPheOzi moieties supports this observation (Figure 6B). The methyl sidechains (of the hydrophilic pMeOx repeat units) are predominantly located close to the aromatic ring of PheOzi sidechains in close proximity to the PheOzi carbonyl group. In contrast, aromatic rings can be found below or above other PheOzi amide groups and near the phenyl ring in the volume which is turned away from the carbonyl group. The pPheOzi backbone atoms are mainly surrounded by other PheOzi residues, only a small fraction of the aromatic repeat units remains solvent-exposed: 17 out of 120 pPheOzi repeat units show an average minimum distance of over 3 Å to any pMeOx in the last 100 ns (taking hydrogen atoms into account). These could be interpreted as sticky patches, which help to mechanically connect different worm-like micelles, adding to the remarkably high storage modulus of the gels.¹² The evidence of such sticky contacts in worm-like micelles was recently discussed by Thurn and Hoffmann.⁵⁹ However, we cannot completely rule out that these patches result (in part) from an insufficient number of polymers in our model, as the exact composition of the micelle was not available as input *a priori* from experimental data. For the PheOzi residues analyzed during density calculation, we measured distances to the nearest polymer moieties, as well as the angle ω between the planes of nearby N-(C=O)-C amide groups and the aromatic ring (Figure 7). Distances D1 – D4 reflect the orange and green densities in Figure 6C. A notable number of distances D1 – D3 below 4 Å can be found, highlighting potential interactions between the MeOx sidechains and the phenyl ring. Overall, distances show distributions similar to the results of our WAXS experiments. The distance to the ring centroid is the lowest for the methyl group, while the backbone is situated further away. These measurements support hydrophobic interactions between the phenyl rings of pPheOzi and the methyl sidechain of MeOx repeat units as seen in NMR experiments. With regard to the MeOx carbonyl groups, $n_{Am} \rightarrow \pi^*_{Ar}$ or $\pi_{Am} \cdots \pi_{Ar}$ interactions may be hypothesized. While it should be mentioned that the existence of specific interactions between lone pairs and aromatic systems was recently challenged⁶³ and that the ability of

classical force fields for capturing these can certainly be questioned, occurrences of an angle $\omega \leq 90^\circ$ in combination with a distance lower than 3.8 Å of the carbonyl oxygen to the ring centroid are in accordance with previously published measurements for potential $n_{Am} \rightarrow \pi_{Ar}^*$ interactions, e.g. in peptoids.^{58, 60} We retrieved very low values for ω with a median of about 19° with the above mentioned distance cutoff, indicating suitable conformations for $n_{Am} \rightarrow \pi_{Ar}^*$ or $\pi_{Am} \cdots \pi_{Ar}$ interactions. Exemplary simulation snapshots which overlap with the described densities illustrate the interactions between MeOx and PheOzi sidechains (Figure 6D). While some MeOx carbonyl groups showed conformations perpendicular to the ring plane (example D-1), in most cases the amide moiety is placed nearly parallel to the phenyl ring (example D-2). Accordingly, the additional stretching mode at 731 cm^{-1} in the Raman spectra in the gel state should correspond to a C-C bond which is weakened compared to the sol state. We believe that this could be attributed to the C-C bond in the MeOx side chain, which, as the amide interacts with the phenyl ring is weakened, leads to an increased Raman shift.

In summary, the MD simulation conclusively supports our extensive analytical data, in particular those obtained by WAXS and NMR spectroscopy, and the formulated mechanism of the hydrophilic MeOx interacting with the hydrophobic repeat units. This results in a notable condensation of the hydrophilic corona and, thus, enables the worm-to-sphere transition upon cooling. This process may be driven by pMeOx sidechains mainly interacting with aromatic systems of the pPheOzi blocks via hydrophobic, as well as possible $\pi_{Am} \cdots \pi_{Ar}$ and $n_{Am} \rightarrow \pi_{Ar}^*$ interactions.

We know from previous studies that small changes in the hydrophobic core prevent worm formation and thermogelation. Specifically, when pPheOzi is exchanged with poly(2-phenyl-2-oxazoline), poly(2-phenyl-2-oxazine) or poly(2-benzyl-2-oxazoline), the resulting ABA triblock copolymers form only spherical micelles and low viscous liquids in water irrespective of the temperature.¹² In contrast, ABA triblock featuring poly(2-phenethyl-2-oxazoline) or poly(2-benzhydryl-2-oxazoline)s form gels but do not undergo any order-order transition but remain spherical micelles.^{61, 62} Having derived this novel mechanism behind the order-order transition, we should expect that different hydrophilic blocks affect

the order-order transition and thermogelation. To do so, ABA triblocks featuring slightly different hydrophilic blocks A, poly(2-methyl-2-oxazine) (pMeOzi) and poly(2-ethyl-2-oxazoline) (pEtOx) were prepared (see Table S3, Figure S7).

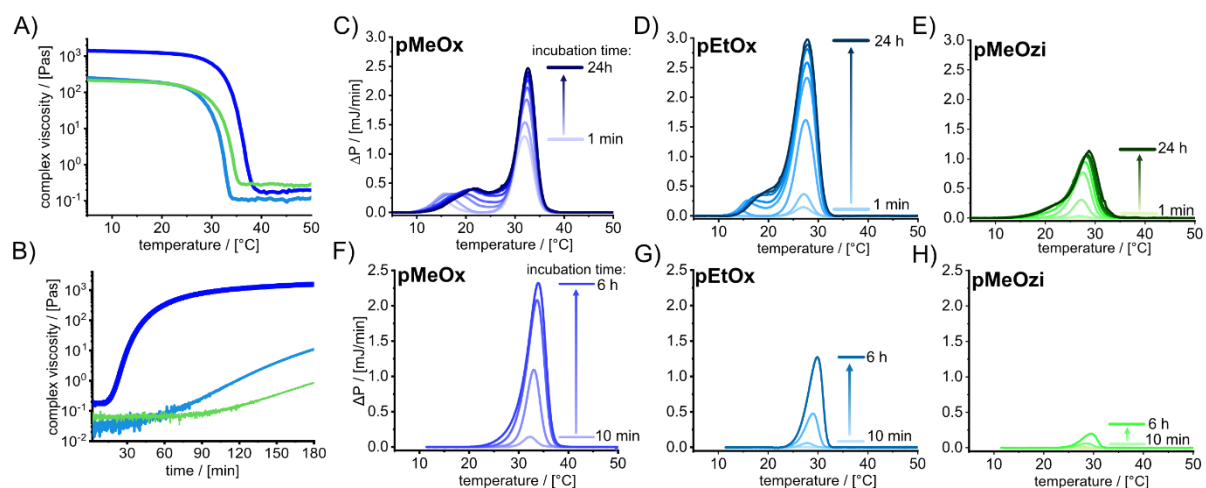


Figure 8 | Modified ABA-type amphiphiles with varying hydrophilic A blocks and the aromatic pPheOzi B block and their thermogelation. A),B) Gel properties of 15 wt.% aqueous sol-gels of the polymers pMeOx-b-pPheOzi-b-pMeOx (dark blue), pEtOx-b-pPheOzi-b-pEtOx (light blue), pMeOzi-b-pPheOzi-b-pMeOzi (green). A) Temperature sweeps of the complex viscosity from 5-50 °C (heat rate: 0.05 °C). B) Gelation kinetics for 180 min. The gelation process was monitored at 5 °C by adding liquid samples at t=0 minutes. C)-H) Micro-DSC thermograms of 10 g/L solutions of C),F) pMeOx-*b*-pPheOzi-*b*-pMeOx, D),G) pEtOx-*b*-pPheOzi-*b*-pEtOx and E),H) pMeOzi-*b*-pPheOzi-*b*-pMeOzi. Solutions were held at 2 °C (C,D,E) and 10 °C (F,G,H) for time indicated prior to the thermoscan.

In aqueous solution, both novel polymers undergo inverse thermogelation (Figure 8 A,B and Figure S8) and form worm-like micelles in the cold as evidenced by TEM investigations (Figure S9). Dynamic light scattering at 5 and 40 °C confirmed a significant difference in self-assembly for all polymers (Figure S10, Table S4), similar as observed pMeOx-*b*-pPheOzi-*b*-pMeOx. Accordingly, the thermogelation again coincides with an order-order transition after exchanging the hydrophilic blocks.

However, significant differences in the complex viscosity at 5 °C (i.e. the gel strength), the T_{gel} upon heating (liquefaction temperature or gel persistence) and gelation kinetics (speed) were obtained in a temperature ramp experiment from 5 °C to 50 °C (polymer gels were stored at 5 °C for 48 h) and in a time sweep experiment for 180 minutes (pre-heated polymer solutions were transferred on a pre-cooled 5 °C plate and subsequently measured). In all three “disciplines” pMeOx-*b*-pPheOzi-*b*-pMeOx, showed the best performance. It exhibits an approximately 7-fold higher complex viscosity value at 5

°C compared to pEtOx-*b*-pPheOzi-*b*-pEtOx and pMeOzi-*b*-pPheOzi-*b*-pMeOzi. With respect to gel strength and persistence, only little differences were observed for the other two polymers. Only minutely higher gel strength (40 Pa*s) and slightly lower persistence (1-2 °C lower T_{gel}) was observed for the polymer pEtOx-*b*-pPheOzi-*b*-pEtOx in comparison to pMeOzi-*b*-pPheOzi-*b*-pMeOzi. In terms of gelation kinetics, pMeOx-*b*-pPheOzi-*b*-pMeOx undergoes a significant viscosity increase after 15 minutes. In contrast, the gelation kinetics of pEtOx-*b*-pPheOzi-*b*-pEtOx and pMeOzi-*b*-pPheOzi-*b*-pMeOzi are significantly delayed (approx. 5 to 8 times).

Finally, micro-DSC gives us an insight into the thermodynamics of the order-order transition in aqueous media. Thermograms were obtained after cooling to 2 °C or 10 °C for different time intervals (Figure 8 D-I). When hydrogels were incubated at 2 °C, the most prominent peak coincides for all three polymers with the sol-gel transition (Figure 8 D-F). The longer samples were cooled, the larger the signal, the maximum of which shifts to slightly larger temperature with longer incubation times. Interestingly, for both pMeOx-*b*-pPheOzi-*b*-pMeOx and pEtOx-*b*-pPheOzi-*b*-pEtOx, a smaller secondary peak starts at 10 °C – 13 °C and has a maximum at 15 °C after short incubation times, which shifts notably to higher temperature with longer incubation. This transition coincides with the step between 12 °C and 15 °C observed in the microviscosity (Figure 2 C,D). In comparison to pMeOx-*b*-pPheOzi-*b*-pMeOx, the transition at lower temperature is shifted to slightly higher temperatures in the case of pEtOx-*b*-pPheOzi-*b*-pEtOx while the larger transition at higher temperature is observed at lower temperatures, leading to a more pronounced overlap of both transitions. In the case of pMeOzi-*b*-pPheOzi-*b*-pMeOzi, only one major transition is observed upon liquefaction of the gel with only a shoulder (at 15-20 °C) emerging after cooling the sample 6 h or more. Interestingly, if the samples are cooled only to 10 °C instead of 2 °C, the secondary transitions at lower temperature are not observed at all (Figure 8 G-I). In addition while the height and integral of the main signal is attenuated by 20 % in the case of pMeOx-*b*-pPheOzi-*b*-pMeOx, the attenuation for both pEtOx-*b*-pPheOzi-*b*-pEtOx and pMeOzi-*b*-pPheOzi-*b*-pMeOzi is much more profound (70 % and 86 %, respectively).

This strong influence of the hydrophilic blocks on the gelation kinetics and thermodynamics as well as macroscopic gel properties clearly give a synthetic proof that the hydrophilic blocks play a crucial role in the gelation mechanism as shown before using a variety of advanced analytical tools. This mechanism described here is rather unusual, as the dehydration of (highly hydrophilic) MeOx units occurs in favor of inter- and intramolecular interaction with hydrophobic repeat units, which is unexpected. Also, this is clearly not simply a hydrophobic effect, as this would then be stronger for the less hydrophilic EtOx and MeOzi. We believe this discovery of a novel self-assembly mechanism opens up new possibilities to design stimulus responsive materials and will generally help to improve our understanding of the complex interactions of polymers in solutions.

Conclusion

Using a wide selection of complementary analytical tools, we gained a detailed picture of a novel and unusual order-order transition in conjunction with an inverse thermogelation of aqueous solutions of a special group of amphiphilic block copolymers. SAXS analysis confirmed the previously described reversible worm-to-sphere transition upon heating. WAXS experiments elucidated small changes during sol-gel transitions at 4-7 Å. Advanced NMR spectroscopic studies, supplemented by Raman and fluorescence spectroscopy at different temperatures revealed novel and unexpected polymer/polymer interactions between the hydrophilic pMeOx blocks and the hydrophobic aromatic pPheOzi moieties in the hydrogel state. Comparison with similar, tertiary amide containing systems in the literature and *in silico* molecular dynamics modeling led us to propose $n_{Am} \rightarrow \pi^*_{Ar}$ and/or $\pi_{Am} \bullet \bullet \pi_{Ar}$ interactions between the carbonyl moieties in the hydrophilic pMeOx block and the aromatic rings in the hydrophobic pPheOzi block to be responsible for the order-order transition and inverse thermogelation, likely in conjunction with more standard $\pi_{Ar} \bullet \bullet \pi_{Ar}$ hydrophobic interactions. To the best of our knowledge, the described system is the only example of a sphere-to-worm order-order transition that leads to inverse thermogelling, and it is also the first example in which non-ionic, non H-bonding interactions between the hydrophilic and hydrophobic compartment are critically affecting

the self-assembly in synthetic polymer amphiphiles. This mechanistic elucidation allowed us a tuning of this unusual system by changing the hydrophilic blocks leading to significant differences with respect to gel properties (strength and kinetics).

Notes

RL and HL are listed as inventors on a patent application pertinent to some materials in the present work. The other authors declare no competing financial interest.

Acknowledgment

The authors would like to gratefully acknowledge support by the Deutsche Forschungsgemeinschaft (DFG, German Research Foundation) – project number 326998133 – TRR 225 (subproject A03), awarded to R.L. and project number 440955393 awarded to A.-C.P. The authors thank Christian May for technical assistance and Bernhard Schummer for valuable discussions. We are very grateful for the HDRC-Software version 6.3.1 provided by O. Nirschl and K. Fischer, Physical Chemistry of Polymers at the Johannes Gutenberg University Mainz led by Prof. Dr. Sebastian Seiffert (formerly Prof. Dr. Manfred Schmidt) for DLS data analysis. Light scattering experiments were possible through support of the Deutsche Forschungsgemeinschaft (INST 93/774-1 FUGG). T.L. and E.S.L. acknowledge Academy of Finland for funding of the current research (Project Nos. 316893 and 323669). The authors are also grateful to Dr. Alexander Efimov for BPC12 synthesis. We gratefully acknowledge access to electron microscopy facilities provided by Prof. Bettina Böttcher at the Rudolf Virchow Center, Julius-Maximilians-University Würzburg. We also thank helpful discussions with Heikki Tenhu and the late Françoise Winnik.

References

1. Zhang, Q. L.; Weber, C.; Schubert, U. S.; Hoogenboom, R., Thermoresponsive polymers with lower critical solution temperature: from fundamental aspects and measuring techniques to recommended turbidimetry conditions. *Mater Horiz* **2017**, *4* (2), 109-116.
2. Seuring, J.; Agarwal, S., Polymers with Upper Critical Solution Temperature in Aqueous Solution. *Macromol Rapid Comm* **2012**, *33* (22), 1898-1920.
3. Niskanen, J.; Tenhu, H., How to manipulate the upper critical solution temperature (UCST)? *Polym Chem-Uk* **2017**, *8* (1), 220-232.
4. Lorson, T.; Jaksch, S.; Lübtow, M. M.; Jüngst, T.; Groll, J.; Lühmann, T.; Luxenhofer, R., A Thermogelling Supramolecular Hydrogel with Sponge-Like Morphology as a Cytocompatible Bioink. *Biomacromolecules* **2017**, *18* (7), 2161-2171.
5. Hoffman, A. S., Application of thermally reversible polymers and hydrogels in therapeutics and diagnostics. *Journal of Controlled Release* **1987**, *6*, 297-305.
6. Klouda, L.; Mikos, A. G., Thermoresponsive hydrogels in biomedical applications. *Eur J Pharm Biopharm* **2008**, *68* (1), 34-45.

7. Hecht, E.; Mortensen, K.; Hoffmann, H., L(3) Phase in a Binary Block Copolymer/Water System. *Macromolecules* **1995**, *28* (16), 5465-5476.
8. Blanazs, A.; Verber, R.; Mykhaylyk, O. O.; Ryan, A. J.; Heath, J. Z.; Douglas, C. W. I.; Armes, S. P., Sterilizable Gels from Thermoresponsive Block Copolymer Worms. *J Am Chem Soc* **2012**, *134* (23), 9741-9748.
9. Cunningham, V. J.; Ratcliffe, L. P. D.; Blanazs, A.; Warren, N. J.; Smith, A. J.; Mykhaylyk, O. O.; Armes, S. P., Tuning the critical gelation temperature of thermo-responsive diblock copolymer worm gels. *Polym Chem-Uk* **2014**, *5* (21), 6307-6317.
10. Penfold, N. J. W.; Lovett, J. R.; Verstraete, P.; Smets, J.; Armes, S. P., Stimulus-responsive non-ionic diblock copolymers: protonation of a tertiary amine end-group induces vesicle-to-worm or vesicle-to-sphere transitions. *Polym Chem-Uk* **2017**, *8* (1), 272-282.
11. Ratcliffe, L. P. D.; Derry, M. J.; Ianiro, A.; Tuinier, R.; Armes, S. P., A Single Thermoresponsive Diblock Copolymer Can Form Spheres, Worms or Vesicles in Aqueous Solution. *Angew Chem Int Edit* **2019**, *58* (52), 18964-18970.
12. Hahn, L.; Maier, M.; Stahlhut, P.; Beudert, M.; Flegler, V.; Forster, S.; Altmann, A.; Töppke, F.; Fischer, K.; Seiffert, S.; Böttcher, B.; Lühmann, T.; Luxenhofer, R., Inverse Thermogelation of Aqueous Triblock Copolymer Solutions into Macroporous Shear-Thinning 3D Printable Inks. *ACS Appl Mater Inter* **2020**, *12* (11), 12445-12456.
13. Haas, H. C.; Moreau, R. D.; Schuler, N. W., Synthetic Thermally Reversible Gel Systems .2. *J Polym Sci A2* **1967**, *5* (5pa2), 915-&.
14. Fu, W. X.; Zhao, B., Thermoreversible physically crosslinked hydrogels from UCST-type thermosensitive ABA linear triblock copolymers. *Polym Chem-Uk* **2016**, *7* (45), 6980-6991.
15. Fu, W. X.; Luo, C. H.; Morin, E. A.; He, W.; Li, Z. B.; Zhao, B., UCST-Type Thermosensitive Hairy Nanogels Synthesized by RAFT Polymerization-Induced Self-Assembly. *ACS Macro Lett* **2017**, *6* (2), 127-133.
16. Parmar, I. A.; Shedge, A. S.; Badiger, M. V.; Wadgaonkar, P. P.; Lele, A. K., Thermo-reversible sol-gel transition of aqueous solutions of patchy polymers. *Rsc Adv* **2017**, *7* (9), 5101-5110.
17. Witte, H.; Seeliger, W., Formation of Cyclic Imidic Esters by Reaction of Nitriles with Amino Alcohols. *Liebigs Ann Chem* **1974**, (6), 996-1009.
18. Hahn, L.; Lübtow, M. M.; Lorson, T.; Schmitt, F.; Appelt-Menzel, A.; Schobert, R.; Luxenhofer, R., Investigating the Influence of Aromatic Moieties on the Formulation of Hydrophobic Natural Products and Drugs in Poly(2-oxazoline)-Based Amphiphiles. *Biomacromolecules* **2018**, *19* (7), 3119-3128.
19. Dreiss, C. A.; Jack, K. S.; Parker, A. P., On the absolute calibration of bench-top small-angle X-ray scattering instruments: a comparison of different standard methods. *J Appl Crystallogr* **2006**, *39*, 32-38.
20. Zhang, F.; Ilavsky, J.; Long, G. G.; Quintana, J. P. G.; Allen, A. J.; Jemian, P. R., Glassy Carbon as an Absolute Intensity Calibration Standard for Small-Angle Scattering. *Metall Mater Trans A* **2010**, *41a* (5), 1151-1158.
21. Pauw, B. R.; Smith, A. J.; Snow, T.; Terrill, N. J.; Thunemann, A. F., The modular small-angle X-ray scattering data correction sequence. *J Appl Crystallogr* **2017**, *50*, 1800-1811.
22. Konefal, R.; Spevacek, J.; Cernoch, P., Thermoresponsive poly(2-oxazoline) homopolymers and copolymers in aqueous solutions studied by NMR spectroscopy and dynamic light scattering. *Eur Polym J* **2018**, *100*, 241-252.
23. Choe, C.; Lademann, J.; Darwin, M. E., Depth profiles of hydrogen bound water molecule types and their relation to lipid and protein interaction in the human stratum corneum in vivo. *Analyst* **2016**, *141* (22), 6329-6337.
24. Unal, M.; Akkus, O., Shortwave-infrared Raman spectroscopic classification of water fractions in articular cartilage ex vivo. *J Biomed Opt* **2018**, *23* (1).
25. Levitt, J. A.; Kuimova, M. K.; Yahioğlu, G.; Chung, P. H.; Suhling, K.; Phillips, D., Membrane-Bound Molecular Rotors Measure Viscosity in Live Cells via Fluorescence Lifetime Imaging. *J Phys Chem C* **2009**, *113* (27), 11634-11642.

26. Lisitsyna, E.; Efimov, A.; Depresle, C.; Cauchois, P.; Vuorimaa-Laukkanen, E.; Laaksonen, T.; Durandin, N., Deciphering Multiple Critical Parameters of Polymeric Self-Assembly by Fluorescence Spectroscopy of a Single Molecular Rotor BODIPY-C12. *Macromolecules* **2021**, *54* (2), 655-664.
27. Bond, S. D.; Leimkuhler, B. J.; Laird, B. B., The Nosé-Poincaré method for constant temperature molecular dynamics. *J Comput Phys* **1999**, *151* (1), 114-134.
28. Sturgeon, J. B.; Laird, B. B., Symplectic algorithm for constant-pressure molecular dynamics using a Nose-Poincare thermostat. *J Chem Phys* **2000**, *112* (8), 3474-3482.
29. Maier, J. A.; Martinez, C.; Kasavajhala, K.; Wickstrom, L.; Hauser, K. E.; Simmerling, C., ff14SB: Improving the Accuracy of Protein Side Chain and Backbone Parameters from ff99SB. *J Chem Theory Comput* **2015**, *11* (8), 3696-3713.
30. Gerber, P. R.; Muller, K., Mab, a Generally Applicable Molecular-Force Field for Structure Modeling in Medicinal Chemistry. *J Comput Aid Mol Des* **1995**, *9* (3), 251-268.
31. Labute, P., The generalized Born/volume integral implicit solvent model: Estimation of the free energy of hydration using London dispersion instead of atomic surface area. *J Comput Chem* **2008**, *29* (10), 1693-1698.
32. MOE. *Molecular Operating Environment 2019.01.*, Chemical Computing Group ULC: 2019.
33. Yan, H.; Han, Z.; Li, K. M.; Li, G. Y.; Wei, X. L., Molecular Dynamics Simulation of the pH-Induced Structural Transitions in CTAB/NaSal Solution. *Langmuir* **2018**, *34* (1), 351-358.
34. Wang, Z. W.; Larson, R. G., Molecular Dynamics Simulations of Threadlike Cetyltrimethylammonium Chloride Micelles: Effects of Sodium Chloride and Sodium Salicylate Salts. *J Phys Chem B* **2009**, *113* (42), 13697-13710.
35. Wiest, J.; Kehrein, J.; Saedtler, M.; Schilling, K.; Cataldi, E.; Sottriffer, C. A.; Holzgrabe, U.; Rasmussen, T.; Bottcher, B.; Cronin-Golomb, M.; Lehmann, M.; Jung, N.; Windbergs, M.; Meinel, L., Controlling Supramolecular Structures of Drugs by Light. *Mol Pharmaceut* **2020**, *17* (12), 4704-4708.
36. Bayly, C. I.; Cieplak, P.; Cornell, W. D.; Kollman, P. A., A Well-Behaved Electrostatic Potential Based Method Using Charge Restraints for Deriving Atomic Charges - the Resp Model. *J Phys Chem-U* **1993**, *97* (40), 10269-10280.
37. Frisch, M. J.; Trucks, G. W.; Schlegel, H. B.; Scuseria, G. E.; Robb, M. A.; Cheeseman, J. R.; Scalmani, G.; Barone, V.; Petersson, G. A.; Nakatsuji, H.; Li, X.; Caricato, M.; Marenich, A.; Bloino, J.; Janesko, B. G.; Gomperts, R.; Mennucci, B.; Hratchian, H. P.; Ortiz, J. V.; Izmaylov, A. F.; Sonnenberg, J. L.; Williams; Ding, F.; Lipparini, F.; Egidi, F.; Goings, J.; Peng, B.; Petrone, A.; Henderson, T.; Ranasinghe, D.; Zakrzewski, V. G.; Gao, J.; Rega, N.; Zheng, G.; Liang, W.; Hada, M.; Ehara, M.; Toyota, K.; Fukuda, R.; Hasegawa, J.; Ishida, M.; Nakajima, T.; Honda, Y.; Kitao, O.; Nakai, H.; Vreven, T.; Throssell, K.; Montgomery Jr., J. A.; Peralta, J. E.; Ogliaro, F.; Bearpark, M. J.; Heyd, J. J.; Brothers, E. N.; Kudin, K. N.; Staroverov, V. N.; Keith, T. A.; Kobayashi, R.; Normand, J.; Raghavachari, K.; Rendell, A. P.; Burant, J. C.; Iyengar, S. S.; Tomasi, J.; Cossi, M.; Millam, J. M.; Klene, M.; Adamo, C.; Cammi, R.; Ochterski, J. W.; Martin, R. L.; Morokuma, K.; Farkas, O.; Foresman, J. B.; Fox, D. J. *Gaussian 16 Rev. C.01*, 2016.
38. Wang, J. M.; Wolf, R. M.; Caldwell, J. W.; Kollman, P. A.; Case, D. A., Development and testing of a general amber force field. *J Comput Chem* **2004**, *25* (9), 1157-1174.
39. Case, D. A.; Cheatham, T. E.; Darden, T.; Gohlke, H.; Luo, R.; Merz, K. M.; Onufriev, A.; Simmerling, C.; Wang, B.; Woods, R. J., The Amber biomolecular simulation programs. *J Comput Chem* **2005**, *26* (16), 1668-1688.
40. Jorgensen, W. L.; Chandrasekhar, J.; Madura, J. D.; Impey, R. W.; Klein, M. L., Comparison of Simple Potential Functions for Simulating Liquid Water. *J Chem Phys* **1983**, *79* (2), 926-935.
41. Phillips, J. C.; Braun, R.; Wang, W.; Gumbart, J.; Tajkhorshid, E.; Villa, E.; Chipot, C.; Skeel, R. D.; Kale, L.; Schulten, K., Scalable molecular dynamics with NAMD. *J Comput Chem* **2005**, *26* (16), 1781-1802.
42. Darden, T.; York, D.; Pedersen, L., Particle Mesh Ewald - an N.Log(N) Method for Ewald Sums in Large Systems. *J Chem Phys* **1993**, *98* (12), 10089-10092.
43. Roe, D. R.; Cheatham, T. E., PTRAJ and CPPTRAJ: Software for Processing and Analysis of Molecular Dynamics Trajectory Data. *J Chem Theory Comput* **2013**, *9* (7), 3084-3095.

44. Humphrey, W.; Dalke, A.; Schulten, K., VMD: Visual molecular dynamics. *J Mol Graph Model* **1996**, *14* (1), 33-38.
45. *The PyMOL Molecular Graphics System*, Version 2.4.1; Schrödinger LLC.
46. Renouprez, A. J., *Catalyst Characterization: Physical Techniques for Solid Materials*. Springer US: Boston, MA, USA, 1994.
47. Hyland, L. L.; Taraban, M. B.; Yu, Y. B., Using small-angle scattering techniques to understand mechanical properties of biopolymer-based biomaterials. *Soft Matter* **2013**, *9* (43), 10218-10228.
48. Baral, A.; Basak, S.; Basu, K.; Dehsorkhi, A.; Hamley, I. W.; Banerjee, A., Time-dependent gel to gel transformation of a peptide based supramolecular gelator. *Soft Matter* **2015**, *11* (24), 4944-4951.
49. Kruszynski, R.; Sieranski, T., Can Stacking Interactions Exist Beyond the Commonly Accepted Limits? *Cryst Growth Des* **2016**, *16* (2), 587-595.
50. Wei, L. F.; Zhang, W. B.; Ma, J. Z.; Bai, S. L.; Ren, Y. J.; Liu, C.; Simion, D.; Qin, J. B., pi-pi stacking interface design for improving the strength and electromagnetic interference shielding of ultrathin and flexible water-borne polymer/sulfonated graphene composites. *Carbon* **2019**, *149*, 679-692.
51. Boireau-Adamezyk, E.; Baillet-Guffroy, A.; Stamatias, G. N., Mobility of Water Molecules in the Stratum Corneum: Effects of Age and Chronic Exposure to the Environment. *J Invest Dermatol* **2014**, *134* (7), 2046-2049.
52. Vyumvuhore, R.; Tfayli, A.; Duplan, H.; Delalleau, A.; Manfait, M.; Baillet-Guffroy, A., Effects of atmospheric relative humidity on Stratum Corneum structure at the molecular level: ex vivo Raman spectroscopy analysis. *Analyst* **2013**, *138* (14), 4103-4111.
53. Dent, M. R.; Lopez-Duarte, I.; Dickson, C. J.; Geoghegan, N. D.; Cooper, J. M.; Gould, I. R.; Krams, R.; Bull, J. A.; Brooks, N. J.; Kuimova, M. K., Imaging phase separation in model lipid membranes through the use of BODIPY based molecular rotors. *Phys Chem Chem Phys* **2015**, *17* (28), 18393-18402.
54. Vysniauskas, A.; Lopez-Duarte, I.; Duchemin, N.; Vu, T. T.; Wu, Y. L.; Budynina, E. M.; Volkova, Y. A.; Cabrera, E. P.; Ramirez-Ornelas, D. E.; Kuimova, M. K., Exploring viscosity, polarity and temperature sensitivity of BODIPY-based molecular rotors. *Phys Chem Chem Phys* **2017**, *19* (37), 25252-25259.
55. Hiller, W.; Engelhardt, N.; Kampmann, A. L.; Degen, P.; Weberskirch, R., Micellization and Mobility of Amphiphilic Poly(2-oxazoline) Based Block Copolymers Characterized by 1-H NMR Spectroscopy. *Macromolecules* **2015**, *48* (12), 4032-4045.
56. Brown, S. P., Advanced solid-state NMR methods for characterising structure and self-assembly in supramolecular chemistry, polymers and hydrogels. *Curr Opin Colloid In* **2018**, *33*, 86-98.
57. Newberry, R. W.; Raines, R. T., The n ->pi* Interaction. *Accounts Chem Res* **2017**, *50* (8), 1838-1846.
58. Gorske, B. C.; Bastian, B. L.; Geske, G. D.; Blackwell, H. E., Local and tunable n ->pi* interactions regulate amide isomerism in the peptoid backbone. *J Am Chem Soc* **2007**, *129* (29), 8928.
59. Thurn, H.; Hoffmann, H., Evidence of Sticky Contacts between Wormlike Micelles in Viscoelastic Surfactant Solutions. *Langmuir* **2019**, *35* (37), 12192-12204.
60. Egli, M.; Sarkhel, S., Lone pair-aromatic interactions: To stabilize or not to stabilize. *Accounts Chem Res* **2007**, *40* (3), 197-205.
61. Hahn, L.; Kessler, L.; Polzin, L.; Fritze, L.; Forster, S.; Helten, H.; Luxenhofer, R., ABA Type Amphiphiles with Poly(2-benzhydryl-2-oxazine) Moieties: Synthesis, Characterization and Inverse Thermogelation. *Macromol Chem Phys* **2021**.
62. Hahn, L.; Karakaya, E.; Zorn, T.; Sochor, B.; Maier, M.; Stahlhut, P.; Forster, S.; Fischer, K.; Seiffert, S.; Poppler, A. C.; Detsch, R.; Luxenhofer, R., An Inverse Thermogelling Bioink Based on an ABA-Type Poly(2-oxazoline) Amphiphile. *Biomacromolecules* **2021**, *22* (7), 3017-3027.

Chapter III

In this chapter, the polymer library of aromatic POx/POzi structures was further expanded. Therefore, ABA type amphiphiles with changing aromatic B blocks (PPhenEtOx, poly(2-phenethyl-2-oxazine) (PPhenEtOzi), PBhOx, PBhOzi) were studied. In the case of PPhenEt-structures, the POx derivative exhibited inverse thermogelation. However, the gel properties and gelation mechanism differed from the described amphiphiles of Chapter II. The polymer A-PPhenEtOzi-A was not in the scope of the manuscript as it did not gel. Therefore, a separate figure was included here showing aqueous solutions at 20 wt.% of A-PPhenEtOzi-A and A-PPhenEtOx-A after equilibration at 5 °C.

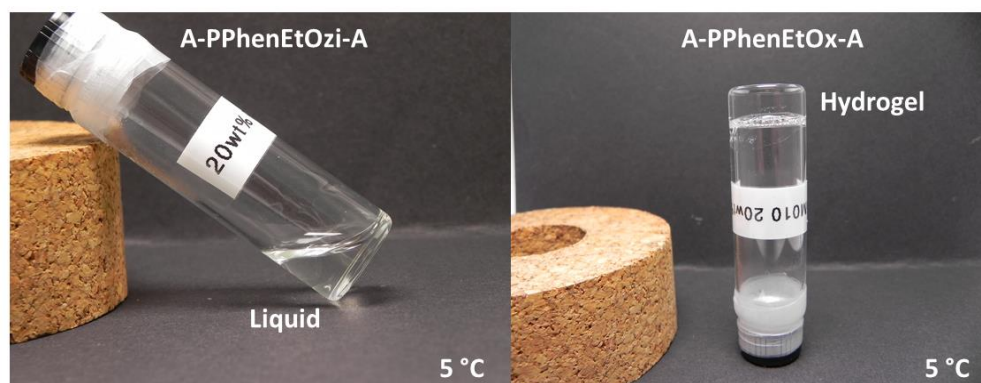


Figure M1. Comparison of A-PPhenEtOzi-A and A-PPhenEtOx-A aqueous samples at 20 wt.% equilibrated at 5 °C. Only A-PPhenEtOx-A showed inverse thermogelation.

The polymer structure and the self-assembly in aqueous solution of A-PPhenEtOzi-A was characterized in detail via NMR, gel permeation chromatography, differential scanning calorimetry and DLS during the master thesis of Matthias Maier (Supervisor: Prof. Dr. Robert Luxenhofer).

The fast and reversible sol/gel transition of A-PPhenEtOx-A samples were used in first cytocompatible bioprinting experiments.

The following publication was reprinted with permission from *Biomacromolecules* **2021**, 22 (7), 3017-3027. <https://doi.org/10.1021/acs.biomac.1c00427>; © 2021 The Authors. Published by American Chemical Society

An Inverse Thermogelling Bioink Based on an ABA-Type Poly(2-oxazoline) Amphiphile

Lukas Hahn, Emine Karakaya, Theresa Zorn, Benedikt Sochor, Matthias Maier, Philipp Stahlhut, Stefan Forster, Karl Fischer, Sebastian Seiffert, Ann-Christin Pöppler, Rainer Detsch, and Robert Luxenhofer*



Cite This: *Biomacromolecules* 2021, 22, 3017–3027



Read Online

ACCESS |



Metrics & More

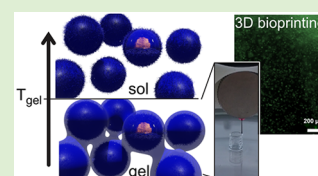


Article Recommendations



Supporting Information

ABSTRACT: Hydrogels are key components in several biomedical research areas such as drug delivery, tissue engineering, and biofabrication. Here, a novel ABA-type triblock copolymer comprising poly(2-methyl-2-oxazoline) as the hydrophilic A blocks and poly(2-phenethyl-2-oxazoline) as the aromatic and hydrophobic B block is introduced. Above the critical micelle concentration, the polymer self-assembles into small spherical polymer micelles with a hydrodynamic radius of approx 8–8.5 nm. Interestingly, this specific combination of hydrophilic and hydrophobic aromatic moieties leads to rapid thermoresponsive inverse gelation at polymer concentrations above a critical gelation concentration (20 wt %) into a macroporous hydrogel of densely packed micelles. This hydrogel exhibited pronounced viscoelastic solid-like properties, as well as extensive shear-thinning, rapid structure recovery, and good strain resistance properties. Excellent 3D-printability of the hydrogel at lower temperature opens a wide range of different applications, for example, in the field of biofabrication. In preliminary bioprinting experiments using NIH 3T3 cells, excellent cell viabilities of more than 95% were achieved. The particularly interesting feature of this novel material is that it can be used as a printing support in hybrid bioink systems and sacrificial bioink due to rapid dissolution at physiological conditions.



INTRODUCTION

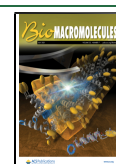
Thermosensitive water-soluble polymers undergo phase separation due to temperature changes. Phase separation upon heating is characterized by a lower critical solution temperature (LCST).¹ In contrast, in a polymer, which exhibits an upper critical solution temperature (UCST), phase separation takes place upon cooling.^{2–7} Exemplarily, Seuring et al. reported and characterized the UCST-type phase separation properties of a nonionic homopolymer poly(*N*-acryloyl glycinamide) in pure water.⁸ In a more recent study poly(acrylic acid) was copolymerized with acrylonitrile resulting in an UCST-type copolymer combining the driving forces of hydrogen bonding and hydrophobic interactions.⁹ In some cases hydrogel formation instead of phase separation/precipitation is observed. Over the last decades, most described systems in the literature are based on synthetic or natural water-soluble polymers exhibiting thermosensitive gelation upon heating.^{10–15} By introducing thermoresponsive units into the polymer structure, gelation can be induced at room or elevated temperatures as was described many times.^{16,17} Only a few examples can be found in the literature where the gelation occurred upon cooling the sample below a critical temperature (inverse gelation). Particularly prominent examples are natural biopolymers like gelatin, agarose, and pectin/chitosan systems.^{18,19} In 1998 Yoshioka et al. reported a gelatin-*g*-poly(*N*-isopropylacrylamide) graft copolymer which undergoes thermogelation (above 34 °C) and inverse thermogelation (below 10 °C) at 5 wt %.²⁰ In addition to rheological investigations, the hypothetical use of

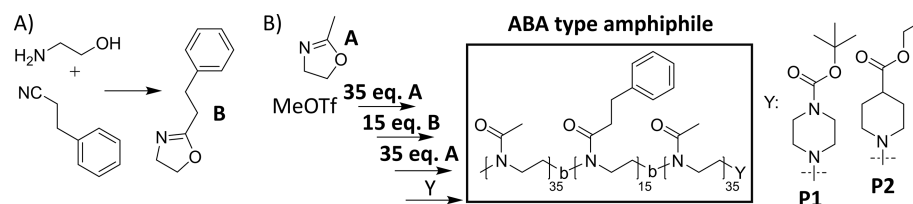
this system in smart 3D cell culture was discussed. In 2016, an inverse thermogelling ABA-type block copolymer comprising a poly(poly(ethylene glycol) methyl ether methacrylate) middle block and thermosensitive poly(acrylamide-*co*-acrylonitrile) (P(AAm-*co*-AN)) outer blocks was described.²¹ The temperature-dependent sol/gel properties were investigated in the temperature range of 8–80 °C and low polymer concentrations of 3 and 5 wt %. At 8 °C, a clear hydrogel was obtained. The sol/gel transition could be modulated by the polymer composition. By modifying a high molecular weight precursor copolymer comprising *N,N*-dimethylacrylamide and acrylic acid with hydrophobic moieties of *n*-dodecyl amine, an inverse thermogelling hydrogel could be realized.²² At 0 °C, a viscosity of approx. 1 kPas was obtained by varying the sol/gel temperature with different polymer concentrations. However, no defined application as biomaterials has been described here either. Inspired by the water transfer of natural mimosa, Chen and co-workers established a thermoresponsive bilayer system in 2018.²³ One part of the system was an inverse thermogelling hydrogel formed by poly(acrylic acid-*co*-acrylamide) (PAAc-*co*-PAAm) layers. The system was discussed as an actuator for the

Received: April 1, 2021

Revised: May 14, 2021

Published: June 8, 2021



Scheme 1. Synthesis Route^a

^a(A) Synthesis of PhenEtOx (B) adapted from Witte and Seeliger.⁴¹ (B) Synthesis of the ABA-type amphiphile by living cationic ring-opening polymerization of the hydrophilic MeOx (A) and the hydrophobic and aromatic PhenEtOx (B) using methyl triflate (MeOTf) as an initiator. To introduce the terminal Y-functionality, BOC-Pip (P1) and EIP (P2) were used as terminating reagents, respectively.

fabrication of intelligent soft materials for bioinspired applications. Nevertheless, the embedding of living cells seems to be challenging as the cells sediment before polymerization and the actual hydrogel formation is performed at 50 °C under ultraviolet light (UV) exposure. The combination of such conditions can be expected to cause significant cytotoxicity. In 2019, Hua et al. reported a multi-thermoreponsive hydrogel system, which offers the possibility of 3D shape transition upon cooling in water and oil systems.²⁴ In the last years, the interest in biofabrication, especially for tissue engineering and regenerative medicine has been rapidly growing into a promising interdisciplinary research field in its own right.²⁵ One major additive manufacturing technique used in the field is extrusion-printing of bioinks.²⁶ Often a hydrogel formulation, which enables printability and cell survival during the printing process, is preferentially used.²⁷ To date, most commonly, hydrogels based on natural biopolymers, such as gelatin, alginate, and hyaluronic acid, are used due to their generally good cytocompatibility.²⁸ However, such systems based on biopolymers can also have limitations such as less-than-ideal printability and often considerable batch-to-batch variations, especially with respect to rheological properties. The synthetic polymer platform formed by cyclic imino ethers, in particular poly(2-substituted-2-oxazoline)s (POx) and poly(2-substituted-5,6-dihydro-4H-1,3-oxazine)s (poly(2-oxazine)s, POzi), was investigated for decades as biomaterials in different applications due to good cytocompatibility and chemical versatility.^{29–32} POx/POzi-based systems were investigated as thermoresponsive materials³² for biomedical applications^{33,34} and drug delivery³⁵ approaches. However, surprisingly few reports can be found that show thermogelation of pure POx/POzi polymers in water. In 2017, Lorson et al. established a thermogelling cytocompatible and printable supramolecular hydrogel based on POx/POzi diblock copolymers.³⁶ The system comprised a hydrophilic poly(2-methyl-2-oxazoline) (PMeOx) block and a thermoresponsive poly(2-*n*-propyl-2-oxazine) (P*n*PrOzi) block of similar block length. Another thermogelling hydrogel was described by Hoogenboom and Monnerly.³⁷ A BAB triblock copolymer bearing poly(2-*n*-propyl-2-oxazoline) (P*n*PrOx) (B) and hydrophilic poly(2-ethyl-2-oxazoline) blocks (A) showed sol/gel transitions upon heating, but extremely high degrees of polymerization were required. In 2019, Lübtow et al. described a different, much shorter ABA triblock copolymer, which forms stable, but relatively weak and barely printable, thermogelling hydrogels.³⁸ Very recently, the first inverse thermogelling hydrogel formed by POx/POzi-based block copolymers was described.³⁹ Here, the ABA triblock copolymer comprising the hydrophilic PMeOx (A) and aromatic hydrophobic poly(2-phenyl-2-oxazine) (PPheOzi, B) blocks undergoes gelation at lower temperatures. The stable hydrogel was

formed by entangled self-assembled wormlike micelles, which form from spherical micelles upon cooling, leading to gelation. A potential application of such system as a biomaterial ink was mentioned. The limiting factor for using this system as a component in a bioink formulation is its gelation kinetics. Upon cooling, it takes about 1 h to form a hydrogel suitable for printing, which is a rather long time if viable cells are to be embedded. Very recently, a novel gelation mechanism driven by interactions between the hydrophilic PMeOx blocks and the aromatic PPheOzi blocks was suggested for this system.⁴⁰ Due to this interaction, the volume fraction of the hydrophilic to hydrophobic domain changes, leading to the morphology switch. Interestingly, polymers containing very similar 2-phenyl- and 2-benzyl-2-oxazoline and 2-benzyl-2-oxazine did not undergo this gelation. Here, a further structural variation and a new ABA triblock copolymer containing aromatic poly(2-phenethyl-2-oxazoline) (PPhenEtOx, B) is described, which can be seen as a higher homologue or structural isomer of previously studied polymers, and it again undergoes inverse thermogelation in aqueous solution. In contrast to previously studied material, a rapid thermoresponsive sol/gel transition was observed, which facilitates its use as a bioink component, as was demonstrated. The additional two CH₂-groups in the sidechain as well as the different backbones compared to the previously described inverse hydrogel platform, leads to distinct differences in the gelation mechanism as in the present case, the size and morphology of the polymer self-assemblies do not change with temperature.

EXPERIMENTAL SECTION

In general, all substances and reagents for the monomer synthesis and polymerization were purchased from Sigma-Aldrich (Steinheim, Germany) and TCI-chemicals (Eschborn, Germany) and were used as-received without further purification unless otherwise stated. For polymerization, all substances were refluxed over CaH₂ for several hours and distilled prior usage. The solvent benzonitrile (PhCN) was dried over phosphorus pentoxide.

The monomer synthesis of 2-phenethyl-2-oxazoline (Schemes 1A and S1) was carried out as described by Witte and Seeliger.⁴¹ For the reaction, 1 equiv of 3-phenylpropionitrile, 1.2 equiv of amino-ethanol, and catalytic amounts of zinc acetate dihydrate were added to a argon-flushed flask and heated to 130 °C under reflux for several days until the color of the reaction mixture turned brown. Reaction progress was controlled by ¹H NMR spectroscopy. After completion, the mixture was dissolved in dichloromethane and washed three times with H₂O. The organic phase was dried with MgSO₄ and concentrated. The raw product was refluxed with CaH₂ and purified with vacuum distillation under an argon atmosphere yielding a colorless liquid. The resulting compound 2-phenethyl-2-oxazoline was characterized via refractive index, gas chromatography-electrospray ionization-mass spectrometry (GC-ESI-MS) analysis, and ¹H and ¹³C nuclear magnetic resonance (NMR) spectroscopy (see the Supporting Information).

Refractive index measurements of the synthesized monomer 2-phenethyl-2-oxazoline was performed on a RFM 870 refractometer from Bellingham + Stanley at 20 °C (Farnborough, England).

The monomer was further analyzed via mass spectrometry using an Agilent 5977B MDS system coupled with a gas chromatography system Agilent 7820A. The GC system was equipped with an Agilent 19091S-433UI HP-5 ms ultraraint column (30 m × 250 μm × 0.25 μm). The temperature gradient was set from 40 to 300 °C with a constant heat rate of 15 °C/min and a constant flow of 1 mL/min.

The ABA-type copolymers were synthesized following a general procedure based on previous reports (detailed description in the Supporting Information).^{42,43}

NMR was performed on a Bruker Fourier 300 (¹H: 300.12 MHz) spectrometer at 298 K from Bruker BioSpin (Rheinstetten, Germany) and calibrated using the residual protonated solvent signal.

Gel permeation chromatography (GPC) was performed on a Polymer Standard Service PSS (Mainz, Germany) SECURITY system with the following specifications: pump mod. 1260 infinity, MDS RI-detector mod. 1260 infinity (Agilent Technologies, Santa Clara, California, USA), precolumn: 50 × 8 mm PSS PFG linear M, and 2 columns: 300 × 8 mm PSS PFG linear M (particle size 7 μm; pore size 0.1–1.000 kg/mol) with hexafluoroisopropanol (HFIP, containing 3 g/L potassium trifluoroacetate (KTFA)) as eluent calibrated against PEG standards with molar masses from 0.1 to 1000 kg/mol. The columns were held at 40 °C and the flow rate was set to 0.7 mL/min. Prior to each measurement, samples were dissolved in the eluent and filtered through 0.2 μm PTFE filters (Rotilabo, Karlsruhe, Germany) to remove particles, if any.

Rolling ball viscosity experiments were performed on a LOVIS 2000 M microviscometer from Anton Paar (Graz, Austria) using a LOVIS 1.8 capillary and a steel ball of 1.5 mm diameter. Prior to viscosity measurements the density was determined at 5 and 40 °C using a DMA 4100 M density meter from Anton Paar (Graz, Austria). A temperature scan from 5 °C → 40 °C and 40 °C → 5 °C of a 10, 15, and 20 wt % aqueous sample was performed in an automated angle mode with 3 min of temperature equilibration to establish the temperature-dependent dynamic viscosity.

For pyrene fluorescence assay, 40 μL pyrene solution (25 μM) in acetone was added to glass vials. The solvent was evaporated and 3 mL of polymer solutions of different concentrations in deionized water were added to yield final polymer concentrations of $1 \times 10^{-7} \rightarrow 5 \times 10^{-5}$ M and a fixed pyrene concentration of 5×10^{-7} M. The pyrene fluorescence emission spectra ($\lambda_{\text{excitation}}$: 330 nm at 25 °C) were recorded on a FP-8300 spectrofluorometer system from Jasco (Gross-Umstadt, Germany) between 360 and 400 nm. To determine the critical micelle concentration (CMC), the I_1/I_3 ratios as a function of polymer concentration were fitted using the Boltzmann fit function, which is given by

$$y = \frac{A_1 - A_2}{1 + e^{(x-x_0)/\Delta x}} + A_2 \quad (1)$$

where A_1 and A_2 are the upper and lower limits of the sigmoid, x_0 is the center of the sigmoid, and Δx is directly related to the range where the abrupt change of the sigmoid occurs. The onset of an abrupt decrease is defined as the CMC and can be determined via eq 2, which is given by

$$x(\text{CAC}) = x_0 - 2\Delta x \quad (2)$$

Rheology investigations were recorded on an Anton Paar (Ostfildern, Germany) Physica MCR 301 system utilizing a plate–plate geometry (25 mm diameter) equipped with a solvent trap and Peltier element for temperature control. All aqueous samples were measured after complete dissolution in Millipore water and a concentration of 20 wt % at 5 °C. A temperature sweep from 5 to 40 °C followed by a cooling sequence to 5 °C was carried out in an oscillation mode (angular frequency 10 rad/s and amplitude 0.1%) and a constant heating or cooling rate of 0.1 °C/s. For investigations of viscoelastic behavior, the linear viscoelastic region (LVE) was determined by performing an amplitude sweep (0.02% → 500%) using a fixed angular frequency of 10 rad/s. Subsequently, a frequency

sweep (0.1 rad/s → 100 rad/s) was performed at a fixed strain deformation of 0.1%. For dispense plotting, rheological preconditions of the hydrogel are shear-thinning properties, defined force resistance profile, and fast structure recovery after deformation. For steady shear experiments, the control shear rate mode was used (0.001 1/s → 1000 1/s). The pronounced viscosity η decrease was fitted using the power law expression (eq 3)

$$\eta = K \cdot (\dot{\gamma})^{n-1} \quad (3)$$

where K is the consistency index, n is the flow index, and $\dot{\gamma}$ is the applied shear rate.

During a steady stress sweep (5 Pa → 1500 Pa) the onset value of viscosity decrease is referred as the yield point of the hydrogel system. To investigate the structure recovery properties, two different recovery testing experiments were performed. During the ORO (oscillation-rotational-oscillation) experiment, a low strain deformation of 0.5% is followed by a high shear rate of 100 1/s. In the ROR (rotational-oscillation-rotational) experiment, a low shear rate region of 0.1 1/s is followed by a high strain of 100%.

Dynamic light scattering (DLS) experiments were performed on an ALV SP125 (Langen, Germany) equipped with a He-Ne laser (22 mW, $\lambda = 632.8$ nm) and a single optical avalanche photodiode detector or an ALV CGS-3 multidetection goniometry system (Langen, Germany) equipped with a He-Ne laser (632.8 nm) and eight optical avalanche photodiode detectors with a detector angle distance of 16°. Scattering angles from 30 to 125° were measured with a 5° angle interval for aqueous samples (15, 20, 25, and 40°) and 30 to 70° for a methanol sample (20 °C, correlation time 60 s, average of 3–5 runs). Prior to each measurement, samples were dissolved in methanol (10 g/L) and filtered through 0.02 μm Anotop membrane filters from Whatman GE Healthcare followed by Millex-LG 0.2 μm. After evaporation of methanol, the samples were dissolved in prefiltered (Millex-LG 0.2 μm) Millipore water (containing 2 mM NaNO₃) or methanol. Samples (1 g/L) were filtered (Millex-LG 0.2 μm) into dust-free cuvettes under laminar flow. The decay of the electric field-time autocorrelation function (ACF) was fitted using biexponential fit functions (eq 4) with respect to polydispersities:

$$g_1(t) = a_1 \cdot e^{-(t/\tau_1)} + a_2 \cdot e^{-(t/\tau_2)} \quad (4)$$

with the amplitudes a_i and the decay time $\tau_i = \frac{1}{q^2 D_i}$, q being the absolute value of the scattering vector and D the translational diffusion coefficient which is indirectly proportional to the hydrodynamic radius R_h (Stokes–Einstein equation):

$$R_h = \frac{k_B \cdot T}{6 \cdot \pi \cdot \eta \cdot D} \quad (5)$$

with Boltzmann constant k_B and the viscosity of the solvent η .

For transmission electron microscopy (TEM) investigations, the polymer was dissolved in ultrapure water to a final concentration of 20 g/L. For the negative stain method, 400 mesh copper–rhodium grids (maxtaform) with a homemade carbon layer were glow-discharged in air for 1.5 min at medium power in a Harrick PDC-002 plasma cleaner. The 20 g/L sample was diluted (1/125) and 8 μL was incubated on the grids for 1 min before blotting (Whatman filter paper No 50). Subsequently, the grids were washed with water (3×) and with 2% (w/v) uranyl acetate (3×). For imaging, a single-tilt room temperature holder in a FEI Tecnai T12 Spirit transmission electron microscope equipped with a LaB₆ emitter at 120 kV was used. Images were recorded with an Eagle CCD camera under low-dose conditions. The micrographs were binned two times resulting in a pixel size of 4.4 Å/pix at the specimen level.

The temperature-dependent ¹H NMR analysis was performed on a Bruker Avance III HD 600 spectrometer (Karlsruhe, Germany) operating at 600.4 MHz with a BBFO 5 mm probe. ¹H NMR experiments at different temperatures (5–40 °C) of a 20 wt % hydrogel sample in D₂O/H₂O (1:1) were performed without sample spinning and 16 scans. The sample was kept for 10 min at the desired temperature prior to each measurement. Temperature calibration was

done using 4% MeOH in MeOD and 80% ethylene glycol in DMSO- d_6 . All recorded spectra were referenced using the temperature-dependent HDO signal. For a more quantitative characterization of the temperature-induced phase transition, the fraction p was calculated with the integrals $I(T)$ and $I(T_0)$ at the respective temperatures T and T_0 using the following equation:⁴⁴

$$p = 1 - \frac{I(T)}{I(T_0) \cdot \frac{T_0}{T}} \quad (6)$$

The highest signal intensity was measured at 40 °C, which was chosen to be T_0 . Reductions of signal intensity caused by inhibited molecular mobility due to gelation and viscosity increase were quantified by values of $p < 0$.

For small-angle X-ray scattering (SAXS) experiments, an in-house setup at the Chair of X-ray Microscopy at the University of Würzburg was used, which was built by Fraunhofer EZRT (Fürth, Germany). It consists of a MicroMax-007 HF X-ray source (Rigaku, Japan) and an EIGER R 1M detector unit (Dectris, Switzerland). The sample-detector distance can be varied between 5 cm and 3.5 m, which corresponds to possible Q -values between 0.005 and 5 Å⁻¹. The complete setup is operated in a vacuum below 0.1 mbar to reduce air scattering. The sample solution (20 wt %) was placed in quartz capillaries (inner diameter: 1 mm, wall thickness: 10 μm) (Hampton Research, Aliso Viejo, California), which were positioned perpendicularly to the X-ray beam. The presented experiments were done at sample-detector distances of 57, 565, and 1560 mm with an integration time of 15 min for the shortest distance and 240 min for the two longer configurations. All distances were calibrated using a silver behenate standard sample. Data were acquired for different temperatures between 5 and 40 °C. To achieve thermal equilibrium, the sample was kept at the desired temperature for 15 min prior to each measurement. The SAXS data, which were obtained at the two largest distances, were calibrated in terms of absolute intensities using glassy carbon as a secondary calibration standard.^{45,46} The scattering curves of the hydrogel were obtained by azimuthal integration and corrections taking the sample thickness, X-ray transmission, detector accuracy, setup geometry, and solvent scattering into account, by following the standard procedures described in the literature.⁴⁷ A detailed description of the fitting procedure using a hard sphere model can be found in the Supporting Information.

For scanning electron microscopy (SEM) of the native hydrogel structure, we investigated a cryogenic sample preparation procedure. For this, hydrogel samples were placed between two aluminum holders ($d = 3$ mm), both containing a notch with a diameter of 2 mm, enclosing the sample and rapidly frozen in slush nitrogen (SN) at -210 °C. The samples were then transferred into a sputter coater with a Leica EM VCT100 cryo-shuttle at -140 °C (Leica Microsystems ACE 400, Wetzlar, Germany). Here, the upper half of the sample was knocked off to create a fresh fractured surface and freeze-etched at -85 °C for 15 min under vacuum ($<1 \times 10^{-3}$ mbar). The samples were finally sputtered with 3 nm platinum and transferred with the cryo-shuttle into the SEM chamber. The morphology of the fractured surfaces was imaged at -140 °C, by detecting SE using acceleration voltages of 2 or 8 kV.

To investigate the printability of 20 wt % hydrogel samples, a compact bench-top 3D bioprinter (BioX, Cellink, Sweden) working on the principle of an extrusion-based technology was used. The printhead and the print bed were cooled to 8 °C prior to each fabrication process. The printing speed was set to 10 mm/s and a pressure of 120–160 kPa was applied (nozzle: 25 G, stainless steel, length of 6.35 mm). First, the printing resolution was investigated by increasing the strand-center to strand-center distance stepwise from 0.5 mm \rightarrow 0.75 mm \rightarrow 1 mm \rightarrow 1.5 mm \rightarrow 2 mm (layer height 0.25 mm). To investigate the steadiness of the hydrogel, a strand collapse test was investigated as described by Ribeiro et al.⁴⁸ The distance between the two edition points increased from 0.1 \rightarrow 0.2 \rightarrow 0.4 \rightarrow 0.9 \rightarrow 1.7 cm. Finally, real 3D-printing was performed by printing a 20-layered tubular construct of 5 mm total height and 5 mm diameter using the parameters already described.

To evaluate the cytocompatibility of POx/alginate (20:1 wt %) bioinks, the viability of embedded NIH 3T3 cells (ATCC, Germany, 1 Mio/mL) was investigated. As a reference, sodium alginate (VIVA Pharm, PH176, 1 wt %) was used. After homogenous cell distribution at 37 °C a simple one-layered square structure (Figure S6) was printed at 10 °C with a printing pressure of 50 kPa and a printing speed of 5 mm/s. Stabilization after printing was performed using a 0.1 M CaCl₂ aqueous solution (10 min). The cross-linked scaffolds were incubated for 24 h at 37 °C in cell culture medium (DMEM high glucose (Gibco from Sigma-Aldrich)) supplemented with 1% pen/strep, 2% glutamine (Thermo Fisher), and 10% bovine calf serum from Corning under controlled conditions (5% CO₂, 95% relative humidity). To assess the cell viability, printed NIH 3T3 cells were stained inside the scaffolds using Calcein AM (Invitrogen, Thermo Fisher) after 24 h of cultivation, whereas blue nuclei acid stain (DAPI) (Thermo Fisher) was used to visualize nuclei of all embedded cells. ImageJ software was used to determine the cell viability using automatic cell counting in three fluorescence images ($n = 3$) of three different samples ($n = 3$) obtained with an epifluorescence microscope (Zeiss Observer, Germany) using the following equation:

$$\text{cell viability} = \frac{[\text{number of living cells}]}{[\text{number of cell nuclei}]} \quad (7)$$

RESULTS AND DISCUSSION

Two batches of an ABA-triblock copolymer PMeOx₃₅-*b*-PPhenEtOx₁₅-*b*-PMeOx₃₅ (=A-PPhenEtOx-A) (Scheme 1B) were synthesized by living cationic ring-opening polymerization (LCROP) and characterized by ¹H NMR spectroscopy (Figures S2 and S5) and GPC (Figures S1 and S4). The successful termination using different terminating agents (P1: 1-Boc-piperazine (BOC-Pip), P2: ethyl isonipecotatate (EIP)), the comparable degree of polymerization of approx 90 repeating units, and a ratio of PMeOx/PPhenEtOx of 4 were verified by the corresponding signal intensities in ¹H NMR spectra.

Via GPC, the number average molar mass M_n and the dispersity \mathcal{D} (M_w/M_n) of both batches were compared after completion of every single block and purification of the final polymer product. Both batches show reasonably narrow molar mass size distributions (\mathcal{D} (P1) = 1.12, \mathcal{D} (P2) = 1.17) and an increase in the number average molar mass during the polymerization reaction, indicative of the living polymerization. The primary structural difference between these novel polymers in comparison to the previously described aromatic amphiphiles is one additional methylene group in the sidechains of every repeat unit in the central B block, which leads to significantly altered physicochemical properties. Very similar to previously described ABA-type amphiphiles, the novel polymers form stable nanoscale micelles in aqueous solutions above the CMC.^{42,49,50} The investigated A-PPhenEtOx-A polymer exhibited a rather low CMC of 0.3 μM as determined by pyrene fluorescence measurement in dependency of the polymer concentration (Figure 1A,B). The hydrodynamic radius of these nanoscale aggregates was determined via DLS at different scattering angles (Figure 1C,D). In the nonselective solvent, methanol, the hydrodynamic radius of an individual polymer chain was determined as ca. 2.4 nm. In contrast, in the selective solvent water, the polymers self-assemble into micelles with a hydrodynamic radius of ca. 8 nm. The low dependence on the scattering angle (30 \rightarrow 125°) suggests spherical micelles of low polydispersity (Figure 1D). The spherical morphology of the micelles could be further corroborated by means of TEM (Figure 1E).

Inspired by our previous finding for a similar ABA triblock,^{39,40} we investigated the thermoresponsive properties.

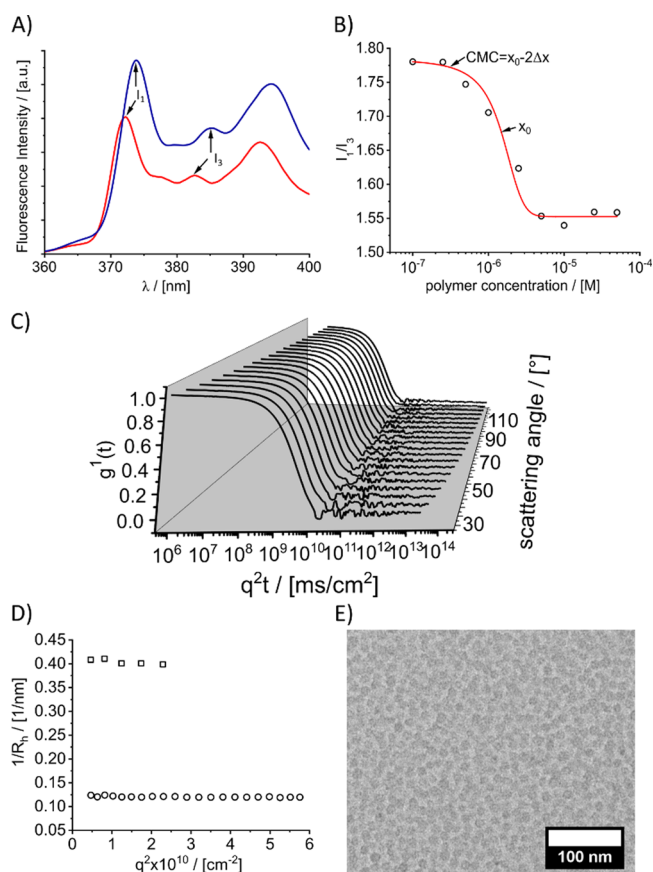


Figure 1. Self-assembly of A-PPhenEtOx-A at low polymer concentration in aqueous solution. (A) Characteristic pyrene emission spectra at 25 °C and polymer concentrations of 10^{-7} M (red) and 10^{-5} M (blue). (B) I_1/I_3 intensity ratio of the pyrene signal at different polymer concentrations fitted with the Boltzmann fit function (R^2 : 0.99707). (C) Autocorrelation functions of DLS experiments of 1 g/L aqueous polymer solution containing 2 mM NaNO_3 at 20 °C and different scattering angles (30 \rightarrow 125° in 5° steps). (D) Inverse hydrodynamic radius in dependency of the scattering vector q^2 of 1 g/L aqueous polymer solution containing 2 mM NaNO_3 (circle) compared to 1 g/L polymer solutions in methanol as nonselective solvent (square). (E) TEM image from aqueous polymer solution stained with uranyl acetate showing spherical micelles.

Indeed it was observed that when the concentration exceeded 20 wt %, a hydrogel was formed at low temperature (Figure 2A,B (P2), Figure S3 (P1)). However, investigating this phenomenon in more detail, crucial differences in gel strength, critical concentration, and temperature compared to the previously described material (PMeOx₃₅-b-PPhEOzi₁₅-b-PMeOx₃₅) were found. The thermoresponsive behavior was evaluated by rolling ball viscosimetry at different concentrations (10, 15, and 20 wt %) combined with a heating (5 °C \rightarrow 40 °C) and cooling (40 °C \rightarrow 5 °C) ramp. At 10 and 15 wt %, the viscosity decreases steadily with increasing temperature ($\eta_{5\text{ °C}}(10\text{ wt \%}) = 9\text{ mPas} \rightarrow \eta_{40\text{ °C}}(10\text{ wt \%}) = 3\text{ mPas}$, $\eta_{5\text{ °C}}(15\text{ wt \%}) = 50\text{ mPas} \rightarrow \eta_{40\text{ °C}}(15\text{ wt \%}) = 11\text{ mPas}$) without any notable features. The cooling and heating ramps yield very similar values. In contrast, at 20 wt % the viscosity increases very fast below a critical temperature of approx. 22 °C eventually trapping the ball, whereupon no further values are obtained (Figure 2C). Increasing the temperature, the polymer solution again flows freely forming a moderately viscous solution with dynamic viscosity values of approx. 70 mPas at 40 °C. A notable hysteresis

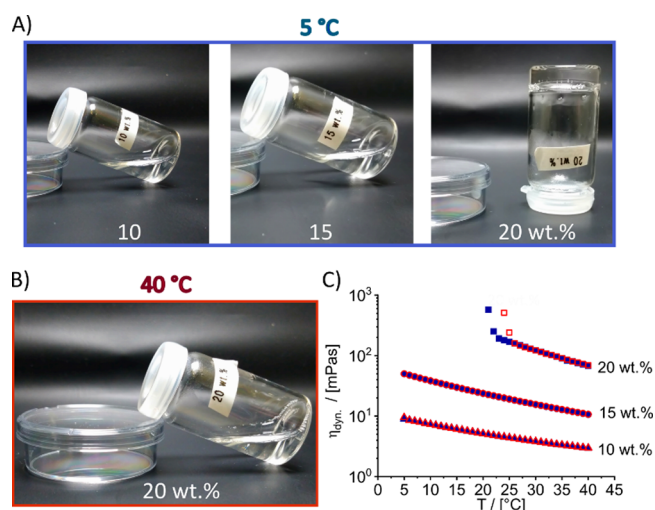


Figure 2. Increasing concentration of A-PPhenEtOx-A leads to hydrogel formation. (A) Pictures of aqueous solutions at 5 °C and different polymer concentrations (10 \rightarrow 15 \rightarrow 20 wt %). (B) Photographic images of aqueous solution at 40 °C and a polymer concentration of 20 wt %. (C) Temperature-dependent viscosity measurements (rolling ball system) at different polymer concentrations (blue and filled symbols: cooling, red and open symbols: heating).

of approximately 3 °C was observed in this experiment. In addition, we characterized the inverse gelation by rheology (Figure S7). Again, a hysteresis of the gel temperature T_{gel} ($G' = G''$) between heating ($T_{\text{gel}} = 25\text{ °C}$) and cooling ($T_{\text{gel}} = 22\text{ °C}$) can be seen. The gelation is fully reversible and a stable hydrogel ($G' \gg G''$) below T_{gel} was observed.

Compared to the recently described ABA triblocks featuring a PPhEOzi hydrophobic B block, there are notable differences in the present system. First, a significantly higher concentration is needed ($c_{\text{gel}}[\text{A-PPhEOzi-A}] = 5\text{ wt \%}$ ³⁹ vs $c_{\text{gel}}[\text{A-PPhenEtOx-A}] = 20\text{ wt \%}$). Second, the critical temperature is lower ($T_{\text{gel}}[\text{A-PPhEOzi-A}] = 32\text{ °C}$ ³⁹ vs $T_{\text{gel}}[\text{A-PPhenEtOx-A}] = 22\text{--}25\text{ °C}$). Third, the gelation kinetics is much faster compared to the previous system (slow gelation³⁹ \leftrightarrow rapid gelation).

To investigate the thermoresponsive aggregation on a molecular level, temperature-dependent ¹H NMR experiments were conducted (Figure 3A,B). At 5 °C, the signals attributed to the polymer backbone (3.45 ppm) and CH_3 -sidechain (2.00 ppm) of the hydrophilic building blocks are visible, albeit broad and featureless. In the aromatic region (6.92 ppm) of the spectrum, no signals are visible at 5 °C. This can be readily explained by very short transversal relaxation times T_2^* of the moieties in the hydrophobic micellar core, which are densely packed and apparently less hydrated so that efficient spin–spin relaxation can occur. As previously discussed, a gradual increase of the temperature from 5 to 40 °C causes liquefaction, and the signals of the hydrophilic as well as the hydrophobic part become narrower and more defined (Figure 3A,B) as molecular mobility increases. Most interestingly, this is particularly visible in the aromatic region of the spectrum. An increasing, albeit still featureless signal is visible with increasing temperature, which is caused by more flexible units of the hydrophobic core. Likewise, the reversibility of aggregation could be demonstrated by a subsequent cooling sequence, whereby the initial aggregation is achieved (Figure 3B). A more quantitative insight was obtained by comparing the integrated NMR intensities of different polymer signals as a function of temperature (Figure 3C). A p -value (eq 6) of zero indicates the highest mobility in the liquid

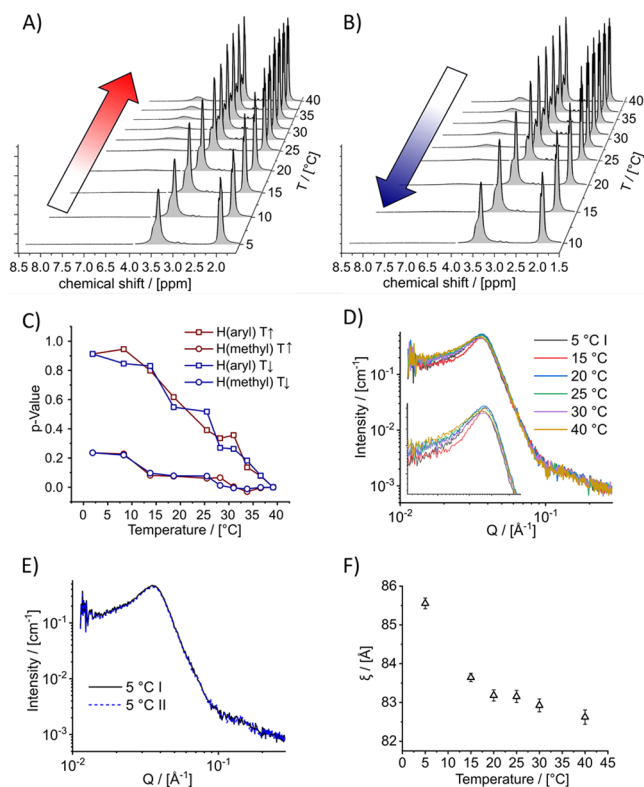


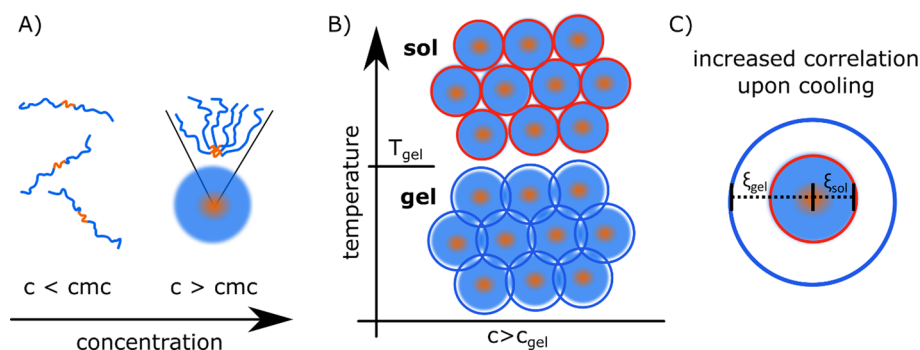
Figure 3. Temperature-dependent aggregation by means of ^1H -NMR spectroscopy and SAXS experiments. ^1H NMR spectra of a 20 wt % hydrogel sample ($\text{H}_2\text{O}/\text{D}_2\text{O}$, 1:1) at different temperatures (A) 5 °C \rightarrow 40 °C, (B) 40 °C \rightarrow 5 °C. (C) p -Values for different polymer signals as a function of temperature. (D) SAXS of a 20 wt % aqueous hydrogel sample at different temperatures (5, 15, 20, 25, 30, and 40 °C). After the initial measurement, the sample was cooled again to 5 °C (E). (F) Correlation length ξ as a function of temperature obtained from the scattering curves (error bars: numerical error).

state (40 °C). The aromatic CH-protons are most strongly influenced yielding high p -values (close to 1 = little signal intensity left) in the gel state. Liquefaction due to increased temperature caused an increasing signal resulting in a steady p -value decrease up to 40 °C for the hydrophobic signals. The previously described slow gelling system based on A-PPheOzi-

A³⁹ showed a constant p -value in the gel state and a rapid p -value decrease upon liquefaction. The hydrophilic shell and the backbone are affected to a much lesser extent, similar to previous reports on the aggregation behavior of thermoresponsive phase separation of different POx-based polymers.⁴⁴ In contrast to DLS, the polymer sol/gel could be investigated at concentrations needed for hydrogel formation (20 wt %) using SAXS. The scattering curves suggest a feature size of 16–18 nm with only small changes with changing the temperature (Figure 3D). However, the small changes observed proved to be fully reversible as evidenced by scattering curves at 5 °C being superimposable after a heating/cooling cycle to 40 °C (Figure 3E). To characterize the scattering curves in more detail, hard-sphere model fit functions were employed (detailed information in the Supporting Information and Table S1). In particular, we focused to obtain the correlation length ξ , the distance in which neighboring micelles correlate with each other. Interestingly, ξ increased with decreasing temperature with a strong increase in particular between 15 and 5 °C. An increased correlation length means that the micelles interact over a greater distance. Interestingly, on comparing the temperature-dependent rheology and correlation length it, becomes apparent that the correlation is not completely straightforward.

In fact, the correlation length only increases strongly below the T_{gel} at 15 °C and below, while gelation ($G' \geq G''$) occurs already at 22 °C. Interestingly, below 15 °C, the p -value for the pMeOx shows a marked increase, indicating reduced mobility. Looking more closely at the temperature-dependent rheology, the longer correlation lengths coincide with the formation of a plateau for both G' and G'' . In contrast, the values for G' and G'' at T_{gel} are about three orders of magnitudes lower than at this plateau. It appears at this point that the hydrogel formation of A-PPhenEtOx-A is caused by densely packed spherical micelles with reduced mobility at low temperature due to increased intermicelle correlation, somewhat resembling the aggregation behavior of Pluronic F127. However, Pluronic F127 forms a hydrogel upon heating because of a thermoresponsive poly-(propylene glycol) block whereas A-PPhenEtOx-A does so upon cooling and does not contain a polymer block which is thermoresponsive in itself. Accordingly, it appears obvious that on the molecular level, the thermogelation of A-PPhenEtOx-A and Pluronic F127 is not related. Also, comparing to the wormlike hydrogel system comprising A-PPheOzi-A⁴⁰

Scheme 2. Self-Assembly of the ABA-Type Triblock Copolymer and Inverse Thermogelation^a



^a(A) At very low polymer concentration single polymer chains are present. The aqueous polymer solution has a low viscosity. Above the CMC, the amphiphile self-assembles into spherical micelles. (B) Increase in concentration above T_{gel} leads to a micellar solution with moderate viscosity and macromolecular mobility. Decrease in temperature below T_{gel} leads to an increase in the intermicelle correlation, physical network formation, and a macroscopic gelation. (C) Schematic illustration of the different correlation lengths at different temperatures. Upon cooling, the correlation of individual micelles increases.

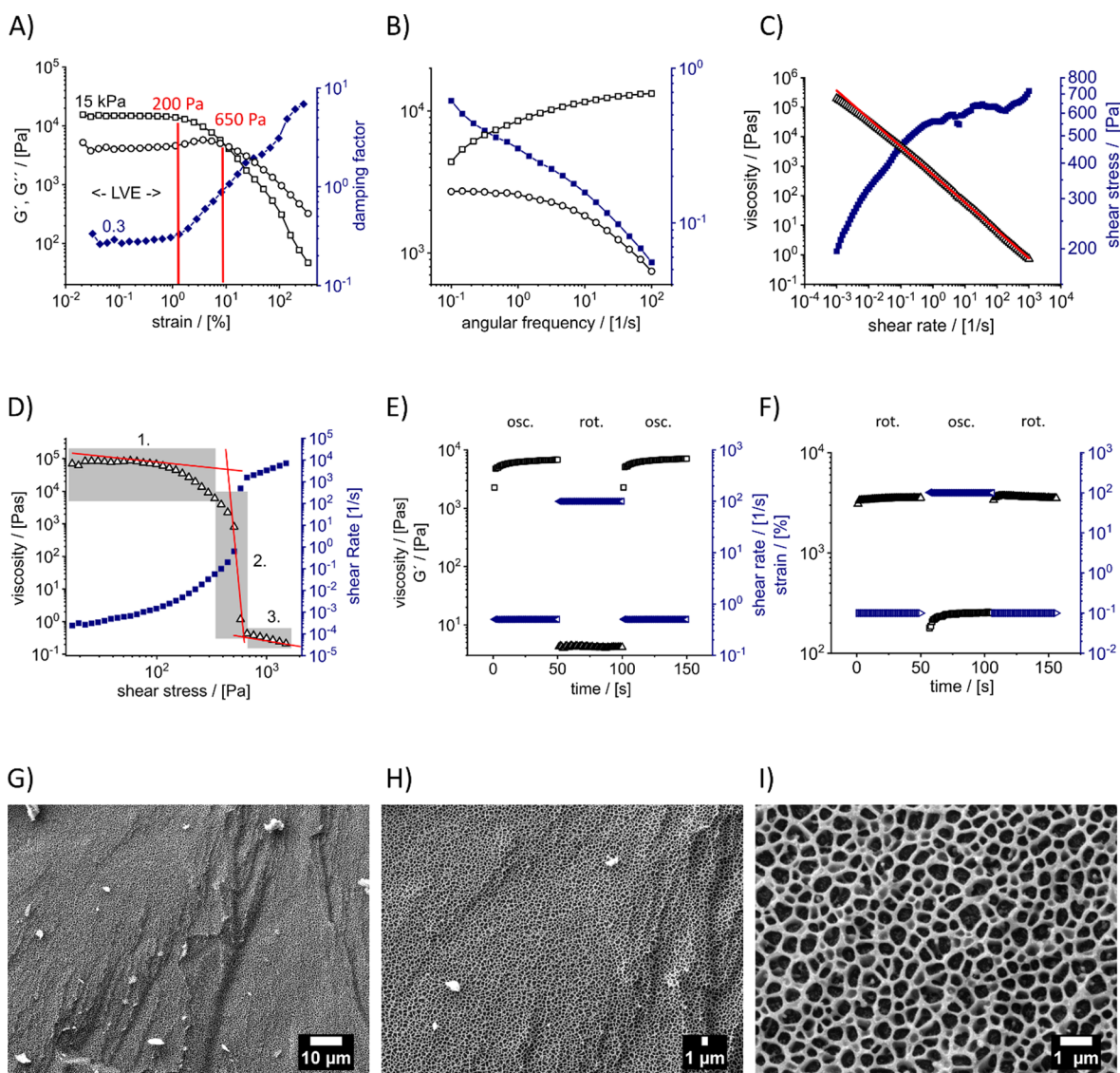


Figure 4. Rheological characterization for dispense plotting applications and cryoSEM analysis of the A-PPhenEtOx-A hydrogel at 5 °C. (A) Amplitude sweep of the 20 wt % hydrogel at 5 °C and an angular frequency of 10 rad/s with storage moduli ($G' = \text{square}$), loss moduli ($G'' = \text{circle}$), and damping factor (filled square) is shown. (B) Frequency sweep with a fixed amplitude of 0.1%. (C) Viscosity (triangle) and shear stress (filled square) in dependency of the applied shear rate for a 20 wt % hydrogel. (D) Viscosity (triangle) and shear rate (filled square) as a function of the applied shear stress in the steady shear stress experiment. (E) ORO recovery test of the hydrogel. (F) ROR three-step recovery. (G–I) CryoSEM images of the 20 wt % hydrogel at 1 k \times , 2 k \times and 10 k \times magnification.

with different slope regions in the SAXS pattern, significant differences were obtained. To summarize, the amphiphile self-assembles into spherical micelles ($R_h(15\text{ °C}) = 8.5 \pm 0.1\text{ nm}$, $R_h(25\text{ °C}) = 8.4 \pm 0.1\text{ nm}$, and $R_h(40\text{ °C}) = 8.5 \pm 0.2\text{ nm}$) at all investigated temperatures above the CMC (0.3 μM). In comparison, the previously described inverse gelling system with PheOzi instead of PhenEtOx as hydrophobic repeat units showed a pronounced temperature dependency of the apparent R_h ($R_h(15\text{ °C}) > 100\text{ nm}$) connected to a change in micellar morphology from spherical to worm.⁴⁰ Here, the increased concentration leads to the formation of highly concentrated dispersion of spherical micelles, similar to the situation well known for Pluronic F127. However, in contrast to the present system, Pluronic F127 only forms micelles above the critical temperature of the poly(propylene glycol) blocks. Decreasing the temperature resulted in reduced micellar mobility which was observed due to an increasing correlation length between

neighboring micelles, consequently leading to the inverse gelation (Scheme 2).

As previously mentioned, stimuli-responsive hydrogels have been utilized in different biomaterial applications.⁵¹ Recently, different approaches were established to overcome limitations in the so-called biofabrication window, especially in bioprinting.⁵² One approach is to improve printability by support materials and sacrificial materials, while retaining cell viability by utilizing biological components, cell-friendly cross-linking, and mild printing conditions. The search for suitable hydrogel platforms is an ongoing challenge due to multiple specific and sometimes contradictive requirements. Appropriate gelation kinetics, good printability, and cytocompatibility are key requirements for hydrogels during bioink design. Therefore, the viscoelastic properties of the present inverse thermogelling platform were thoroughly investigated via rheology. In the pronounced viscoelastic region (LVE, end of LVE and flow point ($G' =$

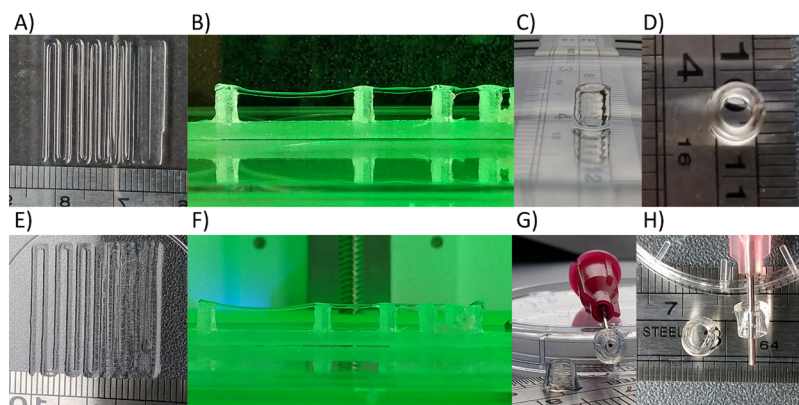


Figure 5. Extrusion printing of a A-PPhenEtOx-A 20 wt % hydrogel (A–D) and a hydrogel blend of A-PPhenEtOx-A and alginate (E–H) at 8 °C (nozzle 25 G, speed: 10 mm/s). (A, E) Filament fusion test to visualize printing resolution. (B, F) Filament collapse test by printing bridges of increasing distances. (C, D, G, H) Printed 20 layer (5 × 5 mm cylindrical tube structures) constructs (top and side view).

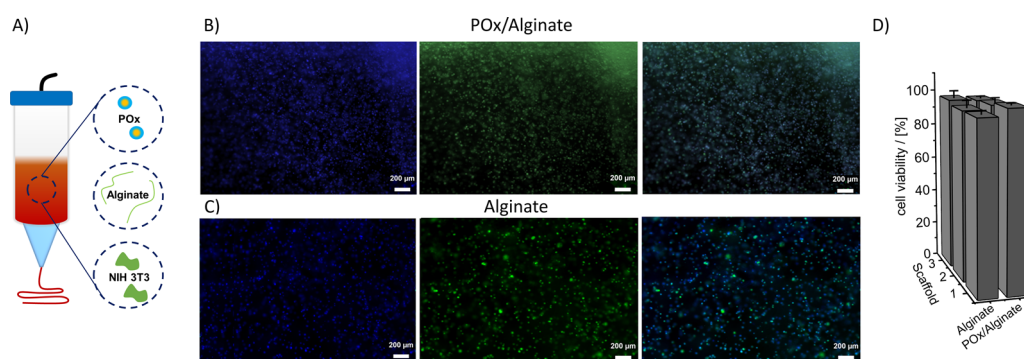


Figure 6. Cytocompatible bioprinting of POx/alginate-based bioinks using NIH 3T3 cells (A). (B, C) Single and merged fluorescence images of embedded NIH 3T3 cells in POx/alginate (upper row) and alginate (bottom row) stained with DAPI (blue) and Calcein AM (green) after printing, stabilization with CaCl_2 , and 24 h of incubation. (D) Cell viability of NIH 3T3 cells in three different printed scaffolds of alginate and POx/alginate hydrogel blend.

G'') marked with red lines), a constant storage modulus G' of 14.8 ± 0.3 kPa was obtained with a low damping factor of 0.3 ± 0.02 , which suggest a stable viscoelastic hydrogel (Figure 4A). Interestingly, the hydrogel exhibits a profound dependency on the frequency (Figure 4B). Increasing the frequency leads to increased G' and decreased G'' values, i.e., the solid-like character is amplified with the dampening factor reaching values <0.03 at 500 s^{-1} . To utilize a hydrogel as 3D-printable ink in different printing applications, three major rheological considerations must be addressed, namely, pronounced shear-thinning, defined force resistance, and fast structure recovery properties.⁵³ With the increasing shear rate, the viscosity of the present hydrogel decreases following a power law expression with a flow index of 0.05 ± 0.004 , indicating very pronounced shear-thinning (Figure 4C). Even at very low shear rates of 0.001 s^{-1} , no viscosity plateau is reached and shear stress values of ca. 200 Pa are measured at this point. In contrast, at very high shear rates of 1000 s^{-1} , the viscosity values are very low (ca. 1 Pa s) with shear stress values increasing up to 750 Pa. To obtain the yield point and the force resistance of the hydrogel, the viscosity was plotted as a function of the applied shear stress and split up in three regions (Figure 4D). Below the critical stress, almost constant viscosity values between 10^4 and 10^5 Pa s with very low shear rates (between 10^{-4} and 10^{-5} 1/s) were determined (1). At a certain stress, the viscosity decreases very fast with increasing shear rate values to low viscosity values (2). The onset of 440 Pa is determined via two tangents. At high shear stress

values of $800 \rightarrow 1500$ Pa, plateau values for the viscosity and shear rate of 0.1 Pa s and $10^3 \rightarrow 10^4 \text{ s}^{-1}$ are reached (3). Structure recovery was tested using a three-step test, designed as ORO and ROR experiments, altering low and high strain regimes (Figure 4E,F). In both cases, the structure recovered very fast and the initial values were obtained during the experiments, which we interpret to show rapid and complete structure recovery. To obtain insights into the hydrogel morphology, we conducted cryogenic scanning electron microscopy (*cryoSEM*) (Figure 4G–I). A rather homogenous porous structure with pores in the range of several hundred nanometers was obtained. In comparison to a recently described hydrogel based on a A-PPhOzi-A triblock copolymer, the presently described A-PPhenEtOx-A hydrogel has significantly smaller pores.³⁹ The strong frequency dependence in combination with smaller pore sizes compared to the previously published hydrogels consisting of wormlike micelles further underlines the differences between the individual gelation mechanism. In summary, the novel hydrogel shows promising viscoelastic characteristics for bioprinting.

Based on favorable rheological properties, the printability of the hydrogel was investigated using extrusion-based printing (Figure 5A–D). Additionally, a hydrogel blend comprising the POx-based hydrogel and alginate was prepared, printed, and stabilized with CaCl_2 (Figure 5E–H). Alginate hydrogels are widely used in biofabrication as alginate is easily cross-linked by the addition of CaCl_2 after printing to stabilize the constructs.

However, the printability of pure sodium alginate without the addition of viscosity enhancers or modifications is very low.⁵⁴ First, we screened for the highest achievable resolution by printing hydrogel lines with a decreasing line distance, from 2 → 1.5 → 1 → 0.75 → 0.5 mm (Figure 5A,E). Even at a layer distance of 0.75 mm every individual strand could be distinguished and no strand fusion was observed. Additionally, the collapse of suspended filaments was investigated.⁴⁸ A free hanging hydrogel strut over a total distance of 1.7 cm could be realized without significant strand sag (Figure 5B,F). Based on these promising results, a first real 3D construct was printed (Figure 5C,D,G,H, Supporting Movie 1). A 20-layered cylindrical construct with a diameter of 5 mm and a total height of 5 mm was printed. The structure stayed intact, and no significant collapse was observed. The structure of the stabilized POx/alginate tubular construct was preserved even after 24 h of incubation in PBS solution at 37 °C (Figure 5G,H).

Finally, a first bioprinting process was performed and the cytocompatibility was investigated using the POx/alginate (20:1 wt %) hydrogel blend in comparison to pure alginate (1 wt %) (Figure 6A–D) after 24 h. After dissolving the polymers in cell culture medium, the cells were dispersed in the homogeneous free flowing viscous liquid at 37 °C. The relatively high viscosity of the bioink precursor at 37 °C (see Figure 2) prevented significant cell sedimentation. The bioink blend was transferred to the precooled bioprinter equipped with a cooling system. Using the pronounced inverse gelation of A-PPhenEtOx-A as described above, cell-laden constructs were obtained and stabilized via cross-linking of alginate using CaCl₂ aqueous solution. After 24 h of incubation, cell staining was performed and quantified. Overall, the bioprinting process of POx-based bioinks was found to be highly cytocompatible (cell viability >95%) and no significant difference with respect to cytocompatibility was observed for the hydrogel blend in comparison to plain alginate solution. Plain A-PPhenEtOx-A was not tested for cytocompatibility during bioprinting. On the one hand, it is known from the literature that very similar polymers do not show cytotoxic properties up to a concentration of 100 g/L.^{39,42} On the other hand, addition of 1 wt % alginate should not have any significant effect in terms of cytocompatibility.

CONCLUSIONS

Here, a new ABA-type amphiphile based on poly(2-oxazoline)s with an aromatic hydrophobic central block of poly(2-phenethyl-2-oxazoline) B was described. Above the CMC, small spherical nanoscale micelles were confirmed. At or above 20 wt %, an inverse and fast sol/gel transition was observed upon cooling, due to densely packed micelles and investigated via temperature-dependent ¹H NMR and SAXS experiments. Favorable rheological properties, such as pronounced viscoelastic solid-like properties, shear-thinning, and structure recovery properties led to very good 3D-printability of the investigated hydrogel. In a hydrogel blend comprising the readily printable POx-based polymer and the biopolymer alginate, stable constructs were obtained. First cytocompatible bioprinting at approximately 10 °C for a A-PPhenEtOx-A/alginate hybrid system concluded the study and opens a wide range of different applications in the field of biofabrication.

ASSOCIATED CONTENT

Supporting Information

The Supporting Information is available free of charge at <https://pubs.acs.org/doi/10.1021/acs.biomac.1c00427>.

Detailed description of monomer and polymer synthesis and characterization and an overview and detailed description of SAXS analysis (PDF)

Additional movie of the extrusion printing process (MP4)

AUTHOR INFORMATION

Corresponding Author

Robert Luxenhofer – Functional Polymer Materials, Chair for Advanced Materials Synthesis, Institute for Functional Materials and Biofabrication, Department of Chemistry and Pharmacy, Julius-Maximilians-University Würzburg, Würzburg 97070, Germany; Soft Matter Chemistry, Department of Chemistry and Helsinki Institute of Sustainability Science, Faculty of Science, University of Helsinki, Helsinki 00014, Finland; orcid.org/0000-0001-5567-7404; Email: robert.luxenhofer@helsinki.fi

Authors

Lukas Hahn – Functional Polymer Materials, Chair for Advanced Materials Synthesis, Institute for Functional Materials and Biofabrication, Department of Chemistry and Pharmacy, Julius-Maximilians-University Würzburg, Würzburg 97070, Germany

Emine Karakaya – Institute of Biomaterials, Friedrich Alexander University of Erlangen-Nürnberg, Erlangen 91058, Germany

Theresa Zorn – Institute of Organic Chemistry, Julius-Maximilians-University Würzburg, Würzburg 97074, Germany

Benedikt Sochor – Chair for X-Ray Microscopy, Julius-Maximilians-University Würzburg, Würzburg 97074, Germany; orcid.org/0000-0002-5772-8065

Matthias Maier – Functional Polymer Materials, Chair for Advanced Materials Synthesis, Institute for Functional Materials and Biofabrication, Department of Chemistry and Pharmacy, Julius-Maximilians-University Würzburg, Würzburg 97070, Germany

Philipp Stahlhut – Department for Functional Materials in Medicine and Dentistry, Julius-Maximilians-University Würzburg, Würzburg 97070, Germany

Stefan Forster – Functional Polymer Materials, Chair for Advanced Materials Synthesis, Institute for Functional Materials and Biofabrication, Department of Chemistry and Pharmacy, Julius-Maximilians-University Würzburg, Würzburg 97070, Germany

Karl Fischer – Department of Chemistry, Johannes Gutenberg University Mainz, Mainz 55128, Germany

Sebastian Seiffert – Department of Chemistry, Johannes Gutenberg University Mainz, Mainz 55128, Germany; orcid.org/0000-0002-5152-1207

Ann-Christin Pöppler – Institute of Organic Chemistry, Julius-Maximilians-University Würzburg, Würzburg 97074, Germany; orcid.org/0000-0002-0624-1708

Rainer Detsch – Institute of Biomaterials, Friedrich Alexander University of Erlangen-Nürnberg, Erlangen 91058, Germany

Complete contact information is available at:

<https://pubs.acs.org/doi/10.1021/acs.biomac.1c00427>

Notes

The authors declare the following competing financial interest(s): L.H. and R.L. are listed as inventors on a patent pertinent to some materials in the present work.

ACKNOWLEDGMENTS

The authors gratefully acknowledge support by the Deutsche Forschungsgemeinschaft (DFG, German Research Foundation)-project number 326998133-TRR225 (subprojects A03, B06). Furthermore, we thank the Deutsche Forschungsgemeinschaft for funding the crossbeam scanning electron microscope Zeiss CB 340 (INST 105022/58-1 FUGG) within the DFG State Major Instrumentation Programme. In addition, light scattering experiments were possible through support of the Deutsche Forschungsgemeinschaft (INST 93/774-1 FUGG). We gratefully acknowledge access to electron microscopy facilities provided by Prof. Bettina Böttcher at the Rudolf Virchow Center, Julius-Maximilians-University Würzburg.

REFERENCES

- (1) Zhang, Q.; Weber, C.; Schubert, U. S.; Hoogenboom, R. Thermoresponsive Polymers with Lower Critical Solution Temperature: From Fundamental Aspects and Measuring Techniques to Recommended Turbidimetry Conditions. *Mater. Horiz.* **2017**, *4*, 109–116.
- (2) Seuring, J.; Agarwal, S. Non-Ionic Homo- and Copolymers with H-Donor and H-Acceptor Units with an UCST in Water. *Macromol. Chem. Phys.* **2010**, *211*, 2109–2117.
- (3) Seuring, J.; Agarwal, S. Polymers with Upper Critical Solution Temperature in Aqueous Solution. *ACS Macro Lett.* **2012**, *33*, 1898–1920.
- (4) Shimada, N.; Ino, H.; Maie, K.; Nakayama, M.; Kano, A.; Maruyama, A. Ureido-Derivatized Polymers Based on Both Poly-(Allylurea) and Poly(L-Citrulline) Exhibit UCST-Type Phase Transition Behavior under Physiologically Relevant Conditions. *Biomacromolecules* **2011**, *12*, 3418–3422.
- (5) Meiswinkel, G.; Ritter, H. A New Type of Thermoresponsive Copolymer with UCST-Type Transitions in Water: Poly(N-Vinylimidazole-co-1-Vinyl-2-(Hydroxymethyl)imidazole). *Macromol. Rapid Commun.* **2013**, *34*, 1026–1031.
- (6) Aseyev, V.; Tenhu, H.; Winnik, F., *Non-Ionic Thermoresponsive Polymers in Water*. Springer, Berlin, Heidelberg, 2010, 242, 29–89.
- (7) Niskanen, J.; Tenhu, H. How to Manipulate the Upper Critical Solution Temperature (UCST)? *Polym. Chem.* **2017**, *8*, 220–232.
- (8) Seuring, J.; Bayer, F. M.; Huber, K.; Agarwal, S. Upper Critical Solution Temperature of Poly(N-acryloyl glycinamide) in Water: A Concealed Property. *Macromolecules* **2012**, *45*, 374–384.
- (9) Zhao, C.; Dolmans, L.; Zhu, X. X. Thermoresponsive Behavior of Poly(acrylic acid-co-acrylonitrile) with a UCST. *Macromolecules* **2019**, *52*, 4441–4446.
- (10) Plunkett, K. N.; Zhu, X.; Moore, J. S.; Leckband, D. E. PNIPAM Chain Collapse Depends on the Molecular Weight and Grafting Density. *Langmuir* **2006**, *22*, 4259–4266.
- (11) Gupta, N. R.; Torris, A. T. A.; Wadgaonkar, P. P.; Rajamohanam, P. R.; Ducouret, G.; Hourdet, D.; Creton, C.; Badiger, M. V. Synthesis and Characterization of PEPO Grafted Carboxymethyl Guar and Carboxymethyl Tamarind as New Thermo-Associating Polymers. *Carbohydr. Polym.* **2015**, *117*, 331–338.
- (12) Karakasyan, C.; Lack, S.; Brunel, F.; Maingault, P.; Hourdet, D. Synthesis and Rheological Properties of Responsive Thickeners Based on Polysaccharide Architectures. *Biomacromolecules* **2008**, *9*, 2419–2429.
- (13) Bokias, G.; Mylonas, Y.; Staikos, G.; Bumbu, G. G.; Vasile, C. Synthesis and Aqueous Solution Properties of Novel Thermoresponsive Graft Copolymers Based on a Carboxymethylcellulose Backbone. *Macromolecules* **2001**, *34*, 4958–4964.
- (14) Koonar, I.; Zhou, C.; Hillmyer, M. A.; Lodge, T. P.; Siegel, R. A. ABC Triblock Terpolymers Exhibiting Both Temperature- and pH-Sensitive Micellar Aggregation and Gelation in Aqueous Solution. *Langmuir* **2012**, *28*, 17785–17794.
- (15) Taribagil, R. R.; Hillmyer, M. A.; Lodge, T. P. Hydrogels from ABA and ABC Triblock Polymers. *Macromolecules* **2010**, *43*, 5396–5404.
- (16) Niu, H.; Wang, F.; Weiss, R. A. Hydrophobic/Hydrophilic Triblock Copolymers: Synthesis and Properties of Physically Cross-Linked Hydrogels. *Macromolecules* **2015**, *48*, 645–654.
- (17) Tuncaboylu, D. C.; Argun, A.; Sahin, M.; Sari, M.; Okay, O. Structure Optimization of Self-Healing Hydrogels Formed Via Hydrophobic Interactions. *Polymer* **2012**, *53*, 5513–5522.
- (18) Djabourov, M.; Leblond, J.; Papon, P. Gelation of Aqueous Gelatin Solutions. II. Rheology of the Sol-Gel Transition. *J. Phys. France* **1988**, *49*, 333–343.
- (19) Birch, N. P.; Barney, L. E.; Pandres, E.; Peyton, S. R.; Schiffman, J. D. Thermal-Responsive Behavior of a Cell Compatible Chitosan/Pectin Hydrogel. *Biomacromolecules* **2015**, *16*, 1837–1843.
- (20) Yoshioka, H.; Mori, Y.; Tsukikawa, S.; Kubota, S. Thermoreversible Gelation on Cooling and on Heating of an Aqueous Gelatin-Poly(N-isopropylacrylamide) Conjugate. *Polym. Adv. Technol.* **1998**, *9*, 155–158.
- (21) Fu, W.; Zhao, B. Thermoreversible Physically Crosslinked Hydrogels from UCST-Type Thermosensitive ABA Linear Triblock Copolymers. *Polym. Chem.* **2016**, *7*, 6980–6991.
- (22) Parmar, I. A.; Shedje, A. S.; Badiger, M. V.; Wadgaonkar, P. P.; Lele, A. K. Thermo-Reversible Sol-Gel Transition of Aqueous Solutions of Patchy Polymers. *RSC Adv.* **2017**, *7*, 5101–5110.
- (23) Zheng, J.; Xiao, P.; Le, X.; Lu, W.; Théato, P.; Ma, C.; Du, B.; Zhang, J.; Huang, Y.; Chen, T. Mimosa Inspired Bilayer Hydrogel Actuator Functioning in Multi-Environments. *J. Mater. Chem. C* **2018**, *6*, 1320–1327.
- (24) Hua, L.; Xie, M.; Jian, Y.; Wu, B.; Chen, C.; Zhao, C. Multiple-Responsive and Amphibious Hydrogel Actuator Based on Asymmetric UCST-Type Volume Phase Transition. *ACS Appl. Mater. Interfaces* **2019**, *11*, 43641–43648.
- (25) Groll, J.; Boland, T.; Blunk, T.; Burdick, J. A.; Cho, D.; Dalton, P. D.; Derby, B.; Frogacs, G.; Li, Q.; Mironov, V. A.; Moroni, L.; Nakamura, M.; Shu, W.; Takeuchi, S.; Vozzi, G.; Woodfield, T. B. F.; Xu, T.; Yoo, J. J.; Malda, J. Biofabrication: Reappraising the Definition of an Evolving Field. *Biofabrication* **2016**, *8*, No. 13001.
- (26) Groll, J.; Burdick, J. A.; Cho, D. W.; Derby, B.; Gelinsky, M.; Heilshorn, S. C.; Jüngst, T.; Malda, J.; Mironov, V. A.; Nakayama, K.; Ovsianikov, A.; Sun, W.; Takeuchi, S.; Yoo, J. J.; Woodfield, T. B. F. A Definition of Bioinks and Their Distinction from Biomaterial Inks. *Biofabrication* **2019**, *11*, No. 013001.
- (27) Chimene, D.; Kaunas, R.; Gaharwar, A. K. Hydrogel Bioink Reinforcement for Additive Manufacturing: A Focused Review of Emerging Strategies. *Adv. Mater.* **2020**, *32*, No. 1902026.
- (28) Valot, L.; Martinez, J.; Mehdi, A.; Subra, G. Chemical Insights into Bioinks for 3D Printing. *Chem. Soc. Rev.* **2019**, *48*, 4049–4086.
- (29) Glassner, M.; Vergaelen, M.; Hoogenboom, R. Poly(2-oxazoline)s: A Comprehensive Overview of Polymer Structures and Their Physical Properties. *Polym. Int.* **2018**, *67*, 32–45.
- (30) Lorson, T.; Lübtow, M. M.; Wegener, E.; Haider, M. S.; Borova, S.; Nahm, D.; Jordan, R.; Sokolski-Papkov, M.; Kabanov, A. V.; Luxenhofer, R. Poly(2-oxazoline)s Based Biomaterials: A Comprehensive and Critical Update. *Biomaterials* **2018**, *178*, 204–280.
- (31) Luxenhofer, R.; Jordan, R. Poly(2-oxazoline)s (POx) in Biomedical Applications. *Mater. Matters* **2013**, *8*, 70–73.
- (32) Dargaville, T. R.; Park, J. R.; Hoogenboom, R. Poly(2-oxazoline) Hydrogels: State-of-the-Art and Emerging Applications. *Macromol. Biosci.* **2018**, *18*, No. e1800070.
- (33) Harris, J. M.; Bentley, M. D.; Moreadith, R. W.; Viegas, T. X.; Fang, Z.; Yoon, K.; Weimer, R.; Dizman, B.; Nordstierna, L. Tuning Drug Release from Polyoxazoline-Drug Conjugates. *Eur. Polym. J.* **2019**, *120*, No. 109241.

- (34) Moreadith, R. W.; Viegas, T. X.; Bentley, M. D.; Harris, J. M.; Fang, Z.; Yoon, K.; Dizman, B.; Weimer, R.; Rae, B. P.; Li, X.; Rader, C.; Standaert, D.; Olanow, W. Clinical Development of a Poly(2-oxazoline) (POz) Polymer Therapeutic for the Treatment of Parkinson's Disease – Proof of Concept of POz as a Versatile Polymer Platform for Drug Development in Multiple Therapeutic Indications. *Eur. Polym. J.* **2017**, *88*, 524–552.
- (35) Sedlacek, O.; Hoogenboom, R. Drug Delivery Systems Based on Poly(2-oxazoline)s and Poly(2-oxazine)s. *Adv. Ther.* **2020**, *3*, No. 1900168.
- (36) Lorson, T.; Jaksch, S.; Lübtow, M. M.; Jüngst, T.; Groll, J.; Lühmann, T.; Luxenhofer, R. A Thermogelling Supramolecular Hydrogel with Sponge-Like Morphology as a Cytocompatible Bioink. *Biomacromolecules* **2017**, *18*, 2161–2171.
- (37) Monnery, B. D.; Hoogenboom, R. Thermoresponsive Hydrogels Formed by Poly(2-oxazoline) Triblock Copolymers. *Polym. Chem.* **2019**, *10*, 3480–3487.
- (38) Lübtow, M. M.; Mrlik, M.; Hahn, L.; Altmann, A.; Beudert, M.; Lühmann, T.; Luxenhofer, R. Temperature-Dependent Rheological and Viscoelastic Investigation of a Poly(2-methyl-2-oxazoline)-b-poly(2-iso-butyl-2-oxazoline)-b-poly(2-methyl-2-oxazoline)-Based Thermogelling Hydrogel. *J. Funct. Biomater.* **2019**, *10*, 36.
- (39) Hahn, L.; Maier, M.; Stahlhut, P.; Beudert, M.; Flegler, V.; Forster, S.; Altmann, A.; Töppke, F.; Fischer, K.; Seiffert, S.; Böttcher, B.; Lühmann, T.; Luxenhofer, R. Inverse Thermogelation of Aqueous Triblock Copolymer Solutions into Macroporous Shear-Thinning 3D Printable Inks. *ACS Appl. Mater. Interfaces* **2020**, *12*, 12445–12456.
- (40) Hahn, L.; Zorn, T.; Kehrein, J.; Kielholz, T.; Sochor, B.; Lisitsyna, E. S.; Durandin, N.; Laaksonen, T.; Aseyev, V.; Sotriffer, C.; Windbergs, M.; Pöppler, A. C.; Luxenhofer, R., *Unravelling a Novel Sol-gel Transition Mechanism in Polymer Self-assemblies: An Order-order Transition Based on Specific Molecular Interactions Between Hydrophilic and Hydrophobic Polymer Blocks*, 2021. DOI: 10.26434/chemrxiv.14362892.v1.
- (41) Witte, H.; Seeliger, W. Simple Synthesis of 2-Substituted 2-Oxazolines and 5,6-Dihydro-4h-1,3-Oxazines. *Angew. Chem., Int. Ed. Engl.* **1972**, *11*, 287–288.
- (42) Hahn, L.; Lübtow, M. M.; Lorson, T.; Schmitt, F.; Appelt-Menzel, A.; Schobert, R.; Luxenhofer, R. Investigating the Influence of Aromatic Moieties on the Formulation of Hydrophobic Natural Products and Drugs in Poly(2-oxazoline)-Based Amphiphiles. *Biomacromolecules* **2018**, *19*, 3119–3128.
- (43) Lübtow, M. M.; Hahn, L.; Haider, M. S.; Luxenhofer, R. Drug Specificity, Synergy and Antagonism in Ultrahigh Capacity Poly(2-oxazoline)/Poly(2-oxazine) Based Formulations. *J. Am. Chem. Soc.* **2017**, *139*, 10980–10983.
- (44) Konefal, R.; Spěváček, J.; Černoch, P. Thermoresponsive Poly(2-oxazoline) Homopolymers and Copolymers in Aqueous Solutions Studied by NMR Spectroscopy and Dynamic Light Scattering. *Eur. Polym. J.* **2018**, *100*, 241–252.
- (45) Dreiss, C. A.; Jack, K. S.; Parker, A. P. On the Absolute Calibration of Bench-Top Small-Angle X-Ray Scattering Instruments: A Comparison of Different Standard Methods. *J. Appl. Crystallogr.* **2006**, *39*, 32–38.
- (46) Zhang, F.; Ilavsky, J.; Long, G. G.; Quintana, J. P. G.; Allen, A. J.; Jemian, P. R. Glassy Carbon as an Absolute Intensity Calibration Standard for Small-Angle Scattering. *Metall. Mater. Trans. A* **2010**, *41*, 1151–1158.
- (47) Pauw, B. R.; Smith, A. J.; Snow, T.; Terrill, N. J.; Thünemann, A. F. The Modular Small-Angle X-Ray Scattering Data Correction Sequence. *J. Appl. Crystallogr.* **2017**, *50*, 1800–1811.
- (48) Ribeiro, A.; Blokzijl, M. M.; Levato, R.; Visser, C. W.; Castilho, M.; Hennink, W. E.; Vermonden, T.; Malda, J. Assessing Bioink Shape Fidelity to Aid Material Development in 3D Bioprinting. *Biofabrication* **2018**, *10*, No. 014102.
- (49) Luxenhofer, R.; Schulz, A.; Roques, C.; Li, S.; Bronich, T. K.; Batrakova, E. V.; Jordan, R.; Kabanov, A. V. Doubly Amphiphilic Poly(2-oxazoline)s as High-Capacity Delivery Systems for Hydrophobic Drugs. *Biomaterials* **2010**, *31*, 4972–4979.
- (50) Seo, Y.; Schulz, A.; Han, Y.; He, Z.; Bludau, H.; Wan, X.; Tong, J.; Bronich, T. K.; Sokolsky, M.; Luxenhofer, R.; Jordan, R.; Kabanov, A. V. Poly(2-oxazoline) Block Copolymer Based Formulations of Taxanes: Effect of Copolymer and Drug Structure, Concentration, and Environmental Factors. *Polym. Adv. Technol.* **2015**, *26*, 837–850.
- (51) Sood, N.; Bhardwaj, A.; Mehta, S.; Mehta, A. Stimuli-Responsive Hydrogels in Drug Delivery and Tissue Engineering. *Drug Delivery* **2016**, *23*, 748–770.
- (52) Malda, J.; Visser, J.; Melchels, F. P.; Jüngst, T.; Hennink, W. E.; Dhert, W. J. A.; Groll, J.; Huttmacher, D. W. 25th Anniversary Article: Engineering Hydrogels for Biofabrication. *Adv. Mater.* **2013**, *25*, 5011–5028.
- (53) Naomi, P.; Willi, S.; Thomas, B.; Ferry, M.; Jürgen, G.; Tomasz, J. Proposal to Assess Printability of Bioinks for Extrusion-Based Bioprinting and Evaluation of Rheological Properties Governing Bioprintability. *Biofabrication* **2017**, *9*, No. 044107.
- (54) Hazur, J.; Detsch, R.; Karakaya, E.; Kaschta, J.; Teßmar, J.; Schneidereit, D.; Friedrich, O.; Schubert, D. W.; Boccaccini, A. R. Improving Alginate Printability for Biofabrication: Establishment of a Universal and Homogeneous Pre-Crosslinking Technique. *Biofabrication* **2020**, *12*, No. 045004.

In the second part of the chapter, POx/POzi based polymers with benzhydryl moieties were described. Interestingly, again an inverse thermogelling polymer was obtained. Here, the POzi derivative showed physical inverse thermogelation. After comprehensive characterization of the polymer structures, the hydrogel was discussed in the context of biofabrication. From a self-assembly perspective, significant differences were obtained in comparison to the two previously described inverse thermogelling systems.

The following open access publication was reprinted from *Macromolecular Chemistry and Physics* **2021**, <https://doi.org/10.1002/macp.202100114>

ABA Type Amphiphiles with Poly(2-benzhydryl-2-oxazine) Moieties: Synthesis, Characterization and Inverse Thermogelation

Lukas Hahn, Larissa Keßler, Lando Polzin, Lars Fritze, Stefan Forster, Holger Helten, and Robert Luxenhofer*

Thermoresponsive polymers are frequently involved in the development of materials for various applications. Here, polymers containing poly(2-benzhydryl-2-oxazine) (pBhOzi) repeating units are described for the first time. The homopolymer pBhOzi and an ABA type amphiphile comprising two flanking hydrophilic A blocks of poly(2-methyl-2-oxazoline) (pMeOx) and the hydrophobic aromatic pBhOzi central B block (pMeOx-*b*-pBhOzi-*b*-pMeOx) are synthesized and the latter is shown to exhibit inverse thermogelling properties at concentrations of 20 wt.% in water. This behavior stands in contrast to a homologue ABA amphiphile consisting of a central poly(2-benzhydryl-2-oxazoline) block (pMeOx-*b*-pBhOx-*b*-pMeOx). No inverse thermogelling is observed with this polymer even at 25 wt.%. For 25 wt.% pMeOx-*b*-pBhOzi-*b*-pMeOx, a surprisingly high storage modulus of ≈ 22 kPa and high values for the yield and flow points of 480 Pa and 1.3 kPa are obtained. Exceeding the yield point, pronounced shear thinning is observed. Interestingly, only little difference between self-assemblies of pMeOx-*b*-pBhOzi-*b*-pMeOx and pMeOx-*b*-pBhOx-*b*-pMeOx is observed by dynamic light scattering while transmission electron microscopy images suggest that the micelles of pMeOx-*b*-pBhOzi-*b*-pMeOx interact through their hydrophilic coronas, which is probably decisive for the gel formation. Overall, this study introduces new building blocks for poly(2-oxazoline) and poly(2-oxazine)-based self-assemblies, but additional studies will be needed to unravel the exact mechanism.


1. Introduction

Materials chemistry and design can be used to develop smart materials that react to external stimuli and thus adapt or change their properties. In recent decades, many new materials and polymers have been developed that respond to various stimuli.^[1–3] A controlled chemical reaction,^[4] modification of polymer properties by changing the temperature,^[5] the pH,^[6] the absorption of electromagnetic radiation^[7] or the action of mechanical,^[8] magnetic,^[9] or electrical forces^[10] have been described in the literature. More specifically, thermoresponsive polymers change their properties by changing temperature beyond critical transition temperature. Turbidity effects, precipitation, and in some cases gelation can be observed. In addition to biomedicine,^[11] these properties are also used in separation science,^[12] water purification,^[13] and optical devices.^[14] The thermoresponsive transitions arise from various changes in polymer–polymer and polymer–solvent interactions at different temperatures. A lower critical solution temperature (LCST) system is characterized by a miscible

L. Hahn, L. Keßler, L. Polzin, S. Forster, R. Luxenhofer
 Functional Polymer Materials, Chair for Advanced Materials Synthesis,
 Institute for Functional Materials and Biofabrication, Department of
 Chemistry and Pharmacy
 Julius-Maximilians-University Würzburg
 Röntgenring 11, Würzburg 97070, Germany
 E-mail: robert.luxenhofer@helsinki.fi

L. Keßler, R. Luxenhofer
 Soft Matter Chemistry, Department of Chemistry and Helsinki Institute
 of Sustainability Science, Faculty of Science
 University of Helsinki
 P.O. Box 55, Helsinki 00014, Finland

L. Fritze, H. Helten
 Institute of Inorganic Chemistry and Institute for Sustainable Chemistry
 & Catalysis with Boron (ICB)
 Julius-Maximilians-University Würzburg
 Am Hubland, Würzburg 97074, Germany

 The ORCID identification number(s) for the author(s) of this article can be found under <https://doi.org/10.1002/macp.202100114>

© 2021 The Authors. Macromolecular Chemistry and Physics published by Wiley-VCH GmbH. This is an open access article under the terms of the Creative Commons Attribution License, which permits use, distribution and reproduction in any medium, provided the original work is properly cited.

DOI: 10.1002/macp.202100114

polymer-solvent phase and strong polymer-solvent interactions below a certain temperature, which abruptly phase separates above that critical temperature.^[15] The opposite is observed in upper critical solution temperature (UCST) systems with relatively weak polymer-solvent interactions, wherein the polymer-polymer interactions exceed polymer-solvent interactions below a critical transition temperature.^[15] In aqueous solution, most described systems fall into the LCST category, due to polar moieties in the polymer and hydrogen-bonding capability between polymers and water molecules. In general, non-covalent interactions play a decisive role in the solvation and self-assembly of synthetic and natural polymers. Hydrogen bonding,^[16] π - π stacking,^[17] dipole-dipole,^[18] metal-ligand coordination,^[19] or hydrophobic interactions^[20] have been established to study and direct the self-assembly of polymers in solution, and to modulate their responsiveness.

Controlled—ideally living—copolymerization is critical to access well-controlled polymer architectures to study defined self-assembly. Living cationic ring-opening polymerization of cyclic imino ethers gives the pseudo-polypeptides of poly(2-oxazolines) (POx) and poly(2-oxazines) (POzi), which have seen attention in the past decades as biomaterials in drug delivery and more recently in tissue engineering and biofabrication.^[21,22] The LCST type behavior of POx and POzi is well understood.^[23–26] The living character of the polymerization allows the synthesis of tailor-made block copolymers with pronounced amphiphilic character leading to self-assembly into spherical^[27] or cylindrical micelles^[28] and vesicles.^[29] Inspired by the family of (thermogelling) Pluronic, Zahoranova et al. synthesized a polymer library of ABA and BAB triblock copolymers based on the hydrophilic poly(2-methyl-2-oxazoline) (pMeOx) (A) and thermoresponsive poly(2-*n*-propyl-2-oxazoline) (pnPrOx) (B), but no thermogelation was observed at the investigated temperature range of 10–50 °C.^[30] In contrast, the ABA triblock copolymer comprising of poly(2-*iso*-butyl-2-oxazoline) (piBuOx) (B) undergoes reversible sol/gel transition upon heating at 20 wt.%.^[31] The hydrogel exhibited a low yield stress in combination with a relatively soft character. Hoogenboom and Monnery described a BAB triblock copolymer bearing pnPrOx (B) and hydrophilic poly(2-ethyl-2-oxazoline) blocks (A), which undergoes thermogelation, but only at extremely high degrees of polymerization.^[32] In contrast to POx, an additional methylene group in the polymer backbone characterizes the polymer class POzi. The additional CH₂ group modifies the polymers physicochemical properties. In 2017, the first thermogelling POx/POzi-based block copolymer was described using a poly(2-*n*-propyl-2-oxazine) (pnPrOzi) block, and cytocompatible and printable physical hydrogels with storage modulus of \approx 5 kPa at 20 wt.% polymer concentration were obtained.^[33]

For decades, one dominant hydrophobic building block to study self-assembly of amphiphilic POx was poly(2-phenyl-2-oxazoline) (pPheOx).^[34,35] More recently, poly(2-benzyl-2-oxazoline) (pBzOx) has been introduced as the hydrophobic block B in ABA triblock copolymers and studied for the solubilization of hydrophobic active pharmaceutical ingredients and natural compounds.^[36–38] Since, additional aromatic hydrophobic B blocks have been introduced, specifically poly(2-phenyl-2-oxazine) (pPheOzi) and poly(2-benzyl-2-oxazine) (pBzOzi).^[39] The difference between these building blocks is one methylene

group in the polymer backbone and/or polymer side chain, allowing to study effects of these small structural changes on its physicochemical properties. Specifically, the rheological properties of aqueous solutions were investigated depending on concentration and temperature. Interestingly, out of the set of four polymers, only pMeOx-*b*-pPheOzi-*b*-pMeOx undergoes reversible inverse thermogelation, that is, it forms a gel upon cooling. This unusual gelation is apparently caused by an order-order transition from spherical- (sol state) to worm-like micelles (gel state), which apparently only occurs for the specific combination of relatively flexible POzi backbone and rigid phenyl sidechain in pPheOzi moieties. Here, we extend the molecular toolkit with respect to aromatic building blocks of POx and POzi by introducing the monomers 2-benzhydryl-2-oxazoline (BhOx) and 2-benzhydryl-2-oxazine (BhOzi), their respective block copolymer amphiphiles, and BhOzi homopolymer. The thermoresponsive properties at different polymer concentrations were analyzed and compared. Interestingly, an inverse thermogelation was once again observed for the POzi-based system while the POx-based polymer did not form a gel.

2. Experimental Section

2.1. Materials and Methods

The substances and reagents in this study were purchased from Sigma-Aldrich (Steinheim, Germany) or TCI-chemicals (Eschborn, Germany) and used without further purification unless otherwise stated. If this was not the case, it will be explicitly mentioned. All substances used for polymerization, specifically methyl trifluoromethylsulfonate (MeOTf) and MeOx were refluxed over CaH₂ for several hours and distilled prior to use. The solvent benzonitrile (PhCN) was dried over phosphorus pentoxide. All dried reagents were stored under dried and inert conditions. The monomers BhOx and BhOzi were recrystallized using methanol followed by co-distillation (three times) with toluene under inert conditions.

2.1.1. Nuclear Magnetic Resonance

Nuclear magnetic resonance (NMR) experiments were performed on a Bruker Fourier 300 (¹H: 300.12 MHz) spectrometer at 298 K from Bruker BioSpin (Rheinstetten, Germany) and calibrated using the solvent signals. Multiplicities of signals were depicted as follows: s, singlet; d, doublet; t, triplet; m, multiplet; b, broad.

2.1.2. Gel Permeation Chromatography

Gel permeation chromatography (GPC) was performed on an OMNISEC RESOLVE combined with an OMNISEC REVEAL from Malvern Panalytical using DMF as solvent as described elsewhere.^[40] Conventional calibration was performed with poly(methyl methacrylate) (PMMA) standards. The system was kept at 45 °C and a flow rate of 1 mL min⁻¹ was used. A precolumn (Dguard), a D2000, and a D3000 column from Malvern were used in series. All samples were filtered through 0.2 μ m PTFE filters, Roth (Karlsruhe, Germany).

2.1.3. X-Ray Diffraction

Crystals suitable for single-crystal X-ray diffraction were selected, coated in perfluoropolyether oil, and mounted on MiTeGen sample holders. Diffraction data were collected on Bruker X8 Apex II 4-circle diffractometers with CCD area detectors using Mo- K_{α} radiation. The crystals were cooled using an Oxford Cryostreams low-temperature device. Data were collected at 100 K. The images were processed and corrected for Lorentz-polarization effects and absorption as implemented in the Bruker software packages. The structures were solved using the intrinsic phasing method (SHELXT)^[41] and Fourier expansion technique. All non-hydrogen atoms were refined in anisotropic approximation, with hydrogen atoms “riding” in idealized positions, by full-matrix least squares against F^2 of all data, using SHELXL^[42] software and the SHELXLE graphical user interface.^[43] Other structural information was extracted using OLEX2 software.^[44]

2.1.4. Thermogravimetric Analysis

Thermogravimetric analysis (TA) was performed on TG 209 F1 IRIS, NETZSCH (Selb, Germany). The freeze-dried polymer samples (10–15 mg) were placed in aluminum oxide crucibles (NETZSCH Selb, Germany) and heated under synthetic air from 30 to 900 °C with the constant heating rate of 10 K min⁻¹.

2.1.5. Differential Scanning Calorimetry

Differential scanning calorimetry (DSC) was performed on DSC 204 F1 Phoenix equipped with a CC200 F1 Controller (NETZSCH, Selb, Germany). The dynamic scans were recorded using a constant N₂ atmosphere with a heating rate of 10 K min⁻¹ (25–200 °C) and subsequently cooled to -50 °C (10 K min⁻¹). Two heating and cooling cycles from -50 to 200 °C (10 K min⁻¹) were performed. The samples were placed into aluminum crucibles.

2.1.6. Dynamic Light Scattering

Dynamic light scattering (DLS) experiments were performed using an ALV CGS-3 multi detection goniometry system (Langen, Germany) equipped with a He-Ne laser (632.8 nm) and eight optical avalanche photodiode detectors with an detector angle distance of 16° (correlation time 45 s, 3 runs). Scattering angles between 41° and 147° were measured in four angle sets and a 5° angle interval for each detector (27 angles) at 15, 25, and 40 °C. Prior to each measurement, samples were filtered in dust-free cuvettes using Millex-LG 0.2 μm filters under laminar flow. The polymer concentration was 0.3 g L⁻¹ (2 mM aqueous NaNO₃ as selective solvent was used). All samples were stored for 24 h at measuring temperature. Additionally, 10 g L⁻¹ samples in acetonitrile (unselective solvent) were also investigated at 25 °C and compared. The decay of the electric field-time autocorrelation function (ACF) was fitted using triexponential fit functions (Equation 1) as described previously.^[37]

$$g_1(t) = a_1 \cdot e^{-\frac{t}{\tau_1}} + a_2 \cdot e^{-\frac{t}{\tau_2}} + a_3 \cdot e^{-\frac{t}{\tau_3}} \quad (1)$$

With the amplitude a_i , decay times $\tau_i = \frac{1}{q^2 \cdot D_i}$, and the absolute value of the scattering vector q . In the case of polydispersity, the Brownian diffusion coefficient D was obtained by extrapolation to zero angle and in the limit of high dilution given by

$$\langle D \rangle_z^{-1} = \frac{\sum_i a_i}{\sum_i a_i \cdot D_i^{-1}} \quad (2)$$

Using the Stokes–Einstein equation, the hydrodynamic radii R_h were obtained

$$R_h = \frac{k_B \cdot T}{6 \cdot \pi \cdot \eta \cdot D} \quad (3)$$

with k_B being the Boltzmann constant, η the viscosity of the solvent, and T the temperature (15, 25, or 40 °C).

Furthermore, the 89° data were fitted using the cumulant method to obtain the polydispersity index (PDI) at different temperatures.

2.1.7. Rolling Ball Viscosity

Rolling ball viscosity experiments were performed on a LOVIS 2000M microviscometer from Anton Paar (Graz, Austria) using a LOVIS 1.8 capillary and a steel ball of 1.5 mm diameter. Prior to the viscosity measurements, the density for every sample was determined at 5 and 40 °C using a DMA 4100 M density meter from Anton Paar (Graz, Austria). A temperature scan from 40 °C → 5 °C and 5 °C → 40 °C of different aqueous sample was performed to establish the temperature-dependent dynamic viscosity.

2.1.8. Rheology

Rheology studies were recorded on an Anton Paar (Ostfildern, Germany) Physica MCR 301 system utilizing a plate–plate geometry (25 mm diameter) equipped with a solvent trap and Peltier element for temperature control. All aqueous samples were measured after complete dissolution in deionized (DI) water at different concentrations at 5 °C. For investigations of viscoelastic behavior, the linear viscoelastic (LVE) region was determined by performing an amplitude sweep (0.01% → 500%) strain deformation using a fixed angular frequency of 10 rad s⁻¹. An oscillatory shear stress sweep (amplitude sweep) can also be used to determine the yield point, yield zone, and flow point. Leaving the LVE region is characterized as yield point. The flow point is defined as $G' = G''$. The region between yield point and flow point is defined as yield zone. A frequency sweep (0.1 rad s⁻¹ → 100 rad s⁻¹) was performed at fixed strain deformation of 0.1%. For steady shear experiments, the control shear rate mode was used (0.01 s⁻¹ → 100 s⁻¹). The pronounced viscosity η decrease was fitted using the power-law expression (Equation 4).

$$\eta = K \cdot (\dot{\gamma})^{n-1} \quad (4)$$

where K is the consistency index and n the flow index.

2.1.9. Transmission Electron Microscopy

For transmission electron microscopy (TEM) experiments, the polymers were dissolved in DI water to a final concentration of 20 g L⁻¹ and stored in the fridge. 400 mesh copper–rhodium grids (maxtaform) with a homemade carbon layer were glow discharged in air for 1.5 min at medium power in a Harrick PDC-002 plasma cleaner. The 20 g L⁻¹ sample was diluted (1/125 or 1/625) and 8 μL were incubated on the grids for 1 min before blotting (Whatman filter paper No 50). The grids were washed with water (three times) and with 2% w/v uranyl acetate (three times). A single-tilt room temperature holder in an FEI Tecnai T12 Spirit transmission electron microscope equipped with a LaB₆ emitter at 120 kV was used. Images were recorded with an Eagle CCD camera under low-dose conditions. The micrographs were binned two times resulting in a pixel size of 2.2 Å per pixel at specimen level.

2.2. Synthesis Procedure

2.2.1. Monomer Synthesis

The monomer synthesis of BhOx and BhOzi were carried out as described by Witte and Seeliger^[45] with a different workup procedure. For the reaction 1 equiv. of diphenylacetonitrile, 1.2 equiv. of amino-ethanol or amino-propanol and catalytic amounts of zinc acetate dihydrate were added and heated to 130 °C under reflux for several days until the reaction mixture turned brown. Reaction progress was controlled by ¹H NMR spectroscopy. After completion, the mixture was dissolved in dichloromethane and washed with H₂O (three times). The organic phase was dried with MgSO₄ and concentrated. The raw product was purified via vacuum distillation under argon atmosphere to yield colorless crystals. The resulting compounds BhOx and BhOzi were characterized via ¹H, ¹³C NMR spectroscopy and DSC.

2.2.2. Homopolymer Synthesis

The synthesis was performed as described previously for similar polymers.^[50] 1 equiv. of the initiator MeOTf was dissolved in PhCN. The monomer BhOzi (50 equiv.) was added. The reaction mixture was stirred for 2 days at 120 °C. After complete monomer consumption, the reaction mixture was precipitated using ice cold diethyl ether. The dried white powder was analyzed using ¹H NMR spectroscopy, GPC, TGA, and DSC.

2.2.3. ABA Type Block Copolymer Synthesis

The synthesis and workup procedures were carried out as described previously for similar polymers.⁵⁰ In general, 1 equiv. of the initiator MeOTf was added to a dried and argon flushed flask and dissolved in the respective amount of solvent (PhCN). The first monomer MeOx (35 equiv.) was added to the reaction mixture and heated to 100 °C for ≈2 h. After complete monomer consumption, the mixture was cooled to room temperature and the monomer for the second block BhOx or BhOzi (10 equiv.) was

added. The reaction mixture was heated to 120 °C overnight. After complete monomer consumption was confirmed, the third block MeOx (35 equiv.) was added and stirred for 2 h at 100 °C. Termination was carried out by the addition of 3 equiv. of 1-Boc-piperazine (PipBoc) at 50 °C and kept on stirring for 6 h. The solvent was removed at reduced pressure. The raw product was dissolved in DI water. The polymer solution was dialyzed (MWCO 1 kDa, cellulose acetate) against DI water for 3 days. The polymer solution was lyophilized and obtained as a white powder.

3. Results and Discussion

3.1. Monomer Synthesis

The synthesis of the monomers was carried out according to a well-known route established by Witte and Seeliger.^[45] The monomer BhOx (Figure S1, Supporting Information) was already synthesized by Culbertson in 2000.^[46] It was further converted to a bisoxazoline and then the first ring-opening reactions were carried out. As far as we know, the substance has not yet been used for the cationic ring-opening polymerization. After purification, the monomer was obtained as a colorless crystalline solid with a melting point comparable to the literature (110 °C, lit: 107–109 °C)^[46] (Figure S3, Supporting Information). The substance was further analyzed by ¹H- and ¹³C NMR spectroscopy (Figure S2, Supporting Information). In contrast, to the best of our knowledge, the monomer BhOzi (Figure S4, Supporting Information) has not yet been described in the literature.

It is also readily accessible by the Witte and Seeliger method (Figure 1A). After purification the structure was verified by ¹H- and ¹³C NMR (Figure 1B and Supporting Information). The additional methylene group (Signal e in Figure 1A,B) leads to a significantly higher melting point of 132 °C compared to the 2-oxazoline monomer (Figure 1C). The solid-state structure of BhOzi was determined by single-crystal X-ray diffraction (Figure 2). It should be noted that only very recently the first crystal structure of any 2-oxazoline and 2-oxazoline used for cationic ring-opening polymerization was reported. Heck et al. reported this for monomers with pending thiophene groups.^[47] The compound crystallizes from a mixture of *n*-hexane and dichloromethane in the monoclinic centrosymmetric space group C 1 2/c 1 (Table S1, Supporting Information). The oxazine ring shows a rotational disorder, with occupancies of 0.609(5) and 0.291(5), which describes a 180° rotation of the ring. No evidence of π–π stacking was observed in the extended structure, probably due to the star-shaped orientation of the three rings (Figure S5, Supporting Information).

3.2. Polymer Synthesis

A first homopolymer was synthesized using the novel BhOzi monomer by living cationic ring-opening polymerization (Figure 3A). ¹H NMR analysis after purification verified the polymerization and all relevant peaks could be assigned to the polymer structure Me-poly(2-benzhydryl-2-oxazine)₅₀-ω-BocPip (Figure 3B and Figure S6, Supporting Information). An essentially monomodal mass distribution with a minor high molar mass shoulder gave rise to a low dispersity ($\mathcal{D} = M_w/M_n: 1.09$) (Figure 3C).

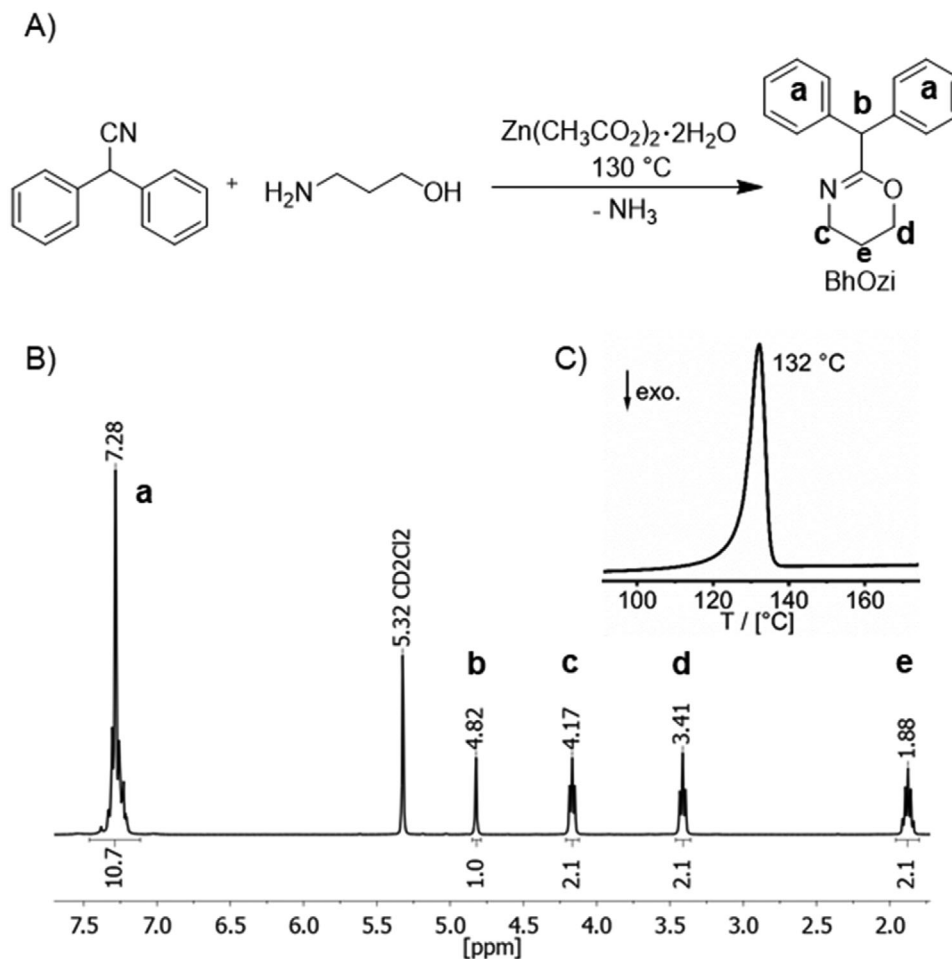


Figure 1. Synthesis of 2-benzhydryl-2-oxazine (BhOzi). A) Synthesis route for BhOzi and B) ^1H NMR of BhOzi in CD_2Cl_2 with the assignment of all relevant peaks. C) Differential scanning calorimetry graph shows the melting point of the crystalline solid (m_p : 132 °C).

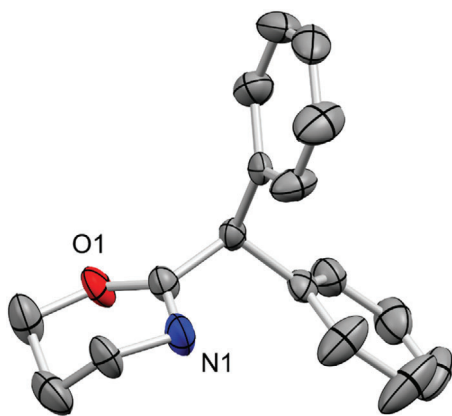


Figure 2. Crystal structure of BhOzi with labeling of heteroatoms. H atoms and disorders are omitted for clarity.

Thermogravimetric analysis showed good thermal stability up to 330 °C, followed by a two-step composition process, which is well known for various POx and POzi (Figure 3D). The polymer appears fully amorphous with a glass transition temper-

ature of 104 °C (Figure 3E). In our ongoing endeavor to understand the structure–property relationship of self-assembly of ABA triblock copolymers for use in drug-delivery systems and hydrogel platforms, we synthesized an ABA type amphiphile with pMeOx A blocks and pBhOzi B blocks (Figure S11, Supporting Information) by using a well-established strategy (Figure 4A). ^1H NMR analysis confirmed the polymer structure of Me-pMeOx₄₀-*b*-pBhOzi₁₄-*b*-pMeOx₄₀-BocPiP (Figure 4B) and a near monomodal mass distribution with a small but noticeable tailing was obtained from GPC analysis, which may be explained by undesired premature termination of a small fraction of the polymers (Figure 4C). DSC analysis showed one defined T_g of 81.3 °C confirming an amorphous polymer structure without significant micro phase separation of individual polymer blocks. Comparing to previously synthesized similar polymers bearing slightly different aromatic cores similar T_g values were obtained.^[37]

3.3. Thermoresponsive Properties in Aqueous Solutions

Surpassing a critical concentration (c_{gel}), self-assembled aggregates can lead to an increase of viscosity and the formation of a

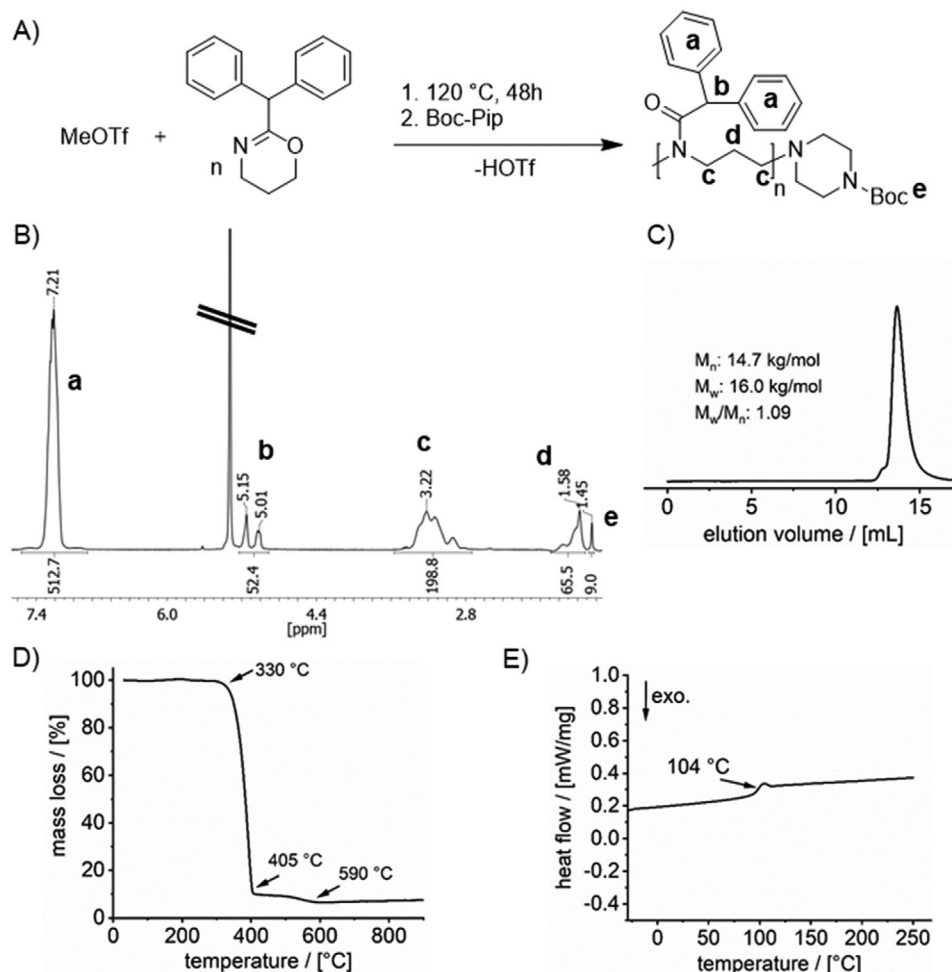


Figure 3. Synthesis of poly(2-benzhydryl-2-oxazine) (pBhOzi). A) Schematic illustration of the polymer synthesis. B) ^1H NMR of the polymer in CD_2Cl_2 (signal 5.32 ppm) with the assignment of all relevant peaks (the signal at 1.45 ppm was set to 9H (Boc group)). C) GPC elugram of the homopolymer pBhOzi in DMF. D) TGA analysis of the purified polymer. E) DSC second heating cycle with the assignment of the glass transition temperature T_g : 104 °C.

physically crosslinked hydrogel. In some cases, the aggregation induced gelation showed pronounced response to temperature leading to a reversible sol/gel transition at the critical temperature (t_{gel}). At 17.5 wt.% and below, an aqueous sample showed unremarkable temperature-viscosity profile. In the investigated temperature range of 5 to 40 °C viscosity values for the free flowing liquid of 120 mPas (5 °C) and 23 mPas (40 °C) are obtained (Figure 5). Interestingly, a 20 wt.% sample showed pronounced inverse thermogelation. Starting at 40 °C as a low viscous liquid (49 mPas), a steady increasing viscosity was observed by cooling the sample. Surpassing a critical temperature (≈ 15 °C for 20 wt.% sample) no viscosity value could be detected. In stable hydrogels, the metal ball, which is used in the measurement, becomes stuck and no values can be obtained. Important to note, the sol/gel transition is fully reversible with only little hysteresis.

Recently, we have observed that such thermogelation can be quite sensitive with respect to the side chain and backbone structure. Accordingly, we prepared a comparable polymer amphiphile bearing pBhOx as the hydrophobic block (Figure S7, Supporting Information) and characterized the polymer by ^1H NMR (Figure S8, supporting Information), GPC (Figure S9, Sup-

porting Information), and DSC (Figure S10, Supporting Information) analyses. Interestingly, even at very high polymer concentration of 25 wt.% the pMeOx-*b*-pBhOx-*b*-pMeOx showed no inverse thermogelation (Figure S12, Supporting Information). Presumably, the additional methylene unit increases the flexibility of the hydrophobic core, which affects self-assembly or its dynamics, which in turn might be crucial for inverse thermogelation. As mentioned, similar specificities between POx and POzi based polymers with the same side chains have been observed in previous studies.^[39] A similar polymer, pMeOx-*b*-pPheOzi-*b*-pMeOx, showed inverse gelation already at 5 wt.%, but the hydrogel formation is very slow in this case (≈ 1 h) and due to the formation of worm-like micelles in the cold (below 32 °C). Recently a triblock copolymer comprising the aromatic poly(2-phenethyl-2-oxazoline) as the hydrophobic core (pMeOx-*b*-pPhenEtOx-*b*-pMeOx) was introduced, which forms a physical hydrogel by increased correlation between spherical micelles in the cold.^[48] In this case, also 20 wt.% was necessary and the critical temperature was slightly higher at about 23 °C. We suspect that the presently investigated pMeOx-*b*-pBhOzi-*b*-pMeOx might gel due to a similar mechanism.

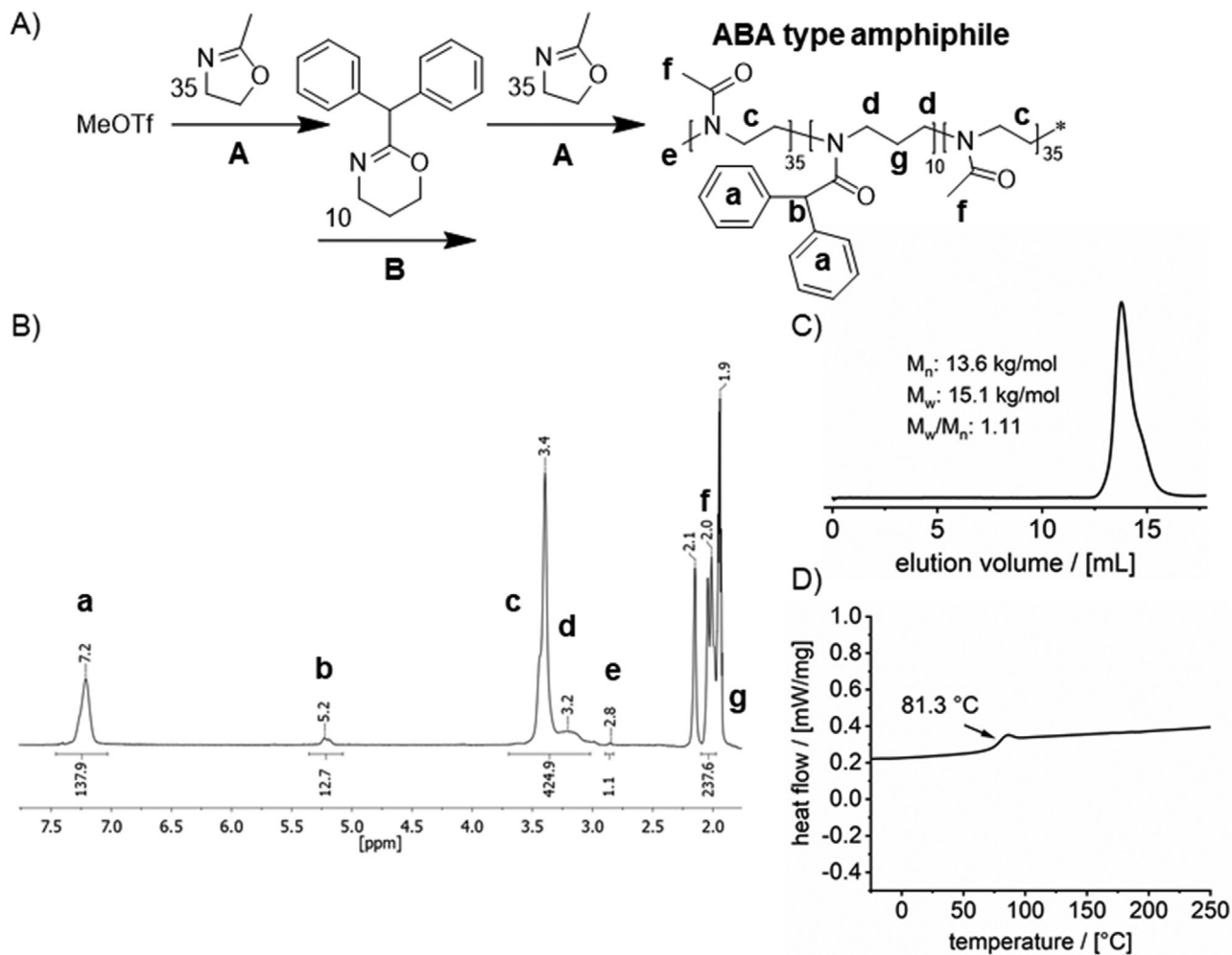


Figure 4. Synthesis of pMeOx-*b*-pBhOzi-*b*-pMeOx amphiphile. A) Scheme of synthesis. B) ^1H NMR of the purified amphiphile in CD_3CN (1.94 + 2.2 ppm) with the assignment of all relevant peaks. C) GPC elugram in DMF. D) DSC second heating cycle with the assignment of the glass transition temperature T_g : 81.3 °C.

3.4. Rheological Properties of the Hydrogel

The viscoelasticity of different pMeOx-*b*-pBhOzi-*b*-pMeOx concentrations were analyzed using oscillatory rheology. Frequency sweeps at 5 °C and different polymer concentration were compared (Figure 6).

At 15 wt.% no values for a storage modulus could be obtained due to fully viscous character of the sample. Increase in concentration to 17.5 wt.% leads to significantly improved G' and G'' values, as described several times for concentrated solutions, and is in agreement with the obtained viscosity values (120 mPas). The 20 wt.% sample showed pronounced viscoelastic solid-like character. However, the system is still highly dynamic leading to $G' < G''$ at low frequencies. At 25 wt.% in the whole investigated frequency range a stable viscoelastic solid-like character was confirmed with almost constant $G' = 19.4 \pm 0.8$ kPa and a pronounced elasticity expressed by a very low loss factor $\tan \delta$ of 0.04 ± 0.02 . As a note, for a 25 wt.% sample of the polymer pMeOx-*b*-pBhOzi-*b*-pMeOx, throughout the investigated frequency range $G'' > G'$ which by definition is a viscoelastic

Table 1. Summary of important key parameter obtained by oscillatory amplitude sweep for a 20 and 25 wt.% hydrogel sample at 5 °C.

c [wt.%]	G'_{LVE} [kPa]	τ_{yield} [Pa]	τ_{flow} [Pa]
20	9.1 ± 0.1	90	350
25	21.8 ± 0.3	480	1300

Average storage modulus G' in kPa in the linear viscoelastic region, yield point τ_{yield} and flow point τ_{flow} in Pa.

fluid (Figure S13, Supporting Information). Using an amplitude sweep, the LVE range of the hydrogel samples ($G' > G''$) can be determined to assess which deformation/shear stress the system can tolerate (Figure 7). The end of the LVE region (G' starts to decrease) is defined as the yield point τ_{yield} , followed by the yield zone, which leads to a liquefaction ($G'' > G'$) of the specimen at the flow point τ_{flow} ($G' = G''$).

Results of the amplitude sweeps are summarized in Table 1. Increase in concentration leads to significantly higher values

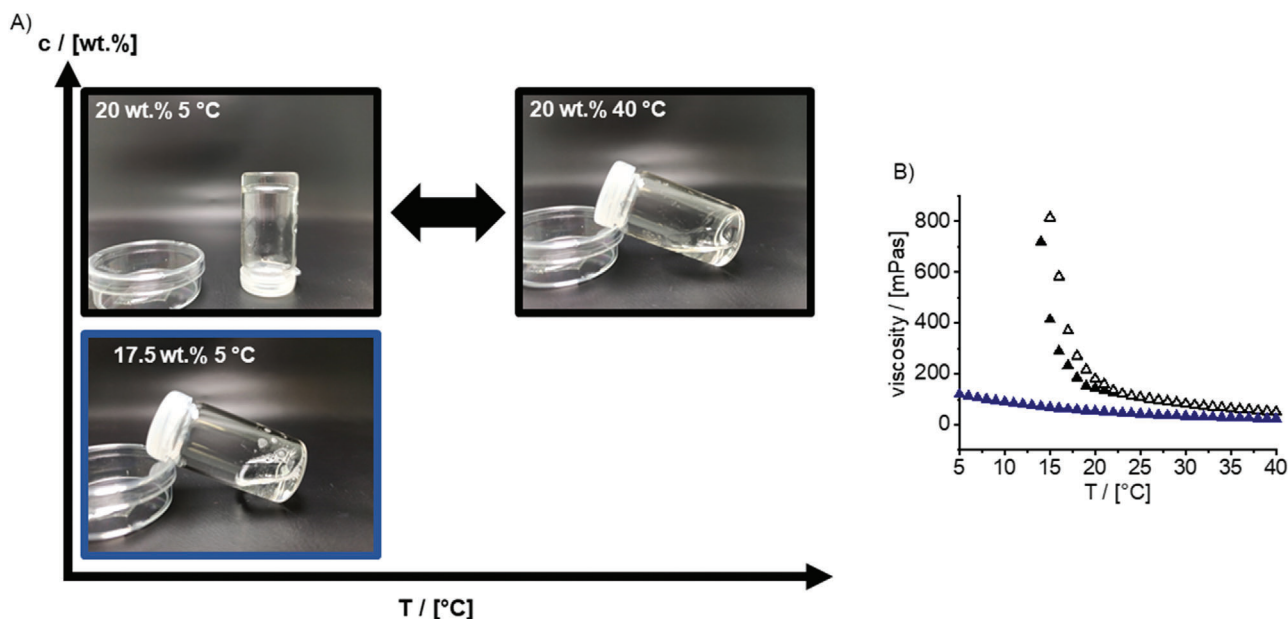


Figure 5. Viscosity of aqueous solutions of pMeOx-*b*-pBhOzi-*b*-pMeOx at 17.5 and 20 wt.%. A) Pictures of the samples at different temperatures (5 and 40 °C). B) Viscosity as a function of temperature investigated using rolling ball viscosity system (filled symbols: cooling, open symbols: heating, blue: 17.5 wt.%, black: 20 wt.%).

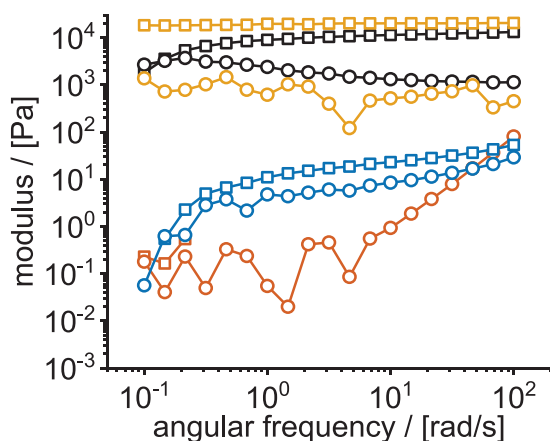


Figure 6. Viscoelasticity of pMeOx-*b*-pBhOzi-*b*-pMeOx aqueous samples at 5 °C and different angular frequencies (squares: storage modulus G' , circles: loss modulus G''). Different polymer concentrations (red: 15 wt.%, blue: 17.5 wt.%, black: 20 wt.%, and yellow: 25 wt.%) were tested.

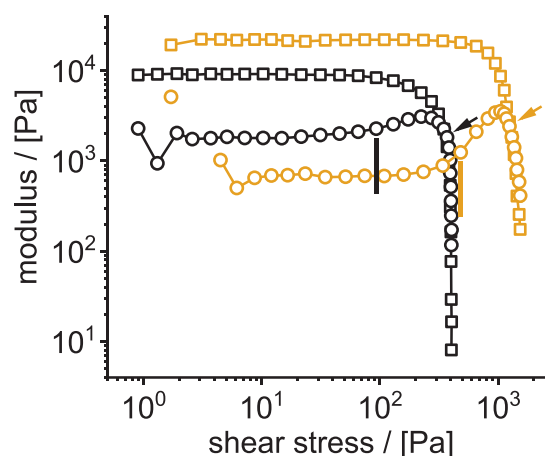


Figure 7. Viscoelasticity of pMeOx-*b*-pBhOzi-*b*-pMeOx aqueous samples (black: 20 wt.% and yellow: 25 wt.%) at 5 °C and different shear stress (squares: storage modulus G' , circles: loss modulus G''). The yield point is marked with vertical lines and the flow point with an arrow.

for both parameters. The storage modulus increased more than twice from ≈ 9 kPa (20 wt.%) to ≈ 22 kPa. Also, the yield point increased more than fivefold from 90 to 480 Pa.

These values are relatively high in comparison to other POx/POzi-based physical hydrogels at similar concentrations.^[31,33,39] Another important rheological parameter is the shear rate-dependent viscosity. The hydrogel exhibited pronounced shear-thinning properties (Figure 8). Low shear-thinning indices n , obtained by fitting the values using a power-law expression, characterize the hydrogels as highly shear-thinning materials (n (20 wt.%) = 0.15 ± 0.02 , n (25 wt.%) = 0.06 ± 0.001). Increasing the concentration leads

to more pronounced shear-thinning properties as evidenced by a decreasing n value. In contrast, the consistency index K increased by increasing concentration (K (20 wt.%) = 201 ± 7 , K (25 wt.%) = 1025 ± 4). In general, much higher viscosity values are obtained for the 25 wt.% sample ($\eta_{20 \text{ wt.}\%}(0.01 \text{ 1/s}) = 9500$ Pas, $\eta_{25 \text{ wt.}\%}(0.01 \text{ 1/s}) = 81\,400$ Pas).

3.5. Self-Assembly of ABA Type Amphiphile

Amphiphilic polymers, including POx/POzi-based systems self-assemble into different nanoscale architectures such as spherical

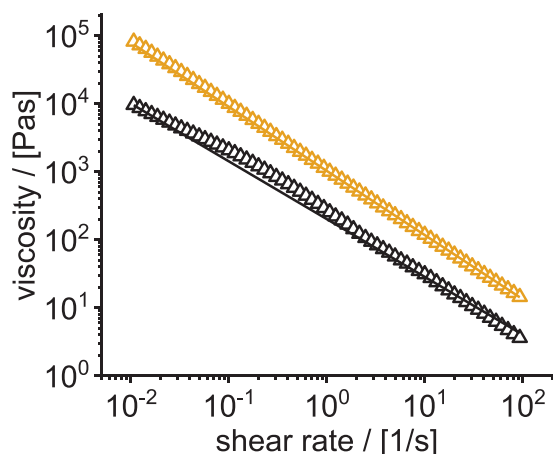


Figure 8. Viscosity as a function of the applied shear rate of pMeOx-*b*-pBhOzi-*b*-pMeOx aqueous samples (black: 20 wt.% and yellow: 25 wt.%) at 5 °C. The shear thinning was fitted using the power-law expression to obtain the flow index n and consistency index K .

micelles,^[28] worm-like micelles^[27] or even vesicles.^[30,33] Recently, we studied very similar ABA type amphiphiles with various aromatic hydrophobic B blocks.^[37,39] At room temperature or above, spherical micelles (8–10 nm) could be detected for all studied systems. Only in one case, for polymers featuring hydrophobic blocks comprising pPheOzi, larger several hundred nanometer sized worm-like aggregates could be detected by DLS experiments and cryogenic TEM at lower temperature. These polymers also showed inverse thermogelation. In addition, a triblock copolymer comprising pPhenEtOx as the hydrophobic block, also showed inverse gelation but did not change the morphology or size of the aggregates upon changes in temperature. However, an enhanced correlation of neighboring micelles was discussed as the driving force for inverse gelation.^[48]

To get first insights into the aggregation process of the benzhydryl comprising triblock copolymer that leads to inverse gelation at high concentration, DLS experiments of aqueous solutions of the polymers pMeOx-*b*-pBhOzi-*b*-pMeOx and pMeOx-*b*-pBhOx-*b*-pMeOx were performed (Table 2). In the unselective solvent acetonitrile, in which no aggregation is expected, only slightly different hydrodynamic radii for the individual polymer chains were obtained.

The slightly higher value of pMeOx-*b*-pBhOzi-*b*-pMeOx of 2.75 ± 0.02 nm compared to 2.58 ± 0.02 nm of pMeOx-*b*-pBhOx-*b*-pMeOx is consistent with the NMR and GPC results, where slightly higher values for the degree of polymerization and the influence of the additional methylene group in the polymer backbone are also evident. In contrast, in the selective solvent water, the polymers self-assemble into micelles with significant higher hydrodynamic radius. At diluted concentrations needed for DLS and at 25 and 40 °C, the inverse thermogelling polymer pMeOx-*b*-pBhOzi-*b*-pMeOx exhibited micelles with a hydrodynamic radius of 10 nm. Interestingly, the micelles of the polymer pMeOx-*b*-pBhOx-*b*-pMeOx are slightly larger (11.7 and 11.9 nm). At 15 °C, the temperature, at which the gelation at higher concentration actually starts for the polymer pMeOx-*b*-pBhOzi-*b*-pMeOx, the micelle size increased significantly by 2.3 nm. The increase for the non-gelling polymer pMeOx-*b*-pBhOx-*b*-pMeOx was much less

Table 2. Hydrodynamic radii obtained via dynamic light scattering experiments. Measurements were performed on a multi angle device.

Polymer	Acetonitrile [10 g L ⁻¹]	aqueous solution [0.3 g L ⁻¹]		
	$R_h^{25\text{ °C}}$ [nm] unselective	$R_h^{15\text{ °C}}$ [nm] selective	$R_h^{25\text{ °C}}$ [nm] selective	$R_h^{40\text{ °C}}$ [nm] selective
A-pBhOx-A	$2.58^* \pm 0.02$	$12.7^* \pm 0.1$ 13 [†] (0.15)	$11.9^* \pm 0.1$ 12 [†] (0.18)	$11.7^* \pm 0.1$ 12 [†] (0.16)
A-pBhOzi-A	$2.75^* \pm 0.02$	$12.3^* \pm 0.2$ 13 [†] (0.26)	$10.0^* \pm 0.1$ 10 [†] (0.11)	$10.0^* \pm 0.1$ 10 [†] (0.09)

The translational diffusion coefficients in dependency of the scattering vector q was extrapolated to zero angle (Figure S14, Supporting Information). Using Stokes Equation (3) the hydrodynamic radius was obtained. Error values originate from triexponential fit functions (*) or by cumulant analysis (†) at 89° which affords the polydispersity index (PDI) given in brackets.

pronounced (0.8 nm). In the whole temperature range, the micelles formed by pMeOx-*b*-pBhOzi-*b*-pMeOx were smaller compared to the pMeOx-*b*-pBhOx-*b*-pMeOx aggregates, respectively.

The described trend can also be observed in the evaluation of the DLS experiments by cumulant method, which gives essentially the same hydrodynamic radii (Table 2). Most interestingly, a significant difference in the development of the dispersity (PDI value) can be observed between the two polymers at different temperatures. In principle, for uniform aggregates in solution the PDI value should approach 0.^[49] The gelling polymer A-pBhOzi-A exhibited a relatively high PDI of 0.260 at gelling temperature (15 °C), which decreases rather markedly upon heating to a PDI value of 0.087, indicative of more uniform micelles. The higher value at the gelling temperature could be caused by a minor portion of aggregated micelles due to increased interactions between the micelles or due to an extended correlation of the micelles, ultimately causing the system to gel at higher concentration. Important to note, this temperature-dependent change in PDI values was not observed with the non-gelling polymer. In this case, a very similar PDI in the range of 0.15–0.17 is observed at all temperatures.

The DLS study was performed in non-gelling concentration and therefore does not allow a simple correlation to the situation at higher concentrations. Nevertheless, it is a first indication of the different aggregation of the two amphiphiles. In addition, negative stain TEM images were obtained from a 20 g L⁻¹ aqueous solution stored at 5 °C.

The non-gelling polymer pMeOx-*b*-pBhOx-*b*-pMeOx clearly self-assembles into rather uniform spherical micelles (Figure 9A,B) similar to previously described non-gelling POx-based polymers with an aromatic hydrophobic block^[37] and thermogelling polymer described very recently.^[48] Interestingly, even though the self-assemblies formed in the case of the gelling polymer pMeOx-*b*-pBhOzi-*b*-pMeOx are also rather uniform and spherical, the overall impression suggests a strongly deviating aggregation behavior (Figure 9C). First, the contrast from the staining reagent is different, which suggests different accessibility of the contrast agent and may be attributed to a higher flexibility of the oxazine backbone in the hydrophobic block compared to the non-gelling oxazoline-based polymer. More importantly, however, the TEM images suggest a strong interaction

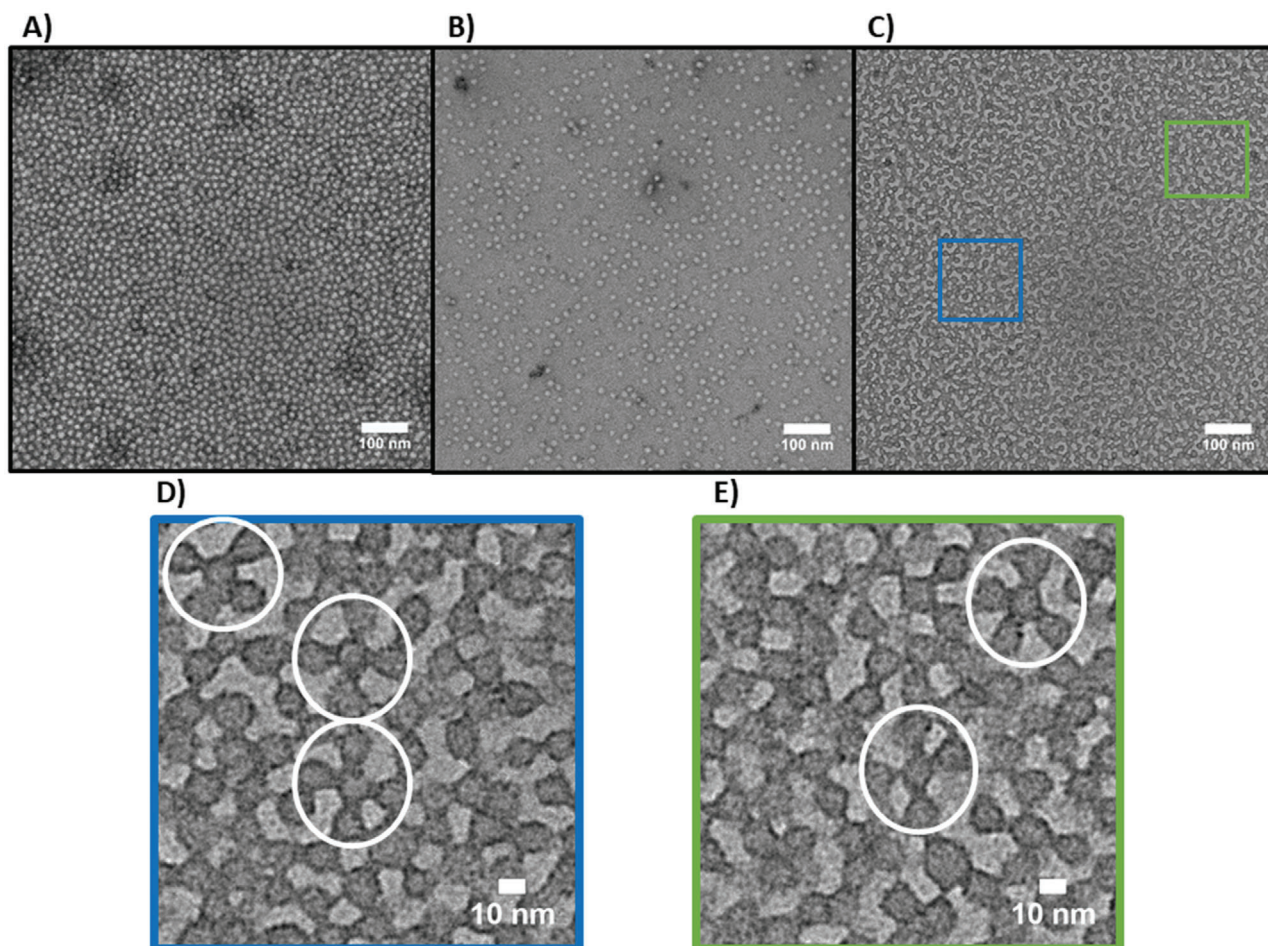


Figure 9. TEM images of pMeOx-*b*-pBhOx-*b*-pMeOx (A, B) and pMeOx-*b*-pBhOzi-*b*-pMeOx (C–E). As staining reagent uranyl acetate was used. A) Image of highly concentrated and B) a more diluted aqueous solution of A-pBhOx-A suggests uniform and non-interacting spherical micelles. C) In contrast, the micrograph of A-pBhOzi-A strongly suggests interacting aggregates of spherical micelles and clustering as highlighted in D and E. D, E) Zoomed view of clustering aggregates. Highlighted in white circles are interesting geometric features which appear common in the image.

tendency among the individual micelles, mediated via the hydrophilic corona, which seems to form sticky patches between the micelles (Figure 9D,E white circles). As a result, a superstructure of self-assemblies is formed, which is likely the underlying reason for the gel formation at high concentration and low temperatures. Interestingly, similar arrangements were not observed in otherwise very similar inverse-gelling POx/POzi platforms,^[37,48] which suggest that these structures might be specific for this particular combination of hydrophilic and hydrophobic blocks.

4. Conclusion

Herein we demonstrated the novel aromatic monomers BhOx and BhOzi and their application in a cationic ring-opening polymerization. ABA type amphiphiles with the aromatic hydrophobic central block of pBhOx and pBhOzi are synthesized and compared. Surprisingly, the polymer pMeOx-*b*-pBhOzi-*b*-pMeOx undergoes rapid inverse thermogelation above 20 wt.% while its homologue pMeOx-*b*-pBhOx-*b*-pMeOx does not. The rheological

properties of the hydrogel, such as pronounced viscoelastic solid appearance and shear thinning, are confirmed. Minor differences in aggregation for the two amphiphiles were observed by light scattering experiments, of particular interest is the temperature-dependent dispersity observed for pMeOx-*b*-pBhOzi-*b*-pMeOx, which is not observed for pMeOx-*b*-pBhOx-*b*-pMeOx. Interestingly, the gel-forming polymer pMeOx-*b*-pBhOzi-*b*-pMeOx showed unique fusion and ordering of micelles in TEM experiments in comparison to the non-gelling polymer pMeOx-*b*-pBhOx-*b*-pMeOx, in which the micelles are also uniform and spherical, but do not seem to interact. The controlled synthesis, reversible and rapid inverse gelation together with the distinct rheological properties open up a range of applications for this novel hydrogel and extends the toolkit for the recently discovered platform of POx- and POzi-based thermogelling polymers. The gel properties, namely the fast sol/gel transition and shear thinning, are promising for use as sacrificial material in biofabrication, especially in bioprinting, or the storage of biologically sensitive materials such as unstable proteins.

Supporting Information

Supporting Information is available from the Wiley Online Library or from the author.

Acknowledgements

The authors would like to gratefully acknowledge support by the Deutsche Forschungsgemeinschaft (DFG, German Research Foundation)—project number 326998133—TRR 225 (subproject A03) and project number 398461692, awarded to R.L.). H.H. thanks the DFG for support through the Heisenberg Programme (HE 6171/7-1, 401738081). The authors are very grateful for the HDRC-Software version 6.3.1 provided by O. Nirschl and K. Fischer, Physical Chemistry of Polymers at the Johannes Gutenberg University Mainz led by Dr. Sebastian Seiffert (formerly Dr. Manfred Schmidt) for DLS data analysis. Light scattering experiments were possible through support of the Deutsche Forschungsgemeinschaft (INST 93/774-1 FUGG). The authors gratefully acknowledge access to electron microscopy facilities provided by Prof. Bettina Böttcher at the Rudolf Virchow Center, Julius-Maximilians-University Würzburg. In addition, the authors would like to thank Maxim Melnikov, Dario Polzin, and Christian May for technical support and Ilona Paulus for GPC support.

Open access funding enabled and organized by Projekt DEAL.

Conflict of Interest

The authors declare no conflict of interest.

Data Availability Statement

The data that support the findings of this study are openly available in ChemRxiv at <https://doi.org/10.26434/chemrxiv.14322194>.

Keywords

inverse thermogels, physical hydrogels, poly(2-oxazine), poly(2-oxazoline), self-assembly

Received: March 31, 2021

Revised: June 23, 2021

Published online: August 2, 2021

- [1] L. Hu, Y. Wan, Q. Zhang, M. J. Serpe, *Adv. Funct. Mater.* **2020**, *30*, 1903471.
- [2] M. A. C. Stuart, W. T. S. Huck, J. Genzer, M. Müller, C. Ober, M. Stamm, G. B. Sukhorukov, I. Szleifer, V. V. Tsukruk, M. Urban, F. Winnik, S. Zauscher, I. Luzinov, S. Minko, *Nat. Mater.* **2010**, *9*, 101.
- [3] Z. Shen, F. Chen, X. Zhu, K.-T. Yong, G. Gu, *J. Mater. Chem. B* **2020**, *8*, 8972.
- [4] K. T. Kim, J. J. L. M. Cornelissen, R. J. M. Nolte, J. C. M. V. Hest, *J. Am. Chem. Soc.* **2009**, *131*, 13908.
- [5] A. P. Constantinou, B. Zhan, T. K. Georgiou, *Macromolecules* **2021**, *54*, 1943.
- [6] F. Ofriidam, M. Tarhini, N. Lebaz, É. Gagnière, D. Mangin, A. Elaissari, *Polym. Adv. Technol.* **2021**, *32*, 1455.
- [7] J. Hrbac, V. Pavelka, J. Crassous, J. Zadny, L. Fekete, J. Pokorny, P. Vanysek, J. Storch, J. Vacek, *Electrochem. Commun.* **2020**, *113*, 106689.
- [8] K.-P. Wang, Y.-P. Deng, T. Wang, Q.-D. Wang, C.-G. Qian, X.-Y. Zhang, *Polymer* **2020**, *210*, 123017.
- [9] H. Meng, J. Wan, J. Jing, D. Sun, B. Jiang, F. Liang, Z. Yang, *Chin. Chem. Lett.* **2020**, *31*, 253.
- [10] C. Rullyani, M. Singh, S.-H. Li, C.-F. Sung, H.-C. Lin, C.-W. Chu, *Org. Electron.* **2020**, *85*, 105818.
- [11] F. Doberenz, K. Zeng, C. Willems, K. Zhang, T. Groth, *J. Mater. Chem. B* **2020**, *8*, 607.
- [12] A. Kikuchi, T. Okano, *Prog. Polym. Sci.* **2002**, *27*, 1165.
- [13] T. Saitoh, K. Asano, M. Hiraide, *J. Hazard. Mater.* **2011**, *185*, 1369.
- [14] J. Zhang, G. Pu, M. R. Dubay, Y. Zhao, S. J. Severtson, *J. Mater. Chem. C* **2013**, *1*, 1080.
- [15] E. Gruber, in *Polymerchemie: Eine Einführung in die Chemie und Physikalische Chemie der Makromoleküle* (Ed: E. Gruber), Steinkopff, Heidelberg **1980**, p. 70.
- [16] X. Hu, M. Vatankhah-Varnoosfaderani, J. Zhou, Q. Li, S. S. Sheiko, *Adv. Mater.* **2015**, *27*, 6899.
- [17] A. M. Smith, R. J. Williams, C. Tang, P. Coppo, R. F. Collins, M. L. Turner, A. Saiani, R. V. Ulijn, *Adv. Mater.* **2008**, *20*, 37.
- [18] T. Bai, P. Zhang, Y. Han, Y. Liu, W. Liu, X. Zhao, W. Lu, *Soft Matter* **2011**, *7*, 2825.
- [19] M. Ahmadi, S. Seiffert, *Soft Matter* **2020**, *16*, 2332.
- [20] E. Su, O. Okay, *Eur. Polym. J.* **2017**, *88*, 191.
- [21] T. Lorson, M. M. Lübtow, E. Wegener, M. S. Haider, S. Borova, D. Nahm, R. Jordan, M. Sokolski-Papkov, A. V. Kabanov, R. Luxenhofer, *Biomaterials* **2018**, *178*, 204.
- [22] A. Zahoranová, R. Luxenhofer, *Adv. Healthcare Mater.* **2021**, *10*, 2001382.
- [23] R. Hoogenboom, H. M. L. Thijs, M. J. H. C. Jochems, B. M. Van Lankvelt, M. W. M. Fijten, U. S. Schubert, *Chem. Commun.* **2008**, <https://doi.org/10.1039/B813140F>.
- [24] M. M. Bloksma, R. M. Paulus, H. P. C. Van Kuringen, F. Van Der Werdt, H. M. L. Lambermont-Thijs, U. S. Schubert, R. Hoogenboom, *Macromol. Rapid Commun.* **2012**, *33*, 92.
- [25] S. Huber, R. Jordan, *Colloid Polym. Sci.* **2008**, *286*, 395.
- [26] J.-S. Park, K. Kataoka, *Macromolecules* **2007**, *40*, 3599.
- [27] A. Schulz, S. Jaksch, R. Schubel, E. Wegener, Z. Di, Y. Han, A. Meister, J. Kressler, A. V. Kabanov, R. Luxenhofer, C. M. Papadakis, R. Jordan, *ACS Nano* **2014**, *8*, 2686.
- [28] S. Jaksch, A. Schulz, Z. Di, R. Luxenhofer, R. Jordan, C. M. Papadakis, *Macromol. Chem. Phys.* **2016**, *217*, 1448.
- [29] D. Daubian, J. Gaitzsch, W. Meier, *Polym. Chem.* **2020**, *11*, 1237.
- [30] A. Zahoranová, M. Mrlik, K. Tomanová, J. Kronek, R. Luxenhofer, *Macromol. Chem. Phys.* **2017**, *218*, 1700031.
- [31] M. M. Lübtow, M. Mrlik, L. Hahn, A. Altmann, M. Beudert, T. Lühmann, R. Luxenhofer, *J. Funct. Biomater.* **2019**, *10*, 36.
- [32] B. D. Monnery, R. Hoogenboom, *Polym. Chem.* **2019**, *10*, 3480.
- [33] T. Lorson, S. Jaksch, M. M. Lübtow, T. Jüngst, J. Groll, T. Lühmann, R. Luxenhofer, *Biomacromolecules* **2017**, *18*, 2161.
- [34] B. Trzebicka, N. Koseva, V. Mitova, A. Dworak, *Polymer* **2010**, *51*, 2486.
- [35] Y. Milonaki, E. Kaditi, S. Pispas, C. Demetzos, *J. Polym. Sci., Part A: Polym. Chem.* **2012**, *50*, 1226.
- [36] Y. Seo, A. Schulz, Y. Han, Z. He, H. Bludau, X. Wan, J. Tong, T. K. Bronich, M. Sokolsky, R. Luxenhofer, R. Jordan, A. V. Kabanov, *Polym. Adv. Technol.* **2015**, *26*, 837.
- [37] L. Hahn, M. M. Lübtow, T. Lorson, F. Schmitt, A. Appelt-Menzel, R. Schobert, R. Luxenhofer, *Biomacromolecules* **2018**, *19*, 3119.
- [38] M. R. Landry, A. N. Duross, M. J. Neufeld, L. Hahn, G. Sahay, R. Luxenhofer, C. Sun, *Materials Today Bio.* **2020**, *8*, 100082.
- [39] L. Hahn, M. Maier, P. Stahlhut, M. Beudert, V. Flegler, S. Forster, A. Altmann, F. Töppke, K. Fischer, S. Seiffert, B. Böttcher, T. Lühmann, R. Luxenhofer, *ACS Appl. Mater. Interfaces* **2020**, *12*, 12445.
- [40] J. Blöbbaum, I. Paulus, A.-C. Pöppler, J. Tessmar, J. Groll, *J. Mater. Chem. B* **2019**, *7*, 1782.
- [41] G. Sheldrick, *Acta Crystallogr. C* **2015**, *71*, 3.
- [42] G. Sheldrick, *Acta Crystallogr. A* **2008**, *64*, 112.

- [43] C. B. Hübschle, G. M. Sheldrick, B. Dittrich, *J. Appl. Crystallogr.* **2011**, *44*, 1281.
- [44] O. V. Dolomanov, L. J. Bourhis, R. J. Gildea, J. A. K. Howard, H. Puschmann, *J. Appl. Crystallogr.* **2009**, *42*, 339.
- [45] H. Witte, W. Seeliger, *Angew. Chem., Int. Ed. Eng.* **1972**, *11*, 287.
- [46] B. M. Culbertson, Y. Tong, S. R. Schrickler, *Polym. Adv. Technol.* **2000**, *11*, 9.
- [47] J. G. Heck, J. Löblein, J. Kade, P. Dalton, R. Luxenhofer, R. Green, *Melt Electrospin Writing (MEW) of Novel Conductive Polymer Composites for Electroactive Fibers* [E-Poster, WBC2020-3735], **2020. WBC 2020, Virtual Conference**: p. <https://virtual.wbc2020.org/page/e-posters>
- [48] L. Hahn, E. Karakaya, T. Zorn, B. Sochor, M. Maier, P. Stahlhut, S. Forster, K. Fischer, S. Seiffert, A.-C. Pöppler, R. Detsch, R. Luxenhofer, *Biomacromolecules* **2021**, *22*, 3017.
- [49] D. E. Koppel, *J. Chem. Phys.* **1972**, *57*, 4814.
- [50] M. M. Lübtow, L. Keßler, A. Appelt-Menzel, T. Lorson, N. Gangloff, M. Kirsch, S. Dahms, R. Luxenhofer, *Macromol. Bioscience* **2018**, *18*, 1800155.

Chapter IV

In the last chapter, thermogelling POx/POzi based copolymers for biofabrication were established. First, a thermogelling ABA type block copolymer was described.

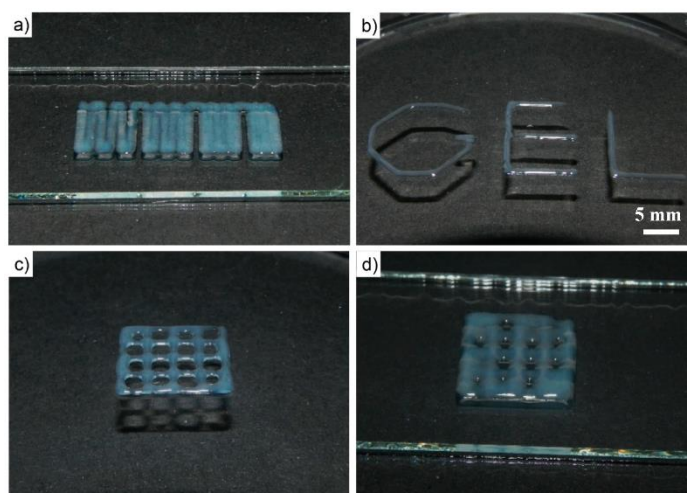
*** The following open access abstract and graphic was reprinted from *Journal of Functional Biomaterials*, **2019**, 10(3), 36, <https://doi.org/10.3390/jfb10030036>

Temperature-Dependent Rheological and Viscoelastic Investigation of a Poly(2-methyl-2-oxazoline)-b-poly(2-iso-butyl-2-oxazoline)-b-poly(2-methyl-2-oxazoline)-Based Thermogelling Hydrogel

Lübtow M.M., Mrlik M., Hahn L., Altmann A., Beudert M., Lühmann T. and Luxenhofer R.

Abstract

The synthesis and characterization of an ABA triblock copolymer based on hydrophilic PMeOx blocks A and a modestly hydrophobic poly(2-iso-butyl-2-oxazoline) block B is described. Aqueous polymer solutions were prepared at different concentrations (1–20 wt %) and their thermogelling capability using visual observation was investigated at different temperatures ranging from 5



to 80 °C. As only a 20 wt % solution was found to undergo thermogelation, this concentration was investigated in more detail regarding its temperature-dependent viscoelastic profile utilizing various modes (strain or temperature sweep). The prepared hydrogels from this particular ABA triblock copolymer have interesting rheological and viscoelastic properties, such as reversible thermogelling and shear thinning, and may be used as bioink, which was supported by its very low cytotoxicity and initial printing experiments using the hydrogels. However, the soft character and low yield stress of the gels do not allow real 3D printing at this point. ***

However, the rheological properties already suggested limited printability, which was further elucidated in first printing experiments. Therefore, in the following studies the polymer already described by Lorson et al.²⁶⁴ in 2017 was used in different approaches.

The printability of the polymer P_{MeOx}-*b*-P_{nPrOzi} was significantly improved by the addition of nanoclay.

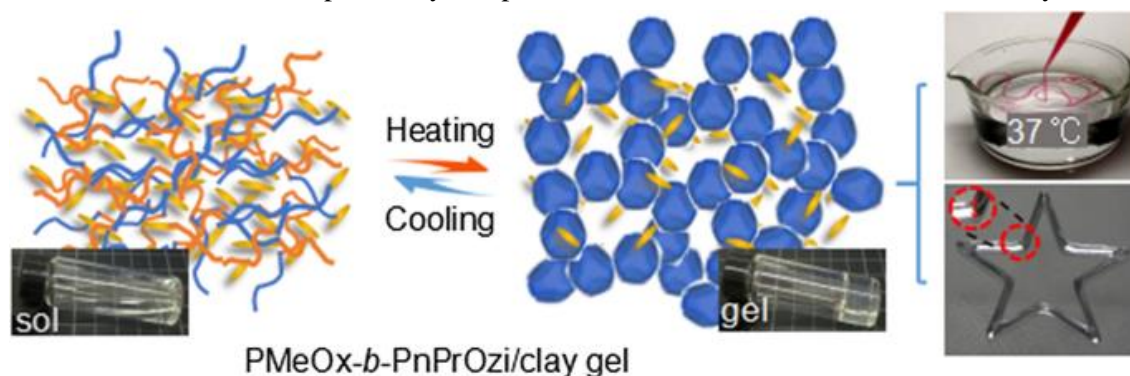
*** The following open access abstract and graphic was reprinted from *Journal of Materials Science*, **2021**, 56 (1), 691-705, <https://doi.org/10.1007/s10853-020-05190-5>

Improving Printability of a Thermoresponsive Hydrogel Biomaterial Ink by Nanoclay Addition

Hu C., Hahn L., Yang M., Altmann A., Stahlhut P., Groll J. and Luxenhofer R.

Abstract

As a promising biofabrication technology, EBB has gained significant attention in the last decade and major advances have been made in the development of bioinks. However, suitable synthetic and stimuli-responsive bioinks are underrepresented in this context. In this work, we described a hybrid system of nanoclay Laponite XLG and thermoresponsive block copolymer P_{MeOx}-*b*-P_{nPrOzi} as a novel biomaterial ink and discussed its critical properties relevant for EBB, including viscoelastic properties and printability. The hybrid hydrogel retains the thermogelling properties but is strengthened by the added clay (over 5 kPa of G' and 240 Pa of yield stress). Importantly, the shear-thinning character is further enhanced, which, in combination with very rapid η recovery (~ 1 s) and structure recovery (~ 10 s), is highly beneficial for EBB. Accordingly, various 3D patterns could be printed with markedly enhanced resolution and shape fidelity compared to the biomaterial ink without added clay.



In this manuscript, no cell studies were conducted. Further, the hydrogel system still lacks permanent crosslinking. Therefore, during cell-culture the construct will collapse and dissolve. To overcome this limitation Alg was added to further stabilize the constructs after the print. In this ternary blend system, several beneficial properties are combined yielding an excellent printable and highly cytocompatible system.

In a further study, instead of Alg an *in situ* polymerizable poly(N,N-dimethylacrylamide) was added. After printing, the hydrogel was chemically cured and a material with excellent mechanical strength and high stretchability was obtained.

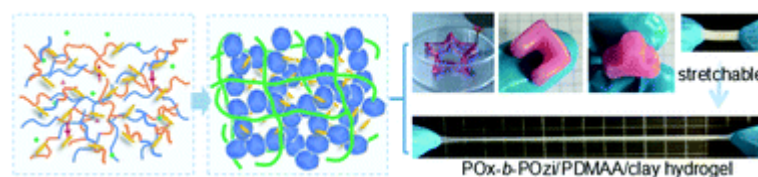
*** The following open access abstract and graphic was reprinted from *Journal of Materials Chemistry B*, **2021**, 9, 4535-4545, <https://doi.org/10.1039/D1TB00484K>

Development of a 3D Printable and Highly Stretchable Ternary Organic-Inorganic Nanocomposite Hydrogel

Hu C., Haider M., Hahn L., Yang M. and Luxenhofer R.

Abstract

Hydrogels that can be processed with AM techniques and concomitantly possess favorable mechanical properties are interesting



for many advanced applications. However, the development of novel ink materials with high intrinsic 3D printing performance has been proven to be a major challenge. Herein, a novel 3D printable organic–inorganic hybrid hydrogel is developed from three components, and characterized in detail in terms of rheological property, swelling behavior and composition. The nanocomposite hydrogel combines a thermoresponsive hydrogel with clay LAPONITE® XLG and *in situ* polymerized poly(N,N-dimethylacrylamide). Before *in situ* polymerization, the thermogelling and shear thinning properties of the thermoresponsive hydrogel provides a system well-suited for EBB. After chemical curing of the 3D-printed constructs by free radical polymerization, the resulting interpenetrating polymer network hydrogel shows excellent mechanical strength with a high stretchability to a tensile strain at break exceeding 550%. Integrating with the advanced 3D-printing technique, the introduced material could be interesting for a wide range of applications including TE, drug delivery, soft robotics and AM in general.

The thermogelling property of the diblock copolymer was further used in two-photon polymerization printing of PEG-diacrylate. The thermogel was used as support hydrogel to realize freeform printing of 3D scaffolds with outstanding resolution and topology.

*** The following open access abstract and graphic was reprinted from *Materials Horizons*, **2021**, 8, 3334-3344. <https://doi.org/10.1039/D1MH00925G>

Freeform Direct Laser Writing of Versatile Topological 3D Scaffolds Enabled by Intrinsic Support Hydrogel

Hasselmann S., Hahn L., Lorson T., Schätzlein E., Sebastien I., Beudert M., Lühmann T., Neubauer J.C., SEXTL G., Luxenhofer R. and Heinrich D.

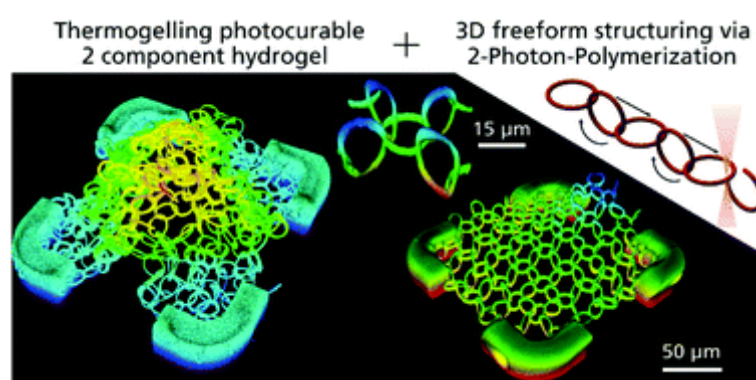
Abstract

In this study, a novel approach to create arbitrarily shaped 3D hydrogel objects is presented, wherein freeform two-photon polymerization (2PP) is enabled by the combination of a photosensitive hydrogel and an intrinsic support matrix. This way, topologies without

physical contact such as a highly porous 3D network of concatenated rings were realized, which are impossible to manufacture with most current 3D printing technologies. Micro-Raman and nanoindentation measurements show the possibility to control water uptake and hence tailor the Young's modulus of the structures via the light dosage, proving the versatility of the concept regarding many scaffold characteristics that makes it well suited for cell specific cell culture as demonstrated by cultivation of human induced pluripotent stem cell derived cardiomyocytes.

New Concepts

This contribution describes how a significant limitation of freeform direct laser writing of low η resins can be overcome to fabricate complex topological 3D structures. When attempting to manufacture very small feature sizes of soft photocurable materials such as hydrogels, the residual mobility of the microstructures from convection or diffusion can prevent a high accuracy and precision, in particular when attempting to connect structures printed at different time points inside a liquid precursor. To overcome this issue, we introduce a thermoresponsive support gel that can be conveniently mixed with the resin at low temperature (5–10 °C) but forms a highly transparent solid gel at room temperature and above. This drastic increase in η of the gel effectively suppresses diffusion and convection, keeping any freeform laser written soft structure securely in place during processing. After 3D freeform structuring is completed, the hydrogel can be easily removed by washing with water, developing intricate soft microstructures such as arrays of 3D concatenated hydrogel rings demonstrated in this contribution. This



very simple approach opens new avenues to create soft microstructures at very high resolution, which are otherwise difficult to realize. ***

In all the presented manuscripts so far in chapter IV, the polymer established by Lorson et al. was used without further polymer modifications. For the next contribution the thermogelling polymer was slightly modified. Instead of PMeOx, polymers comprising PEtOx with a degree of polymerization of 100 and 200 were studied. This modification leads to alteration of the water solubility and gelation behavior. Further, cytocompatible bioprinting was demonstrated.

*** The following open access abstract and graphic was reprinted from *Gels*, **2021**, 7 (3), 78, <https://doi.org/10.3390/gels7030078>

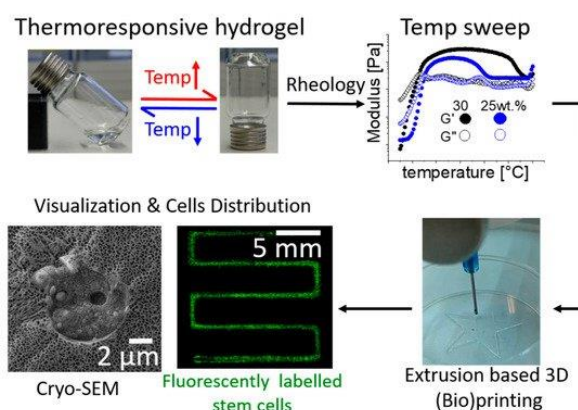
Tuning the Thermogelation and Rheology of Poly(2-oxazoline)/Poly(2-oxazine)s Based Thermosensitive Hydrogels for 3D Bioprinting

Haider M., Ahmad T., Yang M., Hu C., Hahn L., Stahlhut P., Groll J. and Luxenhofer R.

Abstract

As one kind of “smart” material, thermogelling polymers find applications in biofabrication, drug delivery and RM. In this work, we report a thermosensitive POx/POzi based diblock copolymer comprising thermosensitive/moderately hydrophobic PnPrOzi and thermosensitive/moderately hydrophilic PEtOx. Hydrogels were only formed when block length exceeded certain length (≈ 100 repeat units).

The tube inversion and rheological tests showed that the material has then a reversible sol-gel transition above 25 wt.% concentration. Rheological tests further revealed a gel strength around 3 kPa, high shear thinning property and rapid shear recovery after stress, which are highly desirable properties for EBB. Attributed to the rheology profile, well resolved printability and high stackability (with added laponite) was also possible. (Cryo) scanning electron microscopy exhibited a highly porous, interconnected, 3D network. The sol-state at lower temperatures (in ice bath) facilitated the homogeneous distribution of (fluorescently labelled) human adipose derived stem cells (hADSCs) in the hydrogel matrix. Post-printing live/dead assays revealed that the hADSCs encapsulated within the hydrogel remained viable ($\approx 97\%$). This thermoreversible and (bio) printable hydrogel demonstrated promising properties for use in TE applications. ***



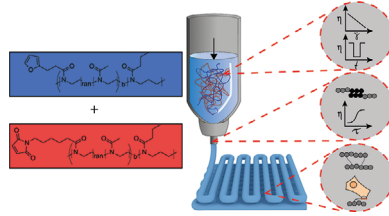
The polymer classes of PO_x/PO_{zi} offers the possibility of several post polymerization modification approaches. In the last manuscript of this thesis, the polymer PMeO_x-b-PnPrO_{zi} was partially hydrolyzed and subsequently modified with furan and maleimide moieties. These modifications ensured *in situ* chemical crosslinking of the construct after printing. Further, the cytocompatibility of the dual-gelling approach was demonstrated in preliminary bioprinting experiments.

The following open access publication was reprinted from *Macromolecular Bioscience*, **2021**, <https://doi.org/10.1002/mabi.202100122>

RESEARCH ARTICLES

L. Hahn, M. Beudert, M. Gutmann,
L. Keßler, P. Stahlhut, L. Fischer,
E. Karakaya, T. Lorson, I. Thievensen,
R. Detsch, T. Lühmann,*
R. Luxenhofer* 2100122

From Thermogelling Hydrogels toward Functional Bioinks: Controlled Modification and Cytocompatible Crosslinking



A new bioink for 3D extrusion printing which combines fast and reversible physical thermogelation and shear-thinning with click-chemistry of permanent crosslinking and modification with biorelevant cues such as RGD peptides, is investigated. Good cytocompatibility and printability with easy modification lays the foundation for further developments.

From Thermogelling Hydrogels toward Functional Bioinks: Controlled Modification and Cytocompatible Crosslinking

Lukas Hahn, Matthias Beudert, Marcus Gutmann, Larissa Keßler, Philipp Stahlhut, Lena Fischer, Emine Karakaya, Thomas Lorson, Ingo Thievensen, Rainer Detsch, Tessa Lühmann,* and Robert Luxenhofer*

Hydrogels are key components in bioink formulations to ensure printability and stability in biofabrication. In this study, a well-known Diels-Alder two-step post-polymerization modification approach is introduced into thermogelling diblock copolymers, comprising poly(2-methyl-2-oxazoline) and thermo-responsive poly(2-*n*-propyl-2-oxazine). The diblock copolymers are partially hydrolyzed and subsequently modified by acid/amine coupling with furan and maleimide moieties. While the thermogelling and shear-thinning properties allow excellent printability, trigger-less cell-friendly Diels-Alder click-chemistry yields long-term shape-fidelity. The introduced platform enables easy incorporation of cell-binding moieties (RGD-peptide) for cellular interaction. The hydrogel is functionalized with RGD-peptides using thiol-maleimide chemistry and cell proliferation as well as morphology of fibroblasts seeded on top of the hydrogels confirm the cell adhesion facilitated by the peptides. Finally, bioink formulations are tested for biocompatibility by incorporating fibroblasts homogeneously inside the polymer solution pre-printing. After the printing and crosslinking process good cytocompatibility is confirmed. The established bioink system combines a two-step approach by physical precursor gelation followed by an additional chemical stabilization, offering a broad versatility for further biomechanical adaptation or bioresponsive peptide modification.

1. Introduction

In the field of biofabrication, researchers try to create functional tissue models by using an additive manufacturing technique. Especially in bioprinting, advances strongly rely on the availability of suitable bioinks.^[1–3] These materials, in turn, are mostly based on polymers—either of synthetic or natural origin—and contain living cells, the required growth factors, as well as nutrition to be processed by an automated biofabrication technology.^[4,5] In most cases, direct ink-writing of a hydrogel is used, allowing the production of clinically relevant designs with respect to time and size.^[6] Bioinks have to be printable at cell friendly conditions, and allow maturation of the printed construct for several weeks. Several key characteristics can be associated with an ideal hydrogel bioink. First, a pronounced shear thinning character of the precursor hydrogel during extrusion facilitates 3D-printing and concurrently the viscoelastic solid like character prevents cell sedimentation in the barrel.^[7] Second, it

L. Hahn, L. Keßler, R. Luxenhofer
 Functional Polymer Materials, Chair for Advanced Materials Synthesis,
 Institute for Functional Materials and Biofabrication, Department of
 Chemistry and Pharmacy and Bavarian Polymer Institute
 Julius-Maximilians-University Würzburg
 Röntgenring 11, Würzburg 97070, Germany
 E-mail: robert.luxenhofer@helsinki.fi


M. Beudert, M. Gutmann, T. Lorson, T. Lühmann
 Institute of Pharmacy and Food Chemistry
 Julius-Maximilians-University Würzburg
 Am Hubland, Würzburg 97074, Germany
 E-mail: tessa.luehmann@uni-wuerzburg.de

P. Stahlhut
 Department for Functional Materials in Medicine and Dentistry
 University of Würzburg
 Pleicherwall 2, Würzburg 97070, Germany

L. Fischer, I. Thievensen
 Center for Medical Physics and Technology, Biophysics Group
 Friedrich-Alexander-University of Erlangen-Nuremberg
 Henkestrasse 91, Erlangen 91052, Germany

E. Karakaya, R. Detsch
 Institute of Biomaterials
 University of Erlangen-Nürnberg
 Cauerstr. 6, Erlangen 91058, Germany

R. Luxenhofer
 Soft Matter Chemistry, Department of Chemistry and Helsinki Institute
 of Sustainability Science, Faculty of Science
 University of Helsinki
 P.O. Box 55, Helsinki FIN-00014, Finland

 The ORCID identification number(s) for the author(s) of this article can be found under <https://doi.org/10.1002/mabi.202100122>

© 2021 The Authors. Macromolecular Bioscience published by Wiley-VCH GmbH. This is an open access article under the terms of the Creative Commons Attribution-NonCommercial-NoDerivs License, which permits use and distribution in any medium, provided the original work is properly cited, the use is non-commercial and no modifications or adaptations are made.

DOI: 10.1002/mabi.202100122

should ideally allow for sufficient and fast stabilization after the printing process. The former, that is, the formation of a precursor hydrogel, can be ensured by a wide variety of approaches, such as specific chemical pre-crosslinking,^[8] pH,^[9] or temperature switch,^[10] as described, for example, for alginate, collagen, and gelatine. The defined control of these approaches to provide a cytocompatible printing process is an ongoing challenge.

Thermogelling polymer solutions that undergo fast gelation are promising candidates for bioinks. A well-known example is the polymer Pluronic F127, also known as Poloxamer 407. This triblock copolymer based on polypropylene glycol as thermoresponsive central block, flanked by two hydrophilic polyethylene glycol (PEG) blocks, forms a physical hydrogel at room temperature. Since Pluronic F127 gels represent excellent printability,^[11] they are used in many applications as a support material and sacrificial structure.^[12] One possible alternative for PEG-based systems is the family of polymers known as poly(2-oxazoline)s (POx) and their close relative poly(2-substituted-5,6-dihydro-4H-1,3-oxazine)s (poly(2-oxazine)s, POzi), which serve as a diverse biomaterials platform for different applications due to good cytocompatibility and chemical versatility.^[13–17]

In the context of biofabrication, only few reports can be found describing POx/POzi based structures used in bioprinting. Lorton et al. reported a thermogelling diblock copolymer comprising hydrophilic poly(2-methyl-2-oxazoline) (PMeOx) and thermoresponsive poly(2-*n*-propyl-2-oxazine) (P*n*PrOzi) moieties.^[18] In first bioprinting experiments excellent cytocompatibility was confirmed. The printability and shape fidelity could be significantly improved by the addition of Laponite XLG.^[19] However, this thermoresponsive hydrogel does not allow for long-term cell culture experiments, as it dissolves upon addition of an excess of cell culture medium. More recently, Trachsel et al. investigated a multi-material approach with enzymatically stabilized hydrophilic poly(2-ethyl-2-oxazoline) hydrogels via sortase linkage.^[20] To use this system in a bioink formulation, alginate was needed to stabilize the constructs after printing by Ca²⁺. Furthermore, cellulose nanofibrils were added to improve printability.^[21]

In recent years, several approaches—mainly based on irradiation with UV-light—have been described to introduce covalent crosslinking after printing,^[22–24] fueling ongoing and controversial discussions about the potential negative effect of UV irradiation on cell viability.^[24,25] More recently, crosslinking using visible light has gained attention. Irrespective of the wavelength used, photoinitiators are typically needed for crosslinking which may affect cells either immediately or during the maturation.^[24] Accordingly, alternative approaches of in situ chemical crosslinking of hydrophilic polymers by the reaction of complementary functional groups, to obtain hydrogels, remain actively investigated. One such alternative is the Diels-Alder chemistry, already introduced for hydrogel synthesis by Chujo et al. a few decades ago^[26] besides other crosslinking strategies^[27,28] and recently studied again by Shoichet et al.^[29–32] as well as Nahm et al.,^[33] among others. Chujo et al. used the hydrophilic PMeOx functionalized with maleimide and furan groups in the polymer side chain. However, these hydrogel precursors would be unlikely candidates for dispense plotting, due to their hydrophilic nature and expected rheological properties.

In this work, we established a double-crosslinked bioink platform obtained by one starting block copolymer and its modifications, combining thermoresponsive precursor gelation together with temperature-controlled Diels-Alder crosslinking, in order to employ the benefits of both crosslinking mechanisms for creating a functional and adaptable bioink platform. Therefore, a previously described diblock copolymer comprising a hydrophilic PMeOx block and a thermoresponsive P*n*PrOzi block (PMeOx-*b*-P*n*PrOzi = P0),^[18] which showed pronounced physical thermogelation in aqueous solutions, was modified with furan and maleimide moieties.^[26] The fast physical sol/gel transition was used to obtain a homogenous cell distribution throughout the construct, in combination with good printability. After the extrusion, the cytocompatible in situ Diels-Alder crosslinking stabilized the construct and offered the possibility to introduce bioinstructive peptides. Beside the two functionalized polymers, no further compound such as crosslinker, initiators or viscosity modulators were used in order to obtain both a physically and chemically crosslinked hydrogel.

2. Results and Discussion

The presented bioink concept builds on two independent crosslinking mechanisms. At first, thermoreversible hydrophobic interactions offer excellent handling and printing properties. Second, a slow but essentially irreversible Diels-Alder crosslinking post-processing provides long-term stability and maturation.

In addition, Diels-Alder functionalities enable the conjugation of bioactive components (**Figure 1A**).^[34–36] In order to introduce the corresponding functionalities, the thermogelling diblock copolymer P0, with a similar degree of polymerization as described previously,^[18] was partially hydrolyzed, yielding secondary amines, which are subsequently coupled with carboxylic acids (**Figure 1B**). Doing so, it is critical that the thermogelling properties of the polymer P0 (**Figure S1**, Supporting Information) are retained after modification and that the crosslinking occurs in a time period suitable for bioprinting. The first step was a carefully controlled partial hydrolysis of the polymer yielding ethyleneimine (EI) moieties in the hydrophilic part of the polymer. We expected that the MeOx repeat units are hydrolyzed significantly faster than the *n*PrOzi units.^[37,38] ¹H-Nuclear magnetic resonance (NMR) spectroscopy confirmed that backbone and sidechain signals attributed to MeOx repeat units decreased significantly with increasing reaction time (**Figures S2, S3A, B**, Supporting Information), while the signals attributed to *n*PrOzi repeat units remained preserved. The degree of hydrolysis has a significant impact on the thermogelling properties (**Figure S3C**, Supporting Information). Here, the polymers with a hydrolysis degree of 10% of the PMeOx block were further investigated ((P(MeOx_{90-co}-EI₁₀)-*b*-P*n*PrOzi₁₀₀ = P1). The thermogelling properties of three different P1 polymer batches performed similar like the unmodified polymers described by Lorton et al. (**Table S1**, Supporting Information),^[18] indicating the reproducibility of the approach.^[39] Modification of P1 with furan or maleimide moieties resulted in the final functionalized polymers P(MeOx_{90-co}-Fu₁₀)-*b*-P*n*PrOzi₁₀₀ (P-Fu) and P(MeOx_{90-co}-Ma₁₀)-*b*-P*n*PrOzi₁₀₀ (P-Ma). The successful and complete modification was verified by ¹H-NMR spectroscopy (**Figure S4**, Supporting Information) and

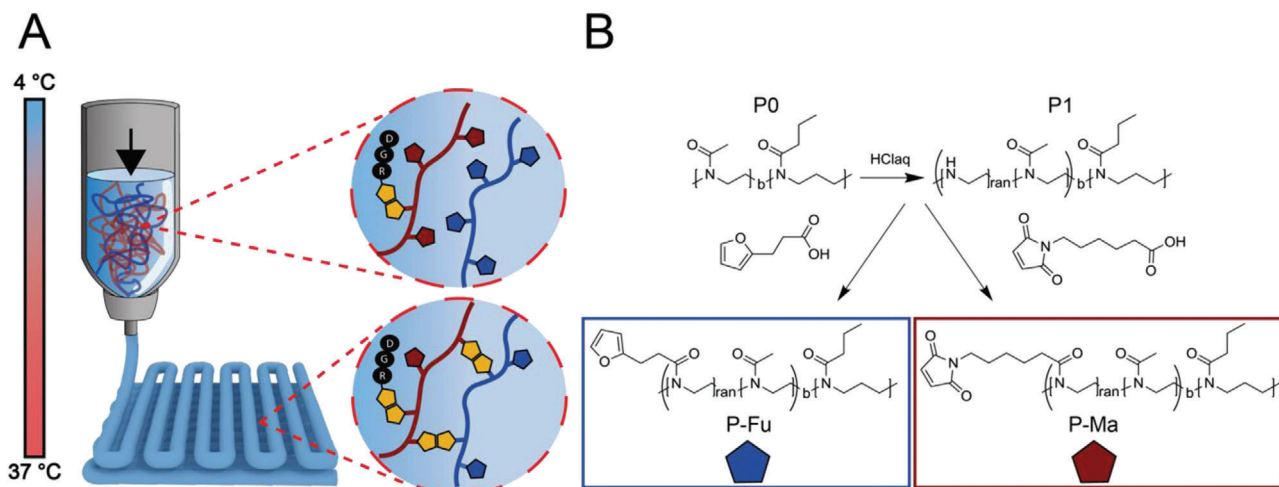


Figure 1. Investigated strategy for functional bioink formulations. A) Schematic illustration of the bioink strategy. At 5 °C the polymer solutions P-Fu and P-Ma are present as low viscous liquids, which can be easily mixed with cells and peptide motifs (e.g., RGD). Increasing the temperature to 37 °C leads to a rapid physical gelation of both P-Fu and P-Ma preventing cell sedimentation and ensuring good printability. After printing, the chemical crosslinking takes place at 37 °C generating stable and biofunctionalized constructs. B) Synthesis route to establish the thermogelling polymers P-Fu and P-Ma: Partial acidic hydrolysis of the thermogelling diblock copolymer P0 followed by the introduction of furan and maleimide moieties by amide coupling (P-Fu and P-Ma).

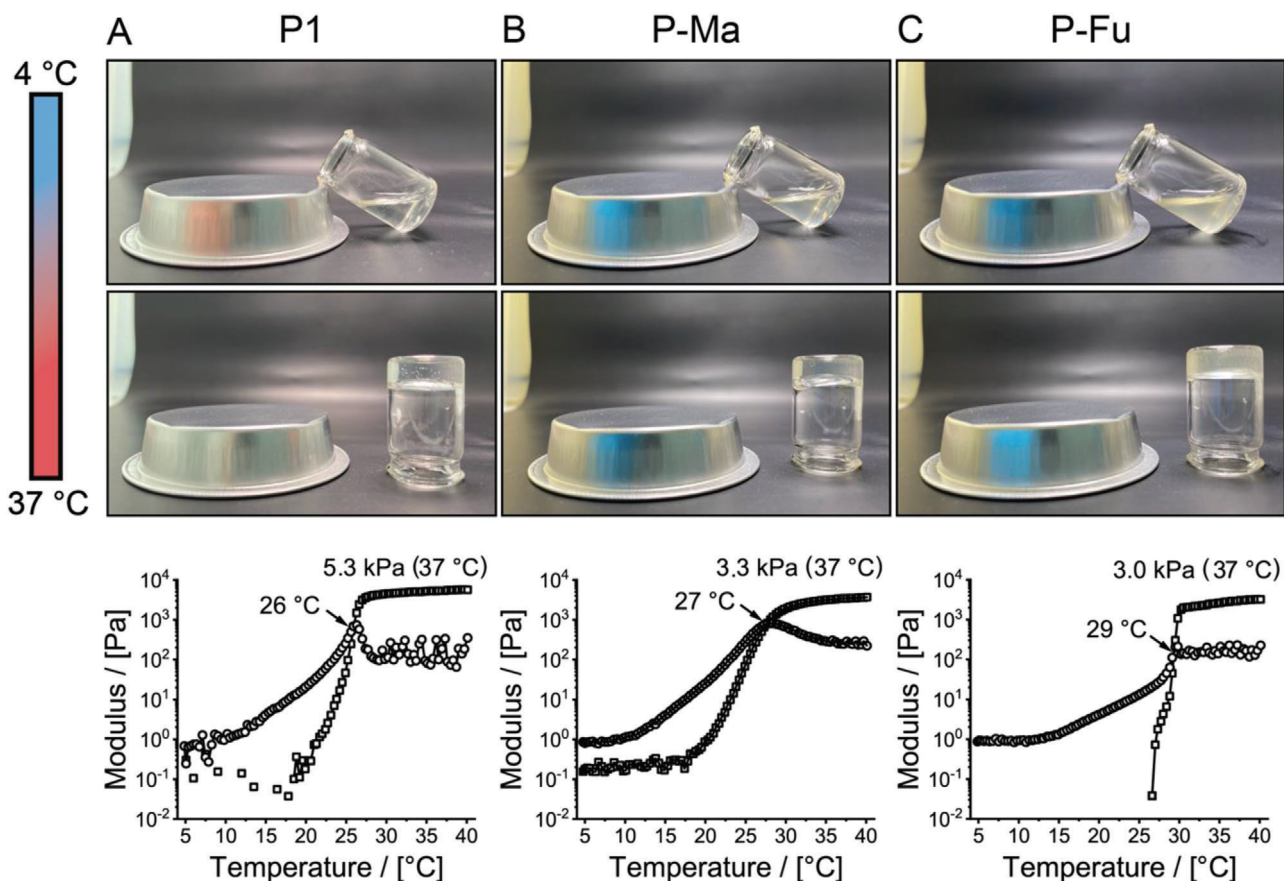


Figure 2. Thermogelling properties of the different modified polymers. A) P1, B) P-Ma, and C) P-Fu in the temperature range of 5–37 °C (heat rate: 0.05 °C s⁻¹) and at 20 wt% aqueous solutions (□: Storage modulus G' , ○: Loss modulus G''). Images were taken at 5 and 37 °C following the described temperature scale.

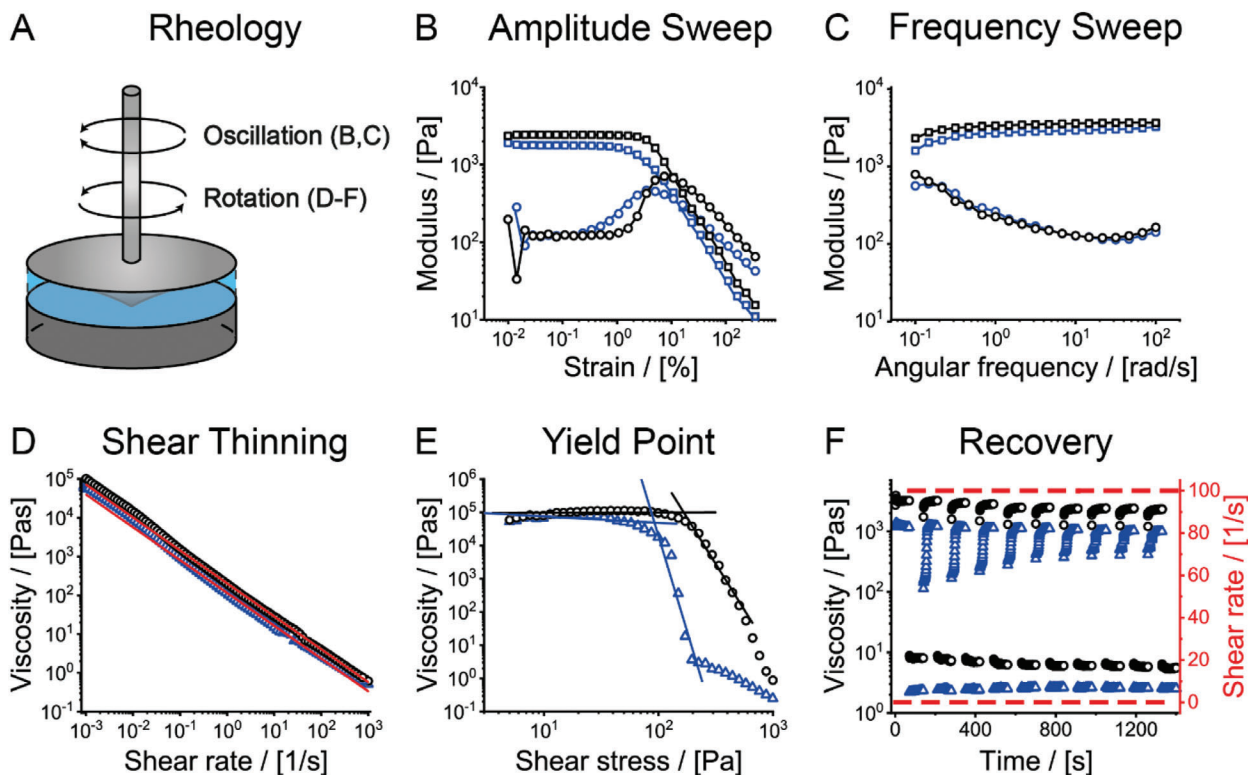


Figure 3. Determination of important rheological properties. A) Rheological properties for direct ink-writing of P-Fu (blue) and P-Ma (black) at a concentration of 20 wt% and 37 °C. B) Amplitude sweep (\square : Storage modulus G' , \circ : Loss modulus G'') and C) frequency sweep. D) Shear thinning properties: Viscosity in dependence of the applied shear rate. Red line: data fitted with a power law function. E) Yield point determination: Viscosity as a function of applied shear stress. The onset of viscosity decrease designates the yield point τ . F) Structure-recovery properties: Alternated high and low-shear regimes.

all relevant signals could be attributed. It is important to note that the signals attributed to EI repeat units completely disappeared. Furthermore, complete modification of all secondary amines (EI units) was confirmed via titration (Figure S4, Supporting Information).

The polymers P1, P-Fu and P-Ma exhibited pronounced thermogelling properties in the temperature range of 5–40 °C (5 °C low viscous liquid, 40 °C stable hydrogel, Figure 2) with sol/gel transitions between 26 and 29 °C (Figure 2). Compared to the precursor polymer P0 the transition temperature increased, which simplifies handling at room temperature (T_{gel} (P0) = 21 °C, Figure S1, Supporting Information). Notably, the storage modulus G' at 37 °C increased from 3.8 kPa for P0 to 5.3 kPa for P1 (Figure 2A). In contrast, the addition of furan and maleimide moieties resulted to a reversal of G' to 3.3 and 3.0 kPa, respectively (Figure 2B,C). Clearly, modifications of the hydrophilic block affect the polymer self-assembly, presumably by affecting the compatibility between the blocks. The physical hydrogels P-Fu and P-Ma at 37 °C and a concentration of 20 wt% were further characterized individually via oscillatory and rotational shear rheology to investigate whether their rheological parameters would be favorable for 3D printing (Figure 3).

Both samples showed a pronounced linear viscoelastic region in the amplitude sweep (Figure 3B). Slightly higher G' values are obtained for the polymer P-Ma, which is in agreement with the values obtained during the temperature sweep (Figure 2). In the

investigated frequency region both polymers exhibited viscoelastic solid-like character throughout (Figure 3C). The pronounced shear-thinning (Figure 3D) with flow indices of $n = 0.15$ for P-Fu and P-Ma, well-defined yield-points (Figure 3E; τ (P-Fu) = 92 Pa and τ (P-Ma) = 166 Pa), high viscosity at low shear stress (≈ 100 kPa s) and fast structure recovery (Figure 3F) suggests good printability for both hydrogels. This rheological profile allows the low viscosity polymer sols to be mixed with cells at ≤ 10 °C, and subsequently printed at 37 °C on a preheated printing dish, where the crosslinking Diels-Alder reaction takes place, subsequently (Figure 4A).

Accordingly, we mixed 20 wt% aqueous solutions of both polymers (1/1, v/v) at 10 °C and followed G' and G'' at 10, 20, and 37 °C over time (Figure 4B). Over the investigated time of 2 h no hydrogel formation was observed at 10 °C and the sample remained a low viscous liquid, ideal for sample preparation, cell distribution, and transfer into a printing syringe. Only a minor increase in viscosity is observed after ≈ 1 h. With a temperature-controlled printing setup, this allows for prolonged printability, if needed. In contrast, at 25 °C, which is below T_{gel} hydrogel, a sol/gel transition is observed after 65 min and must be attributed to the Diels-Alder crosslinking. At 37 °C the mixture thermogelled immediately, followed by additional Diels-Alder crosslinking, as evidenced by an increase of G' and G'' . After less than 50 min a plateau value of more than 10 kPa was reached. Accordingly, printing the bioink at room temperature onto a preheated

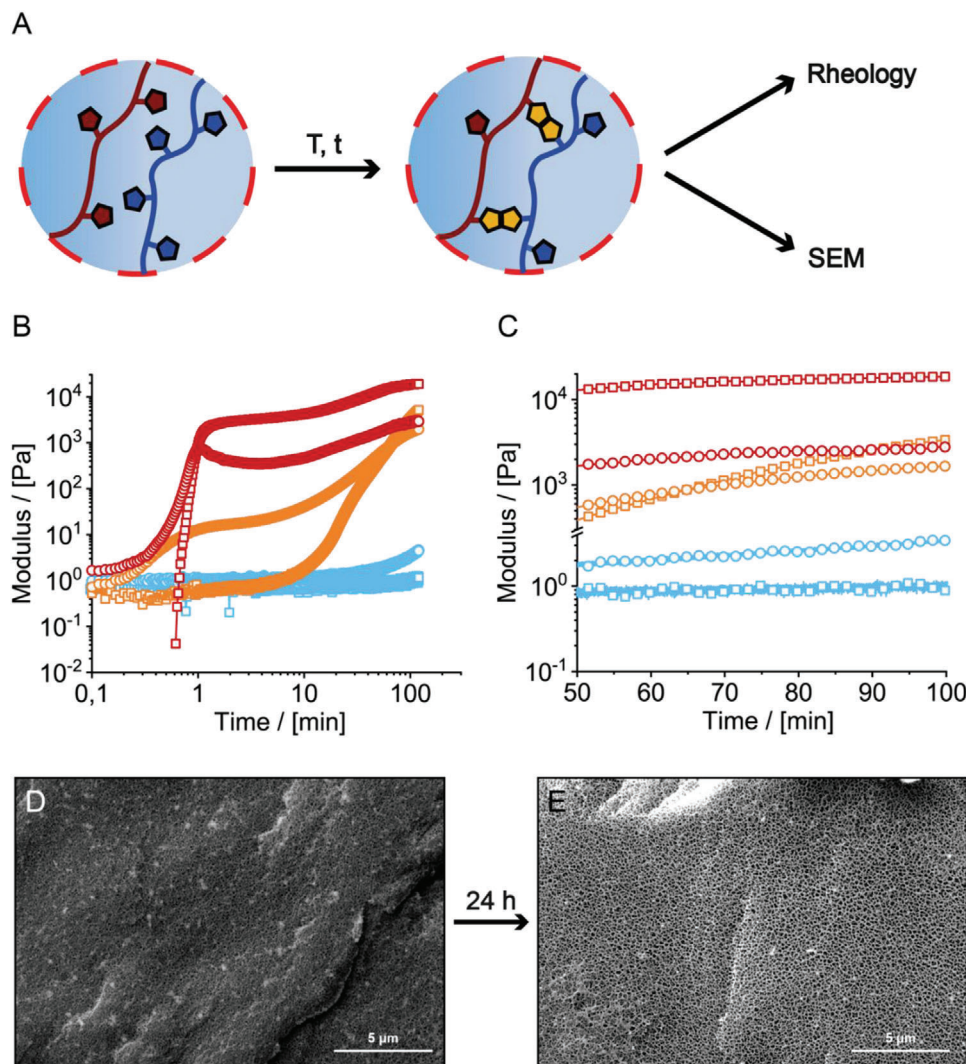


Figure 4. Chemical crosslinking of mixed P-Fu and P-Ma hydrogels. A) Workflow for crosslinking analysis (B–C) Crosslinking kinetics of P-Fu and P-Ma mixtures (1:1) at different temperatures (blue: 10 °C, orange: 20 °C, and red: 37 °C) and 20 wt% concentration (\square : Storage modulus G' , \circ : Loss modulus G''): B) Time scans of 120 min with a fixed amplitude of 0.5 % and an angular frequency of 10 rad s^{-1} with a C) detailed view for 50–100 min which we deem critical for preparing and conducting a typical print. Cryogenic scanning electron microscopy (SEM) investigations to visualize the porous structure of the bioink: Samples were recorded after D) crosslinking of 24 h and E) additional swelling for 24 h.

dish should ensure rapid crosslinking and stability of the printed construct.

Due to the nature of the chemical crosslinked synthetic hydrogel, a highly porous network with features in the range of a few dozen nm was obtained (Figure 4D). Swelling for 24 h led to a significant increase in pore size into the lower 100 nm range (Figure 4E). Although the pore size is sufficiently large for diffusion of nutrients, cells will not be able to migrate through the generated network. Compared to the physical hydrogel of P0 (Figure S1B, Supporting Information) the pore size decreased significantly after chemical crosslinking, due to the formation of a more compact three-dimensional covalent network. In order to highlight the adaptability of the platform in terms of stiffness, the concentration of precursor solutions of P-Fu and P-Ma was decreased by dilution with water leading to softer hydrogels with slower crosslinking kinetics (Figure S5, Supporting Information). Ad-

ditionally, the nature of the crosslinker can be adapted to specific applications. To demonstrate this, we used PEG₆₀₀-bismaleimide as a model crosslinker. The P-Fu-PEG mixtures showed a slower crosslinking and resulted in softer and less dense networks as characterized by rheology and cryogenic scanning electron microscopy, respectively (Figure S6, Supporting Information). Not surprising, this led to a more pronounced swelling of the hydrogels compared to the P-Fu/P-Ma crosslinking.

Based on the favorable rheological properties of the precursor hydrogels and the controlled crosslinking kinetics, first 3D printing experiments were performed. At 5 °C, P-Fu and P-Ma solutions were homogeneously mixed and transferred into a printing cartridge (held at 5 °C) followed by printing onto a preheated (37 °C) printing bed (Figure 5A–C). After 1 h of in situ chemical crosslinking at 37 °C, the constructs were immersed in fresh cell culture medium and incubated for 14 days at 37 °C. The

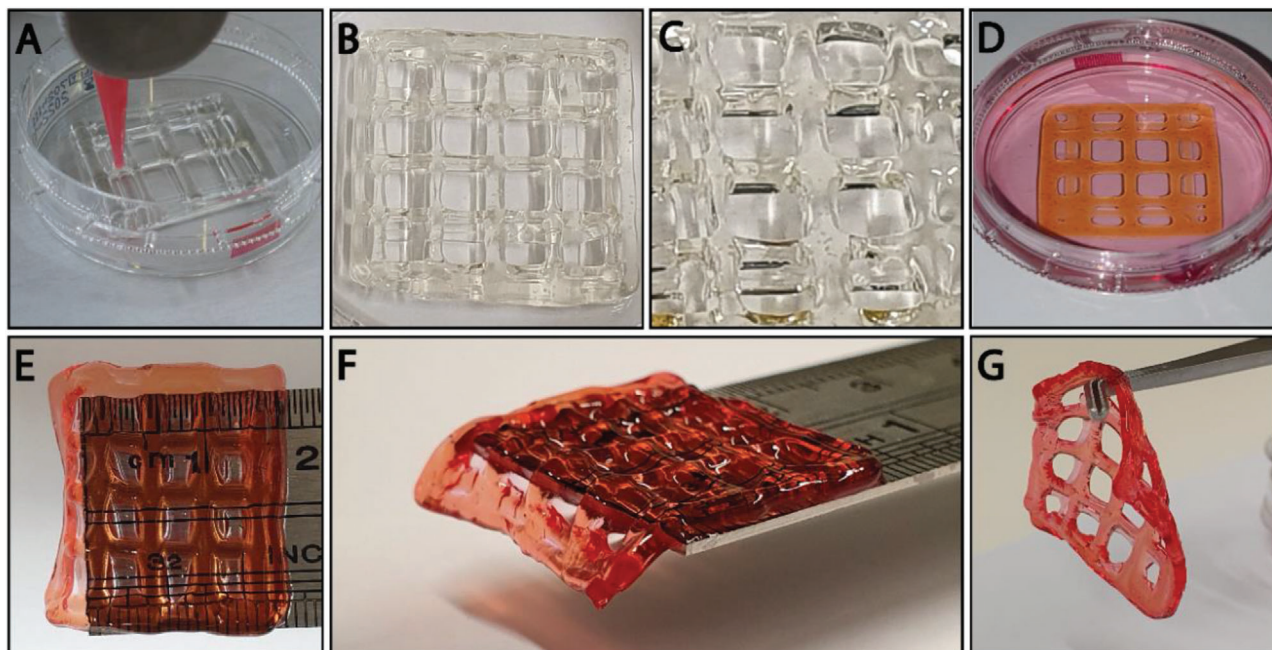


Figure 5. Printing of P-Fu and P-Ma crosslinking hydrogels. A) Image of the printed scaffold during the printing process. B,C) Illustration of the printed scaffold immediately after printing. D) Printed scaffolds after incubation in culture medium for 14 days. E–G) Handling and transfer of P-Fu and P-Ma crosslinked hydrogels after 14 days in culture medium.

constructs remained stable with good structural integrity (Figure 5D). However, fusion of stacked layers with direct contact can be seen. During incubation, swelling increases the contact between individual layers, which can then cross-link with each other. In the end, this leads to a homogeneous construct with relatively low stackability. Even though the hydrogels are soft, as analyzed by rheology and shown above, they were easily handled and transferred while retaining their printed shape (Figure 5D–G).

Furthermore, we analyzed the swelling of the crosslinked P-Fu and P-Ma hydrogels (20 wt%, ratio P-Fu/P-Ma 1:1). Only little swelling was observed (Figure S10A, Supporting Information), which is explained by the combination of physical and chemical crosslinking with several crosslinking functionalities at every polymer molecule. Interestingly, a significant increase of swelling was observed at 5 °C (Figure S10C,D, Supporting Information). Below the lower critical solution temperature of the nPrOzi block the swelling of the hydrogel increased significantly due to an increased solubility of the thermoresponsive nPrOzi block and the removal of physical crosslinks upon cooling. In addition, the stability was further confirmed by mechanical testing. Elastic moduli of approximately 3000–4000 kPa were obtained for the crosslinked hydrogels after 14 days (Figure S10B, Supporting Information).

As mentioned above, it has been shown that different POx-based hydrogels show no cytotoxic effects on cells and therefore present a promising platform for bioinks.^[40–44] However, applicability in biomedicine requires the adhesive functionalization of POx-based hydrogels, as the material per se does not support cell adhesion. To test, whether adhesive functionalization of our hydrogels supports cell adhesion, we functionalized them with integrin-ligating RGD-peptide. We further generated lentivirally transduced, NIH/3T3-based morphology reporter cells, stably ex-

pressing farnesylated tdTomato red-fluorescent protein, to label the plasma membrane and compared the morphology of our reporter cells cultured on top of RGD-functionalized and non-functionalized POx hydrogels. Epifluorescence microscopy analysis after 3 and 4 days of cultivation revealed that cells on non-functionalized POx hydrogels were low in number and showed a rounded morphology (Figure 6A,C), whereas cells on RGD-functionalized hydrogels displayed a well spread fibroblastoid morphology (Figure 6B) and even increased in number over time (Figure 6D). These data demonstrate that adhesive functionalization of our POx hydrogels supports cell adhesion, spreading and proliferation.

To further study cell viability within the gel (3D), NIH3T3 cells were embedded in the hydrogel pre-printing. After the printing process and cross-linking of the hydrogels, the cell viability of the encapsulated cells in the scaffold was analyzed. Cells were pre-stained with Hoechst 33342 prior to the printing process. This was necessary as preliminary work showed that fluorescein diacetate (FDA) was not able to penetrate the gels in a sufficient manner. Dead cells were visualized using propidium iodide (PI) (here no incompatibilities with in-gel penetration were observed) staining after 1 and 2 days. After optimizing the polymer purification process (Figure S8, Supporting Information) as well as the printing protocol, cell viability staining showed no cytotoxic effect of the hydrogel. No difference between the unmodified and RGD-functionalized constructs was observed. The majority of dead cells that were visible, scanning the entire printed hydrogel construct, could be accounted to drying-off effects at the outer layers, which was reported for other hydrogel systems before (Figure S9, Supporting Information).^[45,46] Despite the RGD-functionalization, the cells showed a rounded morphology after the encapsulation in the hydrogel (Figure 7). It

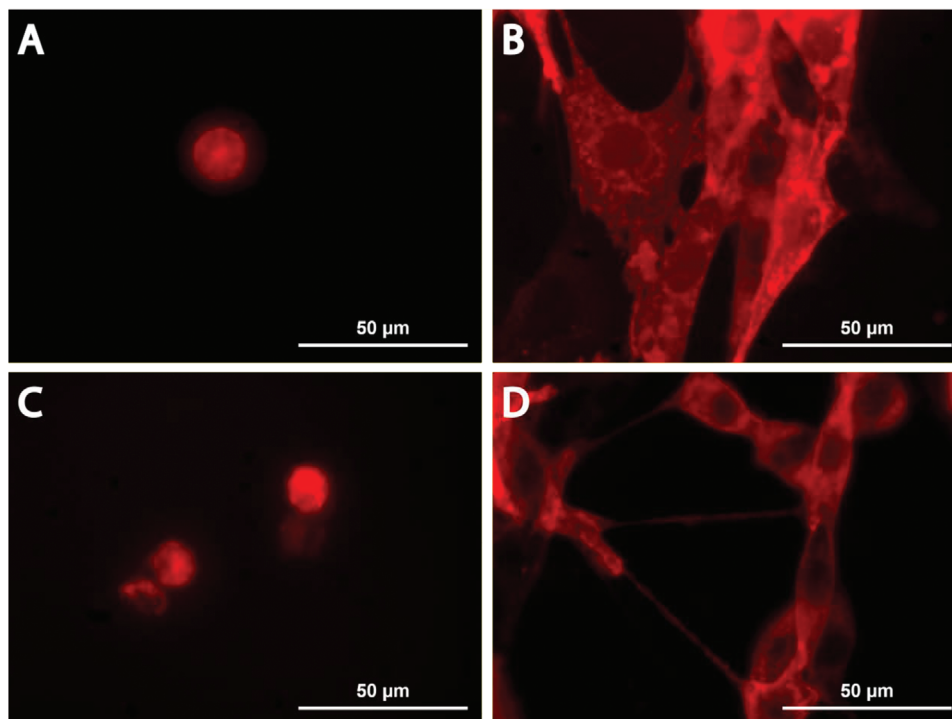


Figure 6. Cell adhesion on the surface of P-Fu and P-Ma crosslinking hydrogels. POx hydrogel without RGD-modification does not allow for good cell adhesion and spreading after A) 3 and C) 4 days. In contrast, cell adhesion and spreading were observed on POx hydrogel with RGD-modification after B) 3 days of and D) 4 days of cultivation.

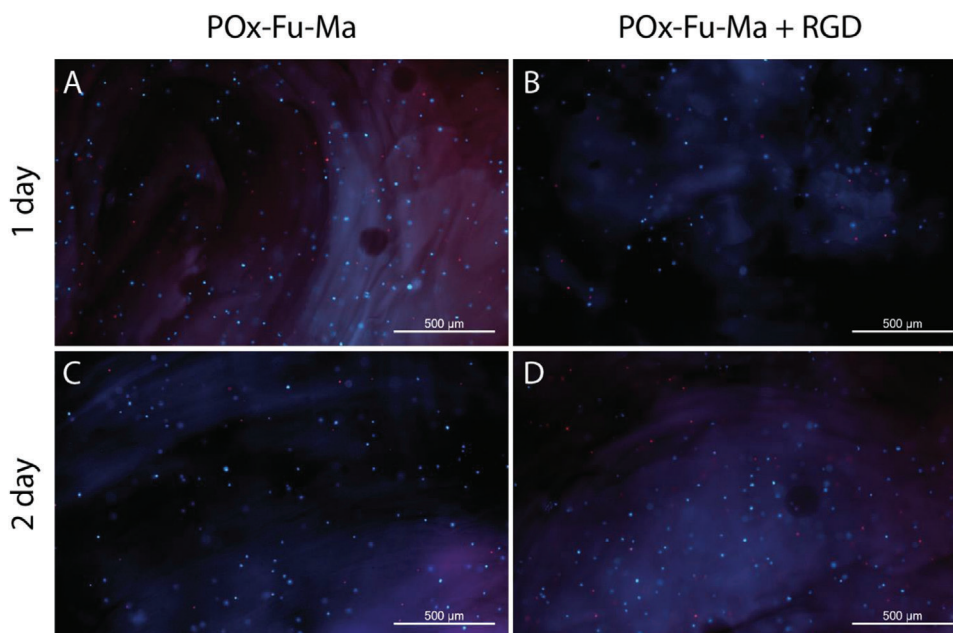


Figure 7. Cell viability of fibroblasts in P-Fu/P-Ma-bioinks after deposition of a bioink drop by extrusion printing. NIH3T3 cells were pre-stained with Hoechst 33 342 (blue) and incorporated, printed, and cultivated in POx-based hydrogels (20 wt%) B,D) with and A,C) without RGD-peptide. Dead cells were assessed by staining with PI (red).

has been previously described that POx hydrogels with moduli of around of around 3.5–4.5 kPa are too stiff for the migration of the cells.^[47,48] Furthermore, small pore sizes, as described above for this system, have been shown to prevent cell spreading and migration.^[49,50] With G' of around 10 kPa and submicron pore size, the hydrogel system, as shown in this study, clearly does not allow the migration and therefore the spreading of the cells.

In an effort to address cell adhesion and migration, we aim at incorporating matrix metalloprotease (MMP) cleavable linkers into the hydrogel network, to ensure cleavage by secreted MMPs and therefore a loosening of the network as demonstrated before.^[51–53] The sequence of the linker (GPQGIAGQ) is derived from collagen. It has been shown to be responsive to MMP cleavage and has already been used in different applications.^[54–57] The linker can be flanked with either thiol or maleimide groups for the cross-linking of both P-Fu and P-Ma and is part of the ongoing research.

3. Conclusion

In this study, favorable thermogelation and shear-thinning properties were combined with cell friendly post-printing chemical crosslinking via Diels-Alder chemistry. The post-polymerization modification preserved the nature of physical crosslinked hydrogels. The crosslinking kinetics and density could be fine-tuned with different temperatures and crosslinking degrees. The second crosslinking step ensured stability of printed constructs over at least two weeks. Biofunctionality was introduced via the attachment of RGD binding motives and NIH 3T3 cells showed cell adhesion and an elongated morphology, when seeded on top of the hydrogels for a couple of days. First bioprinting experiments highlighted the optimized printing setup, the biocompatibility and the functionality of the investigated bioink formulation. With this study, we demonstrate a dual-gelling system based on the versatile and cytocompatible polymer classes of POx and POzi that was used to develop a functional bioinks. Furthermore, the platform can be conveniently decorated with biofunctionalities, which makes it adaptable for many specific applications.

Supporting Information

Supporting Information is available from the Wiley Online Library or from the author.

Acknowledgements

L.H. and M.B. contributed equally to this work. The authors would like to gratefully acknowledge support by the Deutsche Forschungsgemeinschaft (DFG, German Research Foundation)-project number 326998133-TRR225 (subprojects A03, B06). Furthermore, the authors thank the Deutsche Forschungsgemeinschaft for funding the crossbeam scanning electron microscope Zeiss CB 340 (INST 105022/58-1 FUGG) within the DFG State Major Instrumentation Programme.

Open access funding enabled and organized by Projekt DEAL.

Conflict of Interest

The authors declare no conflict of interest.

Data Availability Statement

The data that support the findings of this study are available from the corresponding author upon reasonable request.

Keywords

biofabrication, bioprinting, chemical crosslinking, hydrogels

Received: March 25, 2021

Revised: June 20, 2021

Published online:

- [1] L. Moroni, T. Boland, J. A. Burdick, C. De Maria, B. Derby, G. Forgacs, J. Groll, Q. Li, J. Malda, V. A. Mironov, C. Mota, M. Nakamura, W. Shu, S. Takeuchi, T. B. F. Woodfield, T. Xu, J. J. Yoo, G. Vozzi, *Trends Biotechnol.* **2018**, *36*, 384.
- [2] D. Chimene, K. K. Lennox, R. R. Kaunas, A. K. Gaharwar, *Ann. Biomed. Eng.* **2016**, *44*, 2090.
- [3] L. Valot, J. Martinez, A. Mehdi, G. Subra, *Chem. Soc. Rev.* **2019**, *48*, 4049.
- [4] J. Groll, J. A. Burdick, D. - W. Cho, B. Derby, M. Gelinsky, S. C. Heilshorn, T. Jüngst, J. Malda, V. A. Mironov, K. Nakayama, A. Ovsianikov, W. Sun, S. Takeuchi, J. J. Yoo, T. B. F. Woodfield, *Biofabrication* **2018**, *11*, 013001.
- [5] J. Groll, T. Boland, T. Blunk, J. A. Burdick, D.-W. Cho, P. D. Dalton, B. Derby, G. Forgacs, Q. Li, V. A. Mironov, L. Moroni, M. Nakamura, W. Shu, S. Takeuchi, G. Vozzi, T. B. F. Woodfield, T. Xu, J. J. Yoo, J. Malda, *Biofabrication* **2016**, *8*, 013001.
- [6] D. Chimene, R. Kaunas, A. K. Gaharwar, *Adv. Mater.* **2020**, *32*, 1902026.
- [7] T. Jüngst, W. Smolan, K. Schacht, T. Scheibel, J. Groll, *Chem. Rev.* **2016**, *116*, 1496.
- [8] J. Hazur, R. Detsch, E. Karakaya, J. Kaschta, J. Teßmar, D. Schneiderreit, O. Friedrich, D. W. Schubert, A. R. Boccaccini, *Biofabrication* **2020**, *12*, 045004.
- [9] E. O. Osidak, V. I. Kozhukhov, M. S. Osidak, S. P. Domogatsky, *Int. J. Bioprint.* **2020**, *6*, 270.
- [10] L. Ouyang, R. Yao, Y. u Zhao, W. Sun, *Biofabrication* **2016**, *8*, 035020.
- [11] M. Müller, J. Becher, M. Schnabelrauch, M. Zenobi-Wong, *Biofabrication* **2015**, *7*, 035006.
- [12] D. B. Kolesky, R. L. Truby, A. S. Gladman, T. A. Busbee, K. A. Homan, J. A. Lewis, *Adv. Mater.* **2014**, *26*, 3124.
- [13] T. Lorson, M. M. Lübtow, E. Wegener, M. S. Haider, S. Borova, D. Nahm, R. Jordan, M. Sokolski-Papkov, A. V. Kabanov, R. Luxenhofer, *Biomaterials* **2018**, *178*, 204.
- [14] J. - R. Park, E. C. L. Bolle, A. D. Santos Cavalcanti, A. Podevyn, J. F. R. Van Guyse, A. Forget, R. Hoogenboom, T. R. Dargaville, *Biointerphases* **2021**, *16*, 011001.
- [15] M. M. Lübtow, T. Lorson, T. Finger, F. - K. Gröber-Becker, R. Luxenhofer, *Macromol. Chem. Phys.* **2020**, *221*, 1900341.
- [16] M. M. Lübtow, S. Oerter, S. Quader, E. Jeanclous, A. Cubukova, M. Krafft, M. S. Haider, C. Schulte, L. Meier, M. Rist, O. Sampetean, H. Kinoh, A. Gohla, K. Kataoka, A. Appelt-Menzel, R. Luxenhofer, *Mol. Pharmaceutics* **2020**, *17*, 1835.
- [17] J. Humphries, D. Pizzi, S. E. Sonderegger, N. L. Fletcher, Z. H. Houston, C. A. Bell, K. Kempe, K. J. Thurecht, *Biomacromolecules* **2020**, *21*, 3318.
- [18] T. Lorson, S. Jaksch, M. M. Lübtow, T. Jüngst, J. Groll, T. Lühmann, R. Luxenhofer, *Biomacromolecules* **2017**, *18*, 2161.
- [19] C. Hu, L. Hahn, M. Yang, A. Altmann, P. Stahlhut, J. Groll, R. Luxenhofer, *J. Mater. Sci.* **2021**, *56*, 691.

- [20] L. Trachsel, N. Broguiere, J. - G. Rosenboom, M. Zenobi-Wong, E. M. Benetti, *J. Mater. Chem. B* **2018**, *6*, 7568.
- [21] L. Trachsel, C. Johnbosco, T. Lang, E. M. Benetti, M. Zenobi-Wong, *Biomacromolecules* **2019**, *20*, 4502.
- [22] S. Stichter, T. Jungst, M. Schamel, I. Zilkowski, M. Kuhlmann, T. Böck, T. Blunk, J. Teßmar, J. Groll, *Ann. Biomed. Eng.* **2017**, *45*, 273.
- [23] S. Bertlein, G. Brown, K. S. Lim, T. Jungst, T. Boeck, T. Blunk, J. Tessmar, G. J. Hooper, T. B. F. Woodfield, J. Groll, *Adv. Mater.* **2017**, *29*, 1703404.
- [24] K. S. Lim, B. S. Schon, N. V. Mekhileri, G. C. J. Brown, C. M. Chia, S. Prabakar, G. J. Hooper, T. B. F. Woodfield, *ACS Biomater. Sci. Eng.* **2016**, *2*, 1752.
- [25] W. T. Han, T. Jang, S. Chen, L. S. H. Chong, H.-D.o Jung, J. Song, *Biomater. Sci.* **2020**, *8*, 450.
- [26] Y. Chujo, K. Sada, T. Saegusa, *Macromolecules* **1990**, *23*, 2636.
- [27] Y. Chujo, K. Sada, T. Saegusa, *Macromolecules* **1990**, *23*, 2693.
- [28] Y. Chujo, K. Sada, T. Saegusa, *Polymer Journal* **1993**, *25*, 599.
- [29] C. M. Nimmo, S. C. Owen, M. S. Shoichet, *Biomacromolecules* **2011**, *12*, 824.
- [30] A. E. G. Baker, R. Y. Tam, M. S. Shoichet, *Biomacromolecules* **2017**, *18*, 4373.
- [31] L. J. Smith, S. M. Taimoory, R. Y. Tam, A. E. G. Baker, N. Binth Mohammad, J. F. Trant, M. S. Shoichet, *Biomacromolecules* **2018**, *19*, 926.
- [32] V. Delplace, P. E. B. Nickerson, A. Ortin-Martinez, A. E. G. Baker, V. A. Wallace, M. S. Shoichet, *Adv. Funct. Mater.* **2020**, *30*, 1903978.
- [33] D. Nahm, F. Weigl, N. Schaefer, A. Sancho, A. Frank, J. Groll, C. Villmann, H. - W. Schmidt, P. D. Dalton, R. Luxenhofer, *Mater. Horiz.* **2020**, *7*, 928.
- [34] A. C. Braun, M. Gutmann, T. Lühmann, L. Meinel, *J. Controlled Release* **2018**, *273*, 68.
- [35] A. H. St. Amant, D. Lemen, S. Florinas, S. Mao, C. Fazenbaker, H. Zhong, H. Wu, C. Gao, R. J. Christie, J. Read De Alaniz, *Bioconjugate Chem.* **2018**, *29*, 2406.
- [36] A. H. St. Amant, F. Huang, J. Lin, D. Lemen, C. Chakiath, S. Mao, C. Fazenbaker, H. Zhong, J. Harper, W. Xu, N. Patel, L. Adams, B. Vijayakrishnan, P. W. Howard, M. Marelli, H. Wu, C. Gao, J. Read De Alaniz, R. J. Christie, *Bioconjugate Chem.* **2019**, *30*, 2340.
- [37] M. Mees, E. Haladjova, D. Momekova, G. Momekov, P. S. Sheshtakova, C. B. Tsvetanov, R. Hoogenboom, S. Rangelov, *Biomacromolecules* **2016**, *17*, 3580.
- [38] M. A. Mees, R. Hoogenboom, *Polym. Chem.* **2018**, *9*, 4968.
- [39] R. Luxenhofer, *Nanomedicine* **2015**, *10*, 3109.
- [40] R. Luxenhofer, G. Sahay, A. Schulz, D. Alakhova, T. K. Bronich, R. Jordan, A. V. Kabanov, *J. Controlled Release* **2011**, *153*, 73.
- [41] F. C. Gaertner, R. Luxenhofer, B. Bleichert, R. Jordan, M. Essler, *J. Controlled Release* **2007**, *119*, 291.
- [42] L. Hahn, M. Maier, P. Stahlhut, M. Beudert, V. Flegler, S. Forster, A. Altmann, F. Töppke, K. Fischer, S. Seiffert, B. Böttcher, T. Lühmann, R. Luxenhofer, *ACS Appl. Mater. Interfaces* **2020**, *12*, 12445.
- [43] Lübtow, Mrlik, Hahn, Altmann, Beudert, Lühmann, Luxenhofer, *J. Funct. Biomater.* **2019**, *10*, 36.
- [44] M. Bauer, S. Schroeder, L. Tauhardt, K. Kempe, U. S. Schubert, D. Fischer, *J. Polym. Sci., Part A: Polym. Chem.* **2013**, *51*, 1816.
- [45] Y. Yu, Y. Zhang, J. A. Martin, I. T. Ozbolat, *J. Biomech. Eng.* **2013**, *135*, 91011.
- [46] J. Hauptstein, T. Böck, M. Bartolf-Kopp, L. Forster, P. Stahlhut, A. Nadernezhad, G. Blahetek, A. Zernecke-Madsen, R. Detsch, T. Jüngst, J. Groll, J. Teßmar, T. Blunk, *Adv. Healthcare Mater.* **2020**, *9*, 2000737.
- [47] B. L. Farrugia, K. Kempe, U. S. Schubert, R. Hoogenboom, T. R. Dargaville, *Biomacromolecules* **2013**, *14*, 2724.
- [48] K. Bott, Z. Upton, K. Schrobback, M. Ehrbar, J. A. Hubbell, M. P. Lutolf, S. C. Rizzi, *Biomaterials* **2010**, *31*, 8454.
- [49] C. M. Murphy, F. J. O'brien, *Cell Adhes. Migr.* **2010**, *4*, 377.
- [50] F. Geiger, D. Rüdiger, S. Zahler, H. Engelke, *PLoS One* **2019**, *14*, e0225215.
- [51] M. R. Arkenberg, D. M. Moore, C.-C. Lin, *Acta Biomater.* **2019**, *83*, 83.
- [52] D. Seliktar, A. H. Zisch, M. P. Lutolf, J. L. Wrana, J. A. Hubbell, *J. Biomed. Mater. Res. A* **2004**, *68A*, 704.
- [53] H. P. Wurst, K. Larbi, M. Herrmann, US20130052736, **2013**.
- [54] J. Ritzer, T. Lühmann, C. Rode, M. Pein-Hackelbusch, I. Immohr, U. Schedler, T. Thiele, S. Stübinger, B. V. Rechenberg, J. Waser-Althaus, F. Schlottig, M. Merli, H. Dawe, M. Karpíšek, R. Wyrwa, M. Schnabelrauch, L. Meinel, *Nat. Commun.* **2017**, *8*, 264.
- [55] A. C. Braun, M. Gutmann, T. D. Mueller, T. Lühmann, L. Meinel, *J. Controlled Release* **2018**, *279*, 17.
- [56] A. C. Braun, M. Gutmann, R. Ebert, F. Jakob, H. Gieseler, T. Lühmann, L. Meinel, *Pharm. Res.* **2017**, *34*, 58.
- [57] K. Dodt, S. Lamer, M. Drießen, S. Bölch, A. Schlosser, T. Lühmann, L. Meinel, *ACS Biomater. Sci. Eng.* **2020**, *6*, 5240.

6 Discussion

In the chapters I-III, ABA type POx/POzi based triblock copolymers were described. The arrangement, block length and block ratios were inspired by the early reports by Luxenhofer et al.²³³ and Seo et al.²²².

6.1 Drug Encapsulation

In these studies, predominantly ABA type POx-based block copolymers comprising two hydrophilic PMeOx A blocks and different hydrophobic POx-based B blocks were investigated for their encapsulation capacity of water insoluble drugs. Extraordinary high drug loading of different taxanes, especially PTX, was achieved with the amphiphile A-PnBuOx-A using thin film-method (**See 2.3.3.1 Nanoformulations**). In short, this particular polymer exhibited the right hydrophobic/hydrophilic balance and block length outperforming all other tested amphiphiles with respect to drug loading and colloidal stability of the formulation, among other tested properties. The reason for that was assumed to be a result of the possibility of dipole-dipole interactions of the alkyl sidechain of the PnBuOx blocks with the drug and hydrogen bonds between the amide backbone and the drug. Surprisingly, by changing PnBuOx to the branched PsecBuOx a drastically decrease in drug loading was observed. Further, the implementation of a small fraction of benzyl moieties along the PnBuOx block by random copolymerization reduced the performance by almost half. In short, the sidechain of the hydrophobic core has a significant impact. The influence of the polymer backbone was described by Lübtow et al. in 2017.^[M1] Slightly different amphiphiles with “switched” methylene groups between the polymer backbone and sidechain of the hydrophobic core (PnPrOx, PnBuOx, PnBuOzi, PnPrOzi) were prepared by using POx and POzi moieties and tested comprehensively for the formulation capacity of PTX and CUR. Various interesting structure-property relationships, synergistic and antagonistic effects were observed. This unexpected unique behavior was further elucidated in different studies.^{224,265-267}

In literature it is reported, e.g. by Hennink and co-workers in 2013 for the encapsulation of PTX using amphiphiles with aromatic acrylamide units²⁶⁸ that π - π interactions between the amphiphile and the drug can be beneficial for drug loading and colloidal stability. Therefore, different POx/POzi amphiphiles with varying aromaticity (PnBuOx (no aromaticity)→PnBuOx-co-PBzOx→PBzOx→PPheOx) in the hydrophobic block were synthesized and compared for drug loading, stability and size of the formulations of the drugs PTX, SchA and CUR with increased aromaticity.^[M2] In short, an increase of aromaticity of the polymer decreased the loading capacity for PTX. It should be noted that very similar results, as already described in 2010²³³ and 2015²²², were obtained for the polymers A-PnBuOx-A and A-(PnBuOx-co-PBzOx)-A. This supported the reproducibility of the solubilization platform, which is an important and often underestimated aspect of scientific progress.²⁶⁹ For the natural product SchA

with moderate aromaticity no significant impact of the hydrophobic core was examined. CUR, a drug with high aromatic content, was better formulated in amphiphiles with aromatic moieties. However, in this study, no detailed structural elucidation was performed regarding the nature of the present amphiphile-drug interactions. Interestingly, the polymer A-PBzOx-A performed very well for all three tested drugs, especially in comparison to the PPheOx containing polymer. This might be due to two different reasons. First, the additional methylene group in the polymer sidechain increased the hydrophobicity, which could be beneficial for drug loading. Second, the sidechain flexibility of PBzOx is increased as a result of the additional methylene group. Therefore, more orientations are theoretically possible, which could increase the interactions. However, this has not yet been further evaluated. Investigating the encapsulation capacity of drugs for the amphiphiles described in Chapter II and III would also be of interest, as this could provide insights into the impact of the polymer backbone on the solubilization capacity, as well as into effects of additional methylene groups and steric constraints in aromatic systems.

In a follow up study, the polymer A-PBzOx-A was used as cytocompatible solubilizer of different drugs used in the treatment of colorectal cancer.^[M3] In pretests (data not shown) the polymer outperformed a series of other POx/POzi based amphiphiles with respect to drug loading and colloidal stability. Discussing polymer drug compatibility, all tested drugs exhibited aromatic segments, which again is a hint for increased interactions. However, again no study was performed unravelling this observation with the focus on interactions. In short, the amphiphile was used to solubilize the PARP inhibitor Niraparib and PI3K inhibitor HS173, which showed promising synergistic effects. Therefore, a coformulation strategy was used, in which both drugs were incorporated simultaneously. Also previously, first promising high drug loaded coformulations with the drug combinations CUR/PTX and PTX/SchA were reported.^[M2] The colorectal cancer mouse model showed promising results. From a polymer perspective, stable and small (approximately 14 nm) spherical polymer micelles loaded with Niraparib and HS173 were easily prepared. Here, too, as already demonstrated in the corresponding previous study^[M2], cytocompatibility was reported. Nevertheless, more importantly, no polymer related side effect was observed throughout the *in vivo* evaluation supporting the cytocompatibility of the aromatic PBzOx B block. It should be noted that conclusive *in vivo* studies have already been performed with different POx-based amphiphiles and excellent results were obtained.^{270,271} Furthermore, a polymer/drug conjugate system is in advanced clinical testing.^{5,6} In these examples, no aromatic segments were used. The preliminary *in vivo* data are very promising. However, further studies are now necessary to clarify other effects, such as elucidating the interactions of the aromatic structures with proteins and DNA.

6.2 Self-Assembly and Inverse Thermogelation

As described in the section **2.3.2 Aqueous Solubility and Self-Assembly**, the self-assembly of PPheOx copolymers has mainly been investigated so far. In the present study, the effect of additional methylene units in the polymer sidechain (PPheOx→PBzOx→PPhenEtOx) and polymer backbone (POx vs POzi) in ABA type amphiphiles with aromatic moieties was examined. Furthermore, POx/POzi based polymers with two aromatic rings per repeating units (PBhOx, PBhOzi) were synthesized and analyzed for the first time.

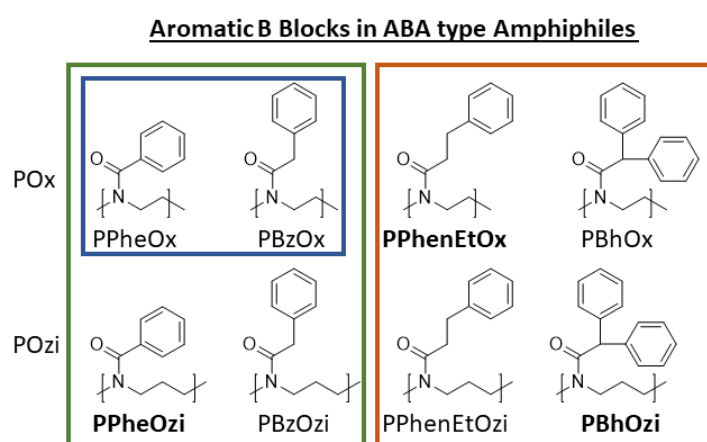


Figure D1. Summary of aromatic B blocks in POx/POzi based ABA type amphiphiles (A: PMeOx) used to study self-assembly and inverse thermogelation. In Chapter I (blue square), the self-assembly of the polymers containing PPheOx and PBzOx as the hydrophobic core were characterized. In Chapter II, additionally, the corresponding POzi derivatives were investigated (green square). In Chapter III, the polymers bearing moieties highlighted in the orange square were studied in detail. The polymers, which showed pronounced inverse thermogelation (PPheOzi, PPhenEtOx and PBhOzi containing polymers) were written in bold letters.

It is known that aromatic units can induce supramolecular self-assembly e.g. via π - π ^{272,273} and CH- π ²⁷⁴ interactions. For certain physical interactions, not only the presence of the right binding partners is crucial, as steric effects can also play a decisive role.²⁷⁵ In this context, the aqueous self-assembly (See **2.3.2 Aqueous Solubility and Self-Assembly**) and associated macroscopic changes such as gelation²⁷⁶ (See **2.1.2 Thermoresponsive Hydrogels**) of all different aromatic amphiphiles were studied.

Surprisingly, comparing the polymers with phenyl and benzyl moieties the polymer A-PPheOzi-A showed unique inverse gelation at low temperature.^[M5] The polymers A-PPheOx-A, A-PBzOx-A and A-PBzOzi-A self-assemble into small spherical micelles (approximately 10 nm).^[M2,M5] Only the polymer A-PPheOzi-A exhibited long worm-like micelles, which create a physical hydrogel. Upon heating (critical temperature approximately 32 °C) the worms rearrange into spherical micelles and the gel turned into a low viscous liquid. The gelation time upon cooling is dependent on the polymer concentration and temperature. The higher the polymer concentration and lower the incubation temperature, the faster the system gels. In addition, the gel strength (G' (5 wt.%)= 0.1→ G' (40 wt.%)=

100 kPa) can be modified very well by altering the concentration. It is very astonishing that only this polymer showed this phenomenon, since the only difference to the other polymers is only a methylene unit in the polymer backbone and/or the polymer side chain.

In addition, the respective polymer does not include a block that has thermoresponsive properties (**See 2.3.2 Aqueous Solubility and Self-Assembly**). Thus, the question arises as to what causes the change in self-organization and the resulting gelation.

The second manuscript from Chapter II was devoted to that question, the focus being on the comparison of the gel state with the sol state. Using various state-of-the-art analytical tools, an unexpected interaction between the hydrophilic PMeOx blocks and hydrophobic aromatic polymer segments was asserted, contrasting to the classical π - π stacking of aromatic units. This interaction leads to a condensation of the hydrophilic corona, which changes the volume fraction of the individual blocks and thereby leading to a morphology switch from spherical to worm-like micelles (**See 2.3.2 Aqueous Solubility and Self-Assembly**). As the hydrophilic part is involved in the interaction, the structure of the respective blocks should have a significant effect on the self-assembly and the gel properties. Therefore, we changed the hydrophilic part slightly by using PMeOzi and PEtOx, moieties with additional methylene units in the polymer backbone or sidechain, respectively and studied the impact on the gelation, self-assembly and thermodynamics. We could observe and explain clear differences. Nevertheless, new questions have arisen, which need to be clarified in further studies.

It should be mentioned that other systems are known in the literature which show similar order-order transitions. Polymerization-induced self-assembly approaches were often used.^{277,278} Thereby, by altering the ratio of the block length, the volume fraction of individual blocks can be tuned and different morphologies can be obtained. In our case, the polymer structure does not change and in comparison to the other tested amphiphiles block length are similar. However, there is a reversible interaction between polymer blocks, which should undergo a clear phase separation into hydrophilic and hydrophobic regions in aqueous solution. Therefore, this system can be distinguished from classical UCST systems⁷⁵ (**See 2.1.2 Thermoresponsive Hydrogels**) and systems with hydrophobic²⁷⁹ and/or π - π interactions²⁷², and thus a new molecular gelation mechanism was provided. Nevertheless, to get a holistic picture of the gelation mechanism and the detailed mechanistic differences compared to all other tested amphiphiles, a large number of further experiments is necessary. More advanced NMR experiments in combination with all-atom molecular modeling for all amphiphiles presented are the next step. To further elucidate the influence of specific polymer blocks on the self-assembly, further SAXS and SANS experiments at different concentrations and temperatures of all amphiphiles are required. In addition, individual polymer blocks could be selectively masked by deuteration, in order to get additional insight. In summary, we know that PPheOzi units are crucial for the gelation and the hydrophilic blocks have a significant influence on gel properties. Further, an ideal ratio of PMeOx/PPheOzi of 70:15 for a polymer with a degree of approximately 85 exists. The influence of the degree of polymerization, the polymer

composition with respect to block arrangement and polymer architecture is still unknown. In addition, novel monomers with specific substitutions along the aromatic phenyl ring could be tested. This effect was inspiring elucidated by Robertson et al. for the design of nanosheets by designing a library of aromatic peptoids.^{280,281} Max Lindner (Bachelor Student, Supervisor: Prof. Dr. Ann-Christin Pöppler and Prof. Dr. Robert Luxenhofer) studied the influence of methylation on the phenyl ring with respect to gel formation. Initial results suggested that this also has a significant influence. However, further studies with novel structures would still need to be performed in this regard.

The benzyl (PBzOx, PBzOzi) containing amphiphiles with intermediate distance of the aromatic ring to the polymer backbone showed no significant change of η as a function of temperature. The introduction of an additional CH₂ unit in the polymer side chain increased the sidechain flexibility and amphiphiles with PPhenEtOx and PPhenEtOzi units were obtained. Interestingly, gel formation was now again observed, however, only for the PPhenEtOx-based polymer at lowered temperature from a concentration of 20 wt.%.^[M8] In contrast to the PPheOzi-based gels, significantly different gel properties such as gelation kinetics, gel strength and differences on the influence of the concentration, temperature, frequency (frequency sweep) and deformation (amplitude sweep) were observed. The amphiphile A-PPhenEtOx-A self-assembled into stable small (approximately 8 nm) spherical micelles as usually observed for amphiphiles with such strong hydrophobic core. In dilution, no change of morphology or size of the aggregates was observed. However, an increased correlation of individual micelles upon gelation was verified via SAXS analysis. In literature, similar gelation mechanisms are discussed predominantly for thermogelling polymers. Phenomena such as packing of individual micelles, bridged packings, micellar corona collapse and gelation induced via hydrophobic channels were described.^{40,264,282} In contrast, here, we observed again inverse thermogelling of a polymer with no UCST-type block. The SAXS data in combination with NMR experiments at different temperatures suggested that it was probably the packing of single micelles with possible presence of hydrophobic channels. Collapse of the hydrophilic part is rather unlikely, which was supported by the NMR experiments. In contrast to the PPhenEtOx part, the mobility of the hydrophilic corona was only slightly affected by the temperature. More advanced studies dealing with molecular analysis have not yet been performed, making it difficult to clearly classify the gelation mechanism. Nevertheless, it is very surprising that this polymer exhibited such gelling behavior, since no thermoresponsive block is present and presumably gel formation is also influenced by more than just hydrophobic effects. Approaches similar to those for the PPheOzi-based system could provide more precise insights. In addition, a combination of fluorescence resonance energy transfer imaging and computer simulation method could provide information of the interaction/crosslinking points as recently demonstrated by Ding and co-workers.²⁸² Since the gelation mechanism on the molecular level is still unclear, it is also impossible to explain exactly why the PPhenEtOzi derivative does not induce gelation. The additional CH₂-group in the polymer backbone could change the packing of the hydrophobic core or, as in the case of the PPheOzi

system, prevent an interaction in the hydrophobic part with the hydrophilic part. However, no data is available to date.

In the previous studies, we changed the distance of the aromatic system from the polymer backbone and investigated its effects. The aim of the last study with aromatic systems was to compare POx/POzi systems with sterically very demanding hydrophobic cores. Therefore, amphiphiles with benzhydryl moieties (PBhOx, PBhOzi) were investigated.^[M10] These particular polymers exhibit two phenyl rings in close proximity to each other in every repeating unit of the hydrophobic core. Interestingly, the sterically demanding benzhydryl units did not have any negative effect on polymerization. Surprisingly, specific inverse gelation of the POzi derivative was observed with defined differences from the first two established inverse gelling platforms. A direct comparison of all three hydrogels with the focus on self-assembly and gel properties is given in the second manuscript of the chapter III. The gel properties are more similar to the PPhenEtOx system, as 20 wt.% is also required for rapid gelation. The aggregation behavior of PBhOzi is, however, temperature-dependent even in dilution, as was confirmed by DLS experiments. In first TEM images in dilution, interesting arrangements of multiple merging micelles could be observed, possibly guaranteeing the assembly of the physical 3D network at high concentration. Again, as with the first two systems, there are still very many unanswered questions, in particular because there is no data available showing the differences at the aggregation and molecular levels at gel concentrations comparing sol/gel and POx/POzi.

In summary, three novel gel systems were established and initial structure-property relationships were presented on the self-assembly level. It is very surprising that these polymers present such behavior, especially the uniqueness in the POx/POzi comparison. Further on, the specific gel properties were used for biofabrication, which will be summarized in the next subsection.

6.3 Inverse Thermogelling Hydrogels for Biofabrication

The characterized inverse gelling systems based on the polymers A-PPheOzi-A, A-PPhenEtOx-A and A-PBhOzi-A were discussed as bioinks and biomaterial inks for biofabrication.^[M5,M8,M10] As discussed in the Section **2.2 Bioprinting: A Technology of Biofabrication for Tissue Engineering and Regenerative Medicine** there is a strong demand for novel materials with stringent material and biological properties in the field of biofabrication. In general, the rheological properties (See **2.2.3.1 Rheology of Bioinks**) of all three established hydrogels are ideal for gel-phase EBB (See **2.2.3 Bioink Development**). An advantage of the PPheOzi-based system is the adjustability of the gel strength over a wide range. Thus, soft but also very solid structures with high yield points can be realized. Therefore, the printability of the pristine PPheOzi-hydrogel is excellent (See **2.2.3.2 Printability of Bioinks**). However, upon heating and dilution the construct collapses as there are no permanent crosslinks in the structure. This is also true for the other two hydrogels. However, this dissolving property upon heating can be used in support structure printing and sacrificial printing approaches as described in the section **2.2.3.3 Materials for Bioink Development**. We used the PPheOzi-hydrogel to enhance the printability of Alg the most commonly material in the community of bioprinting (See **2.2.3.3 Materials for Bioink Development**), which generally lacks good printability. Interestingly, we observed not only very good printability of the blend system, but also increased strength and stability compared to the pristine Alg constructs when incubating in aqueous solutions for several days after crosslinking via CaCl_2 . In theory, the PPheOzi polymer should be washed out of the construct during incubation and Alg should remain as residual material. The increased stability could be caused by an interaction of the PPheOzi polymer and the Alg. In addition, the effect of increasing the local concentration of Alg by using PPheOzi in the system could improve CaCl_2 crosslinking. However, clear phase separation could not be observed visually. The investigation of the stability increase caused by the addition of POx/POzi support materials could be a good starting point for further studies. It should be mentioned that the material has not yet been used as a pure support material to realize overhangs or perfusable channels. The properties, especially the adjustable yield point (See **2.2.3.1 Rheology of Bioinks**) in the gel state and the rapid dissolution of the gel when heated, makes the material an excellent candidate to realize complex architectures. Further, multi-material approaches, coaxial- and in-gel printing should be in the focus of the future.

In bioprinting the cells are embedded in the bioink during the whole fabrication process. Therefore, materials with rapid sol/gel transitions in gel-phase EBB are favorable (**See 2.2.3 Bioink Development**). The gelation of PPheOzi is a time dependent process, in which the sample is stored at low temperatures, which could cause problems during sample preparation especially when cells are involved. However, this has not yet been tested. In contrast, the PPhenEtOx-gel exhibited a fast sol/gel transition, which easily opens the possibility of bioprinting as the material fulfills all other relevant requirements for printing (**See 2.2.3.1 Rheology of Bioinks**). Again, Alg was added to rapidly stabilize the final construct via CaCl₂ addition. Overall, very promising cytocompatibility data were obtained for the blend system after printing, stabilization and cultivation for 24 h. For the future more advanced application relevant studies should be designed with respect to the architecture of the construct and the biology relevant readouts.

For the PBhOzi-based hydrogel the rheological properties suggested good printability (**See 2.2.3.1 Rheology of Bioinks**). However, no printing experiments were performed so far.

In short, the established hydrogels are ideal candidates for further investigations in the field of biofabrication as demonstrated by first preliminary printing experiments.

In addition, another possible application will be discussed here, which has not yet been presented in this study. The stabilization of protein-based drugs, which are becoming more and more important, by embedding them in a hydrogel matrix.²⁴⁰ Many of these drugs are very sensitive to external influences such as temperature, pH and agitation, among others, and suffer from reduced activity. Accordingly, both storage and application of these agents is difficult. Proteins are usually stored aliquoted at -20 °C. As a solution in the refrigerator, they can normally only be stored for a few days to weeks. By embedding these compounds in e.g. the PPheOzi-based hydrogel, improved storage stability could perhaps be achieved. In addition, the polymer class is known for its antifouling properties, so this could also have a positive influence. The PPheOzi-based system also offers many interesting possibilities in terms of application. On the one hand, the gel can be stored in a syringe and, if desired, the shear-thinning material can be extruded by means of a syringe pump. On the other hand, the gel can be liquefied by heating it to physiological 37 °C. As already shown, this type of amphiphiles is excellent for solubilization of active ingredients in the form of drug-loaded polymer micelles. Therefore, the transformation of the worm-like micelles could lead to drug-loaded spherical micelles which can be applied directly. Transport of the hydrogel/drug mixture could be provided in the gel state or in the lyophilized state. So far, there is no data on this application with this particular systems.

6.4 Thermogelling POx/POzi Hydrogels for Biofabrication

The Chapter IV of the main part mainly deals with the thermogelling diblock copolymer PMeOx-b-PnPrOzi established by Lorson et al. in 2017^[264] and its usage in biofabrication. The focus was on improving printability and increasing stability of the constructs through additional crosslinking. The principles already presented in sections **2.1 Hydrogels as Biomaterials** and **2.2 Bioprinting: A Technology of Biofabrication for Tissue Engineering and Regenerative Medicine** were taken into account and implemented. In particular, dual-gelling systems were realized using the synthetic toolbox of POx/POzi. The strategy of introducing complementary functional groups (**See 2.1.3 In Situ Chemical Crosslinking**) for additional stabilization and various multi-material approaches (**See 2.1.4 Double Network-, Multi-Component- and Composite Hydrogels**) were established. Further, the thermogelling properties were used to support other barely printable materials in blend systems (**See 2.2.3 Bioink Development**).

The addition of nanoclay improved the printability especially the stackability.^[M6] This can be explained by the enhanced yield point of the blend system. However, this blend still dissolved upon solvent addition. Therefore, further stabilization was necessary to conduct long-term cell studies. One approach was to add Alg to improve the stability after CaCl₂ addition.^[M13] These materials are perfect suitable as a proof-of-principle combination, but are also accompanied by a few limitations. None of the materials carried any cell biological motifs such as cell adhesion peptides. This could be changed by decorating the Alg with RGD-sequences in the future. However, CaCl₂ has to be added and therefore the stabilization is dependent on the diffusion of CaCl₂ through the construct. This can lead to undesirable and uncontrollable crosslinking gradients. For further studies, the Alg component can be changed by more biological relevant materials such as recombinant spider silk or collagen. It should be noted that the PMeOx-b-PnPrOzi/Alg system has already been tested in initial bioreactor trials, in which the construct is continuously perfused for several weeks. For example, to improve perfusion, the inverse gelling materials could be used to introduce additional defined channels.

As demonstrated for the PEG-DA/PMeOx-b-PnPrOzi blend system used in 2PP^[M14], the thermogelling property can be used in different applications. Among other things, the hydrogel offers the possibility to act as support bath for unprintable formulations. In this regard, a promising master thesis was conducted within the research group of Prof. Dr. Robert Luxenhofer by Alexander Altmann.

As already described in the section **2.3.1 Synthesis**, there are a variety of post polymerization modification strategies available for the polymer classes of POx/POzi. This was used to combine additional permanent chemical crosslinking with the thermogelling mechanism. The polymer was modified with furan and maleimide moieties for Diels-Alder chemistry.^[M7] It was shown that the system remained printable and was additionally stabilized at 37 °C without the need of further supplements or crosslinking agents. Here, too, there are now a large number of starting points for further studies. First,

the crosslinking kinetics of the Diels-Alder chemistry seems to be critical when printing over a longer time period is required. Therefore, a printing system with a mixing chamber directly in front of the nozzle should be tested. So far, the dual-gelling system exhibited no biofunctionality as the introduced RGD motifs showed no function in the very dense chemically crosslinked network. Therefore, temporal crosslinkers could now be incorporated, for example matrix metalloproteinase sequences, which can be post temporal cleaved. In this context, different approaches to modify the mechanical properties of the constructs for tissue-specific applications could also be addressed. In addition to the variation in mechanical properties, diffusivity also plays a crucial role in cell-induced maturation of the construct. However, this has not yet been investigated, which would be a next step.

Finally, a combination with nanoclay could improve printability also in the case of the crosslinkable furan/maleimide system. Further, overhangs and channels could be introduced using the inverse thermogelling PPheOzi-gel.

As already presented in sections **2.2.3.1 Rheology of Bioinks** and **2.2.3.2 Printability of Bioinks**, it is very difficult to establish a clear relationship between rheology and printability of inks, since bioprinting is an interplay of different parameters. Through the work described here, different inks have been established. Now, defined benchmark experiments to correlate the rheological properties with the printability should be performed. Thus, the influence of different parameters such as yield point and shear-thinning on the printability could possibly be classified in a rating system.

7 References

In this section, the references, which were used in the sections **1 Introduction**, **2 State of Knowledge** and **6 Discussion** are listed.

1. WHO COVID-19 Dashboard. Geneva: World Health Organization, **2020**. Available online: <https://covid19.who.int/> (last cited: 22.04.2021).
2. Ciaramella G.; Sunny, H., Betacoronavirus mRNA vaccine. **2020** (U.S. Patent No. 10,702,600B1)
3. Staudinger, H., Über Polymerisation. *Berichte der Deutschen Chemischen Gesellschaft (A and B Series)* **1920**, 53 (6), 1073-1085.
4. Zhang, P.; Sun, F.; Liu, S.; Jiang, S., Anti-PEG antibodies in the clinic: Current issues and beyond PEGylation. *Journal of Controlled Release* **2016**, 244, 184-193.
5. Moreadith, R. W.; Viegas, T. X.; Bentley, M. D.; Harris, J. M.; Fang, Z.; Yoon, K.; Dizman, B.; Weimer, R.; Rae, B. P.; Li, X.; Rader, C.; Standaert, D. G.; Olanow, W., Clinical development of a poly(2-oxazoline) (POZ) polymer therapeutic for the treatment of Parkinson's disease – Proof of concept of POZ as a versatile polymer platform for drug development in multiple therapeutic indications. *European Polymer Journal* **2017**, 88, 524-552.
6. Olanow, C. W.; Standaert, D. G.; Kieburtz, K.; Viegas, T. X.; Moreadith, R., Once-weekly subcutaneous delivery of polymer-linked rotigotine (SER-214) provides continuous plasma levels in Parkinson's disease patients. *Movement Disorders* **2020**, 35 (6), 1055-1061.
7. Almdal, K.; Dyre, J.; Hvidt, S.; Kramer, O., Towards a phenomenological definition of the term 'gel'. *Polymer Gels and Networks* **1993**, 1 (1), 5-17.
8. Graham, T., XXXV.—On the properties of silicic acid and other analogous colloidal substances. *Journal of the Chemical Society* **1864**, 17 (0), 318-327.
9. Lloyd, D. J., The problem of gel structure. *Colloid Chemistry* **1926**, 1, 767-782.
10. Flory, P. J., Introductory lecture. *Faraday Discussions of the Chemical Society* **1974**, 57 (0), 7-18.
11. Kopecek, J., Hydrogels: From soft contact lenses and implants to self-assembled nanomaterials. *Journal of Polymer Science Part A: Polymer Chemistry* **2009**, 47 (22), 5929-5946.
12. Buwalda, S. J.; Boere, K. W. M.; Dijkstra, P. J.; Feijen, J.; Vermonden, T.; Hennink, W. E., Hydrogels in a historical perspective: From simple networks to smart materials. *Journal of Controlled Release* **2014**, 190, 254-273.
13. Hicks, G. P.; Updike, S. J., The preparation and characterization of lyophilized polyacrylamide enzyme gels for chemical analysis. *Analytical Chemistry* **1966**, 38 (6), 726-730.
14. Freeman, A.; Aharonowitz, Y., Immobilization of microbial cells in crosslinked, prepolymerized, linear polyacrylamide gels: Antibiotic production by immobilized *Streptomyces clavuligerus* cells. *Biotechnology and Bioengineering* **1981**, 23 (12), 2747-2759.
15. Wichterle, O.; LÍM, D., Hydrophilic gels for biological use. *Nature* **1960**, 185 (4706), 117-118.
16. Peppas, N. A.; Moynihan, H. J.; Lucht, L. M., The structure of highly crosslinked poly(2-hydroxyethyl methacrylate) hydrogels. *Journal of Biomedical Materials Research* **1985**, 19 (4), 397-411.
17. Roorda, W. E.; de Vries, M. A.; de Leede, L. G. J.; de Boer, A. G.; Breimer, D. D.; Junginger, H. E., Zero-order release of oxprenolol-HCl, a new approach. *Journal of Controlled Release* **1988**, 7 (1), 45-52.
18. Song, S. Z.; Cardinal, J. R.; Kim, S. H.; Kim, S. W., Progesterin permeation through polymer membranes V: progesterone release from monolithic hydrogel devices. *Journal of Pharmaceutical Sciences* **1981**, 70 (2), 216-219.
19. Yean, L.; Bunel, C.; Vairon, J.-P., Reversible immobilization of drugs on a hydrogel matrix, 2. Diffusion of free chloramphenicol from poly(2-hydroxyethyl methacrylate) hydrogels. *Die Makromolekulare Chemie* **1990**, 191 (5), 1119-1129.

20. Huglin, M. B.; Sloan, D. J., Release of ergotamine from poly (2-hydroxyethyl methacrylate). *British Polymer Journal* **1983**, *15* (4), 165-171.
21. Trigo, R. M.; Blanco, M. D.; Teijón, J. M.; Sastre, R., Anticancer drug, ara-C, release from pHEMA hydrogels. *Biomaterials* **1994**, *15* (14), 1181-1186.
22. Korsmeyer, R. W.; Peppas, N. A., Effect of the morphology of hydrophilic polymeric matrices on the diffusion and release of water soluble drugs. *Journal of Membrane Science* **1981**, *9* (3), 211-227.
23. McNeill, M. E.; Graham, N. B., Vaginal pessaries from crystalline/rubbery hydrogels for the delivery of prostaglandin E2. *Journal of Controlled Release* **1984**, *1* (2), 99-117.
24. Edelman, D. A.; McIntyre, S. L.; Harper, J., A comparative trial of the Today contraceptive sponge and diaphragm. *American Journal of Obstetrics and Gynecology* **1984**, *150* (7), 869-876.
25. Mandy, S. H., A new primary wound dressing made of polyethylene oxide gel. *The Journal of Dermatologic Surgery and Oncology* **1983**, *9* (2), 153-155.
26. Graham, N. B.; McNeill, M. E., Hydrogels for controlled drug delivery. *Biomaterials* **1984**, *5* (1), 27-36.
27. Huber, H. E.; Dale, L. B.; Christenson, G. L., Utilization of hydrophilic gums for the control of drug release from tablet formulations I. disintegration and dissolution behavior. *Journal of Pharmaceutical Sciences* **1966**, *55* (9), 974-976.
28. Ford, J. L.; Rubinstein, M. H.; McCaul, F.; Hogan, J. E.; Edgar, P. J., Importance of drug type, tablet shape and added diluents on drug release kinetics from hydroxypropylmethylcellulose matrix tablets. *International Journal of Pharmaceutics* **1987**, *40* (3), 223-234.
29. Ford, J. L.; Rubinstein, M. H.; Hogan, J. E., Propranolol hydrochloride and aminophylline release from matrix tablets containing hydroxypropylmethylcellulose. *International Journal of Pharmaceutics* **1985**, *24* (2), 339-350.
30. Loulergue, P.; Amela-Cortes, M.; Cordier, S.; Molard, Y.; Lemiègre, L.; Audic, J.-L., Polyurethanes prepared from cyclocarbonated broccoli seed oil (PUcc): New biobased organic matrices for incorporation of phosphorescent metal nanocluster. *Journal of Applied Polymer Science* **2017**, *134* (45), 45339.
31. Kim, Y.-J.; Matsunaga, Y. T., Thermo-responsive polymers and their application as smart biomaterials. *Journal of Materials Chemistry B* **2017**, *5* (23), 4307-4321.
32. Zhang, H.; Li, J.; Cui, H.; Li, H.; Yang, F., Forward osmosis using electric-responsive polymer hydrogels as draw agents: Influence of freezing–thawing cycles, voltage, feed solutions on process performance. *Chemical Engineering Journal* **2015**, *259*, 814-819.
33. Kohri, M.; Yanagimoto, K.; Kohaku, K.; Shiimoto, S.; Kobayashi, M.; Imai, A.; Shiba, F.; Taniguchi, T.; Kishikawa, K., Magnetically responsive polymer network constructed by poly(acrylic acid) and holmium. *Macromolecules* **2018**, *51* (17), 6740-6745.
34. Wei, X.; Chang, G.; Li, J.; Wang, F.; Cui, L.; Fu, T.; Kong, L., Preparation of pH- and salinity-responsive cellulose copolymer in ionic liquid. *Journal of Polymer Research* **2014**, *21* (8), 535.
35. Zhang, Q.; Weber, C.; Schubert, U. S.; Hoogenboom, R., Thermoresponsive polymers with lower critical solution temperature: from fundamental aspects and measuring techniques to recommended turbidimetry conditions. *Materials Horizons* **2017**, *4* (2), 109-116.
36. Niskanen, J.; Tenhu, H., How to manipulate the upper critical solution temperature (UCST)? *Polymer Chemistry* **2017**, *8* (1), 220-232.
37. Heskins, M.; Guillet, J. E., Solution properties of poly(N-isopropylacrylamide). *Journal of Macromolecular Science: Part A - Chemistry* **1968**, *2* (8), 1441-1455.
38. Fujishige, S.; Kubota, K.; Ando, I., Phase transition of aqueous solutions of poly(N-isopropylacrylamide) and poly(N-isopropylmethacrylamide). *The Journal of Physical Chemistry* **1989**, *93* (8), 3311-3313.
39. Tam, K. C.; Wu, X. Y.; Pelton, R. H., Viscometry—a useful tool for studying conformational changes of poly(N-isopropylacrylamide) in solutions. *Polymers* **1992**, *33* (2), 436-438.
40. Zhang, K.; Xue, K.; Loh, X. J., Thermo-responsive hydrogels: From recent progress to biomedical applications. *Gels* **2021**, *7* (3), 77.
41. Desai, S. D.; Blanchard, J., In vitro evaluation of pluronic F127-based controlled-release ocular delivery systems for pilocarpine. *Journal of Pharmaceutical Sciences* **1998**, *87* (2), 226-230.
42. Bae, W. K.; Park, M. S.; Lee, J. H.; Hwang, J. E.; Shim, H. J.; Cho, S. H.; Kim, D.-E.; Ko, H. M.; Cho, C.-S.; Park, I.-K.; Chung, I.-J., Docetaxel-loaded thermoresponsive conjugated linoleic

acid-incorporated poloxamer hydrogel for the suppression of peritoneal metastasis of gastric cancer. *Biomaterials* **2013**, *34* (4), 1433-1441.

43. Katakam, M.; Ravis, W. R.; Banga, A. K., Controlled release of human growth hormone in rats following parenteral administration of poloxamer gels. *Journal of Controlled Release* **1997**, *49* (1), 21-26.

44. Jeong, B.; Lee, D. S.; Shon, J.-I.; Bae, Y. H.; Kim, S. W., Thermoreversible gelation of poly(ethylene oxide) biodegradable polyester block copolymers. *Journal of Polymer Science Part A: Polymer Chemistry* **1999**, *37* (6), 751-760.

45. Choi, S. W.; Choi, S. Y.; Jeong, B.; Kim, S. W.; Lee, D. S., Thermoreversible gelation of poly(ethylene oxide) biodegradable polyester block copolymers. II. *Journal of Polymer Science Part A: Polymer Chemistry* **1999**, *37* (13), 2207-2218.

46. Hiemstra, C.; Zhong, Z.; Dijkstra, P. J.; Feijen, J., Stereocomplex mediated gelation of PEG-(PLA)₂ and PEG-(PLA)₈ block copolymers. *Macromolecular Symposia* **2005**, *224* (1), 119-132.

47. Li, S.; Molina, I.; Martinez, M. B.; Vert, M., Hydrolytic and enzymatic degradations of physically crosslinked hydrogels prepared from PLA/PEO/PLA triblock copolymers. *Journal of Materials Science: Materials in Medicine* **2002**, *13* (1), 81-86.

48. Jeong, B.; Bae, Y. H.; Kim, S. W., Thermoreversible gelation of PEG-PLGA-PEG triblock copolymer aqueous solutions. *Macromolecules* **1999**, *32* (21), 7064-7069.

49. Jeong, B.; Han Bae, Y.; Wan Kim, S., Biodegradable thermosensitive micelles of PEG-PLGA-PEG triblock copolymers. *Colloids and Surfaces B: Biointerfaces* **1999**, *16* (1), 185-193.

50. Jeong, B.; Bae, Y. H.; Kim, S. W., In situ gelation of PEG-PLGA-PEG triblock copolymer aqueous solutions and degradation thereof. *Journal of Biomedical Materials Research* **2000**, *50* (2), 171-7.

51. Jeong, B.; Bae, Y. H.; Kim, S. W., Drug release from biodegradable injectable thermosensitive hydrogel of PEG-PLGA-PEG triblock copolymers. *Journal of Controlled Release* **2000**, *63* (1), 155-163.

52. Lee, P.-Y.; Li, Z.; Huang, L., Thermosensitive hydrogel as a Tgf- β 1 gene delivery vehicle enhances diabetic wound healing. *Pharmaceutical Research* **2003**, *20* (12), 1995-2000.

53. Lee, D. S.; Shim, M. S.; Kim, S. W.; Lee, H.; Park, I.; Chang, T., Novel thermoreversible gelation of biodegradable PLGA-block-PEO-block-PLGA triblock copolymers in aqueous solution. *Macromolecular Rapid Communications* **2001**, *22* (8), 587-592.

54. Shim, M. S.; Lee, H. T.; Shim, W. S.; Park, I.; Lee, H.; Chang, T.; Kim, S. W.; Lee, D. S., Poly(D,L-lactic acid-co-glycolic acid)-b-poly(ethylene glycol)-b-poly(D,L-lactic acid-co-glycolic acid) triblock copolymer and thermoreversible phase transition in water. *Journal of Biomedical Materials Research* **2002**, *61* (2), 188-96.

55. Zentner, G. M.; Rathi, R.; Shih, C.; McRea, J. C.; Seo, M.-H.; Oh, H.; Rhee, B. G.; Mestecky, J.; Moldoveanu, Z.; Morgan, M.; Weitman, S., Biodegradable block copolymers for delivery of proteins and water-insoluble drugs. *Journal of Controlled Release* **2001**, *72* (1), 203-215.

56. Samlowski, W. E.; McGregor, J. R.; Jurek, M.; Baudys, M.; Zentner, G. M.; Fowers, K. D., ReGel[®] polymer-based delivery of interleukin-2 as a cancer treatment. *Journal of Immunotherapy* **2006**, *29* (5).

57. Hwang, M. J.; Suh, J. M.; Bae, Y. H.; Kim, S. W.; Jeong, B., Caprolactonic poloxamer analog: PEG-PCL-PEG. *Biomacromolecules* **2005**, *6* (2), 885-890.

58. Bae, S. J.; Suh, J. M.; Sohn, Y. S.; Bae, Y. H.; Kim, S. W.; Jeong, B., Thermogelling poly(caprolactone-b-ethylene glycol-b-caprolactone) aqueous solutions. *Macromolecules* **2005**, *38* (12), 5260-5265.

59. Gong, C.; Shi, S.; Wu, L.; Gou, M.; Yin, Q.; Guo, Q.; Dong, P.; Zhang, F.; Luo, F.; Zhao, X.; Wei, Y.; Qian, Z., Biodegradable in situ gel-forming controlled drug delivery system based on thermosensitive PCL-PEG-PCL hydrogel. Part 2: Sol-gel-sol transition and drug delivery behavior. *Acta Biomaterialia* **2009**, *5* (9), 3358-3370.

60. Petit, A.; Müller, B.; Meijboom, R.; Bruin, P.; van de Manakker, F.; Versluijs-Helder, M.; de Leede, L. G. J.; Doornbos, A.; Landin, M.; Hennink, W. E.; Vermonden, T., Effect of polymer composition on rheological and degradation properties of temperature-responsive gelling systems composed of acyl-capped PCLA-PEG-PCLA. *Biomacromolecules* **2013**, *14* (9), 3172-3182.

61. Petit, A.; Müller, B.; Bruin, P.; Meyboom, R.; Piest, M.; Kroon-Batenburg, L. M. J.; de Leede, L. G. J.; Hennink, W. E.; Vermonden, T., Modulating rheological and degradation properties of

temperature-responsive gelling systems composed of blends of PCLA–PEG–PCLA triblock copolymers and their fully hexanoyl-capped derivatives. *Acta Biomaterialia* **2012**, *8* (12), 4260-4267.

62. Sandker, M. J.; Petit, A.; Redout, E. M.; Siebelt, M.; Müller, B.; Bruin, P.; Meyboom, R.; Vermonden, T.; Hennink, W. E.; Weinans, H., In situ forming acyl-capped PCLA–PEG–PCLA triblock copolymer based hydrogels. *Biomaterials* **2013**, *34* (32), 8002-8011.

63. Lee, J.; Bae, Y. H.; Sohn, Y. S.; Jeong, B., Thermogelling aqueous solutions of alternating multiblock copolymers of poly(L-lactic acid) and poly(ethylene glycol). *Biomacromolecules* **2006**, *7* (6), 1729-1734.

64. Joo, M. K.; Sohn, Y. S.; Jeong, B., Stereoisomeric effect on reverse thermal gelation of poly(ethylene glycol)/poly(lactide) multiblock copolymer. *Macromolecules* **2007**, *40* (14), 5111-5115.

65. Li, F.; Li, S.; Vert, M., Synthesis and rheological properties of polylactide/poly(ethylene glycol) multiblock copolymers. *Macromolecular Bioscience* **2005**, *5* (11), 1125-1131.

66. Park, S. Y.; Han, B. R.; Na, K. M.; Han, D. K.; Kim, S. C., Micellization and gelation of aqueous solutions of star-shaped PLLA–PEO block copolymers. *Macromolecules* **2003**, *36* (11), 4115-4124.

67. Velthoen, I. W.; van Beek, J.; Dijkstra, P. J.; Feijen, J., Thermo-responsive hydrogels based on highly branched poly(ethylene glycol)–poly(L-lactide) copolymers. *Reactive and Functional Polymers* **2011**, *71* (3), 245-253.

68. Buwalda, S. J.; Dijkstra, P. J.; Calucci, L.; Forte, C.; Feijen, J., Influence of amide versus ester linkages on the properties of eight-armed PEG-PLA star block copolymer hydrogels. *Biomacromolecules* **2010**, *11* (1), 224-232.

69. Calucci, L.; Forte, C.; Buwalda, S. J.; Dijkstra, P. J.; Feijen, J., Self-aggregation of gel forming PEG-PLA star block copolymers in water. *Langmuir* **2010**, *26* (15), 12890-12896.

70. Nasatto, P. L.; Pignon, F.; Silveira, J. L. M.; Duarte, M. E. R.; Nosedá, M. D.; Rinaudo, M., Methylcellulose, a cellulose derivative with original physical properties and extended applications. *Polymers* **2015**, *7* (5), 777-803.

71. Bello, J.; Bello, H. R.; Vinograd, J. R., The mechanism of gelation of gelatin. The influence of pH, concentration, time and dilute electrolyte on the gelation of gelatin and modified gelatins. *Biochimica et Biophysica Acta* **1962**, *57*, 214-21.

72. Seuring, J.; Agarwal, S., Polymers with upper critical solution temperature in aqueous solution. *Macromolecular Rapid Communications* **2012**, *33* (22), 1898-1920.

73. Fu, W.; Zhao, B., Thermoreversible physically crosslinked hydrogels from UCST-type thermosensitive ABA linear triblock copolymers. *Polymer Chemistry* **2016**, *7* (45), 6980-6991.

74. Haas, H. C.; Schuler, N. W., Thermally reversible homopolymer gel systems. *Journal of Polymer Science Part B: Polymer Letters* **1964**, *2* (12), 1095-1096.

75. Xu, Z.; Liu, W., Poly(N-acryloyl glycinamide): A fascinating polymer that exhibits a range of properties from UCST to high-strength hydrogels. *Chemical Communications* **2018**, *54* (75), 10540-10553.

76. Boustta, M.; Colombo, P.-E.; Lenglet, S.; Poujol, S.; Vert, M., Versatile UCST-based thermoresponsive hydrogels for loco-regional sustained drug delivery. *Journal of Controlled Release* **2014**, *174*, 1-6.

77. Majstorović, N.; Agarwal, S., Thermosensitive fluorescence of an UCST-type hybrid functional hydrogel. *ACS Applied Polymer Materials* **2021**.

78. Hu, W.; Wang, Z.; Xiao, Y.; Zhang, S.; Wang, J., Advances in crosslinking strategies of biomedical hydrogels. *Biomaterials Science* **2019**, *7* (3), 843-855.

79. Occhetta, P.; Visone, R.; Russo, L.; Cipolla, L.; Moretti, M.; Rasponi, M., VA-086 methacrylate gelatin photopolymerizable hydrogels: A parametric study for highly biocompatible 3D cell embedding. *Journal of Biomedical Materials Research Part A* **2015**, *103* (6), 2109-17.

80. Bryant, S. J.; Nuttelman, C. R.; Anseth, K. S., Cytocompatibility of UV and visible light photoinitiating systems on cultured NIH/3T3 fibroblasts in vitro. *Journal of Biomaterials Science, Polymer Edition* **2000**, *11* (5), 439-57.

81. Williams, C. G.; Malik, A. N.; Kim, T. K.; Manson, P. N.; Elisseeff, J. H., Variable cytocompatibility of six cell lines with photoinitiators used for polymerizing hydrogels and cell encapsulation. *Biomaterials* **2005**, *26* (11), 1211-8.

82. Hoeijmakers, J. H., DNA damage, aging, and cancer. *N Engl J Med* **2009**, *361* (15), 1475-85.

83. Panich, U.; Sittithumcharee, G.; Rathviboon, N.; Jirawatnotai, S., Ultraviolet radiation-induced skin aging: The role of DNA damage and oxidative stress in epidermal stem cell damage mediated skin aging. *Stem Cells International* **2016**, *2016*, 7370642.
84. Dakup, P.; Gaddameedhi, S., Impact of the circadian clock on UV-induced DNA damage response and photocarcinogenesis. *Photochemistry and Photobiology* **2017**, *93* (1), 296-303.
85. Kolb, H. C.; Finn, M. G.; Sharpless, K. B., Click chemistry: Diverse chemical function from a few good reactions. *Angewandte Chemie International Edition English* **2001**, *40* (11), 2004-2021.
86. Fu, S.; Dong, H.; Deng, X.; Zhuo, R.; Zhong, Z., Injectable hyaluronic acid/poly(ethylene glycol) hydrogels crosslinked via strain-promoted azide-alkyne cycloaddition click reaction. *Carbohydrate Polymers* **2017**, *169*, 332-340.
87. Smith, L. J.; Taimoory, S. M.; Tam, R. Y.; Baker, A. E. G.; Bintah Mohammad, N.; Trant, J. F.; Shoichet, M. S., Diels–Alder click-cross-linked hydrogels with increased reactivity enable 3D cell encapsulation. *Biomacromolecules* **2018**, *19* (3), 926-935.
88. Nayab, S.; Trouillet, V.; Gliemann, H.; Weidler, P. G.; Azeem, I.; Tariq, S. R.; Goldmann, A. S.; Barner-Kowollik, C.; Yameen, B., Reversible Diels–Alder and Michael addition reactions enable the facile postsynthetic modification of metal–organic frameworks. *Inorganic Chemistry* **2021**, *60* (7), 4397-4409.
89. Xu, J.; Liu, Y.; Hsu, S.-H., Hydrogels based on Schiff base linkages for biomedical applications. *Molecules* **2019**, *24* (16), 3005.
90. Li, S.; Pei, M.; Wan, T.; Yang, H.; Gu, S.; Tao, Y.; Liu, X.; Zhou, Y.; Xu, W.; Xiao, P., Self-healing hyaluronic acid hydrogels based on dynamic Schiff base linkages as biomaterials. *Carbohydrate Polymers* **2020**, *250*, 116922.
91. Boehnke, N.; Cam, C.; Bat, E.; Segura, T.; Maynard, H. D., Imine hydrogels with tunable degradability for tissue engineering. *Biomacromolecules* **2015**, *16* (7), 2101-2108.
92. Censi, R.; Schuurman, W.; Malda, J.; di Dato, G.; Burgisser, P. E.; Dhert, W. J. A.; van Nostrum, C. F.; di Martino, P.; Vermonden, T.; Hennink, W. E., A printable photopolymerizable thermosensitive p(HPMAM-lactate)-PEG hydrogel for tissue engineering. *Advanced Functional Materials* **2011**, *21* (10), 1833-1842.
93. Cascone, M. G.; Sim, B.; Sandra, D., Blends of synthetic and natural polymers as drug delivery systems for growth hormone. *Biomaterials* **1995**, *16* (7), 569-574.
94. Coombes, A. G. A.; Verderio, E.; Shaw, B.; Li, X.; Griffin, M.; Downes, S., Biocomposites of non-crosslinked natural and synthetic polymers. *Biomaterials* **2002**, *23* (10), 2113-2118.
95. Censi, R.; Fieten, P. J.; di Martino, P.; Hennink, W. E.; Vermonden, T., In situ forming hydrogels by tandem thermal gelling and michael addition reaction between thermosensitive triblock copolymers and thiolated hyaluronan. *Macromolecules* **2010**, *43* (13), 5771-5778.
96. Yao, S.; Xu, Y.; Zhou, Y.; Shao, C.; Liu, Z.; Jin, B.; Zhao, R.; Cao, H.; Pan, H.; Tang, R., Calcium phosphate nanocluster-loaded injectable hydrogel for bone regeneration. *ACS Applied Bio Materials* **2019**, *2* (10), 4408-4417.
97. Raucci, M. G.; Demitri, C.; Soriente, A.; Fasolino, I.; Sannino, A.; Ambrosio, L., Gelatin/nano-hydroxyapatite hydrogel scaffold prepared by sol-gel technology as filler to repair bone defects. *Journal of Biomedical Materials Research Part A* **2018**, *106* (7), 2007-2019.
98. Nikpour, P.; Salimi-Kenari, H.; Fahimipour, F.; Rabiee, S. M.; Imani, M.; Dashtimoghadam, E.; Tayebi, L., Dextran hydrogels incorporated with bioactive glass-ceramic: Nanocomposite scaffolds for bone tissue engineering. *Carbohydrate Polymers* **2018**, *190*, 281-294.
99. Castilho, M.; Hochleitner, G.; Wilson, W.; van Rietbergen, B.; Dalton, P. D.; Groll, J.; Malda, J.; Ito, K., Mechanical behavior of a soft hydrogel reinforced with three-dimensional printed microfibre scaffolds. *Scientific Reports* **2018**, *8* (1), 1245.
100. Ravanbakhsh, H.; Bao, G.; Mongeau, L., Carbon nanotubes promote cell migration in hydrogels. *Scientific Reports* **2020**, *10* (1), 2543.
101. Zhang, X.; Fan, J.; Lee, C.-S.; Kim, S.; Chen, C.; Lee, M., Supramolecular hydrogels based on nanoclay and guanidine-rich chitosan: injectable and moldable osteoinductive carriers. *ACS Applied Materials & Interfaces* **2020**, *12* (14), 16088-16096.
102. Gao, S.-Q.; Maeda, T.; Okano, K.; Palczewski, K., A microparticle/hydrogel combination drug-delivery system for sustained release of retinoids. *Investigative Ophthalmology & Visual Science* **2012**, *53* (10), 6314-6323.

103. Moorcroft, S. C. T.; Roach, L.; Jayne, D. G.; Ong, Z. Y.; Evans, S. D., Nanoparticle-loaded hydrogel for the light-activated release and photothermal enhancement of antimicrobial peptides. *ACS Applied Materials & Interfaces* **2020**, *12* (22), 24544-24554.
104. Nicolas, J.; Magli, S.; Rabbachin, L.; Sampaolesi, S.; Nicotra, F.; Russo, L., 3D extracellular matrix mimics: Fundamental concepts and role of materials chemistry to influence stem cell fate. *Biomacromolecules* **2020**, *21* (6), 1968-1994.
105. ASTM F2792-12a, S. T. f. A. M. T., (Withdrawn 2015), ASTM International, West Conshohocken, PA, 2012, www.astm.org.
106. Groll, J.; Boland, T.; Blunk, T.; Burdick, J. A.; Cho, D. W.; Dalton, P. D.; Derby, B.; Forgacs, G.; Li, Q.; Mironov, V. A.; Moroni, L.; Nakamura, M.; Shu, W.; Takeuchi, S.; Vozzi, G.; Woodfield, T. B.; Xu, T.; Yoo, J. J.; Malda, J., Biofabrication: reappraising the definition of an evolving field. *Biofabrication* **2016**, *8* (1), 013001.
107. Guillemot, F.; Mironov, V.; Nakamura, M., Bioprinting is coming of age: Report from the International Conference on Bioprinting and Biofabrication in Bordeaux (3B'09). *Biofabrication* **2010**, *2* (1), 010201.
108. Wilson, H. V., On some phenomena of coalescence and regeneration in sponges. *Journal of Experimental Zoology* **1907**, *5* (2), 245-258.
109. Wilson Jr., W. C.; Boland, T., Cell and organ printing 1: Protein and cell printers. *The Anatomical Record Part A: Discoveries in Molecular, Cellular, and Evolutionary Biology* **2003**, *272A* (2), 491-496.
110. Boland, T.; Mironov, V.; Gutowska, A.; Roth, E. A.; Markwald, R. R., Cell and organ printing 2: Fusion of cell aggregates in three-dimensional gels. *The Anatomical Record Part A: Discoveries in Molecular, Cellular, and Evolutionary Biology* **2003**, *272A* (2), 497-502.
111. Thompson, R. P.; Reckova, M.; deAlmeida, A.; Bigelow, M. R.; Stanley, C. P.; Spruill, J. B.; Trusk, T. T.; Sedmera, D., The oldest, toughest cells in the heart. *Novartis Foundation Symposia* **2003**, *250*, 157-74; discussion 174-6, 276-9.
112. Mironov, V.; Boland, T.; Trusk, T.; Forgacs, G.; Markwald, R. R., Organ printing: computer-aided jet-based 3D tissue engineering. *Trends in Biotechnology* **2003**, *21* (4), 157-161.
113. Sun, W.; Starly, B.; Daly, A. C.; Burdick, J. A.; Groll, J.; Skeldon, G.; Shu, W.; Sakai, Y.; Shinohara, M.; Nishikawa, M.; Jang, J.; Cho, D.-W.; Nie, M.; Takeuchi, S.; Ostrovidov, S.; Khademhosseini, A.; Kamm, R. D.; Mironov, V.; Moroni, L.; Ozbolat, I. T., The bioprinting roadmap. *Biofabrication* **2020**, *12* (2), 022002.
114. Mobaraki, M.; Ghaffari, M.; Yazdanpanah, A.; Luo, Y.; Mills, D. K., Bioinks and bioprinting: A focused review. *Bioprinting* **2020**, *18*, e00080.
115. Mazzocchi, A.; Soker, S.; Skardal, A., 3D bioprinting for high-throughput screening: Drug screening, disease modeling, and precision medicine applications. *Applied Physics Reviews* **2019**, *6* (1), 011302.
116. Li, J.; Chen, M.; Fan, X.; Zhou, H., Recent advances in bioprinting techniques: approaches, applications and future prospects. *Journal of Translational Medicine* **2016**, *14* (1), 271.
117. Viola, M.; Piluso, S.; Groll, J.; Vermonden, T.; Malda, J.; Castilho, M., The importance of interfaces in multi-material biofabricated tissue structures. *Advanced Healthcare Materials* **2021** <https://doi.org/10.1002/adhm.202101021>.
118. Malda, J.; Visser, J.; Melchels, F. P.; Jüngst, T.; Hennink, W. E.; Dhert, W. J. A.; Groll, J.; Huttmacher, D. W., 25th Anniversary article: Engineering hydrogels for biofabrication. *Advanced Materials* **2013**, *25* (36), 5011-5028.
119. Groll, J.; Burdick, J. A.; Cho, D. W.; Derby, B.; Gelinsky, M.; Heilshorn, S. C.; Jüngst, T.; Malda, J.; Mironov, V. A.; Nakayama, K.; Ovsianikov, A.; Sun, W.; Takeuchi, S.; Yoo, J. J.; Woodfield, T. B. F., A definition of bioinks and their distinction from biomaterial inks. *Biofabrication* **2018**, *11* (1), 013001.
120. Rutz, A. L.; Lewis, P. L.; Shah, R. N., Toward next-generation bioinks: Tuning material properties pre- and post-printing to optimize cell viability. *MRS Bulletin* **2017**, *42* (8), 563-570.
121. Ouyang, L.; Yao, R.; Zhao, Y.; Sun, W., Effect of bioink properties on printability and cell viability for 3D bioplotting of embryonic stem cells. *Biofabrication* **2016**, *8* (3), 035020.
122. Wilson, S. A.; Cross, L. M.; Peak, C. W.; Gaharwar, A. K., Shear-thinning and thermo-reversible nanoengineered inks for 3D bioprinting. *ACS Applied Materials & Interfaces* **2017**, *9* (50), 43449-43458.

123. Alruwaili, M.; Lopez, J. A.; McCarthy, K.; Reynaud, E. G.; Rodriguez, B. J., Liquid-phase 3D bioprinting of gelatin alginate hydrogels: influence of printing parameters on hydrogel line width and layer height. *Bio-Design and Manufacturing* **2019**, *2* (3), 172-180.
124. Xu, H.; Zhang, Z.; Xu, C., Sedimentation study of bioink containing living cells. *Journal of Applied Physics* **2019**, *125* (11), 114901.
125. Mancha Sánchez, E.; Gómez-Blanco, J. C.; López Nieto, E.; Casado, J. G.; Macías-García, A.; Díaz Díez, M. A.; Carrasco-Amador, J. P.; Torrejón Martín, D.; Sánchez-Margallo, F. M.; Pagador, J. B., Hydrogels for bioprinting: A systematic review of hydrogels synthesis, bioprinting parameters, and bioprinted structures behavior. *Frontiers in Bioengineering and Biotechnology* **2020**, *8*, 776-776.
126. Sun, Y.; Nan, D.; Jin, H.; Qu, X., Recent advances of injectable hydrogels for drug delivery and tissue engineering applications. *Polymer Testing* **2020**, *81*, 106283.
127. Cooke, M. E.; Rosenzweig, D. H., The rheology of direct and suspended extrusion bioprinting. *APL Bioengineering* **2021**, *5* (1), 011502.
128. Mezger, T., The Rheology Handbook: For users of rotational and oscillatory rheometers. Vincentz Network: 2020. <https://doi.org/10.1515/9783748603702>.
129. Guvendiren, M.; Lu, H. D.; Burdick, J. A., Shear-thinning hydrogels for biomedical applications. *Soft Matter* **2012**, *8* (2), 260-272.
130. Schwab, A.; Levato, R.; D'Este, M.; Piluso, S.; Eglín, D.; Malda, J., Printability and shape fidelity of bioinks in 3D bioprinting. *Chemical Reviews* **2020**, *120* (19), 11028-11055.
131. Paxton, N.; Smolan, W.; Böck, T.; Melchels, F.; Groll, J.; Jungst, T., Proposal to assess printability of bioinks for extrusion-based bioprinting and evaluation of rheological properties governing bioprintability. *Biofabrication* **2017**, *9* (4), 044107.
132. Suntornnond, R.; An, J.; Chua, C. K., Bioprinting of thermoresponsive hydrogels for next generation tissue engineering: A review. *Macromolecular Materials and Engineering* **2017**, *302* (1), 1600266.
133. Du, Z.; Li, N.; Hua, Y.; Shi, Y.; Bao, C.; Zhang, H.; Yang, Y.; Lin, Q.; Zhu, L., Physiological pH-dependent gelation for 3D printing based on the phase separation of gelatin and oxidized dextran. *Chemical Communications* **2017**, *53* (97), 13023-13026.
134. Lee, M.; Bae, K.; Levinson, C.; Zenobi-Wong, M., Nanocomposite bioink exploits dynamic covalent bonds between nanoparticles and polysaccharides for precision bioprinting. *Biofabrication* **2020**, *12* (2), 025025.
135. Hu, T.; Cui, X.; Zhu, M.; Wu, M.; Tian, Y.; Yao, B.; Song, W.; Niu, Z.; Huang, S.; Fu, X., 3D-printable supramolecular hydrogels with shear-thinning property: fabricating strength tunable bioink via dual crosslinking. *Bioactive Materials* **2020**, *5* (4), 808-818.
136. Hazur, J.; Detsch, R.; Karakaya, E.; Kaschta, J.; Teßmar, J.; Schneidereit, D.; Friedrich, O.; Schubert, D. W.; Boccaccini, A. R., Improving alginate printability for biofabrication: establishment of a universal and homogeneous pre-crosslinking technique. *Biofabrication* **2020**, *12* (4), 045004.
137. Gillispie, G.; Prim, P.; Copus, J.; Fisher, J.; Mikos, A. G.; Yoo, J. J.; Atala, A.; Lee, S. J., Assessment methodologies for extrusion-based bioink printability. *Biofabrication* **2020**, *12* (2), 022003.
138. Gao, T.; Gillispie, G. J.; Copus, J. S.; Pr, A. K.; Seol, Y. J.; Atala, A.; Yoo, J. J.; Lee, S. J., Optimization of gelatin-alginate composite bioink printability using rheological parameters: a systematic approach. *Biofabrication* **2018**, *10* (3), 034106.
139. Osidak, E. O.; Karalkin, P. A.; Osidak, M. S.; Parfenov, V. A.; Sivogrivov, D. E.; Pereira, F. D. A. S.; Gryadunova, A. A.; Koudan, E. V.; Khesuani, Y. D.; Kasyanov, V. A.; Belousov, S. I.; Krashennnikov, S. V.; Grigoriev, T. E.; Chvalun, S. N.; Bulanova, E. A.; Mironov, V. A.; Domogatsky, S. P., Viscoll collagen solution as a novel bioink for direct 3D bioprinting. *Journal of Materials Science: Materials in Medicine* **2019**, *30* (3), 31.
140. Contessi Negrini, N.; Celikkin, N.; Tarsini, P.; Farè, S.; Świążkowski, W., Three-dimensional printing of chemically crosslinked gelatin hydrogels for adipose tissue engineering. *Biofabrication* **2020**, *12* (2), 025001.
141. Ribeiro, A.; Blokzijl, M. M.; Levato, R.; Visser, C. W.; Castilho, M.; Hennink, W. E.; Vermonden, T.; Malda, J., Assessing bioink shape fidelity to aid material development in 3D bioprinting. *Biofabrication* **2017**, *10* (1), 014102.
142. Jungst, T.; Smolan, W.; Schacht, K.; Scheibel, T.; Groll, J., Strategies and molecular design criteria for 3D printable hydrogels. *Chemical Reviews* **2016**, *116* (3), 1496-1539.

143. Khoeni, R.; Nosrati, H.; Akbarzadeh, A.; Eftekhari, A.; Kavetsky, T.; Khalilov, R.; Ahmadian, E.; Nasibova, A.; Datta, P.; Roshangar, L.; Deluca, D. C.; Davaran, S.; Cucchiaroni, M.; Ozbolat, I. T., Natural and synthetic bioinks for 3D bioprinting. *Advanced NanoBiomed Research* **2021**, *1* (8), 2000097.
144. Suntornnond, R.; An, J.; Chua, C. K., Roles of support materials in 3D bioprinting - Present and future. *International Journal of Bioprinting* **2017**, *3* (1), 006-006.
145. Kolesky, D. B.; Homan, K. A.; Skylar-Scott, M. A.; Lewis, J. A., Three-dimensional bioprinting of thick vascularized tissues. *Proceedings of the National Academy of Sciences* **2016**, *113* (12), 3179.
146. Ahlfeld, T.; Köhler, T.; Czichy, C.; Lode, A.; Gelinsky, M., A Methylcellulose hydrogel as support for 3D plotting of complex shaped calcium phosphate scaffolds. *Gels* **2018**, *4* (3), 68.
147. Hinton, T. J.; Jallerat, Q.; Palchesko, R. N.; Park, J. H.; Grodzicki, M. S.; Shue, H.-J.; Ramadan, M. H.; Hudson, A. R.; Feinberg, A. W., Three-dimensional printing of complex biological structures by freeform reversible embedding of suspended hydrogels. *Science Advances* **2015**, *1* (9), e1500758.
148. Jia, W.; Gungor-Ozkerim, P. S.; Zhang, Y. S.; Yue, K.; Zhu, K.; Liu, W.; Pi, Q.; Byambaa, B.; Dokmeci, M. R.; Shin, S. R.; Khademhosseini, A., Direct 3D bioprinting of perfusable vascular constructs using a blend bioink. *Biomaterials* **2016**, *106*, 58-68.
149. Gao, G.; Lee, J. H.; Jang, J.; Lee, D. H.; Kong, J.-S.; Kim, B. S.; Choi, Y.-J.; Jang, W. B.; Hong, Y. J.; Kwon, S.-M.; Cho, D.-W., Tissue engineered bio-blood-vessels constructed using a tissue-specific bioink and 3D coaxial cell printing technique: A novel therapy for ischemic disease. *Advanced Functional Materials* **2017**, *27* (33), 1700798.
150. Gao, Q.; He, Y.; Fu, J.-z.; Liu, A.; Ma, L., Coaxial nozzle-assisted 3D bioprinting with built-in microchannels for nutrients delivery. *Biomaterials* **2015**, *61*, 203-215.
151. Armstrong, J. P. K.; Burke, M.; Carter, B. M.; Davis, S. A.; Perriman, A. W., 3D bioprinting using a templated porous bioink. *Advanced Healthcare Materials* **2016**, *5* (14), 1724-1730.
152. Kang, H.-W.; Lee, S. J.; Ko, I. K.; Kengla, C.; Yoo, J. J.; Atala, A., A 3D bioprinting system to produce human-scale tissue constructs with structural integrity. *Nature Biotechnology* **2016**, *34* (3), 312-319.
153. De Pieri, A.; Byerley, A. M.; Musumeci, C. R.; Saleemizadehparizi, F.; Vanderhorst, M. A.; Wuertz-Kozak, K., Electrospinning and 3D bioprinting for intervertebral disc tissue engineering. *JOR SPINE* **2020**, *3* (4), e1117.
154. Ross, M. T.; Kilian, D.; Lode, A.; Ren, J.; Allenby, M. C.; Gelinsky, M.; Woodruff, M. A., Using melt-electrowritten microfibrils for tailoring scaffold mechanics of 3D bioprinted chondrocyte-laden constructs. *Bioprinting* **2021**, *23*, e00158.
155. Zhang, J.; Wehrle, E.; Rubert, M.; Müller, R., 3D bioprinting of human tissues: biofabrication, bioinks, and bioreactors. *International Journal of Molecular Sciences* **2021**, *22* (8), 3971.
156. Park, J. Y.; Jang, J.; Kang, H.-W., 3D Bioprinting and its application to organ-on-a-chip. *Microelectronic Engineering* **2018**, *200*, 1-11.
157. Jia, J.; Richards, D. J.; Pollard, S.; Tan, Y.; Rodriguez, J.; Visconti, R. P.; Trusk, T. C.; Yost, M. J.; Yao, H.; Markwald, R. R.; Mei, Y., Engineering alginate as bioink for bioprinting. *Acta Biomaterialia* **2014**, *10* (10), 4323-4331.
158. Lee, H.; Kim, J.; Choi, Y.; Cho, D.-W., Application of gelatin bioinks and cell-printing technology to enhance cell delivery capability for 3D liver fibrosis-on-a-chip development. *ACS Biomaterials Science & Engineering* **2020**, *6* (4), 2469-2477.
159. Montero, F. E.; Rezende, R. A.; da Silva, J. V. L.; Sabino, M. A., Development of a smart bioink for bioprinting applications. *Frontiers in Mechanical Engineering* **2019**, *5* (56).
160. Gungor-Ozkerim, P. S.; Inci, I.; Zhang, Y. S.; Khademhosseini, A.; Dokmeci, M. R., Bioinks for 3D bioprinting: an overview. *Biomaterials science* **2018**, *6* (5), 915-946.
161. Camacho, P.; Busari, H.; Seims, K. B.; Tolbert, J. W.; Chow, L. W., Materials as bioinks and bioink design. In *3D Bioprinting in Medicine: Technologies, Bioinks, and Applications*, Guvendiren, M., Ed. Springer International Publishing: Cham, 2019; pp 67-100.
162. Levato, R.; Jungst, T.; Scheuring, R. G.; Blunk, T.; Groll, J.; Malda, J., From shape to function: The next step in bioprinting. *Advanced Materials* **2020**, *32* (12), 1906423.
163. Frump, J. A., Oxazolines. Their preparation, reactions, and applications. *Chemical Reviews* **1971**, *71* (5), 483-505.

164. Gant, T. G.; Meyers, A., The chemistry of 2-oxazolines (1985–present). *Tetrahedron* **1994**, *50* (8), 2297-2360.
165. Hargaden, G. C.; Guiry, P. J., Recent applications of oxazoline-containing ligands in asymmetric catalysis. *Chemical Reviews* **2009**, *109* (6), 2505-2550.
166. Witte, H.; Seeliger, W., Simple synthesis of 2-substituted 2-oxazolines and 5,6-dihydro-4H-1,3-oxazines. *Angewandte Chemie International Edition in English* **1972**, *11* (4), 287-288.
167. Beck, M.; Birnbrich, P.; Eicken, U.; Fischer, H.; Fristad, W. E.; Hase, B.; Krause, H.-J., Polyoxazoline auf fettchemischer Basis. *Die Angewandte Makromolekulare Chemie* **1994**, *223* (1), 217-233.
168. Taubmann, C.; Luxenhofer, R.; Cesana, S.; Jordan, R., First aldehyde-functionalized poly(2-oxazoline)s for chemoselective ligation. *Macromolecular Bioscience* **2005**, *5* (7), 603-612.
169. Wenker, H., The synthesis of α -2-oxazolines and α -2-thiazolines from N-acyl-2-aminoethanols. *Journal of the American Chemical Society* **1935**, *57* (6), 1079-1080.
170. Rossegger, E.; Schenk, V.; Wiesbrock, F., Design strategies for functionalized poly(2-oxazoline)s and derived materials. *Polymers* **2013**, *5* (3), 956-1011.
171. Guillerm, B.; Monge, S.; Lapinte, V.; Robin, J.-J., How to modulate the chemical structure of polyoxazolines by appropriate functionalization. *Macromolecular Rapid Communications* **2012**, *33* (19), 1600-1612.
172. Kempe, K., Chain and step growth polymerizations of cyclic imino ethers: From poly(2-oxazoline)s to poly(ester amide)s. *Macromolecular Chemistry and Physics* **2017**, *218* (11), 1700021.
173. Tomalia, D. A.; Sheetz, D. P., Homopolymerization of 2-alkyl- and 2-aryl-2-oxazolines. *Journal of Polymer Science Part A-1: Polymer Chemistry* **1966**, *4* (9), 2253-2265.
174. Seeliger, W.; Aufderhaar, E.; Diepers, W.; Feinauer, R.; Nehring, R.; Thier, W.; Hellmann, H., Recent syntheses and reactions of cyclic imidic esters. *Angewandte Chemie International Edition in English* **1966**, *5* (10), 875-888.
175. Bassiri, T. G.; Levy, A.; Litt, M., Polymerization of cyclic imino ethers. I. Oxazolines. *Journal of Polymer Science Part B: Polymer Letters* **1967**, *5* (9), 871-879.
176. Kagiya, T.; Narisawa, S.; Maeda, T.; Fukui, K., Ring-opening polymerization of 2-substituted 2-oxazolines. *Journal of Polymer Science Part B: Polymer Letters* **1966**, *4* (7), 441-445.
177. Levy, A.; Litt, M., Polymerization of cyclic imino ethers. II. Oxazines. *Journal of Polymer Science Part B: Polymer Letters* **1967**, *5* (9), 881-886.
178. Glassner, M.; Vergaalen, M.; Hoogenboom, R., Poly(2-oxazoline)s: A comprehensive overview of polymer structures and their physical properties. *Polymer International* **2018**, *67* (1), 32-45.
179. Varanaraja, Z.; Kim, J.; Becer, C. R., Poly(2-oxazine)s: A comprehensive overview of the polymer structures, physical properties and applications. *European Polymer Journal* **2021**, *147*, 110299.
180. Delaittre, G., Telechelic poly(2-oxazoline)s. *European Polymer Journal* **2019**, *121*, 109281.
181. Gress, A.; Völkel, A.; Schlaad, H., Thio-click modification of poly[2-(3-butenyl)-2-oxazoline]. *Macromolecules* **2007**, *40* (22), 7928-7933.
182. Agrawal, M.; Rueda, J. C.; Uhlmann, P.; Müller, M.; Simon, F.; Stamm, M., Facile approach to grafting of poly(2-oxazoline) brushes on macroscopic surfaces and applications thereof. *ACS Applied Materials & Interfaces* **2012**, *4* (3), 1357-1364.
183. Mees, M. A.; Hoogenboom, R., Full and partial hydrolysis of poly(2-oxazoline)s and the subsequent post-polymerization modification of the resulting polyethylenimine (co)polymers. *Polymer Chemistry* **2018**, *9* (40), 4968-4978.
184. Lambermont-Thijs, H. M. L.; Heuts, J. P. A.; Hoepfener, S.; Hoogenboom, R.; Schubert, U. S., Selective partial hydrolysis of amphiphilic copoly(2-oxazoline)s as basis for temperature and pH responsive micelles. *Polymer Chemistry* **2011**, *2* (2), 313-322.
185. Kem, K. M., Kinetics of the hydrolysis of linear poly[(acylimino)-ethylenes]. *Journal of Polymer Science: Polymer Chemistry Edition* **1979**, *17* (7), 1977-1990.
186. Lambermont-Thijs, H. M. L.; van der Woerd, F. S.; Baumgaertel, A.; Bonami, L.; Du Prez, F. E.; Schubert, U. S.; Hoogenboom, R., Linear poly(ethylene imine)s by acidic hydrolysis of poly(2-oxazoline)s: kinetic screening, thermal properties, and temperature-induced solubility transitions. *Macromolecules* **2010**, *43* (2), 927-933.
187. van Kuringen, H. P. C.; de la Rosa, V. R.; Fijten, M. W. M.; Heuts, J. P. A.; Hoogenboom, R., Enhanced selectivity for the hydrolysis of block copoly(2-oxazoline)s in ethanol–water resulting in

- linear poly(ethylene imine) copolymers. *Macromolecular Rapid Communications* **2012**, *33* (9), 827-832.
188. Mees, M.; Haladjova, E.; Momekova, D.; Momekov, G.; Shestakova, P. S.; Tsvetanov, C. B.; Hoogenboom, R.; Rangelov, S., Partially hydrolyzed poly(n-propyl-2-oxazoline): Synthesis, aqueous solution properties, and preparation of gene delivery systems. *Biomacromolecules* **2016**, *17* (11), 3580-3590.
189. Van Kuringen, H. P. C.; Lenoir, J.; Adriaens, E.; Bender, J.; De Geest, B. G.; Hoogenboom, R., Partial hydrolysis of poly(2-ethyl-2-oxazoline) and potential implications for biomedical applications? *Macromolecular Bioscience* **2012**, *12* (8), 1114-1123.
190. Saegusa, T.; Nagura, Y.; Kobayashi, S., Isomerization polymerization of 1,3-oxazine. I. Polymerization of unsubstituted 5,6-dihydro-4H-1,3-oxazine giving poly(N-formyltrimethylenimine) and its alkaline hydrolysis of poly(trimethylenimine). *Macromolecules* **1973**, *6* (4), 495-498.
191. Overberger, C. G.; Chang, J. Y.; Gunn, V. E., Synthesis of optically active polynucleotide analogs with polytrimethylenimine backbones and thymine moieties. *Journal of Polymer Science Part A: Polymer Chemistry* **1989**, *27* (1), 99-106.
192. Hu, L.; Frech, R.; Glatzhofer, D. T.; Mason, R.; York, S. S., Linear poly(propylenimine)/lithium triflate as a polymer electrolyte system. *Solid State Ionics* **2008**, *179* (11), 401-408.
193. Nahm, D.; Weigl, F.; Schaefer, N.; Sancho, A.; Frank, A.; Groll, J.; Villmann, C.; Schmidt, H.-W.; Dalton, P. D.; Luxenhofer, R., A versatile biomaterial ink platform for the melt electrowriting of chemically-crosslinked hydrogels. *Materials Horizons* **2020**, *7* (3), 928-933.
194. Pang, S. H.; Lively, R. P.; Jones, C. W., Oxidatively-stable linear poly(propylenimine)-containing adsorbents for CO₂ capture from ultradilute streams. *ChemSusChem* **2018**, *11* (15), 2628-2637.
195. Vlasi, E.; Pispas, S., Solution behavior of hydrolyzed gradient methyl/phenyl oxazoline copolymers and complexation with DNA. *Macromolecular Chemistry and Physics* **2015**, *216* (8), 873-883.
196. Litt, M. H.; Lin, C. S., Selective hydrolysis of oxazoline block copolymers. *Journal of Polymer Science Part A: Polymer Chemistry* **1992**, *30* (5), 779-786.
197. Luxenhofer, R.; Bezen, M.; Jordan, R., Kinetic investigations on the polymerization of 2-oxazolines using pluritriflate initiators. *Macromolecular Rapid Communications* **2008**, *29* (18), 1509-1513.
198. Zhang, N.; Huber, S.; Schulz, A.; Luxenhofer, R.; Jordan, R., Cylindrical molecular brushes of poly(2-oxazoline)s from 2-isopropenyl-2-oxazoline. *Macromolecules* **2009**, *42* (6), 2215-2221.
199. Motokucho, S.; Furukawa, M.; Kawashima, M.; Kojio, K.; Yoshinaga, K., Physical properties of poly(tetrahydrofuran)-block-poly(2-ethyl-2-oxazoline) triblock copolymer. *Polymer Journal* **2013**, *45* (11), 1115-1119.
200. Hoogenboom, R.; Thijs, H. M. L.; Jochems, M. J. H. C.; van Lankvelt, B. M.; Fijten, M. W. M.; Schubert, U. S., Tuning the LCST of poly(2-oxazoline)s by varying composition and molecular weight: alternatives to poly(N-isopropylacrylamide)? *Chemical Communications* **2008**, (44), 5758-5760.
201. Bloksma, M. M.; Paulus, R. M.; van Kuringen, H. P. C.; van der Woerd, F.; Lambermont-Thijs, H. M. L.; Schubert, U. S.; Hoogenboom, R., Thermoresponsive poly(2-oxazine)s. *Macromolecular Rapid Communications* **2012**, *33* (1), 92-96.
202. Zahoranová, A.; Luxenhofer, R., Poly(2-oxazoline)- and poly(2-oxazine)-based self-assemblies, polyplexes, and drug nanoformulations—an update. *Advanced Healthcare Materials* **2021**, *10* (6), 2001382.
203. Hamley, I. W., Nanotechnology with soft materials. *Angewandte Chemie International Edition* **2003**, *42* (15), 1692-1712.
204. Schmidt, H.-W.; Würthner, F., A periodic system of supramolecular elements. *Angewandte Chemie International Edition* **2020**, *59* (23), 8766-8775.
205. Förster, S.; Konrad, M., From self-organizing polymers to nano- and biomaterials. *Journal of Materials Chemistry* **2003**, *13* (11), 2671-2688.
206. Giacomelli, C.; Schmidt, V.; Aissou, K.; Borsali, R., Block copolymer systems: From single chain to self-assembled nanostructures. *Langmuir* **2010**, *26* (20), 15734-15744.

207. Hyde, S., Curvature and the global structure of interfaces in surfactant-water systems. *Le Journal De Physique Colloques* **1990**, *51*.
208. Antonietti, M.; Förster, S., Vesicles and liposomes: A self-assembly principle beyond lipids. *Advanced Materials* **2003**, *15* (16), 1323-1333.
209. Mai, Y.; Eisenberg, A., Self-assembly of block copolymers. *Chemical Society Reviews* **2012**, *41* (18), 5969-5985.
210. Oleszko-Torbus, N.; Utrata-Wesołek, A.; Wałach, W.; Dworak, A., Solution behavior of thermoresponsive random and gradient copolymers of 2-n-propyl-2-oxazoline. *European Polymer Journal* **2017**, *88*, 613-622.
211. Trinh, L. T. T.; Lambermont-Thijs, H. M. L.; Schubert, U. S.; Hoogenboom, R.; Kjøniksen, A.-L., Thermoresponsive poly(2-oxazoline) block copolymers exhibiting two cloud points: complex multistep assembly behavior. *Macromolecules* **2012**, *45* (10), 4337-4345.
212. Zahoranová, A.; Mrlík, M.; Tomanová, K.; Kronek, J.; Luxenhofer, R., ABA and BAB triblock copolymers based on 2-methyl-2-oxazoline and 2-n-propyl-2-oxazoline: synthesis and thermoresponsive behavior in water. *Macromolecular Chemistry and Physics* **2017**, *218* (13), 1700031.
213. Lübtow, M. M.; Keßler, L.; Appelt-Menzel, A.; Lorson, T.; Gangloff, N.; Kirsch, M.; Dahms, S.; Luxenhofer, R., More is sometimes less: curcumin and paclitaxel formulations using poly(2-oxazoline) and poly(2-oxazine)-based amphiphiles bearing linear and branched C9 side chains. *Macromolecular Bioscience* **2018**, *18* (11), 1800155.
214. Hiller, W.; Engelhardt, N.; Kampmann, A.-L.; Degen, P.; Weberskirch, R., Micellization and mobility of amphiphilic poly(2-oxazoline) based block copolymers characterized by ¹H NMR spectroscopy. *Macromolecules* **2015**, *48* (12), 4032-4045.
215. Hoogenboom, R.; Thijs, H. M. L.; Fijten, M. W. M.; van Lankvelt, B. M.; Schubert, U. S., One-pot synthesis of 2-phenyl-2-oxazoline-containing quasi-diblock copoly(2-oxazoline)s under microwave irradiation. *Journal of Polymer Science Part A: Polymer Chemistry* **2007**, *45* (3), 416-422.
216. Fustin, C.-A.; Lefèvre, N.; Hoogenboom, R.; Schubert, U. S.; Gohy, J.-F., Micellization of poly(2-oxazoline)-based quasi-diblock copolymers on surfaces. *Macromolecular Chemistry and Physics* **2007**, *208* (18), 2026-2031.
217. Hoogenboom, R.; Thijs, H. M. L.; Wouters, D.; Hoepfener, S.; Schubert, U. S., Solvent responsive micelles based on block and gradient copoly(2-oxazoline)s. *Macromolecules* **2008**, *41* (5), 1581-1583.
218. Milonaki, Y.; Kaditi, E.; Pispas, S.; Demetzos, C., Amphiphilic gradient copolymers of 2-methyl- and 2-phenyl-2-oxazoline: self-organization in aqueous media and drug encapsulation. *Journal of Polymer Science Part A: Polymer Chemistry* **2012**, *50* (6), 1226-1237.
219. Krumm, C.; Fik, C. P.; Meuris, M.; Dropalla, G. J.; Geltenpoth, H.; Sickmann, A.; Tiller, J. C., Well-defined amphiphilic poly(2-oxazoline) ABA-triblock copolymers and their aggregation behavior in aqueous solution. *Macromolecular Rapid Communications* **2012**, *33* (19), 1677-1682.
220. Bera, D.; Sedlacek, O.; Jager, E.; Pavlova, E.; Vergaelen, M.; Hoogenboom, R., Solvent-control over monomer distribution in the copolymerization of 2-oxazolines and the effect of a gradient structure on self-assembly. *Polymer Chemistry* **2019**, *10* (37), 5116-5123.
221. Filippov, S. K.; Verbraeken, B.; Konarev, P. V.; Svergun, D. I.; Angelov, B.; Vishnevetskaya, N. S.; Papadakis, C. M.; Rogers, S.; Radulescu, A.; Courtin, T.; Martins, J. C.; Starovoytova, L.; Hruby, M.; Stepanek, P.; Kravchenko, V. S.; Potemkin, I. I.; Hoogenboom, R., Block and gradient copoly(2-oxazoline) micelles: strikingly different on the inside. *The Journal of Physical Chemistry Letters* **2017**, *8* (16), 3800-3804.
222. Seo, Y.; Schulz, A.; Han, Y.; He, Z.; Bludau, H.; Wan, X.; Tong, J.; Bronich, T. K.; Sokolsky, M.; Luxenhofer, R.; Jordan, R.; Kabanov, A. V., Poly(2-oxazoline) block copolymer based formulations of taxanes: effect of copolymer and drug structure, concentration, and environmental factors. *Polymers for Advanced Technologies* **2015**, *26* (7), 837-850.
223. Bauer, M.; Schroeder, S.; Tauhardt, L.; Kempe, K.; Schubert, U. S.; Fischer, D., In vitro hemocompatibility and cytotoxicity study of poly(2-methyl-2-oxazoline) for biomedical applications. *Journal of Polymer Science Part A: Polymer Chemistry* **2013**, *51* (8), 1816-1821.
224. Lübtow, M. M.; Nelke, L. C.; Seifert, J.; Kühnemundt, J.; Sahay, G.; Dandekar, G.; Nietzer, S. L.; Luxenhofer, R., Drug induced micellization into ultra-high capacity and stable curcumin nanoformulations: Physico-chemical characterization and evaluation in 2D and 3D in vitro models. *Journal of Controlled Release* **2019**, *303*, 162-180.

225. Luxenhofer, R.; Sahay, G.; Schulz, A.; Alakhova, D.; Bronich, T. K.; Jordan, R.; Kabanov, A. V., Structure-property relationship in cytotoxicity and cell uptake of poly (2-oxazoline) amphiphiles. *Journal of Controlled Release* **2011**, *153* (1), 73-82.
226. Kronek, J.; Kroneková, Z.; Lustoň, J.; Paulovičová, E.; Paulovičová, L.; Mendrek, B., In vitro bio-immunological and cytotoxicity studies of poly (2-oxazolines). *Journal of Materials Science: Materials in Medicine* **2011**, *22* (7), 1725-1734.
227. Kroneková Z, L. T., Kronek J, Luxenhofer R. Cytotoxicity of 2-oxazines and poly(2-oxazine)s in mouse fibroblast. ChemRxiv. Cambridge: Cambridge Open Engage; 2018; This content is a preprint and has not been peer-reviewed.
228. Kronek, J.; Paulovičová, E.; Paulovičová, L.; Kroneková, Z.; Lustoň, J., Immunomodulatory efficiency of poly (2-oxazolines). *Journal of Materials Science: Materials in Medicine* **2012**, *23* (6), 1457-1464.
229. Gaertner, F. C.; Luxenhofer, R.; Blechert, B.; Jordan, R.; Essler, M., Synthesis, biodistribution and excretion of radiolabeled poly(2-alkyl-2-oxazoline)s. *Journal of Controlled Release* **2007**, *119* (3), 291-300.
230. Sedlacek, O.; Hoogenboom, R., Drug delivery systems based on poly(2-oxazoline)s and poly(2-oxazine)s. *Advanced Therapeutics* **2020**, *3* (1), 1900168.
231. Mero, A.; Pasut, G.; Via, L. D.; Fijten, M. W. M.; Schubert, U. S.; Hoogenboom, R.; Veronese, F. M., Synthesis and characterization of poly(2-ethyl 2-oxazoline)-conjugates with proteins and drugs: Suitable alternatives to PEG-conjugates? *Journal of Controlled Release* **2008**, *125* (2), 87-95.
232. Jeong, J. H.; Song, S. H.; Lim, D. W.; Lee, H.; Park, T. G., DNA transfection using linear poly (ethylenimine) prepared by controlled acid hydrolysis of poly (2-ethyl-2-oxazoline). *Journal of controlled Release* **2001**, *73* (2-3), 391-399.
233. Luxenhofer, R.; Schulz, A.; Roques, C.; Li, S.; Bronich, T. K.; Batrakova, E. V.; Jordan, R.; Kabanov, A. V., Doubly amphiphilic poly (2-oxazoline) s as high-capacity delivery systems for hydrophobic drugs. *Biomaterials* **2010**, *31* (18), 4972-4979.
234. Dargaville, T. R.; Forster, R.; Farrugia, B. L.; Kempe, K.; Voorhaar, L.; Schubert, U. S.; Hoogenboom, R., Poly(2-oxazoline) hydrogel monoliths via thiol-ene coupling. *Macromolecular Rapid Communications* **2012**, *33* (19), 1695-1700.
235. Schulz, A.; Stocco, A.; Bethry, A.; Lavigne, J.-P.; Coudane, J.; Nottelet, B., Direct photomodification of polymer surfaces: unleashing the potential of aryl-azide copolymers. *Advanced Functional Materials* **2018**, *28* (30), 1800976.
236. Han, Y.; He, Z.; Schulz, A.; Bronich, T. K.; Jordan, R.; Luxenhofer, R.; Kabanov, A. V., Synergistic combinations of multiple chemotherapeutic agents in high capacity poly(2-oxazoline) micelles. *Molecular Pharmaceutics* **2012**, *9* (8), 2302-2313.
237. Schulz, A.; Jaksch, S.; Schubel, R.; Wegener, E.; Di, Z.; Han, Y.; Meister, A.; Kressler, J.; Kabanov, A. V.; Luxenhofer, R.; Papadakis, C. M.; Jordan, R., Drug-induced morphology switch in drug delivery systems based on poly(2-oxazoline)s. *ACS Nano* **2014**, *8* (3), 2686-2696.
238. Jaksch, S.; Schulz, A.; Di, Z.; Luxenhofer, R.; Jordan, R.; Papadakis, C. M., Amphiphilic triblock copolymers from poly(2-oxazoline) with different hydrophobic blocks: changes of the micellar structures upon addition of a strongly hydrophobic cancer drug. *Macromolecular Chemistry and Physics* **2016**, *217* (13), 1448-1456.
239. Zahoranová, A.; Kroneková, Z.; Zahoran, M.; Chorvát Jr., D.; Janigová, I.; Kronek, J., Poly(2-oxazoline) hydrogels crosslinked with aliphatic bis(2-oxazoline)s: Properties, cytotoxicity, and cell cultivation. *Journal of Polymer Science Part A: Polymer Chemistry* **2016**, *54* (11), 1548-1559.
240. Hartlieb, M.; Schubert, S.; Kempe, K.; Windhab, N.; Schubert, U. S., Stabilization of factor VIII by poly(2-oxazoline) hydrogels. *Journal of Polymer Science Part A: Polymer Chemistry* **2015**, *53* (1), 10-14.
241. Zschoche, S.; Rueda, J.; Boyko, V.; Krahl, F.; Arndt, K.-F.; Voit, B., Thermo-responsive nanogels based on poly[NIPAAm-graft-(2-alkyl-2-oxazoline)]s crosslinked in the micellar state. *Macromolecular Chemistry and Physics* **2010**, *211* (9), 1035-1042.
242. El-Hag Ali, A.; AlArifi, A. S., Swelling and drug release profile of poly(2-ethyl-2-oxazoline)-based hydrogels prepared by gamma radiation-induced copolymerization. *Journal of Applied Polymer Science* **2011**, *120* (5), 3071-3077.
243. Chujo, Y.; Sada, K.; Kawasaki, T.; Saegusa, T., Synthesis of non-ionic hydrogel from star-shaped polyoxazoline. *Polymer Journal* **1992**, *24* (11), 1301-1306.

244. Chujo, Y.; Sada, K.; Matsumoto, K.; Saegusa, T., Synthesis of nonionic hydrogel, lipogel, and amphigel by copolymerization of 2-oxazolines and a bisoxazoline. *Macromolecules* **1990**, *23* (5), 1234-1237.
245. Chujo, Y.; Sada, K.; Naka, A.; Nomura, R.; Saegusa, T., Synthesis and redox gelation of disulfide-modified polyoxazoline. *Macromolecules* **1993**, *26* (5), 883-887.
246. Chujo, Y.; Sada, K.; Nomura, R.; Naka, A.; Saegusa, T., Photogelation and redox properties of anthracene-disulfide-modified polyoxazolines. *Macromolecules* **1993**, *26* (21), 5611-5614.
247. Chujo, Y.; Sada, K.; Saegusa, T., Cobalt(III) bipyridyl-branched polyoxazoline complex as a thermally and redox reversible hydrogel. *Macromolecules* **1993**, *26* (24), 6320-6323.
248. Chujo, Y.; Sada, K.; Saegusa, T., Synthesis of bipyridyl-branched polyoxazoline and its gelation by means of metal coordination. *Polymer Journal* **1993**, *25* (6), 599-608.
249. Chujo, Y.; Sada, K.; Saegusa, T., Cobalt (III) bipyridyl-branched polyoxazoline complex as a thermally and redox reversible hydrogel. *Macromolecules* **1993**, *26* (24), 6320-6323.
250. Chujo, Y.; Sada, K.; Saegusa, T., Iron (II) bipyridyl-branched polyoxazoline complex as a thermally reversible hydrogel. *Macromolecules* **1993**, *26* (24), 6315-6319.
251. Chujo, Y.; Sada, K.; Saegusa, T., Reversible gelation of polyoxazoline by means of Diels-Alder reaction. *Macromolecules* **1990**, *23* (10), 2636-2641.
252. Chujo, Y.; Sada, K.; Saegusa, T., Polyoxazoline having a coumarin moiety as a pendant group. Synthesis and photogelation. *Macromolecules* **1990**, *23* (10), 2693-2697.
253. Chujo, Y.; Yoshifuji, Y.; Sada, K.; Saegusa, T., A novel nonionic hydrogel from 2-methyl-2-oxazoline. *Macromolecules* **1989**, *22* (3), 1074-1077.
254. Farrugia, B. L.; Kempe, K.; Schubert, U. S.; Hoogenboom, R.; Dargaville, T. R., Poly(2-oxazoline) hydrogels for controlled fibroblast attachment. *Biomacromolecules* **2013**, *14* (8), 2724-2732.
255. Luef, K. P.; Petit, C.; Ottersböck, B.; Oreski, G.; Ehrenfeld, F.; Grassl, B.; Reynaud, S.; Wiesbrock, F., UV-mediated thiol-ene click reactions for the synthesis of drug-loadable and degradable gels based on copoly(2-oxazoline)s. *European Polymer Journal* **2017**, *88*, 701-712.
256. Hartlieb, M.; Pretzel, D.; Kempe, K.; Fritzsche, C.; Paulus, R. M.; Gottschaldt, M.; Schubert, U. S., Cationic poly(2-oxazoline) hydrogels for reversible DNA binding. *Soft Matter* **2013**, *9* (18), 4693-4704.
257. Englert, C.; Tauhardt, L.; Hartlieb, M.; Kempe, K.; Gottschaldt, M.; Schubert, U. S., Linear poly(ethylene imine)-based hydrogels for effective binding and release of DNA. *Biomacromolecules* **2014**, *15* (4), 1124-1131.
258. Teo, W. E.; Ramakrishna, S., A review on electrospinning design and nanofibre assemblies. *Nanotechnology* **2006**, *17* (14), R89-R106.
259. Dalton, P. D., Melt electrowriting with additive manufacturing principles. *Current Opinion in Biomedical Engineering* **2017**, *2*, 49-57.
260. Kalaoglu-Altan, O. I.; Verbraeken, B.; Lava, K.; Gevrek, T. N.; Sanyal, R.; Dargaville, T.; De Clerck, K.; Hoogenboom, R.; Sanyal, A., Multireactive poly(2-oxazoline) nanofibers through electrospinning with crosslinking on the fly. *ACS Macro Letters* **2016**, *5* (6), 676-681.
261. Stubbe, B.; Li, Y.; Vergaelen, M.; Van Vlierberghe, S.; Dubruel, P.; De Clerck, K.; Hoogenboom, R., Aqueous electrospinning of poly(2-ethyl-2-oxazoline): Mapping the parameter space. *European Polymer Journal* **2017**, *88*, 724-732.
262. Li, Y.; Vergaelen, M.; Pan, X.; Du Prez, F. E.; Hoogenboom, R.; De Clerck, K., In situ cross-linked nanofibers by aqueous electrospinning of selenol-functionalized poly(2-oxazoline)s. *Macromolecules* **2018**, *51* (15), 6149-6156.
263. Hochleitner, G.; Hümmer, J. F.; Luxenhofer, R.; Groll, J., High definition fibrous poly(2-ethyl-2-oxazoline) scaffolds through melt electrospinning writing. *Polymer* **2014**, *55* (20), 5017-5023.
264. Lorson, T.; Jaksch, S.; Lübtow, M. M.; Jüngst, T.; Groll, J.; Lühmann, T.; Luxenhofer, R., A thermogelling supramolecular hydrogel with sponge-like morphology as a cytocompatible bioink. *Biomacromolecules* **2017**, *18* (7), 2161-2171.
265. Pöppler, A.-C.; Lübtow, M. M.; Schlauersbach, J.; Wiest, J.; Meinel, L.; Luxenhofer, R., Loading-dependent structural model of polymeric micelles encapsulating curcumin by solid-state NMR spectroscopy. *Angewandte Chemie International Edition* **2019**, *58* (51), 18540-18546.
266. Sochor, B.; Düdükü, Ö.; Lübtow, M. M.; Schummer, B.; Jaksch, S.; Luxenhofer, R., Probing the complex loading-dependent structural changes in ultrahigh drug-loaded polymer micelles by small-angle neutron scattering. *Langmuir* **2020**, *36* (13), 3494-3503.

267. Lübtow, M. M.; Marciniak, H.; Schmiedel, A.; Roos, M.; Lambert, C.; Luxenhofer, R., Ultra-high to ultra-low drug-loaded micelles: Probing host-guest interactions by fluorescence spectroscopy. *Chemistry* **2019**, *25* (54), 12601-12610.
268. Shi, Y.; van Steenberg, M. J.; Teunissen, E. A.; Novo, L.; Gradmann, S.; Baldus, M.; van Nostrum, C. F.; Hennink, W. E., π - π stacking increases the stability and loading capacity of thermosensitive polymeric micelles for chemotherapeutic drugs. *Biomacromolecules* **2013**, *14* (6), 1826-1837.
269. Eisner, D. A., Reproducibility of science: Fraud, impact factors and carelessness. *Journal of Molecular and Cellular Cardiology* **2018**, *114*, 364-368.
270. Hwang, D.; Ramsey, J. D.; Kabanov, A. V., Polymeric micelles for the delivery of poorly soluble drugs: From nanoformulation to clinical approval. *Advanced Drug Delivery Reviews* **2020**, *156*, 80-118.
271. Hwang, D.; Vinod, N.; Skoczen, S. L.; Ramsey, J. D.; Snapp, K. S.; Montgomery, S. A.; Wang, M.; Lim, C.; Frank, J. E.; Sokolsky-Papkov, M.; Li, Z.; Yuan, H.; Stern, S. T.; Kabanov, A. V., Bioequivalence assessment of high-capacity polymeric micelle nanoformulation of paclitaxel and Abraxane® in rodent and non-human primate models using a stable isotope tracer assay. *Biomaterials* **2021**, *278*, 121140.
272. Smith, A. M.; Williams, R. J.; Tang, C.; Coppo, P.; Collins, R. F.; Turner, M. L.; Saiani, A.; Ulijn, R. V., Fmoc-diphenylalanine self assembles to a hydrogel via a novel architecture based on π - π interlocked β -Sheets. *Advanced Materials* **2008**, *20* (1), 37-41.
273. Murnen, H. K.; Rosales, A. M.; Jaworski, J. N.; Segalman, R. A.; Zuckermann, R. N., Hierarchical self-assembly of a biomimetic diblock copolypeptoid into homochiral superhelices. *Journal of the American Chemical Society* **2010**, *132* (45), 16112-16119.
274. Birchall, L. S.; Roy, S.; Jayawarna, V.; Hughes, M.; Irvine, E.; Okorogheye, G. T.; Saudi, N.; De Santis, E.; Tuttle, T.; Edwards, A. A., Exploiting CH- π interactions in supramolecular hydrogels of aromatic carbohydrate amphiphiles. *Chemical Science* **2011**, *2* (7), 1349-1355.
275. Ma, M.; Kuang, Y.; Gao, Y.; Zhang, Y.; Gao, P.; Xu, B., Aromatic-aromatic interactions induce the self-assembly of pentapeptidic derivatives in water to form nanofibers and supramolecular hydrogels. *Journal of the American Chemical Society* **2010**, *132* (8), 2719-2728.
276. Xing, B.; Yu, C.-W.; Chow, K.-H.; Ho, P.-L.; Fu, D.; Xu, B., Hydrophobic interaction and hydrogen bonding cooperatively confer a vancomycin hydrogel: A potential candidate for biomaterials. *Journal of the American Chemical Society* **2002**, *124* (50), 14846-14847.
277. Fielding, L. A.; Lane, J. A.; Derry, M. J.; Mykhaylyk, O. O.; Armes, S. P., Thermo-responsive diblock copolymer worm gels in non-polar solvents. *Journal of the American Chemical Society* **2014**, *136* (15), 5790-5798.
278. Warren, N. J.; Armes, S. P., Polymerization-induced self-assembly of block copolymer nano-objects via RAFT aqueous dispersion polymerization. *Journal of the American Chemical Society* **2014**, *136* (29), 10174-10185.
279. Ratcliffe, L. P. D.; Derry, M. J.; Ianiro, A.; Tuinier, R.; Armes, S. P., A single thermoresponsive diblock copolymer can form spheres, worms or vesicles in aqueous solution. *Angewandte Chemie International Edition* **2019**, *58* (52), 18964-18970.
280. Robertson, E. J.; Nehls, E. M.; Zuckermann, R. N., Structure-rheology relationship in nanosheet-forming peptoid monolayers. *Langmuir* **2016**, *32* (46), 12146-12158.
281. Robertson, E. J.; Battigelli, A.; Proulx, C.; Mannige, R. V.; Haxton, T. K.; Yun, L.; Whitlam, S.; Zuckermann, R. N., Design, synthesis, assembly, and engineering of peptoid nanosheets. *Accounts of Chemical Research* **2016**, *49* (3), 379-389.
282. Cui, S.; Yu, L.; Ding, J., Semi-bald micelles and corresponding percolated micelle networks of thermogels. *Macromolecules* **2018**, *51* (16), 6405-6420.

8 Materials and Methods

All publications listed under “**List of Publications**” exhibit detailed material and methods sections, either in the main text or in the supporting information (SI) files. No other materials or methods than listed there were performed.

For the manuscripts **M5**, **M8**, **M10**, **M12** in the SI files additional methods, results and the detailed characterization of the synthesized monomers and polymers are presented. Furthermore, a printing video for the hydrogel established in **M8** is available. In the following the SI files are listed:

M5

https://pubs.acs.org/doi/suppl/10.1021/acsami.9b21282/suppl_file/am9b21282_si_001.pdf

M8

https://pubs.acs.org/doi/suppl/10.1021/acs.biomac.1c00427/suppl_file/bm1c00427_si_001.pdf

https://pubs.acs.org/doi/suppl/10.1021/acs.biomac.1c00427/suppl_file/bm1c00427_si_002.mp4

M10

<https://onlinelibrary.wiley.com/action/downloadSupplement?doi=10.1002%2Fmacp.202100114&file=macp202100114-sup-0001-SuppMat.pdf>

M12

<https://chemrxiv.org/engage/api-gateway/chemrxiv/assets/orp/resource/item/612cfeecd5f080d3a9b6809f/original/phe-ozu-gelation-mechanism-si-chem-rxiv.pdf>

In the case of **M2** and **M7**, the detailed material and method section can be found in the SI file.

M2

https://pubs.acs.org/doi/suppl/10.1021/acs.biomac.8b00708/suppl_file/bm8b00708_si_001.pdf

M7

<https://onlinelibrary.wiley.com/action/downloadSupplement?doi=10.1002%2Fmabi.202100122&file=mabi202100122-sup-0001-SuppMat.pdf>

Declaration of Authorship

Investigating the Influence of Aromatic Moieties on the Formulation of Hydrophobic Natural Products and Drugs in Poly(2-oxazoline)-Based Amphiphiles					
Hahn L., Lübtow M.M., Lorson T., Schmitt F., Appelt-Menzel A., Schobert R., Luxenhofer R., <i>Biomacromolecules</i> 2018 , 19 (7), 3119-3128.					
Participated in	Author Initials , Responsibility decreasing from left to right				
Study Design and Methods Development	LR	SR	HL, LMM		
Data Collection	HL, LMM	LT	SF, AMA		
Data Analysis and Interpretation	HL, LMM	LR	SR	AMA	
Manuscript Writing	HL, LR	LMM	LT, SR	SF, AMA	
Writing of Introduction					
Writing of Materials & Methods					
Writing of Discussion					
Writing of First Draft					
Writing of Supporting Information					

Inverse Thermogelation of Aqueous Triblock Copolymer Solutions into Macroporous Shear Thinning 3D Printable Inks					
Hahn L., Maier M., Stahlhut P., Beudert M., Flegler V., Forster S., Altmann A., Töppke, F., Fischer K., Seiffert S., Böttcher B., Lühmann T., Luxenhofer R., <i>ACS Applied Materials and Interfaces</i> 2020 , 12 (11), 12445-12456.					
Participated in	Author Initials , Responsibility decreasing from left to right				
Study Design and Methods Development	HL,LR,	MM, SP, AA, FK, SS, BM, FV, FS			
Data Collection	HL	MM, SP, BM, FV, FS, AA, TF, FK	FT		
Data Analysis and Interpretation	HL, LR	FK, SP, BM,	AA, MM, FS, FV, FT	SS, BB, LT	
Manuscript Writing	HL, LR	BM, SP, FK	AA, MM, FV, FS, TF, SS,	BB, LT	
Writing of Introduction					
Writing of Materials & Methods					
Writing of Discussion					
Writing of First Draft					
Writing of Supporting Information					

An Inverse Thermogelling Bioink Based on an ABA Type Poly(2-oxazoline) Amphiphile
Hahn L., Karakaya E., Zorn T., Sochor B., Maier M., Stahlhut P., Forster S., Fischer K., Seiffert S., Pöppler A.-C., Detsch R., Luxenhofer R.,
Biomacromolecules, **2021**, 22 (7), 3017-3027.

Participated in	Author Initials , Responsibility decreasing from left to right				
Study Design Methods Development	HL	LR	SB		
Data Collection	HL	SB, SP, ZT, KE, FK	FS	MM	
Data Analysis and Interpretation	HL, LR	SB	ZT, PAC, SP	FK, SS, DR, KE	FS
Manuscript Writing Writing of Introduction Writing of Materials & Methods Writing of Discussion Writing of First Draft Writing of Supporting Information	HL, LR	PAC, SB	KE, DR	MM, FK, SS	FS, SP

From Thermogelling Hydrogels towards Functional Bioinks: Controlled Modification and Cytocompatible Crosslinking
Hahn L.*, Beudert M.*, Gutmann M., Keßler L., Stahlhut P., Fischer L., Karakaya E., Lorson T., Thievensen I., Detsch R., Lühmann T., Luxenhofer R.,
Macromolecular Bioscience, **2021**, <https://doi.org/10.1002/mabi.202100122>

*Contributed equally to this manuscript

Participated in	Author Initials , Responsibility decreasing from left to right				
Study Design Methods Development	HL, BM, LR, LT	GM, LT			
Data Collection	HL, BM	GM, KL	SP, KE	FL	
Data Analysis and Interpretation	HL, BM, LR, LT	GM, SP, KE	TI, DR		
Manuscript Writing Writing of Introduction Writing of Materials & Methods Writing of Discussion Writing of First Draft Writing of Supporting Information	HL, BM, LR, LT	GM,	FL, KE, TI, DR		

ABA Type Amphiphiles with Poly(2-benzhydryl-2-oxazine) Moieties: Synthesis, Characterization and Inverse Thermogelation

Hahn L., Keßler L., Polzin L., Fritze L., Forster S., Helten H., Luxenhofer R.,
Macromolecular Chemistry and Physics, **2021**, <https://doi.org/10.1002/macp.202100114>

Participated in	Author Initials, Responsibility decreasing from left to right				
Study Design Methods Development	HL, LR				
Data Collection	HL	KL	PL	FL, FS	
Data Analysis and Interpretation	HL, LR	KL, PL, FL	FS	HH	
Manuscript Writing Writing of Introduction Writing of Materials & Methods Writing of Discussion Writing of First Draft Writing of Supporting Information	HL, LR	FL, HH	KL, PL		

Unravelling a Novel Mechanism in Polymer Self-Assemblies: An Order-Order Transition Based on Molecular Interactions Between Hydrophilic and Hydrophobic Polymer Blocks

Hahn L., Zorn T., Kehrein J., Kielholz T., Ziegler A.-L., Forster S., Sochor B., Lisitsyna E.S., Durandin N., Laaksonen T., Aseyev V., Sottriffer C., Windbergs M., Pöppler A.-C., Luxenhofer R.,
ChemRxiv. Cambridge: Cambridge Open Engage; 2021; This content is a preprint and has not been peer-reviewed.

Participated in	Author Initials, Responsibility decreasing from left to right				
Study Design and Methods Development	LR, HL	ZT, KJ, KT, LES, DN, PAC	SB, LT, AV, SC, WM	ZAL	FS
Data Collection	HL, ZT, KJ, KT, SB, LES, PAC	ZAL, FS, DN	AV		
Data Analysis and Interpretation	LR, HL, PAC	ZT, KJ, KT, SB, LES, DN, LT, AV, SC, WM	ZAL	FS	
Manuscript Writing Writing of Introduction Writing of Materials & Methods Writing of Discussion Writing of First Draft Writing of Supporting Information	HL, LR	PAC, KJ, SB, LES, DN,	KT, ZAL, LT, AV,	ZT, WM, SC	

The doctoral researcher confirms that she/he has obtained permission from both the publishers and the co-authors for legal second publication.

The doctoral researcher and the primary supervisor confirm the correctness of the above mentioned assessment.

_____ Doctoral Researcher's Name	_____ Date	_____ Place	_____ Signature
Robert Luxenhofer	13.10.2021	Helsinki	
_____ Primary Supervisor's Name	_____ Date	_____ Place	_____ Signature

Investigating the Influence of Aromatic Moieties on the Formulation of Hydrophobic Natural Products and Drugs in Poly(2-oxazoline)-Based Amphiphiles

Hahn L., Lübtow M.M., Lorson T., Schmitt F., Appelt-Menzel A., Schobert R., Luxenhofer R., *Biomacromolecules* **2018**, 19 (7), 3119-3128.

Figure	Author Initials, Responsibility decreasing from left to right				
1	SF	AMA	LMM	LR	HL
2	HL	LMM	LR		
3	HL	LMM	LR		
4	HL	LMM	LR		
5	HL	LT	LMM	LR	
6	HL	LT	LMM	LR	
Table	Author Initials, Responsibility decreasing from left to right				
1	HL	LMM	LR		
Scheme	Author Initials, Responsibility decreasing from left to right				
1	LR	HL			
2	HL	LR	LMM		
TOC	Author Initials, Responsibility decreasing from left to right				
	HL	LMM	LR		

Inverse Thermogelation of Aqueous Triblock Copolymer Solutions into Macroporous Shear Thinning 3D Printable Inks

Hahn L., Maier M., Stahlhut P., Beudert M., Flegler V., Forster S., Altmann A., Töppke, F., Fischer K., Seiffert S., Böttcher B., Lühmann T., Luxenhofer R., *ACS Applied Materials and Interfaces* **2020**, 12 (11), 12445-12456.

Figure	Author Initials, Responsibility decreasing from left to right				
1	HL	FK	FV, FS, TF	LR	BB,SS
2	HL	MM	LR		
3	HL	FS, FV	LR	BB	
4	HL	LR			
5	HL	LR			
6	HL	LR			
7	HL	LR			
8	SP	HL, LR			
9	BM	HL	LR	LT	
10	HL, AA	LR			
11	HL, AA	LR			
Table	Author Initials, Responsibility decreasing from left to right				
1	HL	MM, TF	LR		
2	HL	LR			
Scheme	Author Initials, Responsibility decreasing from left to right				
1	LR	HL			
TOC	Author Initials, Responsibility decreasing from left to right				
	HL	LR			

An Inverse Thermogelling Bioink Based on an ABA Type Poly(2-oxazoline) Amphiphile
Hahn L., Karakaya E., Zorn T., Sochor B., Maier M., Stahlhut P., Forster S., Fischer K., Seiffert S., Pöppler A.-C., Detsch R., Luxenhofer R.,
Biomacromolecules, **2021**, 22 (7), 3017-3027.

Figure	Author Initials , Responsibility decreasing from left to right				
1	HL	LR	FK	MM, FS	SS
2	HL	LR	PAC		
3	SB	ZT	HL	PAC, LR	
4	HL	SP	LR		
5	HL	KE, DR	LR		
6	KE	HL	DR, LR		
Scheme	Author Initials , Responsibility decreasing from left to right				
1	HL	LR			
2	HL	LR	SB		
TOC	Author Initials , Responsibility decreasing from left to right				
	LR	HL			

From Thermogelling Hydrogels towards Functional Bioinks: Controlled Modification and Cytocompatible Crosslinking

Hahn L.*, Beudert M.*, Gutmann M., Keßler L., Stahlhut P., Fischer L., Karakaya E., Lorson T., Thievensen I., Detsch R., Lühmann T., Luxenhofer R.,

Macromolecular Bioscience, **2021**, <https://doi.org/10.1002/mabi.202100122>

*Contributed equally to this manuscript

Figure	Author Initials , Responsibility decreasing from left to right				
1	BM	HL	GM	LT, LR	
2	HL	BM	KL	LT, LR	
3	HL	BM	KL	LR	
4	HL	BM	SP	GM, LT, LR	
5	HL, BM				
6	BM	GM, HL	FL, TI	TL, LR	
7	BM	GM	HL	TL, LR	
TOC	Author Initials , Responsibility decreasing from left to right				
	BM	HL	GM	LT, LR	

ABA Type Amphiphiles with Poly(2-benzhydryl-2-oxazine) Moieties: Synthesis, Characterization and Inverse Thermogelation					
Hahn L., Keßler L., Polzin L., Fritze L., Forster S., Helten H., Luxenhofer R., <i>Macromolecular Chemistry and Physics</i> , 2021 , https://doi.org/10.1002/macp.202100114					
Figure	Author Initials , Responsibility decreasing from left to right				
1	HL	KL	LR		
2	FL	HL	HH, LR		
3	HL	KL			
4	HL	PL	KL	LR	
5	HL				
6	HL				
7	HL				
8	HL				
9	FS	HL	LR		
Table	Author Initials , Responsibility decreasing from left to right				
1	HL				
2	HL	PL	LR		
TOC	Author Initials , Responsibility decreasing from left to right				
	HL	LR			

Publication:					
Unravelling a Novel Mechanism in Polymer Self-Assemblies: An Order-Order Transition Based on Molecular Interactions Between Hydrophilic and Hydrophobic Polymer Blocks					
Hahn L., Zorn T., Kehrein J., Kielholz T., Ziegler A.-L., Forster S., Sochor B., Lisitsyna E.S., Durandin N., Laaksonen T., Aseyev V., Sottriffer C., Windbergs M., Pöppler A.-C., Luxenhofer R., <i>ChemRxiv. Cambridge: Cambridge Open Engage; 2021; This content is a preprint and has not been peer-reviewed.</i>					
Figure	Author Initials , Responsibility decreasing from left to right				
1	HL	LR			
2	KT, SB, LES, DN,	HL, LR	WM, LT		
3	ZT, HL	PAC	LR		
4	ZT, HL	PAC	LR		
5	PAC				
6	KJ	HL	LR, SC		
7	KJ	HL	LR, SC		
8	ZAL	HL, LR	AV		

I also confirm my primary supervisor's acceptance.

Doctoral Researcher's Name

Date

Place

Signature

Affidavit

I hereby confirm that my thesis entitled “**Novel Thermoresponsive Hydrogels Based on Poly(2-oxazoline)s and Poly(2-oxazine)s and their Application in Biofabrication**” is the result of my own work. I did not receive any help or support from commercial consultants. All sources and/or materials applied are listed and specified in the thesis.

Furthermore, I confirm that this thesis has not yet been submitted as a part of another examination process neither in identical nor in similar form.

Eidesstattliche Erklärung

Hiermit erkläre ich an Eides statt, die Dissertation „**Neuartige Thermoresponsive Hydrogele Basierend auf Poly(2-oxazoline) und Poly(2-oxazine) und die Anwendung in der Biofabrikation**“ eigenständig, d.h. insbesondere selbstständig und ohne Hilfe eines kommerziellen Promotionsberaters, angefertigt und keine anderen als die von mir angegeben Quellen und Hilfsmittel verwendet zu haben.

Ich erkläre außerdem, dass die Dissertation weder in gleicher noch in ähnlicher Form bereits in einem anderen Prüfungsverfahren vorgelegen hat.

Curriculum Vitae

Lukas Hahn (born: 19.02.1992, Haßfurt, Germany)

Professional Experience

Since 01.11.2021 Scientific Coworker Julius-Maximilians University Würzburg

Pharmaceutical Technology and Food Technology, Institute for Pharmacy and Food Chemistry, Department of Chemistry and Pharmacy, Am Hubland, 97074, Würzburg

01.08.2018-31.10.2021 Scientific Coworker Julius-Maximilians University Würzburg

Functional Polymer Materials, Chair for Advanced Materials Synthesis, Institute for Functional Materials and Biofabrication, Department of Chemistry and Pharmacy, Röntgenring 11, 97070, Germany

16.11.2017-31.07.2018 BASF Coatings GmbH Würzburg

Academic Education

01.10.2015-30.09.2017 Natural products and drug chemistry (M.Sc.) University Bayreuth

01.10.2012-30.09.2015 Biochemistry (B.Sc.) Julius-Maximilians University Würzburg

01.10.2011-30.09.2012 Functional Materials (2 Semester) Julius-Maximilians University Würzburg